Imperial College London

Department of Mechanical Engineering

Simulation and Feedback Control of the Flow Past the Ahmed body

Dania Elsadig Elmammon Ahmed

July 26, 2023

Submitted in part fulfilment of the requirements for the degree of Doctor of Philosophy in Mechanical Engineering of Imperial College London

Declaration of Originality

I hereby declare that the results presented in this thesis are my own research work. The information taken from other sources, whether published or not are cited in the body of the text. The findings reported throughout this thesis have been presented at several conferences and published in scientific journals, as listed in page 1.

Abstract

This research investigates the turbulent flow past a blunt bluff body. The square-back Ahmed body is considered a canonical bluff body, representing a simplified road vehicle. Wall resolving Large Eddy Simulations (LES) were used to investigate the dynamics of the unforced flow and accordingly inform control strategies for drag reduction.

The turbulent wake behind a square-back Ahmed body in close proximity to the ground exhibits bi-modal switching. This manifests as the centre of the wake switching between one of two asymmetric positions, either horizontally or vertically. Switches occur over random timescales, with the wake recovering symmetry in the long time-average. The present work investigates numerically feedback control for suppressing horizontal (lateral) wake bi-modality of a square-back Ahmed body at $Re_H \sim 3.3 \times 10^4$ based on the body height. Base-mounted pressure sensors are used to estimate the position of the wake as an input signal for the controller, while actuation targets the near-wake region via synthetic jets emanating from a gap around the perimeter of the Ahmed body base. A nonlinear feedback controller based on a Langevin model of the wake dynamics is synthesised. This successfully suppresses the wake lateral bi-modal switching. However, this switching is replaced by a time-periodic streamwise motion of the large coherent structure occupying the near-wake region. Further, the controller amplifies the higher frequency dynamical wake modes. The action of feedback control also leads to base pressure recovery and a reduction in pressure drag. A trade-off between the degree of bi-modality suppression and drag reduction is observed upon varying the controller parameters. A maximum drag reduction of 7.4% is achieved for a semi-symmetrised wake, with a fully symmetrised wake achieving a 2.5% reduction.

Wake bi-modality is found to be sensitive to different parameters, including the free stream turbulent intensity, the underbody flow and the dynamics of the upstream boundary layers developed along the longitudinal surfaces. Boundary layers separate and reattach close to the body's fore-end before reaching the base. Following this recently-established link by Hesse and Morgans (2021), the second part of this research investigates the effect of suppressing boundary layer separations on wake bi-modality. Hairpin vortices, formed at the reattachment points, grow along the surfaces before breaking down upstream of the base. The resultant smaller vortices from the top and side surfaces interact as they are convected downstream, which is suggested to be a trigger of the wake bi-modal switching. Suppressing boundary layer separations interrupts this interaction, which is found to have a damping effect on the fluctuations just upstream of the base. Steady suction was applied on the longitudinal surfaces of the body to suppress boundary layer separations. The results showed that horizontal bi-modality is completely suppressed by suppressing the separation

of the boundary layers on the surfaces normal to the switching direction without affecting the vertical wake position. Different configurations for suppressing boundary layer separations affect the momentum and the turbulent kinetic energy of underbody flow. The wake can fully be symmetrised by reducing the momentum of the underbody flow with a reflected vertical asymmetric position. The results of these cases open doors for using feed-forward controllers with actuation significantly upstream the base separation to reduce the drag rather than forcing the wake directly, which involves some trade-offs between different dynamics in the wake.

Acknowledgements

I would like to express my sincere gratitude to my supervisor, Prof. Aimee S. Morgans. This work would never have been achieved without her support, technical guidance, and encouragement. She was always open to discussing and pursuing new ideas. She supports me in securing extra funding. I strongly appreciate her flexibility in dealing with the research during the uncertain pandemic period. I appreciate having this chance to work under her supervision.

I would also like to thank the Islamic Development Bank (IsDB), Gordon Memorial College Trust and the British Federation of Women Graduates for funding this research. I extend my thanks to Imperial High-Performance Computing (HPC), the UK National Supercomputer ARCHER and ARCHER2 and the UK Turbulence Consortium for providing the computational facilities for this research. I would like to thank Morgans' lab team, who were quite supportive and created a unique research environment. Special thanks to Dr. Juan Guzman Inigo for the brainstorming discussions and continuous support. Dr. Faron Hesse, who was an excellent guide from the start and kept his support throughout. I appreciate the time and discussions with Dr. Renaud Gaudron, Dr. Lionel Hirschberg, Dr. Xiao Hu, Dr. Dong Yang and Dr. Saikumar Reddy.

Finally, a sincere note of gratitude to my family and friends, who always had faith in me. Special thanks to my mother Dr. Lubna Abbadi, for her unwavering support. Special thanks to my sister Mariam, who motivates me to do my best.

Publications

Some of the results presented in this thesis have been presented in the following articles:

1. Ahmed, D. and Morgans, A., 2022, ”Wake bi-modality: the effect of upstream boundary layer dynamics”, Journal of Fluid Mechanics (submitted).

2. Ahmed, D. and Morgans, A., 2022, ”Nonlinear feedback control of bimodality in the wake of a three dimensional bluff body”, Physical Review Fluids 7, no. 8 (2022): 084401.

3. Ahmed, D., Hesse, F., Morgans, A., 2020, ”Nonlinear feedback control of the bi-modal flow behind a three-dimensional blunt bluff body”, 55th 3AF International Conference on Applied Aerodynamics, Poitiers, France.

Conferences

Some of the results presented in this thesis have been presented in the following conferences:

1. 14th European Fluid Mechanics conference, "Wake bi-modal switching and its dependence on the upstream bluff body boundary layers", 2022, Athens, Greece.

2. Parallel CFD conference, "Feedback control of the bi-modal flow behind a blunt bluff body", 2022, Alba, Italy.

3. Aerovehicles4, "Nonlinear feedback control of the bi-modal wake past an Ahmed body", 2021, Berlin, Germany.

4. 74th Annual Meeting of the APS Division of Fluid Dynamics, "Wake bi-modal switching and its dependence on the upstream bluff body boundary layers", 2021, Phoenix, USA.

5. 55th 3AF International Conference on Applied Aerodynamics, "Nonlinear feedback control of the bi-modal flow behind a three-dimensional blunt bluff body", 2021, Poitiers, France.

6. 73rd Annual Meeting of the APS Division of Fluid Dynamics, "Feedback control of the bi-modal flow behind a blunt bluff body", 2020, Chicago, USA.

7. UK Turbulence Consortium online talks; ”Towards industrial and real life cases”, 2020, London, UK.

8. UK Fluids Conference, "Non-linear feedback control of the bimodal behaviour behind a three-dimensional blunt bluff body", 2019, Cambridge, UK.

Contents

List of Figures

List of Tables

Nomenclature

$a(t)$	Time Coefficient
C	Height of the gap to ground
C_{ij}	Cross Stresses
C_μ	Momentum Coefficient
C_P	Pressure Coefficient
Δ	Cut-off width for LES
Δt	Time step
$D(t)$	Drag force
f	Frequency
H	Ahmed body Height
L	Ahmed body Length
l	Integral Length Scale
L_{ij}	Leonard Stresses
L_R	Length of the recirculation region
n_i	Unit vector of the face i
$P(x, y, z, t)$	Pressure
P_∞	Free Stream Pressure
Pw	Power
q	General Flow Property
R	Radius of the frontal edge of the Ahmed body

R_{ij}	Reynolds Stresses
$r(t)$	Centre of Pressure
S_i	Surface area of the face i
S_{ij}	Strain rate tensor
$S_{\Phi C}$	Linear source term
$S_{\Phi P}$	Nonlinear source term
St	Strouhal Number
t	Time
$u^{'}$	Fluctuated Velocity
u_i	velocity component in i^{th} direction
U_∞	Free stream Velocity
U_{jet}	Jet Velocity
$u(r)$	The Controlled signal
U_s	Suction Velocity
V	Volume of the control volume
$V(r)$	Lyapunov function
W	Ahmed body Width

Greek Symbols

α	Growth rate
δ	Boundary Layer Thickness
ϵ	Energy Dissipation Rate
η_{Actuator}	Actuator Efficiency
λ_Φ	Diffusivity of Φ
λ	Saturation Parameter
ν	Viscosity

Φ	General Flow Property (vector)
Φ_k	Spatial Modes
ρ	Fluid Density
σ^2	Noise Intensity
τ_{ij}	Sub-grid-scale Stresses

List of Abbreviations

2D	Two Dimensional
3D	Three Dimensional
BL	Boundary Layer
CFD	Computational Fluid Dynamics
CFL	Courant–Friedrichs–Lewy
CV	Control Volume
DES	Detached Eddy Simulations
DFT	Discrete Fourier Transform
DMD	Dynamic Mode Decomposition
DNS	Direct Numerical Simulations
EEA	European Environmental Agency
FFT	Fast Fourier Transform
FVM	Finite Volume Method
GHG	Greenhouse Gas
HDV	Heavy Duty Vehicles
ICE	Internal Combustion Engine
IDDES	Improved Delayed Detached Eddy Simulations
IEA	International Energy Agency
KH	Kelvin-Helmholtz

LDV Light Duty Vehicles

LES Large Eddy Simulations

MSD Mean Square Displacement

NS Navier-Stokes equation

OpenFOAM Open Source Field Operation and Manipulation

PANS Partially-Averaged Navier-Stokes

PDF Probability Density Function

PIMPLE Pressure IMplicit with splitting of operator for Pressure-Linked Equations

PISO Pressure Implicit with Splitting of Operator

POD Proper Orthogonal Decomposition

PSD Power Spectral Density

QUICK Quadratic Upwind Interpolation for Convective Kinematics

RANS Reynolds Average Navier Stokes

Re Reynolds Number

RSB Reflectional Symmetry Breaking

SB Separation Bubble

SGS Sub-Grid Scale

SIMPLE Semi-Implicit Method for Pressure-Linked Equations

SPOD Spectral Proper Orthogonal Decomposition

SVD Singular Value Decomposition

TKE Turbulent Kinetic Energy

TVD Total Variation Diminishing

WALE Wall-Adaptive Local Eddy-Viscosity

ZNMF Zero-Net-Mass-Flux

Chapter 1

Introduction

This chapter covers a brief discussion about the motivation behind this research, followed by the objective and the outlines of this thesis.

1.1 Motivation

Driven by the imperative of climate change associated with greenhouse gas (GHG) emissions, reducing the rapidly increasing energy demand is targeted. The International Energy Agency (IEA) reported that the transportation sector accounts for 27% of carbon dioxide emissions in 2018 (IEA, 2018). Transport emissions grow with an average annual rate of 1.7%, outweighing other sectors (IEA, 2022). Similarly, the European Environmental Agency (EEA) reported a decline in GHG emissions across different sectors except for transportation, in which the emissions are increased by 33% since 1990 (European Environmental Agency, 2022). The statistics of 2018 showed that transportation is responsible for 29% of total economy-wide GHG emissions in Europe (figure 1.1). The most significant contributor to this is the light-duty vehicles (LDV), which include passenger cars and vans. LDV is followed by heavy-duty vehicles (HDV), including trucks and busses, which contributes 5% to GHG emissions, as shown in figure 1.1. These figures only highlight the direct emissions from vehicles, excluding the fuel production processes. The recent rebound in transport activity after the COVID lockdowns increases GHG emissions. The EU commitment to reducing GHG emissions by 55% by 2030 and the "no net emission" by 2050, i.e. the European Green Deal, impose challenges for the transportation sector to reduce GHG emissions (Buysse and Miller, 2021).

GHG emissions are related to conventional road vehicles, where internal combustion engines (ICE) burn fuel to overcome the aerodynamic drag, the vehicle's inertia and the rolling resistance. Figure 1.2 compares the power consumption for the aerodynamic drag and the rolling resistance as a function of the vehicle speed. It can be seen that the aerodynamic drag increases rapidly

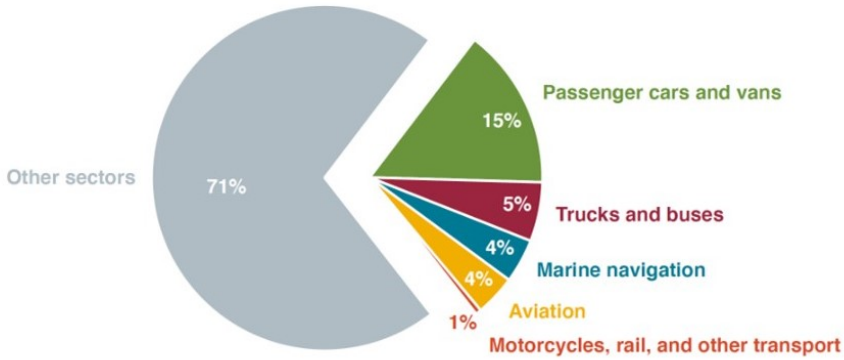

Figure 1.1: 2018 statistics of the GHG emissions from the transport sector in the EU, adapted from Buysse and Miller (2021).

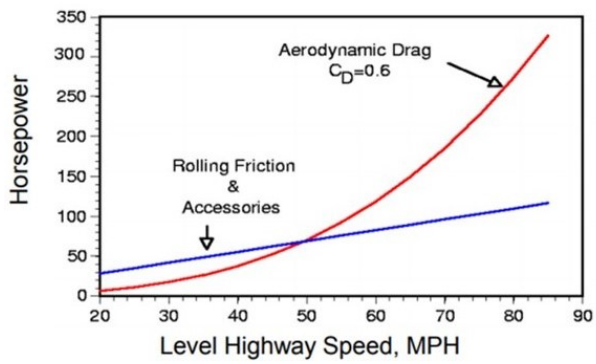

Figure 1.2: Power required to overcome the rolling friction and the aerodynamic drag as function of the vehicle speed, adapted from Office of Scientific and Technical Information (U.S. Department of Energy) (2000).

with speed compared to the rolling resistance, making it an essential element in reducing GHG emissions. The recent development of electric vehicles (EVs) is expected to reduce GHG emissions. A reduction of 3.3 mb/d in fuel consumption is expected by 2040, if half of the total LDV fleet is replaced by electric vehicles (IEA, 2018). The uptake of EVs faces different challenges, such as the range anxiety, charging anxiety, charging time and purchase cost (Burkert et al., 2021). Range anxiety was the most commonly reported concern amongst potential EV buyers in the UK (Berkeley et al., 2018). This anxiety is caused by the driver's perception of not having enough range to reach the destination. The range of EVs depends on different design factors, which include batteries' capacity, aerodynamic drag and the size/weight of the electric motor (Mruzek et al., 2016). A reduction of 0.01 in aerodynamic drag increases the EV's range by 2.5% (based on Mercedes Vision EQXX model) (Hubbard, 2022). This confirms the importance of aerodynamic drag for the range of EVs.

Considering those figures, reducing the drag force of road vehicles is targeted. The aerodynamic drag of the road vehicle consumes at least 50% of the vehicle's power at typical high speeds (Hucho and Sovran, 1993, Moghaddam and Neishabouri, 2017). Two major components comprise

the aerodynamic drag; the pressure drag (also known as form drag) and the skin friction drag. The first causes approximately around 80% of the total aerodynamic drag, and it is essentially caused by the flow separation over the rear of the road vehicle, which creates a low-pressure wake region. The magnitude of the pressure drag force depends on the location of the flow separation and, consequently, the size and dynamics of the wake generated. Investigating the structures and topology of the wake generated behind the body is therefore essential to identify the form drag and inform the strategy of drag-reduction (Evstafyeva et al., 2017). Thus, controlling the flow separation is of immense importance in this case. Many techniques have been considered to control the flow separation, some preventing or delaying the separation occurrence, which affect the wake's size and topology. Other control techniques manipulate the wake topology by directly forcing the wake region (Choi et al., 2008). This research focuses on employing feedback control for reducing form drag for a flow past the canonical Ahmed body. Due to the fixed position of the flow separation point, in this case, drag reduction is targeted by forcing the wake region directly. Feedback control uses body-mounted pressure sensor signals to force the actuators at the vehicle's rear in response. A numerical technique to simulate the flow domain is employed to investigate the dynamical behaviours of the wake and their contribution to drag reduction.

1.2 Objectives

This research focuses on analysing the topology and dynamics of the turbulent wake behind the square-back Ahmed body numerically and designing a feedback control for drag reduction. The main objectives of this research are to:

1. Explore the potential of a non-linear model-based feedback controller to suppress wake bi-modality and investigate its effect on other dynamics behaviour in the wake.

2. Investigate the link between the bi-modal switching in the wake and the upstream boundary layer separations. This includes investigating different configurations of suppressing boundary layer separations, i.e. suppressing the top and bottom boundary layers, the boundary layers on the sides and all four longitudinal body surfaces.

3. Provide further understanding of the Ahmed body wake flow and its sensitivities to help inform future bi-modality suppression and drag reduction strategies.

1.3 Thesis outlines

This thesis is subdivided into eight chapters, as follows:

1. Chapter 2 covers a background about the flow past the square-back Ahmed body and the control techniques used to reduce drag.

2. Chapter 3 shows the mathematical basis of the flow simulations and the data analysis techniques used in this research.

3. Chapter 4 investigates the unforced flow past the square-back Ahmed body numerically and validates the results with the literature body.

4. Chapter 5 reviews different techniques for nonlinear model-based feedback control on a toy-model first, then investigates implementing them in the real case, with a detailed comparison of the wake flow in the presence and the absence of the control.

5. Chapter 6 explains the link between wake bi-modality and the upstream boundary layer separations just aft the body nose. This is done by investigating the wake flow in the absence of these separations.

6. Chapter 7 extends the investigation of the effect of upstream dynamics using reduced order modelling, the Spectral Proper Orthogonal Decomposition (SPOD).

7. Chapter 8 provides conclusions and outlook of this research.

Chapter 2

Background

This chapter covers an overview of the previous research on flow past bluff bodies and the different control methods for drag reduction. It is subdivided into two sections; the flow past bluff bodies and flow control.

2.1 Bluff Body Flows

The relevance of bluff bodies to the transportation industry drives the need for bluff body aerodynamic drag reduction, targeting a decrease in energy consumption. Ground vehicles such as lorries, buses and light-duty vehicles are classified as bluff bodies. Sudin et al. (2014) indicated that the aerodynamic drag consumes 50% of the total fuel burnt by a passenger car at typical highway speeds, compared to 65% for trucks, as reported by Seifert et al. (2009). The drag force exerted on a solid body moving in a fluid stream is classified into pressure drag and friction drag (Hucho, 1987). The former is related to the pressure difference between the frontal and rear sections of the body in the streamwise direction, while the latter is associated with the friction between the surfaces of the solid body and the moving fluid, i.e. the development of boundary layers. This is shown in figure 2.1 for a schematic of a car model. For bluff bodies, pressure drag (also known as form drag) dominates, constituting approximately 80% of the total drag in case of flow past an Ahmed body (Ahmed et al., 1984). This dominance makes pressure drag the focus of the studies targeting drag reduction.

The pressure drag of a bluff body primarily arises due to the pressure deficit on the rear part of the body caused by large-scale flow separation, which is forced by the abrupt change in the body geometry, as shown in figure 2.1. It depends on the location of flow separation as well as the dynamics and topology of the wake flow downstream of the body. For three-dimensional bluff bodies whose flow separation position is fixed, such as the axisymmetric bodies in the studies by

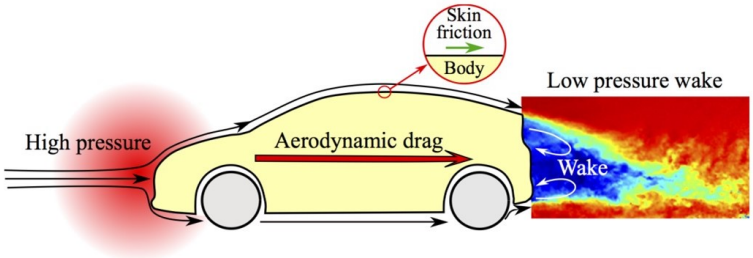

Figure 2.1: A sketch explaining the pressure and skin friction drag for a flow past a car model, adapted from Li (2017).

Figure 2.2: The general models of the canonical Ahmed body and the most relevant real road vehicles. The fast-back with the slant angle of α is shown in (a) and the square-back with $\alpha = 0$ is shown in (b), adapted from Choi et al. (2014).

Rigas et al. (2014), Grandemange et al. (2014a) and rectilinear bluff bodies (Ahmed et al., 1984, Duell and George, 1999, Krajnovic and Davidson, 2003), some key common dynamical features can be identified. These include the development of multiple boundary layers along the surfaces of the body, which separate at the rear edges of the body, creating free shear layers which bound the recirculation region in the near wake. The recirculation region extends from the rear part of the body up to the so-called free stagnation point. The shear layers experience Kelvin-Helmholtz instability, thus amplifying disturbances in the wake downstream of the body. The interaction between each parallel pair of separated shear layers leads to coherent vortex shedding in the wake (Bearman, 1997, Grandemange et al., 2013a, Lahaye et al., 2014, Volpe et al., 2015). The whole recirculation region also exhibits a pumping motion in the streamwise direction, which is associated with oscillations of the free stagnation point in the wake (Duell and George, 1999, Khalighi et al., 2001, Verzicco et al., 2002).

2.1.1 Flow past the Ahmed body

The present research considers a three-dimensional blunt bluff body in the form of the square-back Ahmed body, representing a simplified road vehicle geometry. This geometry reproduces most of the essential flow features presented in the wake of an actual road vehicle. Two types of this

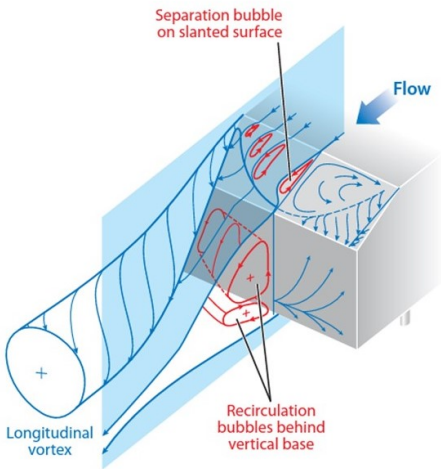

Figure 2.3: Time-averaged wake past the Ahmed body with a slant angle of α between the top and slant surfaces, adapted from Choi et al. (2014)

canonical geometry were presented in the literature, the slanted and the square-back Ahmed body, with zero slant angle (α), shown in figure 2.2. The time-averaged wake topology and characteristic frequencies of the Ahmed body were the focus of early studies by Ahmed et al. (1984) and Mason and Beebe (1978) and are now well-established. A slanted-back geometry was used in the study by Ahmed et al. (1984). In this case, the separation point on the body back, and accordingly the wake dynamics and the drag, depend on the slant angle α. In the time-averaged wake, when the flow separates and reattaches on the slanted surface, two counter-rotating longitudinal vortices were observed to emanate from the vertical sides. A pair of horseshoe vortices were observed in the near-wake region, as shown in figure 2.3, which form a ring vortex when the two horseshoe vortices have the same strength. Similarly, Barlow et al. (1999) used the time-averaged analysis to investigate the effect of the body aspect ratio on the drag coefficient. They intended to replicate the results of a commercial van, which showed that taller bodies exhibited relatively lower drag compared to shorter bodies, opposite to the trend reported in the literature. On the other hand, the time-averaged flow past the Ahmed body was simulated by Han (1989) using Reynolds Average Naiver-Stokes $K - \epsilon$ turbulence model, as one of the earliest numerical investigations. Later on, Krajnovic and Davidson (2003) simulated the flow past a simplified bus geometry at Reynolds number of 2.1×10^5, resolving coherent structures similar to those described by Ahmed et al. (1984). These include the ring vortex in the near wake region, W, and the longitudinal counter-rotating pair of vortices, P, further downstream in the wake, as shown in figure 2.4. Another pair of longitudinal corner vortices were evidenced, T, and a thin vortex core was captured around the base perimeter, B.

The focus was then shifted to investigate the unsteady flow field, as the dynamics of the instantaneous flow field have quite different features from that of time-averaged ones. This affects

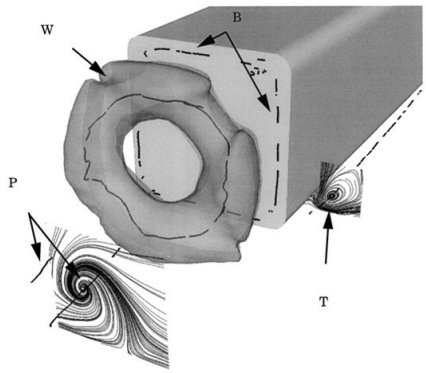

Figure 2.4: Time-averaged wake past the a simplified bus geometry, showing the ring vortex in the near wake region, W, using pressure iso-surfaces ($p = -0.2$) and the longitudinal vortex core, P, on one side of the wake, depicted with streamlines. This figure is adapted from Krajnovic and Davidson (2003).

the aerodynamic properties of the flow past road vehicles and informs different control strategies for drag reduction Choi et al. (2008, 2014). An unsteady behaviour of the wake past the square-back Ahmed body has recently been identified experimentally (Grandemange et al., 2012, 2013a,b), known as bi-modality, or bi-stability. It manifests as random switching of the wake between off-centred (asymmetric) preferred positions. While the time-averaged turbulent wake exhibits symmetry, instantaneously, the wake exhibits a random switching between two asymmetric states, with the timescales between switching events being relatively long. Similar wake-switching behaviour has been observed in the wakes of other bluff bodies. The laminar flow past a sphere at a sufficiently high Reynolds number exhibits axisymmetry breaking in the wake, which increases the drag, the degree of increase increasing with Reynolds number (Bouchet et al., 2006). A planar symmetry replaces axisymmetry in the laminar wake of blunt-based axisymmetric bodies. In the turbulent wake behind the latter, the rotational symmetry breaking is preserved, with a random dynamical behaviour in the azimuthal position of the symmetry plane (Rigas et al., 2014, 2015) – this is known as multi-modality or multi-stability. Similar behaviour is observed in the turbulent wake of the sphere (Grandemange et al., 2014a). Compared to axisymmetric bodies, the symmetry of the base surface of the square-back Ahmed body permits only two azimuthal positions of the wake, promoting bi-modality instead of multi-modality.

The evolution of instabilities in the wake of the Ahmed body follows a similar pattern to that alluded to for axisymmetric bodies. Reflectional Symmetry Breaking (RSB), observed initially in the laminar flow regime, first occurs when the Reynolds number exceeds a critical value, $Re_{critical}$. This value has been experimentally found to be 365 (based on body height) for the square-back Ahmed body with ground proximity of 60% of the body height (Grandemange et al., 2012). The value of $Re_{critical}$ was found to be inversely proportional to the clearance between the body and the

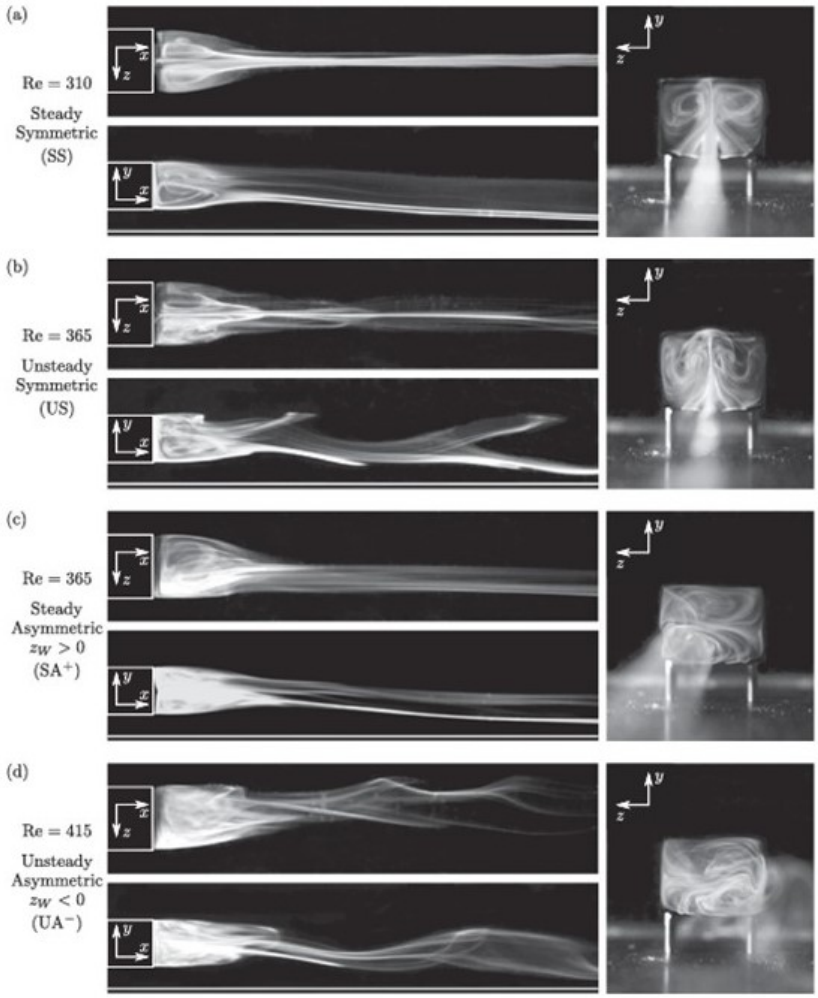

Figure 2.5: Top (xz), side (xy) and rear (yz) views of the wake past the square-back Ahmed body, indicates the evolution of instabilities as Re number increases from 310 to 415. This figure is adapted from Grandemange et al. (2012).

ground (Cadot et al., 2015). The steady horizontal symmetric state of the wake in the z direction (shown in figure 2.5a, at $Re = 310$) transitions to steady asymmetric (figure 2.5c) after a short unsteadiness period (figure 2.5b), as Re increases. The wake maintains this asymmetric state at higher Re numbers in the laminar flow regime. As Reynolds number increases, an unsteady bifurcation emerges, causing periodic vortex shedding in the wake, i.e. breaking the temporal symmetry in the wake. The same laminar flow sequence of *RSB* was captured numerically by Evstafyeva et al. (2017) using LES with an in-house Finite Volume Solver (FVM) as the first numerical investigation to capture *RSB*. The simulated flow field allowed a thorough wake description compared to the experiment. Their study showed that wake symmetry is associated with a centered vortex in the near-wake region, while *RSB* forced it towards one side of the base. It also concluded that the wake retains its horizontal asymmetry in the laminar flow regime.

In the turbulent regime, the *RSB* static modes arising from the laminar flow bifurcations have been shown to persist. However, turbulent perturbations now cause the wake to switch randomly between off-centred preferred positions (Rigas et al., 2015). The wake resides at one stable asymmetric position until it is sufficiently perturbed to be able to switch to the other reflected position. This behaviour is found to be Re-independent in the turbulent flow regime at least up to a value of Re of 3×10^6 (based on the body height), matching the scale of actual road vehicles in real driving conditions (Grandemange et al., 2013a). The asymmetric wake forces the horizontal vortex shedding to be one-sided following its asymmetry state. The associated topology shift is the skewness of the near wake toroidal-vortex towards and away from the base surface (Grandemange et al., 2013b, Kourta and Leclerc, 2013, Dalla Longa et al., 2019) – the instantaneous asymmetric position of the wake is correlated with the proximity of one of the sides of the toroidal-vortex structure to the base.

Bi-modality or random reflectional symmetry breaking (*RSB*) in the wake has been the subject of several recent experimental studies (Grandemange et al., 2012, 2013a,b, Cadot et al., 2015, Volpe et al., 2015, Brackston et al., 2016, Barros et al., 2017, Haffner et al., 2020, Plumejeau et al., 2020). It has been found to be a uni-directional behaviour that occurs either in the horizontal (side to side) or vertical (top-bottom) direction, depending on the aspect ratio of the body base, the ground proximity and the yaw angle. Grandemange et al. (2013a) mapped the direction of the bi-modality, for a 0° yaw angle, as a function of the base aspect ratio and the ground clearance, which affects the development of the under-body flow, shown in figure 2.6. Three regimes were identified depending on the ground proximity normalized by the body width, C^*. For low ground clearances, $C^* < 0.05$, horizontal switching occurred for $0.3 < H/W < 0.65$, where H and W are the base height and width, respectively. For slighter larger ground clearances, $0.05 < C^* < 0.09$, wake switching was inhibited as a result of the detachment of the under-body flow. For $C^* > 0.09$,

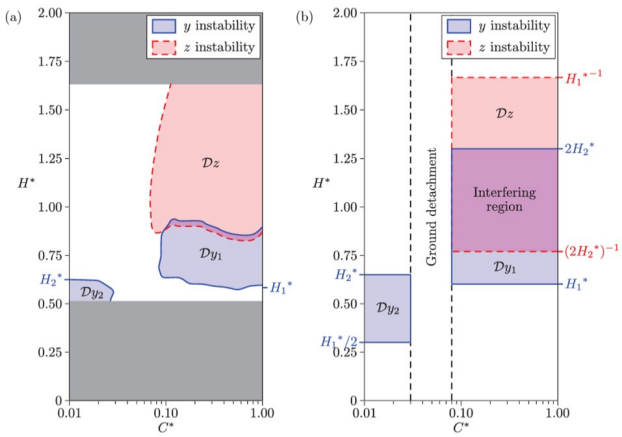

Figure 2.6: A map for bi-modality direction in the turbulent wake past a square-back Ahmed body, as a function the height to ground $C^* = C/W$ and the body height $H^* = H/W$, where W is the body width. Experimental data is shown on the left side, and model-based data is shown on the right. Note that the cross-flow directions y and z here represents the horizontal and vertical directions, respectively, and opposite to the directions used in this research. This figure is adapted from Grandemange et al. (2013a).

bi-modal switching occur in the direction of the longest edge. Plumejeau et al. (2020) recently investigated the effect of the under-body flow on the interactions of the wake dynamics, noting a change in the frequency of the vortex shedding mode accompanied by the transition of the wake from stable to bi-stable. Barros et al. (2017) investigated the sensitivity of the wake dynamics to disturbances induced in the under-body flow, introducing a coupling based on Langevin dynamics between the vertical wake asymmetry and the horizontal bi-modality. The study concluded that the sensitivity of the wake to the under-body flow could be represented by a bifurcation scenario, as the vertical asymmetric wake transitions to a horizontal bi-modal wake.

In terms of numerical investigations, Rao et al. (2018) captured the asymmetry state of the turbulent wake past the Ahmed body, using unsteady partially-averaged Navier-Stokes (PANS) simulations. Eddy-resolving techniques employing Large Eddy Simulations (LES) and Detached Eddy Simulations (DES) captured the spatial symmetry breaking of the wake but not the switching (Serre et al., 2013, Pasquetti and Peres, 2015, Lucas et al., 2017). Wassen et al. (2010) reported a low-frequency lateral motion in the wake using LES, although the phenomenon was not well-defined by then. This study is probably one of the first attempts to indicate the wake horizontal switching. The study of Dalla Longa et al. (2019) captured the bi-modal switching behaviour of the wake behind three-dimensional blunt bluff bodies; a square-back Ahmed body and a lorry model. The study employed wall-resolved LES to simulate the flow using a Finite Volume Solver. It suggested that wake-switching events are associated with a stochastic shedding of a hairpin vortex in the near wake region, as shown in figure 2.7. The figure depicts a top-to-bottom switching (vertical bi-modality) in the wake past a lorry model, with the skewed toroidal vortex indicating

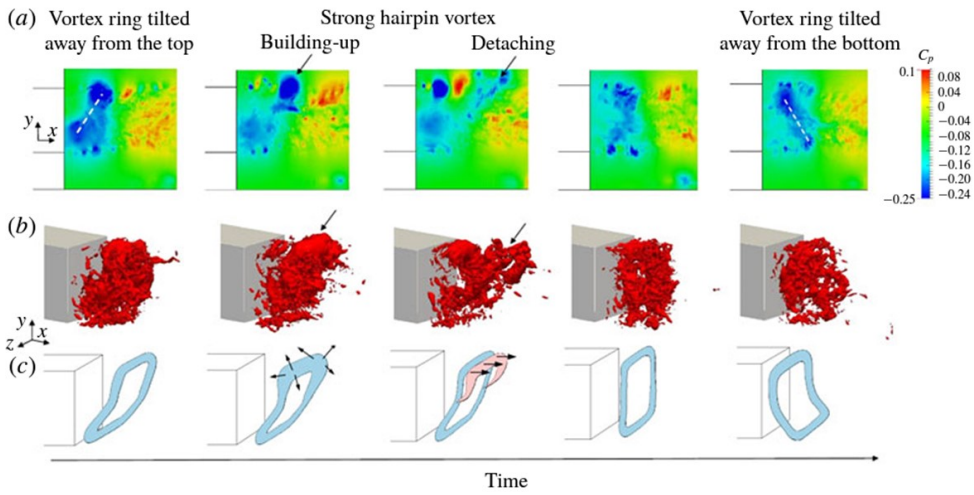

Figure 2.7: Vertical bi-modality, i.e. top to bottom switching event in the wake past a lorry, suggesting link between a stochastic shedding of the hairpin vortex and the wake switching. The top row shows time-resolved pressure coefficient on the central plane, the second row shows the toriodal vortex as an iso-surface of the pressure coefficient ($C_P = -0.2$) and the bottom row shows a schematic view of the switching event. This figure is adapted from Dalla Longa et al. (2019).

the asymmetric wake. The recent LES study by Hesse and Morgans (2021) suggested that the upstream separation bubble just aft of the body nose is linked to the wake switching. When this separation bubble and its associated disturbances are suppressed, the wake locks in one asymmetric position and random switching does not occur. The direct numerical simulation (DNS) results by Podvin et al. (2020) captured the deviation of the wake and indicated the same dynamics shown in the LES results except for bi-modality. Simulating wake bi-modality is challenging given its long and random time scales compared to other wake dynamics, requiring longer simulation time.

Wake bi-modality has been found to have implications for drag. The experimental study by Grandemange et al. (2013b) found that wake bi-modality contributes up to 9% to pressure drag and creates unfavourable side forces and moments that affect the stability of the body. Haffner et al. (2020) showed that the averaged base pressure coefficient reduced by 9% during the switching events of the wake compared to the asymmetric wake. The wake is instantaneously symmetric during these switching events, indicating that wake re-symmetrisation has a favourable effect on the base pressure and, consequently, the pressure drag. Previous studies presume that the wake's state affects the drag by influencing base pressure recovery. The effect of wake re-symmetrisation on drag has been exploited in passive and active flow control studies, which will be discussed in section 2.2.

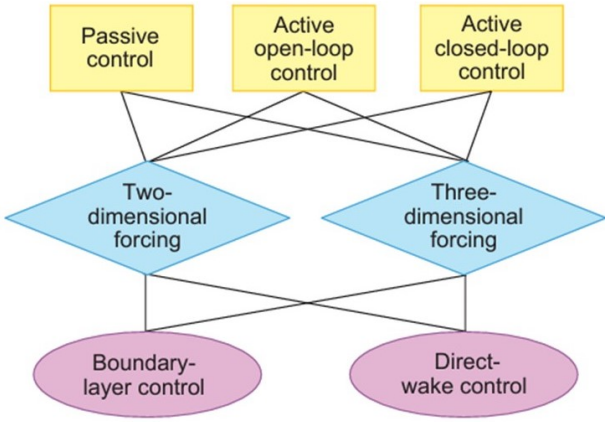

Figure 2.8: A schematic for the classification of the control methods used to control the flow past bluff bodies, adapted from Choi et al. (2008).

2.2 Flow Control

Flow control techniques are the methods by which the flow field dynamics are manipulated to achieve a specific goal, such as drag reduction, lift enhancement and noise suppression. Techniques of controlling the flow around the bluff body can be classified into three main categories based on the energy expenditure; passive, active open-loop (predetermined active control) and feedback (closed loop) control (figure 2.8) (Choi et al., 2008). Passive flow control methods require geometry modifications without any power input for actuation. Numerous passive techniques have been reported in the literature, such as modifying surface roughness, surface groves, helical wires, splitter plate, and secondary control cylinders. The most effective method for reducing drag is the geometric modifications near the flow separation point in the spanwise direction. Although most of these techniques prove successful in drag reduction, they are only rarely utilized industrially due to their impracticality for most applications (Choi et al., 2014). In addition, the controller loses its efficiency at the off-design operating points, which can enhance rather than suppress the drag (Flinois, 2015).

Active flow control methods utilise external power to control the flow field, whether open-loop or closed-loop. For open-loop flow control, actuators with power input are required without sensors, as in the closed-loop control, also known as feedback control. The main difference between the two methods is that the closed-loop controller actuates the flow based on the feedback signal from the sensors in the flow system, while in the open-loop case, the flow is actively actuated, neglecting the response of the flow system. Numerous studies have shown that forcing the wake of a two or three-dimensional bluff body at high frequencies reduces the drag and forces the vortices shed in the two shear layers to be in phase (Tokumaru and Dimotakis, 1991, Cabitza, 2014, Oxlade et al., 2015). Compared to passive flow control, active open-loop control has the advantage that it has

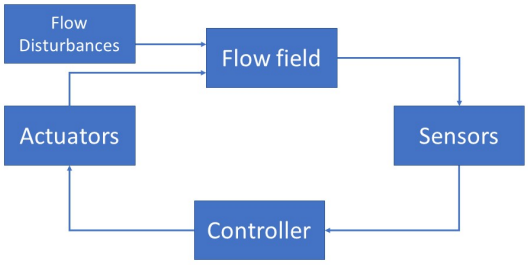

Figure 2.9: A schematic of the general elements of the closed-loop control.

the ability to be switched on and off at any given time, yet the common feature is that open-loop control can also generate more disturbances in the flow, accordingly increasing the drag. Feedback or closed-loop control can offer improvement for these cases. As shown in figure 2.9 the signal of the targeted flow property is measured by the sensor and translated into an actuation through the controller. In this case, energy is utilised efficiently to favourably modify the flow compared to the open-loop active control case.

Examples of active flow control applied for bluff bodies include; steady or periodic suction and blowing, rotary, streamwise and transverse oscillations, which are categorised as secondary flow techniques. The magnetic field is another technique that controls the boundary layers by utilising the force generated when an electric-conducting fluid moves in a magnetic field (Lorentz force). The electric discharge is also used to control the flow when electric force is produced to modify the velocity field in the fluid (Rashidi et al., 2016). Bluff body flow control techniques can further be classified into two-dimensional and three-dimensional forcing. If the actuation property varies along the spanwise or azimuthal direction, the control method is known as three-dimensional forcing, and if not, it is categorised as two-dimensional forcing. Another classification for bluff body flow control techniques, based on the strategy of manipulating the dynamics of the flow, is boundary layer control or direct wake control. In the boundary layer control method, the flow separation is delayed, for example by triggering the transition of the boundary layer flow from laminar to turbulent, significantly reducing the drag. Separation is delayed by enhancing the streamwise momentum in the near-wall region close to the separation point to overcome the adverse pressure gradient in the rear part of the bluff body. This method is applicable for bluff bodies with movable separation points, such as the flow around a circular cylinder. Direct wake control targets controlling the wake characteristics, which is applicable for bluff bodies with both movable and fixed separation points. A splitter plate located at the rear surface of the bluff body and base bleed are examples of direct wake control, which delays the interaction of the top and

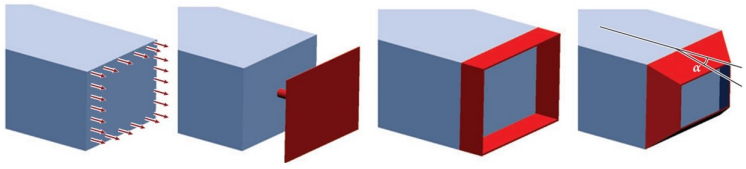

Figure 2.10: A schematic for the different control techniques used to control the wake of the square-back Ahmed body, adapted from Choi et al. (2014). From left to right, streamwise blowing, splitter plate, base-cavity and boat tail.

bottom separated shear layers, thus stabilising the near wake region and suppressing the vortex shedding in case of a two-dimensional bluff body. This, consequently, increases the base pressure of the rear surface of the bluff body and reduces the drag.

2.2.1 Control of flow past the Ahmed body

For flow past the square-back Ahmed body, the recirculation bubble formed downstream of the rear surface is the primary source of pressure drag; reducing its size (cross-section) or shifting it further downstream of the base – elongating the bubble– is seen to increase the base pressure and significantly reduced the drag (Balkanyi et al., 2002, Gilliéron and Kourta, 2010, Littlewood and Passmore, 2012). The common control devices/techniques reported in the literature employing these mechanisms are shown in figure 2.10. Blowing air at the base of the bluff body successfully reduces the drag as it moves the low-pressure recirculation region further downstream, allowing for base pressure recovery (Englar, 2001, Howell et al., 2003, Littlewood and Passmore, 2012). However, the usage of this method is limited in practice due to the power required for blowing.

Different passive control techniques, which promote base pressure recovery, have been reported in the literature. One of these is placing a vertical splitter plate in the near wake region (Gilliéron and Kourta, 2010), which would disturb the formation of the recirculation bubble and consequently reduce the drag; however, it is an impractical choice for the realistic cases, as for heavy vehicles, for instance (Choi et al., 2014). Employing a base cavity or a boat tail appears more practical and effective for drag reduction than the vertical splitter plate. A base cavity comprises four extensions from the four base edges, forming a cavity. While, a boat tail is a tapered extension with a slant angle α from the base edges. The cavity pushes the recirculation region downstream by delaying the flow separation, whereas the boat tail deflects the flow inwards (Balkanyi et al., 2002, Verzicco et al., 2002, Yi et al., 2007, Choi et al., 2014).

Balkanyi et al. (2002) investigated experimentally the effect of the boat tail and base cavity on the generic model (GM) (very similar to the square-back Ahmed body with slightly different lengths). The experimental study found that significant drag reduction (up to 48%) is achieved using the base cavity. It further showed that combining the base cavity and the boat tail enhances

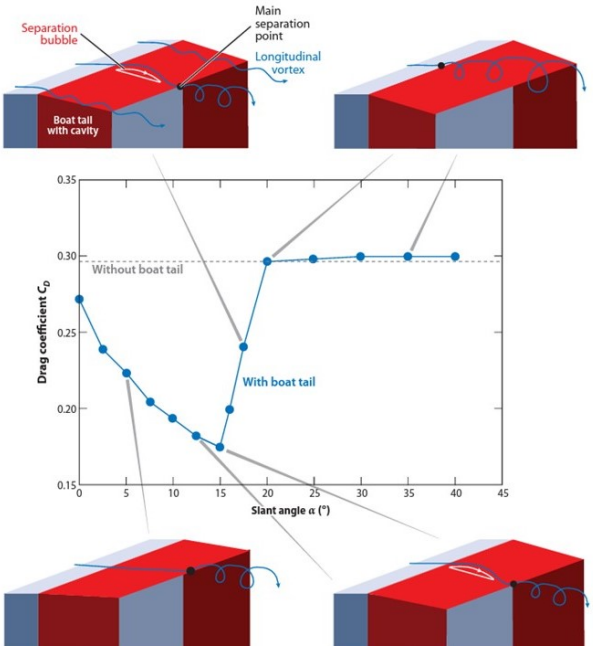

Figure 2.11: Change in drag coefficient C_D for different slant angles of the boat tail for the GM model (equivalent to square-back Ahmed body), adapted from Choi et al. (2014). Schematics of the flow pattern are shown for different slant angles (Yi et al., 2007).

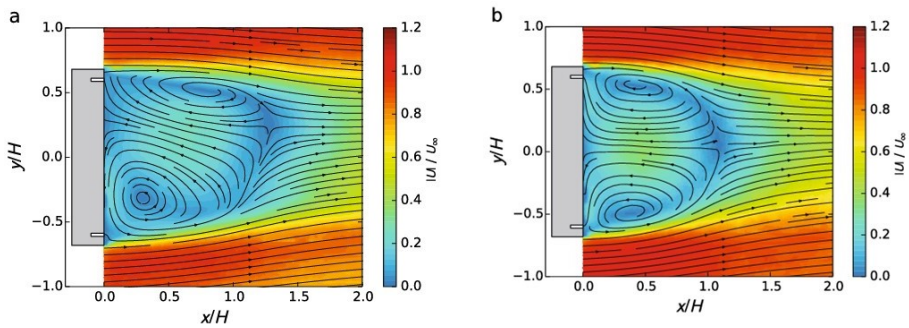

Figure 2.12: Conditional averaged velocity field on a horizontal plane for the asymmetric wake in the absence and presence of base suction shown in (a) and (b), respectively, adapted from Hsu et al. (2021).

the base pressure recovery and drag reduction. The drag reduction is found to be sensitive to both the length and the angle of the boat tail (Choi et al., 2014). The study by Yi et al. (2007) showed the influence of the boat tail slant angle on the drag. Figure 2.11 depicts the change in the drag coefficient C_D with the boat tail slant angle, α, based on Yi et al. (2007) study. The drag is reduced for a range of α between 0° and 15°. The maximum drag reduction is achieved when the flow separates over the slanted surfaces and reattaches before reaching the end of the slanted surface. This is similar to the flow structure of the Ahmed body with a slant angle $\alpha \sim 15°$. When α exceeded 20°, a pair of longitudinal vortices were seen to emanate from the sides, increasing the drag, as seen in figure 2.11.

Most of the studies mentioned in the previous paragraph focused on the effect of the control on the time-averaged wake topology. Following the recent focus on the instantaneous dynamics

of the wake, specifically wake bi-modality, the effect of wake re-symmetrisation on drag has been exploited in passive and active flow control studies. Evrard et al. (2016) used a base cavity to control the turbulent wake past the square-back Ahmed body. The study found that for a cavity depth of 27% of the body height, the bi-modal switching of the wake was suppressed, achieving a 9% drag reduction and 18% base pressure recovery. Grandemange et al. (2014b) examined the wake sensitivity experimentally by placing a vertical cylinder in the recirculation region. The study found that the most receptive position for symmetrising the wake is the centre of the recirculation region. In this case, wake symmetry was preserved, elongating the recirculation region, increasing the base pressure recovery and reducing drag by 5%.

Active flow control has managed much smaller drag reductions through targeting wake symmetrisation compared to these passive flow control approaches. The restriction of forcing with body-mounted actuators may be a possible reason, as the latter study concluded that the most receptive position to force the wake is located in the centre of the recirculation region. Barros et al. (2016) investigated the impact of periodic forcing around the base of the wake. It was found that when the wake was forced with a lower frequency ($0.1 \leq St_H \leq 3.7$), the jet enhanced the wake entrainment, shortened the recirculation length and increased the drag. The opposite occurred when the wake was forced with a higher frequency, equivalent to $St_H \geq 4$, as drag reduction and base pressure recovery were seen. These were attributed to two mechanisms; shear layer deviations caused a fluidic boat-tailing effect in the wake and reduction in momentum entrainment in the wake. A gradual increase in base pressure with forcing frequency was observed, with a maximum recovery of 16% for a $St_H \sim 12$. The maximum drag reduction reported in this case was 10%. An even higher drag reduction of $\sim 20\%$ was achieved, when high-frequency periodic forcing was combined with the Coanda effect caused by installing curved surfaces. Similar to Schmidt et al. (2018), drag reduction is enhanced when combined flow control mechanisms are used.

Fluidic oscillators were used around the base perimeter to actuate the Ahmed body wake in the experimental study by Schmidt et al. (2018). The study investigated the effect of active flow control on the vertical bi-modality in the presence of flaps, which extended from the base and tilted inwards. Vertical bi-modality was found to persist for flap angles $\geq 15°$, while other dynamics in the wake were weakened. Applying active flow control through the fluidic oscillator with an oscillating frequency of $St_H \sim 24$ suppressed both the vertical bi-modality and the higher frequency dynamics, but the bubble pumping mode persisted. This was found to reduce the drag by 14% and significantly reduce the base pressure for a shorter recirculation region. These studies showed that forcing the shear layers with different time scales can control the absolute and convective instabilities in the wake of the square-back Ahmed body. Low-frequency forcing amplifies the vortex shedding and shear layer mixing, while high-frequency forcing suppresses these

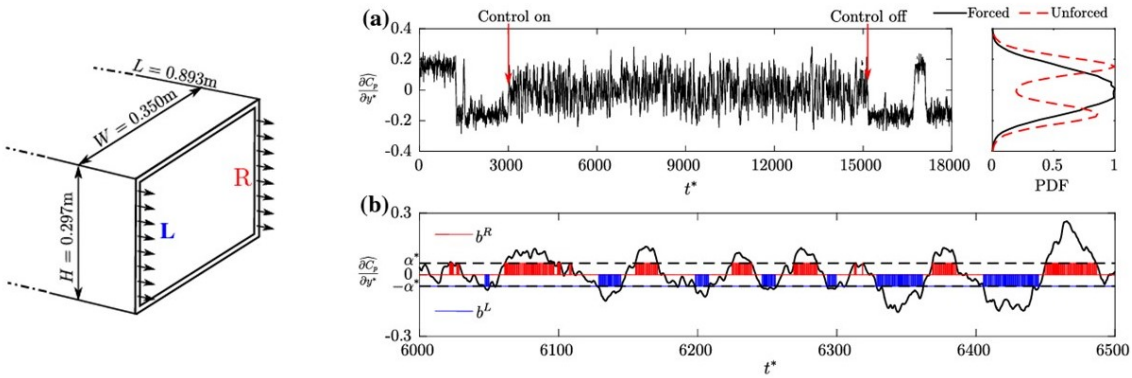

Figure 2.13: Left: schematic of the base of the square-back Ahmed body, showing the lateral slits R and L. Right: time-resolved filtered horizontal pressure gradient $\frac{\partial \widehat{C_P}}{\partial y^*}$ with the associated probability density function (top) and zoomed view indicating the threshold value of $\frac{\partial \widehat{C_P}}{\partial y^*}$, α^* for the actuator to switch on, adapted from Li et al. (2016).

and the long-time dynamics related to bi-modality.

The recent experimental study by Hsu et al. (2021) investigated the effect of steady suction around the base perimeter on the bi-modal wake past the square-back Ahmed body. They found that steady suction shortened the recirculation region for all the values of suction flow rates investigated. Weak suction was found to intensify the *RSB* modes of the wake, while higher suction suppressed these modes and symmetrised the wake. This can be seen in figure 2.12, where the velocity fields in the presence and absence of the base suction are shown, indicating a symmetric wake for the latter case. Wake symmetry was related to the increased curvature of the free shear layers in the wake. Steady blowing was used in the study by Khan et al. (2022); however, it was applied through a centrally square aperture on the base. They found that the optimum blowing coefficient correlated with a symmetrised wake and a drag reduction of 6%. A lower drag reduction of 3% was achieved using a sweeping jet actuator at mid-base height (Veerasamy et al., 2022). Similarly, Wassen et al. (2010) used steady blowing through slits along the base perimeter to reduce the drag of the square-back Ahmed body. They found that the wake is symmetrised when the jet is tilted by 20°, reducing the drag by 7%. Blowing was also used in the numerical study by Pasquetti and Peres (2015) employing micro-jets around the base edges. A relatively high frequency inclined jet (45°) reduced the drag by 4%, but does not affect much the horizontal asymmetry of the wake. Pulsed-blowing was used in the experimental study by Fan et al. (2020a), where the explorative gradient method was used to optimise the actuation parameters. For optimised parameters, the pulsed-blowing suppressed wake bi-modality and reduced the drag by 11%. These studies showed that the jet dynamics and the actuator position are key factors in enhancing drag reduction.

Fewer studies were conducted using feedback control for drag reduction than open-loop active flow control. The experimental study by Brackston et al. (2016) applied a linear feedback control,

using side flaps on the square-back Ahmed body to suppress wake bi-modality. Their feedback control was designed based on the stochastic Langevin dynamics, which was used previously by Rigas et al. (2015) to model the multi-modality in the wake of an axisymmetric body. The latter study employed a two-dimensional model, while for the Ahmed body, the unidirectional nature of the bi-modality required a one-dimensional Langevin model. Although the model used here was nonlinear, it was linearised around the base center for designing a linear controller. The controller suppressed bi-modality and symmetrised the wake achieving 2% drag reduction. Feedback control is proved to be more efficient than the steady suction cases reported earlier. In this case, the controller used 24% of the total power saved due to drag reduction.

An opposition control strategy was experimentally applied by Li et al. (2016) to symmetrise the turbulent wake past the square-back Ahmed body. Lateral slits on the sides of the base were used to actuate the wake. Following the base pressure gradient (input signal), actuation occurred on one side at a time, either the left or right slit, shown as L and R, respectively, in figure 2.13. When the actuator was activated, a jet pulsed with a frequency of $St_H = 0.8$, which was found to be the optimum frequency to symmetrise the wake. The controller suppressed bi-modality, as seen in figure 2.13. The drag was slightly affected, as the favourable effect of symmetrising the wake was balanced by the adverse effect of the control amplifying the shear layers mixing and vortex shedding. These match with the results from Barros et al. (2016), where periodic wake forcing at the same frequency induced higher entertainment and amplified shear layers mixing. In most cases, the use of linear feedback control to suppress bi-modality was found to significantly augment wake fluctuations around the center compared to the fluctuations around the uncontrolled asymmetric position. Additionally, forcing the flow in the near-wake region enhances turbulent activity in the free shear layers, promoting high-frequency dynamics in the wake and inhibiting drag reduction.

Recently, Hesse (2021) used a linear feedback controller to actuate the wake of the square-back Ahmed body using LES. The wake response to actuation was represented as a dynamically linear system, which was identified by measuring its response to harmonic forcing at various amplitudes and frequencies, i.e. treating the wake as a black box. The feedback control was synthesised by tuning the sensitivity transfer function to be less than unity in the range of targeted frequencies ($0.01 \leq St_H \leq 0.20$). The resulting feedback controller suppressed the base pressure fluctuations as designed, but there was no accompanying increase in mean base pressure or reduction in drag. Similar attempts were tried previously for the square-back Ahmed body by Evstafyeva (2018) with negligible drag reduction.

Previous studies confirmed that wake symmetry allows base pressure recovery promoting drag reduction. However, this mechanism depends on the control strategy and its effect on the wake dynamics. The control strategies reported in the open-loop framework forced the wake directly

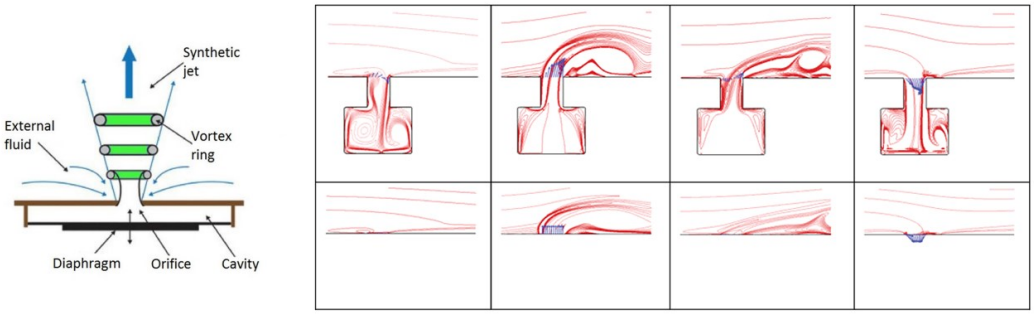

Figure 2.14: Right: a schematic for the typical components of a synthetic jet actuator, adapted from Strzelczyk and Gil (2016). Left: instantaneous vorticity of the flow in the cavity superimposed with velocity vectors (blue arrows) on the top and the equivalent top-hat velocity profiles on the bottom, adapted from Aram et al. (2010)

using steady/periodic suction, blowing and sweeping jets. The reported mechanisms of actuating the wake using feedback control were the side flaps, opposition side blowing and synthetic jets.

In this research, both active open-loop and feedback control will be used to control the wake past the square-back Ahmed body. The feedback control employs synthetic jets to manipulate the wake dynamics to suppress bi-modal switching and reduce drag. The synthetic jet (also known as zero-net-mass-flux (ZNMF) jets) working principle is based on generating linear momentum in the flow with zero net mass flux. The actuator consists of an oscillating diaphragm in a cavity and a small hole upstream of the cavity, transferring the fluid into the main stream, as shown in figure 2.14. The oscillation of the diaphragm motivates the fluid flow inwards or outwards with respect to the cavity. The unique feature of the synthetic jet is that it transfers momentum into the fluid domain with zero net mass injection, which is achieved by intermittent suction from the same domain, i.e. altering momentary suction and ejection through the hole or the orifice (Glezer and Amitay, 2002). It has been used previously in experimental (Oxlade et al., 2015, Henning and King, 2005) and numerical (Dahan et al., 2012, Dalla Longa et al., 2017) bluff body flow control studies. Experimentally, the jet is generated using a loudspeaker in the cavity, which forces the diaphragm to pulse the air in and out of the cavity alternately. A zero net mass flux is maintained over a single cycle with a non-zero net momentum (Glezer and Amitay, 2002). In numerical studies, simulating the flow dynamics through the cavity is computationally expensive. Alternatively, a time-varying top-hat velocity signal can be specified on the exit of the cavity, which generates a similar jet flow (Aram et al., 2010, Leschziner and Lardeau, 2011). These equivalent velocity

profiles are shown in figure 2.14 at different time instants. This method is adopted in the current research, applying a time-varying top-hat velocity signal on the actuation surfaces.

Chapter 3

Numerical Setup and Data Analysis

This chapter briefly describes the methodology used to solve the equations governing the fluid flow, i.e. details of the computational fluid dynamics involved in the different cases. The first section describes the governing equations and the discretisation schemes used to convert them to algebraic equations, followed by a description of the turbulence modelling technique and the flow solver. The second section summarises the equations used to analyse simulation results. Finally, the third section explores the reduced-order modelling techniques used in the following chapters.

3.1 Flow Simulation

The governing equations for external aerodynamics generally are the incompressible Navier-Stokes equations, which employ the conservation of mass and momentum. Equations 3.1 and 3.2 represent the incompressible NS in the tensor form.

$$\frac{\partial u_i}{\partial x_i} = 0 \tag{3.1}$$

$$\frac{\partial u_i}{\partial t} + \frac{\partial u_i u_j}{\partial x_j} = -\frac{1}{\rho}\frac{\partial p}{\partial x_i} + \nu \frac{\partial^2 u_i}{\partial x_j^2} \tag{3.2}$$

Where u_i is the i velocity component $i \in (x, y, z)$, ρ is the density, p is the pressure and ν is the kinematic viscosity (Versteeg and Malalasekera, 2007). These partial differential equations are solved numerically over the flow domain to obtain the flow field using the finite volume method. The solution domain is discretized into smaller control volumes (CV), where the NS equations are applied in integral form on every CV. The partial differential equations are converted into algebraic equations by discretizing (or integrating) them spatially over every CV and temporally. The resulting algebraic equations approximate the values of any flow transported property (Φ) at

the centre of each CV. Differencing schemes are used to approximate the transported property and their derivatives on the faces of the CVs, using the nodal values. Finally, the linear algebraic equations system is solved for the transported property value for each CV with additional equations to account for the turbulence, in this case, (Versteeg and Malalasekera, 2007). This is the general idea of simulating the flow field using the finite volume method (FVM). Details of these steps are provided in the following subsections.

3.1.1 Numerical methods

The governing equations are discretised spatially and temporally, forming a set of linear algebraic equations, i.e. transformed from the continuous domain to discrete points (centre of CVs) in the solution domain. These algebraic equations are used to construct a matrix, which is presented as $[A][\Phi] = [b]$, where A is the coefficients matrix, Φ is the discretised form of a general transported property Φ and b is the source coefficients matrix. A separate matrix is constructed for each flow property, which is then solved to approximate the flow field.

The conservation concept leads to a general form for the evolution of a flow property $\Phi(x, y, z, t)$ in space and time, shown in equation 3.3, where $j = 1, 2, 3$ and Γ_Φ is the diffusivity of Φ. The first and second terms on the left-hand side represent the rate of change of Φ and the convection of Φ due to the flow, respectively. The right-hand side represents the diffusion of Φ and the source term S_Φ. Integrating equation 3.3 in space and time leads to equation 3.4, where V is the volume of the control volume, and Δt is the time step. Gauss's divergence theorem is then applied to convert the volume integrals to surface integrals, which can be approximated as a summation of the integrated property over the faces of the CV. This is shown in equation 3.5, where S is the surfaces area of the CV, N is the total number of faces of the CV and $\vec{n}$ is the unit vector normal to the surface element dS, as shown in figure 3.1. The final form of the discretised equation of the general flow property Φ is shown in equation 3.6, where P is the centre of the CV, S_i is the surface area of the face i whose normal unit vector is n_i, $S_{\Phi c}$ and $S_{\Phi P}$ are the linear and nonlinear source terms, respectively. This equation will then be discretised temporally to form the final equations matrix for the flow property Φ.

$$\frac{\partial(\rho\Phi)}{\partial t} + \frac{\partial(\rho u_j \Phi)}{\partial x_j} = \frac{\partial}{\partial x_j}\left(\Gamma_\Phi \frac{\partial \Phi}{\partial x_j}\right) + S_\Phi \tag{3.3}$$

$$\int_V \left[\int_t^{t+\Delta t} \frac{\partial(\rho\Phi)}{\partial t} dt\right] dV + \int_t^{t+\Delta t} \left[\int_V \frac{\partial(\rho u_j \Phi)}{\partial x_j} dV\right] dt = \int_t^{t+\Delta t} \left[\int_V \frac{\partial}{\partial x_j}\left(\Gamma_\Phi \frac{\partial \Phi}{\partial x_j}\right) dV\right] dt + \int_t^{t+\Delta t} \left[\int_V S_\Phi dV\right] dt \tag{3.4}$$

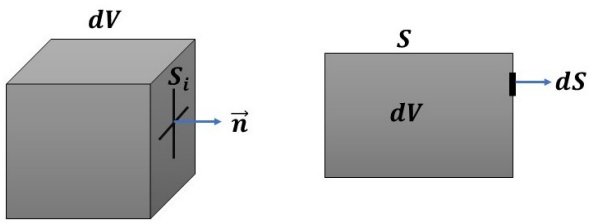

Figure 3.1: General arbitrary shape of a control volume (cell). dV is the volume, dS is the surfaces area of the CV. S_i is the area on the face i, whose unit vector is $\vec{n}$.

$$\int_V (div\ \vec{\Phi})\ dV = \int_S (\vec{n}.\vec{\Phi})\ dS = \sum_{i=1}^{N} \int_{S_i} (\vec{n}.\vec{\Phi})\ dS \tag{3.5}$$

$$\int_t^{t+\Delta t} \left[\left(\frac{\partial(\rho\Phi)}{\partial t} \right)_P V_P + \sum_S \left(\rho u_j \Phi \right)_S n_i S_i - \sum_S \left(\Gamma_\Phi \frac{\partial \Phi}{\partial x_j} \right)_S n_i S_i \right] dt = \int_t^{t+\Delta t} \left[\left(S_{\Phi c} V_P + S_{\Phi P} V_P \Phi_P \right) \right] dt \tag{3.6}$$

In order to estimate the flow property Φ and its derivatives on the CV faces, interpolation and differencing schemes are applied. Different spatial discretisation schemes are used, including central differencing, upwind, power low, and Quadratic Upwind Interpolation for Convective Kinematics (QUICK) schemes. Choosing the suitable scheme is based on a compromise between the solution stability and accuracy. The temporal schemes are the explicit, fully implicit and semi-implicit or Crank-Nicolson schemes. The latter is considered for all the simulations in this research. It is a second-order accurate scheme and unconditionally stable. It gives more realistic results for $\Delta t \leq (\Delta x)^2/\Gamma_\Phi$, where Δx is the minimum length of the CV.

The present work uses OpenFOAM (Open Source Field Operation and Manipulation) to simulate the flow past the square-back Ahmed body, which employs an open-source $C++$ code to solve the governing equations. OpenFOAM requires setting the discretisation schemes for the gradient (∇), divergence ($\nabla.$), Laplacian (∇^2), interpolation and surface normal gradient terms. The discretisation scheme used for the gradient is the Gauss linear with cellMDlimited using a blending factor ≤ 0.2 at the beginning and 0 after the first transient period. This is to ensure solution stability at the beginning. For the divergence, Gauss limited linearV is used with TVD (total-variation-diminishing) blending factor of 0.2 for the vectors and Gauss linear for scalars. These schemes are highly recommended for LES. Gauss linear limited corrected scheme is used for the Laplacian terms, with a blending factor of one. The choice of these schemes strongly depends on the mesh quality. The schemes mentioned above require the mesh non-orthogonality to be less than 70 (Greenshields and Weller, 2022, Versteeg and Malalasekera, 2007). The mesh details

and boundary conditions will be provided in the next chapter. Both the spatial and temporal discretisation schemes used are second-order accurate.

3.1.2 Turbulence modelling

In this study, Large Eddy Simulations (LES) are employed. LES is a hybrid turbulence modelling technique between the Direct Numerical Simulation (DNS) -that resolves all the turbulence length scales (Moin and Mahesh, 1998) and Reynold Average Navier-Stokes (RANS), which models all the turbulence scales (Wilcox, 2001). This technique of turbulence modelling resolves the large eddies and models the small eddies. It represents a good compromise between the resolution of turbulence scales and the computational cost. Reviews on LES are provided by Piomelli (1999) and Meneveau and Katz (2000).

The essence of the LES approach is to resolve the large eddies with a time-dependent simulation and to capture the smaller ones with a suitable model. This is based on the premise that the smaller eddies behave universally and are characterised as isotropic, while larger eddies' behaviour depends on the geometry of the solution domain, the boundary conditions and the body forces acting on the flow. These different behaviours complicate using a single model to accurately describe all the turbulence length scales in the flow field. LES employs linear spatial filtering to isolate the eddies based on their length scale. The minimum resolvable turbulence length scale for LES is the Taylor microscale, which corresponds to the wave number at the upper limit of the inertial subrange of the turbulent energy spectrum. It represents an intermediate scale between the integral (largest) and the Kolmogorov (smallest) length scales. Taylor length scale (λ) can be estimated using equation 3.7, where $u^{'}$ is the fluctuating velocity, ν is the viscosity, ϵ is the energy dissipation rate, and l is the integral length scale. The indicative measure of the turbulence length scale of the eddies is called the cut-off width. Eddies whose length scales are greater than the cut-off width are resolved while the rest are modelled. A specific filtering function and cut-off width are to be selected and applied to the time-dependent governing equation of the flow field.

$$\lambda = u^{'}(\frac{\nu}{\epsilon})^{0.5} = lRe_l^{-0.5} \tag{3.7}$$

Applying the linear spatial filtering on the unsteady NS equations generates a new set of equations, i.e. the filtered NS equations, which characterize the behaviour of the resolved structures in the flow field. The filtering process also generates additional terms related to the filtered-out small eddies, and other terms represent the interaction between those small unresolved eddies and the larger resolved ones; this, in turn, generates sub-grid-scale (SGS) stresses resembling Reynolds stresses in RANS. Those stresses are modelled using SGS models that will be solved together with

the resolved flow to get the entire flow field. For a transported property Φ, the filtered version is defined in equation 3.8.

$$\overline{\Phi}(x,t) = \iiint_{-\infty}^{\infty} G(x,x^{'},\Delta)\Phi(x^{'},t)dx_1{}^{'}dx_2{}^{'}dx_3{}^{'} \tag{3.8}$$

Where $\overline{\Phi}(x,t)$ is the filtered property, $G(x,x^{'},\Delta)$ is the filtering function and Δ is the filter cut-off width. Numerous filtering functions have been reported in the literature, including Gaussian, Spectral (Fourier) and Box filters. The latter is used in the finite volume method and is represented mathematically with equation 3.9.

$$G(x,x^{'},\Delta) = \begin{cases} \frac{1}{\Delta^3} & |x-x^{'}| \leq \frac{\Delta}{2} \\ 0 & |x-x^{'}| > \frac{\Delta}{2} \end{cases} \tag{3.9}$$

The cut-off width for LES in finite volume methods is selected in the same order as the grid size. For a non-uniform grid with dimensions of $(\Delta x, \Delta y, \Delta z)$, the cut-off width is expressed as shown in equation 3.10.

$$\Delta = \sqrt[3]{\Delta x\ \Delta y\ \Delta z} \tag{3.10}$$

The filtered version of the unsteady, incompressible NS equations, applying constant filtering function (independent of x), are shown in equations 3.11 and 3.12. The overbar indicates the filtered version of the flow property.

$$div(\rho\overline{u}) = 0 \tag{3.11}$$

$$\frac{\partial(\rho\overline{u_j})}{\partial t} + div(\rho\overline{u_j}\ \overline{u}) = -\frac{\partial\overline{p}}{\partial x} + \mu\ div(grad(\overline{u_j})) - (div(\rho\overline{u_j u}) - div(\rho\overline{u_j}\ \overline{u})) \tag{3.12}$$

Equation 3.11 represents the continuity equation, and equations 3.12 represents the momentum equation; both resemble the RANS equations, except that the averaging process is spatial rather than temporal. The first term of the momentum equations is the rate of the change of the filtered momentum. The second, third and fourth terms are the convective fluxes of filtered momentum, the gradient of the filtered pressure and the diffusive fluxes of the filtered momentum, respectively. The last two terms are generated due to the spatial filtering operations and can be considered as divergence of stress τ_{ij}, i.e. sub-grid-scale stresses shown in equation 3.13 and decomposed into three components.

$$\tau_{ij} = \underbrace{\rho\overline{\overline{u_i}\ \overline{u_j}} \ - \ \rho\overline{u_i}\ \overline{u_j}}_{L_{ij}} + \underbrace{\rho\overline{\overline{u_i}\ u_j{}'} \ + \ \rho\overline{u_i{}'\ \overline{u_j}}}_{C_{ij}} + \underbrace{\rho\overline{u_i{}'\ u_j{}'}}_{R_{ij}} \tag{3.13}$$

- Leonard Stresses, L_{ij}, resulting from the resolved eddies, which can be computed from the filtered flow field (Leonard, 1975). These are caused by the second spatial filtering of the variables, for instance $\overline{\overline{\phi}} \neq \overline{\Phi}$ unlike the temporal filtering used in RANS.

- Cross-Stresses, C_{ij}, resulting from the interaction of the resolved and modelled eddies, and expressed by an expression suggested by (Ferziger, 1977).

- LES Reynolds Stresses, R_{ij}, resulting from the interaction between the SGS eddies. SGS models are used here. Numerous models are available, such as Smagorinsky and Lilly, Wall adaptive local eddy viscosity (WALE), mixed model, and dynamic SGS model.

Most of the SGS models are based on the Boussinesq hypothesis for SGS eddy viscosity, assuming that R_{ij} is proportional to the mean strain rate as shown in equations 3.14. Thus, models are seeking expressions for the SGS eddy viscosity.

$$R_{ij} = -2\mu_{sgs}(\frac{\partial \tilde{u_i}}{\partial x_j} + \frac{\partial \tilde{u_j}}{\partial x_i}) + \frac{1}{3}R_{ii}S_{ij} \tag{3.14}$$

In this study, the Wall-Adapting Local Eddy-Viscosity Model (WALE) is employed based on applying the isotropic filter to anisotropic flow (shear flow). This model alleviates the problem of high dissipation levels observed in the near wall regions (shear flow) when using basic SGS models. The model was developed by Nicoud and Ducros (Nicoud and Ducros, 1999), based on recovering the "asymptotic behaviour in the vicinity of a solid wall in equilibrium turbulent boundary layer on a fine grid without additional damping function"(Sagaut, 2006). Nicoud and Ducros found that in the near-wall region, the spatial derivative of the resolved velocity is proportional to the distance from the wall. The sub-grid scale viscosity expressed as shown in equation 3.15, where $\overline{S_{ij}} = 0.5(\frac{\partial \overline{u_i}}{\partial x_j} + \frac{\partial \overline{u_j}}{\partial x_i})$ represents the strain rate tensor. The advantage of the WALE model is that it accounts for both strain and rotational rates. It also achieves a zero SGS viscosity near the wall. The model has proved realistic results in capturing the physics in the literature (Dahan et al., 2012, Hesse and Morgans, 2021).

$$\nu_{sgs} = (C_w\overline{\Delta})^2 \frac{({S_{ij}}^d {S_{ij}}^d)^{3/2}}{(\overline{S_{ij}S_{ij}})^{5/2} + ({S_{ij}}^d {S_{ij}}^d)^{5/4}}, \quad C_w = 0.55 - 0.6 \tag{3.15}$$

Finally, the near-wall treatment considered in all the simulation cases is based on resolving the boundary layers. This means wall models are not applied requiring refined mesh in the vicinity of the walls to resolve the boundary layers fully. Details about the meshes used are provided in the

next chapter.

3.1.3 Flow solver

OpenFOAM software is used for simulating the flow around the bluff body. PimpleFoam, one of the OpenFOAM solvers used for incompressible unsteady flows, is considered. The PIMPLE algorithm (Barton, 1998) merges both PISO (Pressure Implicit with Splitting of Operator) (Issa, 1986) and SIMPLE (Semi-Implicit Method for Pressure-Linked Equations) (Patankar and Spalding, 1972) algorithms. PIMPLE and PISO algorithms are transient iterative solvers, while SIMPLE is a steady-state iterative solver.

PISO algorithm applies SIMPLE algorithm over successive time steps with the size of the time step being Δt. The number of iterations in each timestep to achieve solution convergence is called outer correctors. Once the solution converges at one timestep, the algorithm moves on to the next time step. The SIMPLE algorithm solves the discretised momentum equations using an initial pressure guess to find the velocity components. Pressure and velocity components are coupled through the Poisson equation, shown in 3.16, which is derived by taking the divergence of the momentum equation and applying the continuity equation. This is solved to correct the pressure field and accordingly update the velocity components enforcing the conservation of mass. At a specific time step, convergence is reached when the relative error of each flow property is less than the value set, which is set to 10^{-9} in all the simulation cases. In the transient solution, the value of the time step Δt needs to be relatively small to maintain the accuracy of the solution to resolve the minimum timescale and to assure the solver stability (Greenshields and Weller, 2022).

$$\nabla^2 p \ + \nabla.[\nabla.(uu)] = 0 \tag{3.16}$$

PIMPLE algorithm is similar to PISO algorithm, with the PISO algorithm being repeated more than once at every time step. This improves the solution accuracy for Courant number greater than one if a second-order time scheme is used. Further, better stability is obtained from PIMPLE over PISO for this reason (Greenshields and Weller, 2022).

In all the LES cases, the flow field is initialized with steady flow using the SIMPLE algorithm and RANS, which captured the mean flow with an acceptable accuracy for initialisation. The solution algorithm used for LES is PIMPLE with the two correctors, i.e. the PIMPLE algorithm solves the pressure equation and momentum corrector twice in each time step. The PIMPLE algorithm loops twice over the entire system of equations, i.e. the number of outer correctors is two. If the number of outer corrections is set to one, the algorithm will be equivalent to PISO.

3.2 Data Analysis

This section provides the mathematical formulae for the different quantities used to analyse the flow field. It covers the definition of these quantities in both the time and the frequency domains.

The drag and pressure coefficients used in analysing the data in the following sections are calculated as shown in equations (3.17) and (3.18), respectively. $D(t)$, ρ, and U_∞ represent the drag force, air density and the free stream velocity, respectively. $P(x, y, z, t)$ represents the pressure at a position (x, y, z) in space at an instant t. P_∞ is the free stream pressure. The spatial gradient of the coefficient of pressure (C_P) in a direction $\boldsymbol{n}$ is calculated as shown in equation (3.19), where $\boldsymbol{n}$ represents a cross-flow direction (y, z), n_1 and n_2 are the distances between the pressure probes on the base (on the positive and negative sides relative to the base centre line), and the centre of the base in the direction n, M is the number of the probes, and N is the total length of the base in the same direction, as shown in figure 4.1.

$$C_D(t) = \frac{D(t)}{\frac{1}{2}HW\rho{U_\infty}^2} \tag{3.17}$$

$$C_P(x, y, z, t) = \frac{P(x, y, z, t) - P_\infty}{\frac{1}{2}\rho{U_\infty}^2} \tag{3.18}$$

$$\frac{\partial C_P(t)}{\partial n} = \frac{\sum_M C_P(n_1, t) - \sum_M C_P(n_2, t)}{\frac{M(n_1+n_2)}{N}} \tag{3.19}$$

The momentum coefficient C_μ is defined as the ratio of momentum imposed through the actuators to the free stream momentum and calculated as shown in equation 3.20, where $A_{\text{Actuator}} = W_{\text{Actuator}} \times H$ and $A_{\text{Base}} = W \times H$ are the actuator and the base cross-section area, respectively. Equation 3.21 is used to calculate the actuation power, where $\overline{U_{\text{jet}}}$ and η_{Actuator} represent the time-averaged jet velocity and the efficiency of the actuator, respectively. The total power saved due to drag reduction is calculated as shown in equation 3.22, where ΔF_{Drag} is the change in the drag force.

$$C_\mu(t) = \frac{A_{\text{Actuator}}\overline{U_{\text{jet}}^2}}{A_{\text{Base}}U_\infty^2} \tag{3.20}$$

$$Pw_{\text{Actuation}} = \frac{1}{\eta_{\text{Actuator}}}\frac{\rho\overline{U_{\text{jet}}^3}}{2} \tag{3.21}$$

$$Pw_{\text{saved}} = \Delta D U_\infty \tag{3.22}$$

In order to analyse the data in the frequency domain, the Fast Fourier Transform function is employed, which computes the Discrete Fourier Transform (DFT) of a signal as an approximation of the continuous Fourier transform. The governing equation for that is shown in equation 3.23, where q_k represents N samples of $q(kf)$ in the frequency domain and q_m represents N samples of $q(mT)$ of the continuous signal $q(t)$ in the time domain (Nussbaumer, 1981).

$$q_k = \sum_{m=0}^{N-1} q_m \, W^{mk}, \quad k = 0, ..., N-1, \quad W = e^{-2\pi i/N} \tag{3.23}$$

The power spectral density is also used for data analysis purposes. It describes the distribution of the signal's power in the frequency domain, i.e. determining the power or the strength of the frequency content. For a random flow variable $q(t)$ with N samples, the power spectral density is calculated as shown in equation 3.24, where f_s is the sampling frequency equals to $1/T$ with T being the sampling period of the signal $q(t)$ (Howard, 2004).

$$PSD = \frac{1}{f_s N} |q_k|^2 \tag{3.24}$$

3.3 Reduced Order Modelling

This section provides an overview of the techniques used for reduced-order modelling. These include the use of the standard Proper Orthogonal Decomposition (POD) and the Spectral Proper Orthogonal Decomposition (SPOD) to analyse the flow past the squareback Ahmed body in the presence and absence of the control.

3.3.1 Proper Orthogonal Decomposition

Proper Orthogonal Decomposition (POD), introduced by Lumley (1967), is one of the widely used techniques for model reduction in turbulent flows. It decomposes any flow property into a set of deterministic functions (POD modes), each of which captures some of the fluctuation energy of the flow and is modulated by a time coefficient. Considering a flow property $q(x, y, z, t)$, which can be a scalar or a vector field, with the independent variables (x, y, z) in space and t time. $q^{'}(x, y, z, t)$ represents the fluctuating property around the mean, i.e. $q^{'}(x, y, z, t) = q(x, y, z, t) - \overline{q}$, where $\overline{q}$ is the temporal mean of $q(x, y, z, t)$. POD decomposes $q^{'}(x, y, z, t)$ into $\Phi(x, y, z)$ spatial modes, each associated with a time coefficient of $a(t)$, as shown in equation 3.25, where n is the total number of modes.

$$q^{'}(x, y, z, t) = \sum_{k=1}^{n} a_k(t) \; \Phi_k(x, y, z) \tag{3.25}$$

There are two important properties of POD; first, it is optimal or proper in the sense that $\sum_{k=1}^{n} a_k(t)\ \Phi_k(x,y,z)$ maximises the flow energy captured by the first n modes. The second property is that the modes are orthonormal, i.e. $< \Phi_{k1}(x,y,z)\ .\ \Phi_{k2}(x,y,z) >= \delta_{k1k2}$. Orthonormality implies that each time coefficient depends only on the associated spatial mode. Three methods are identified in the literature to calculate this decomposition; direct POD, snapshot POD (Sirovich, 1987) and the Singular Value Decomposition (SVD). The choice between these methods depends on the size of the data and the computational power (Weiss, 2019).

In the direct method, we first construct the data matrix of the random variable $p^{'}(x,y,z,t)$ using the snapshots from the flow field, as shown in equation 3.26. N and M represent the number of spatial points and snapshots, respectively. $p^{'}(x,y,z,t)$ is constructed such that every column presents the time evolution of $p^{'}$ at a specific spatial point (x,y,z) and each row represents one snapshot at a time t. For simplicity we will denote $p^{'}(x,y,z,t)$ as $p^{'}$ to represent the fluctuating flow variable at the point (x,y,z) at a time t (Weiss, 2019).

$$p^{'}(x,y,z,t) = \begin{bmatrix} p^{'}(x_1,y_1,z_1,t_1) & p^{'}(x_2,y_2,z_2,t_1) & ... & p^{'}(x_N,y_N,z_N,t_1) \\ p^{'}(x_1,y_1,z_1,t_2) & p^{'}(x_2,y_2,z_2,t_2) & ... & (x_N,y_N,z_N,t_2) \\ | & | & ... & | \\ p^{'}(x_1,y_1,z_1,t_M) & p^{'}(x_2,y_2,z_2,t_M) & ... & p^{'}(x_N,y_N,z_N,t_M) \end{bmatrix} \tag{3.26}$$

The next step is to calculate the covariance matrix C such that $C = \frac{1}{M-1}(p^{'})^{'}p^{'}$, where $(p^{'})^{'}$ is the transpose of $p^{'}$. The size of the covariance matrix, C, is $N \times N$. The eigenvalues Λ and the eigenvectors Φ are then calculated and reordered in a descending order based on the eigenvalues, as shown in equation 3.27. The N eigenvectors represent the spatial or POD modes of the data set. The time coefficients matrix, A, is calculated by projecting the data on the spatial modes, i.e. $A = p^{'}\Phi$. A, which is $M \times N$, has a number of columns that corresponds to the number of the spatial modes N. Thus, column i in A is referred to as the time coefficients of mode i, where $i = 1, 2, ..., N$ (Weiss, 2019).

$$\Phi = \begin{bmatrix} \phi_{11} & \phi_{12} & ... & \phi_{1N} \\ \phi_{21} & \phi_{22} & ... & \phi_{2N} \\ | & | & ... & | \\ \phi_{N1} & \phi_{N2} & ... & \phi_{NN} \end{bmatrix}, \quad \Lambda = \begin{bmatrix} \lambda_1 & 0 & ... & 0 \\ 0 & \lambda_2 & ... & 0 \\ | & | & ... & | \\ 0 & 0 & ... & \lambda_N \end{bmatrix}, \quad where \ \ \lambda_1 > \lambda_2 > ... > \lambda_N \tag{3.27}$$

Finally, the flow variable $p(x,y,z,t)$ can be reconstructed using n POD modes. As $p^{'}(x,y,z,t) \simeq \sum_{k=1}^{n} a_k(t)\ \Phi_k(x,y,z)$, the reconstructed flow field can be calculated as shown in equation 3.28,

where $n = 1, 2, ..., N$. The value of n is chosen to achieve statistical convergence of the flow energy captured.

$$p(x, y, z, t) = \sum_{k=1}^{n} a_k(t)\ \Phi_k(x, y, z) + \overline{p} \tag{3.28}$$

The snapshot POD method, introduced by Sirovich (1987), can be seen as a decomposition of the flow variable into deterministic temporal modes and random spatial coefficients, i.e. switching (x, y, z) and t in the data matrix. Mathematically, this could be done by transposing the data matrix $p^{'}(x, y, z, t)$, then following the same algorithm discussed for the direct POD. If the same data matrix is used, then the covariance matrix should be $C_s = \frac{1}{M-1} p^{'}(p^{'})^{'}$ and the following steps are similar to direct POD. Finally, POD modes are found to be equivalent to the SVD of $\frac{1}{\sqrt{M-1}} p^{'}(x, y, z, t)$, where the spatial modes are equivalent to the right singular vector, the eigenvalues are equivalent to the square of the diagonal matrix and time coefficients can be found by projecting the data on the spatial modes (Weiss, 2019).

3.3.2 Spectral Proper Orthogonal Decomposition

Spectral Proper Orthogonal Decomposition (SPOD) is used in the present work to extract coherent structures of the fluid flow past the squreback Ahmed body. Compared to standard POD, SPOD modes vary in both space and time rather than space only in the case of POD (Schmidt and Colonius, 2020). SPOD combines the time-correlation of the Dynamic mode Decomposition (DMD) (Schmid, 2010) and the optimal space-correlation of the standard POD. DMD is more general than SPOD because its structures are time-dependent, i.e. grow and decay in time; however, they are neither optimal nor orthogonal. SPOD identifies orthogonal energy-ranked modes that oscillate at each specific frequency (Schmidt and Colonius, 2020). The main idea of the SPOD is that the data realizations are subdivided into a number of blocks with possible overlaps between the blocks. Then the data is Fourier transformed to the frequency domain, then reordered by frequency. POD is performed at each frequency, giving optimal orthogonal modes oscillating at the given frequency. SPOD modes represent structures that evolve coherently in space and time, while space-only POD modes generally do not (Towne et al., 2018).

SPOD modes are the eigenvectors of the cross-spectral density (CSD) matrix at each frequency. This is generated using the Welch method, which performs an ensemble averaging of the data to reduce the spectrum uncertainty. The Welch method requires subdividing the data into N_{blk} segments or blocks. Each block contains N_{FFT} realizations and an overlap with the next block by N_{ovlp} realizations (Bendat and Piersol, 2011).

Following the same notation used in Schmidt and Colonius (2020), assuming $q^{(k)}(t_j)$ to be the kth realization of the flow property at the time t_j. The sampling period of each block is T, and the constant timestep between each successive realization is $\Delta t = \frac{T}{N_{FFT}}$, then $t_j = t_o + j\Delta t$, $j = 1, 2, ..., N_{FFT}$ where t_o is the starting time for the block. The discrete Fourier Transform and its inverse are calculated as shown in equations 3.29 and 3.30, respectively.

$$\hat{q}^{(k)}(f_m) = \sum_{j=0}^{N_{FFT}-1} q^{(k)}(t_{j+1})\ e^{-i2\pi jm/N_{FFT}}, \quad k = -N_{FFT}/2 + 1, ..., N_{FFT}/2 \tag{3.29}$$

$$q^{(k)}(t_{j+1}) = \frac{1}{N_{FFT}} \sum_{m=-N_{FFT}/2+1}^{N_{FFT}/2} \hat{q}^{(k)}(f_m)\ e^{i2\pi jm/N_{FFT}}, \quad j = 0, ..., N_{FFT} - 1 \tag{3.30}$$

After transforming the realizations to the frequency domain, the data is then grouped based on the associated frequency (f_m), which ranges between $-{N_{FFT}}^2/T$ and ${N_{FFT}}^2/T$. If the sampled data were real, only positive frequencies need to be considered, as the negative frequencies are their conjugates. In the following analysis, all the quantities with $\hat{(.)}$ are in the frequency domain.

The next step is to perform the standard POD for the grouped data one frequency at a time. This is similar to the POD analysis discussed previously. The realizations matrix $\hat{Q}$ of the flow property $\hat{q}$ in the frequency domain is constructed as shown in equation 3.31.

$$\hat{Q} = \begin{bmatrix} | & | & & | \\ \hat{q}^{(1)} & \hat{q}^{(2)} & ... & \hat{q}^{(N)} \\ | & | & & | \end{bmatrix} \tag{3.31}$$

Where the number of rows (M) of $\hat{Q}$ represents the spatial points (multiplied by the number of variables if a vector property is used, such as the velocity) and the number of columns (N) represents the snapshots or realizations. There will be a single data matrix $\hat{Q}$ per frequency, with the following steps being repeated for every targeted frequency. The CDS matrix, $\hat{C}$, at each frequency, which is equivalent to the correlation matrix of the standard POD, is then formulated using equation 3.32, where $\hat{Q}^{'}$ is the transpose of $\hat{Q}$.

$$\hat{C} = \frac{1}{N-1}\ \hat{Q}\ \hat{Q}^{'} \tag{3.32}$$

The SPOD modes are the eigenvectors of $\hat{C}$, following equation 3.33. When the snapshot POD method is used, it is more likely to use equation 3.34 to find the SPOD modes and the eigenvalues

for a given frequency; the choice is based on the computational requirements. W represents the weighting matrix, which is considered to be I in the following analysis.

$$\hat{C}W\hat{\Phi} = \hat{\Phi}\hat{\Lambda} \tag{3.33}$$

$$\hat{Q}^{'}W\hat{Q}\hat{\Psi} = \hat{\Psi}\hat{\Lambda} \qquad \hat{\Phi} = \hat{Q}\hat{\Psi} \tag{3.34}$$

For a given frequency, the SPOD modes are spatially orthonormal, i.e. $\hat{\Phi}^{'}W\hat{\Phi} = I$. These steps are summarised using the schematic shown in figure 3.2, which is adapted from Schmidt and Towne (2019). As shown in the first two rows, the slices represent the data snapshots subdivided into overlapped blocks in the time domain. The Fourier transform is applied on each block, switching the data to the frequency domain. A frequency-based categorisation of the data is then applied before performing the POD, which will be done once per frequency.

The accuracy of the SPOD analysis strongly depends on the sampling and the spectral estimation parameters. The maximum resolvable frequency f_{max}, also known as the Nyquist frequency, is equivalent to half of the sampling frequency f_s. The latter is determined by the sampling time step Δt, as shown in equation 3.35. The minimum non-zero resolvable frequency Δf, is determined by the period of the block or segment, T, as shown in equation 3.36. Accordingly, the choice of these parameters is essential to assure that Δf and f_s are small and large enough, respectively, to capture the flow phenomena.

$$f_{max} = \frac{f_s}{2}, \qquad f_s = \frac{1}{\Delta t} \tag{3.35}$$

$$\Delta f = \frac{1}{T} = \frac{f_s}{N_{FFT}}, \qquad T = N_{FFT}\Delta t \tag{3.36}$$

The algorithm would not capture any frequency higher than the Nyquist frequency if it existed. Underestimating the sampling frequency might introduce an aliasing error, which could be solved by introducing anti-aliasing filters (low pass filters) or oversampling. On the other hand, if N_{FFT} is not large enough, the spectrum will be biased as the bounding frequencies will be smeared over the bounded frequency bin, i.e. frequency peaks will not be fine enough. However, large N_{FFT} reduces the number of blocks (segments) in the ensemble, which might affect the statistical convergence of the spectrum and increase the variance in the estimate. This could be mitigated by blocks overlapping, which increases the number of blocks. The total number of blocks N_{blk} can be calculated as shown in equation 3.37. The best practice to for choosing both N_{FFT} and N_{blk} is to be 2^n and 2^{n-1}, respectively, where $n = 1, 2, ..., \infty$, i.e. an overlap of 50% of the data. Finally,

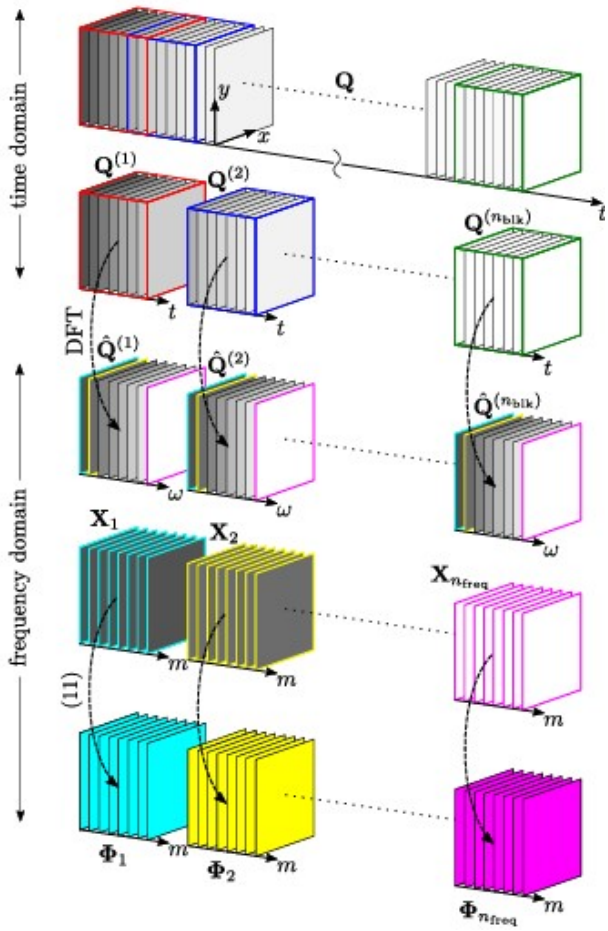

Figure 3.2: The main steps of the SPOD algorithm, adapted from Schmidt and Towne (2019). The slices indicate the snapshots of the data in both the time and the frequency domains. The first two rows shows the data ($Q^{(n_{blk})}$) subdivided into N_{blk} blocks in the time domain. The third row shows the blocks' data ($\hat{Q}^{(n_{blk})}$) transformed to the frequency domain using Fourier transform. Frequency based categorisation is applied, as shown in the fourth row ($X_{n_{freq}}$). Finally the POD is applied per frequency, shown in the last row, indicating the SPOD modes $\Phi_{n_{freq}}$ per frequency. Note that n_{blk} in the figure is equivalent to N_{blk} in the text.

to avoid the effect of spectral leakage, which is associated with the non-periodicity of the data, a Hamming window with optimized parameters was applied to the SPOD algorithm (Schmidt and Colonius, 2020).

$$N_{blk} = \frac{N_t - N_{ovlp}}{N_{FFT} - N_{ovlp}} \tag{3.37}$$

Chapter 4

Unforced flow past the Ahmed body

This chapter explores, numerically, the flow past the square-back Ahmed body. Both the time-averaged and time-varying flows are then discussed. This provides insight into the unforced wake dynamics and comparisons with both the experimental and the numerical cases in the literature. Modal reduction of this case will be shown in the following chapters for comparison purposes.

4.1 Simulation setup for the Ahmed body

LES is used to investigate the dynamics of the turbulent wake downstream of a square-back Ahmed body. The body dimensions are similar to those used by Ahmed et al. (1984), scaled by one quarter, as shown in figure 4.1. The aspect ratio of the body cross-section is W/H=1.35, where W and H are the body width and height, respectively. The length of the body is $L^* = L/H = 3.63$. The clearance between the bottom surface of the body and the ground is $C^* = C/H = 0.174$. The frontal part is rounded with a radius of $R^* = R/H = 0.35$. The dimensions of the body and the ground clearance match those used in the experimental study by Grandemange et al. (2013b). The Reynolds number based on the body height is $Re_H = 3.3 \times 10^4$. The solution domain is $(L_{inlet}, L_x, L_y, L_z) = (2L, 8L, 2L, 2L)$, where L_{inlet}, L_x, L_y and L_z are the domain length upstream of the body, total domain length in the streamwise direction, vertical domain length and the domain length in spanwise direction respectively, as shown in figure 4.2. The blockage factor, defined as the ratio of the Ahmed body cross-section to the domain cross-section, is 2.5%, which is small enough to neglect confinement effects. The domain size has been chosen according to ERCOFTAC recommendations (Jakirlic et al. (2001), Manceau (2003)). The ground boundary layer thickness upstream the body at $x/L = -1$ is $\delta/H \sim 0.09$, matching the approach boundary layer thickness in the study by Grandemange et al. (2013b) and Kang et al. (2021).

The inflow used is a steady uniform velocity profile corresponding to the value of Re_H. The

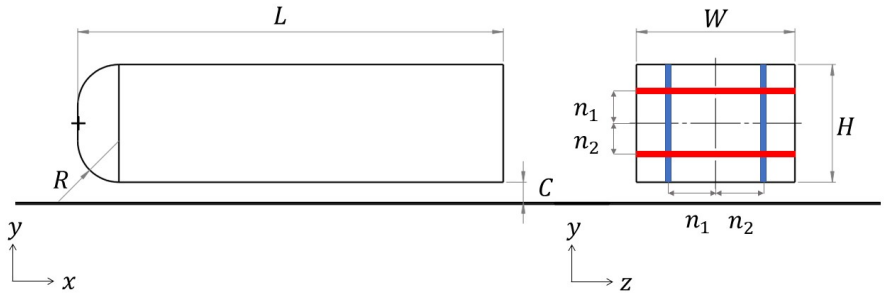

Figure 4.1: Square-back Ahmed body scaled by one fourth, with body height $H = 72mm$. Pressure sensors on the base are marked by the blue and red lines in the vertical (y) and the horizontal (z) directions, respectively. Point $(0, 0, 0)$ is positioned at the center of the front surface indicated with the black +.

boundary condition on the ground and the body surfaces is a no-slip condition. A free-slip condition was set on the domain sides, and a convective outlet condition was set on the domain outlet to avoid backflow. The OpenFOAM CFD toolbox (version 6.0 (TheOpenFOAMFoundation, 2018)), employing a finite volume formulation, was used for the simulations. The governing incompressible Navier-Stokes equations are solved using the PIMPLE algorithm, which is a hybrid algorithm of the Pressure Implicit with Splitting of Operators (PISO) and Semi-Implicit Method for Pressure-Linked Equations (SIMPLE) algorithms described in more detail in chapter 3. The LES employs the Wall-Adapting Local Eddy-viscosity (WALE) model to account for turbulence at sub-grid scales (Nicoud and Ducros (1999)). Second-order spatial and temporal discretisation schemes were employed. The simulation time step was chosen, maintaining a unit value of CFL (Courant–Friedrichs–Lewy).

Unstructured hexahedral cells were used employing the trimmer cells model in StarCCM+ software. This model creates hexahedral cells in the solution domain and trims the mesh core at the boundaries forming polyhedral cells. The prism layers model was used near the solid surfaces to create orthogonal cells, resolving the near-wall flow, as indicated in figure 4.3 and figure 4.4. Three spatial resolutions of $9, 11$ and 15 million cells were considered. The refinement criteria were based on minimising the sizes of the cells in the prism layers, the refined region around the body and the far field region. The size of the mesh near the wall (prism layers) is refined to fully resolve the boundary layer in the three cases, with a maximum value of $\overline{y^+} \leq 1$, as shown in figure 4.5 for the case of 11×10^6 cells. y^+ is defined as $\Delta n u_\tau/\nu$, where Δn is the height of the first cell in the direction n normal to the body surfaces, $n \in [y, z]$, u_τ is the friction velocity and ν is the kinematic viscosity. The friction velocity is defined as $\sqrt{\tau_{wall}/\rho}$, where τ_{wall} is the wall shear stress and ρ is the density. The normalised near-wall grid sizes in the streamwise and spanwise directions are $\overline{l^+} \leq 39$ and $\overline{s^+} \leq 40$, respectively, where $l^+ = \Delta l u_\tau/\nu$ and $s^+ = \Delta s u_\tau/\nu$. Δl is the cell size in the streamwise direction, and Δs is the cell size in the direction normal to both the streamwise and the surface, $s \in [y, z]$. The values $\overline{l^+}$ and $\overline{s^+}$ follow the mesh requirement for LES (Piomelli and Chasnov, 1996). A growth rate of 1.1 is used between the different mesh zones, as indicated in figures 4.3 and 4.4, to minimise the computational cost (Hesse and Morgans, 2021). The values

Mesh size ($\times 10^6$ cells)	$\overline{C_D}$	$\overline{C_{\text{PBase}}}$	$\overline{\frac{L_R}{H}}$	$\overline{y^+}$	y^+_{Max}
15	0.362	-0.22	1.43	0.10	0.6
11	0.360	-0.22	1.42	0.58	1.0
9	0.352	-0.20	1.45	0.95	3.0
Exp. (Grandemange et al. (2013b))	0.257	-0.19	1.41	-	-
Sim. (Hesse and Morgans (2021))	0.364	-0.20	1.42	-	< 1

Table 4.1: Mesh Independence study, based on the time-averaged drag ($\overline{C_D}$), time-averaged base pressure ($\overline{C_{\text{Pbase}}}$), time-averaged recirculation length ($\overline{L_R}$), time-averaged and maximum y^+. Re_H for Grandemange et al. (2013b) experimental study and Hesse and Morgans (2021) numerical study was 9.2×10^4 and 3.3×10^4, respectively.

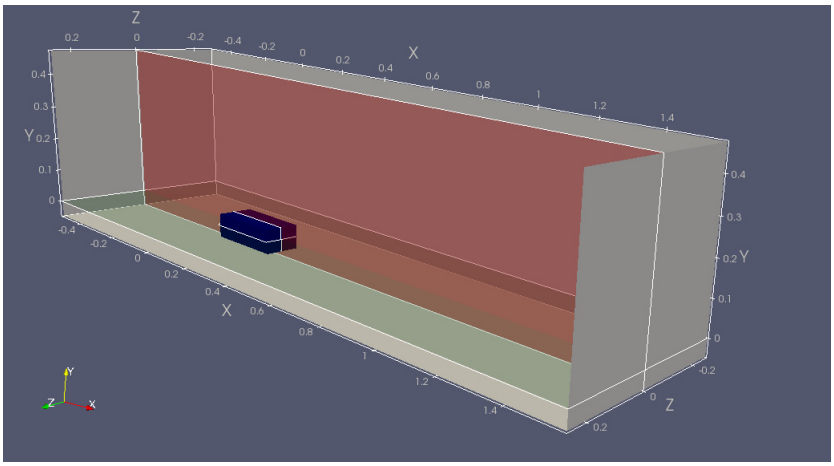

Figure 4.2: Solution domain with a vertical body-centred plane (red) and horizontal body-centred plane (green). Air flows in $+x$ direction.

of the mean flow properties (drag coefficient, base pressure and length of the recirculation region) were validated versus the experiment of Grandemange et al. (2013b) and the numerical study of Hesse and Morgans (2021), as summarised in table 4.1. The maximum error in the length of the recirculation region length and the average base pressure were about 2% and 15%, respectively, compared to the corresponding values from experiments, which was conducted at $Re_H \sim 9.2 \times 10^4$. Fan et al. (2020b) conducted an experimental study using the same geometry considered in the current study at $Re_H \sim 9.2 \times 10^4$, similar to Grandemange et al. (2013b). A difference of 6% in the averaged base pressure between Fan et al. (2020b) and Grandemange et al. (2013b) can be seen, which might be attributed to measurement uncertainties, making the current difference acceptable. The values of the averaged base pressure and the time-averaged drag are comparable to the simulation results of Hesse and Morgans (2021), at the same Re_H. The time-averaged drag exhibits a maximum difference of 3% compared to Hesse and Morgans (2021). Based on these comparisons and the value of y^+_{max} indicated in (table 4.1), the mid-size (11 million cells) is selected for the simulations. In this case, the value of $y^+_{\text{Max}} \leq 1$ confirms that the near-wall regions are fully-resolved. The average cell size in the wake region resolves the Taylor microscale, representing the minimum turbulent length scale to be resolved by the LES (Howard and Pourquie, 2002).

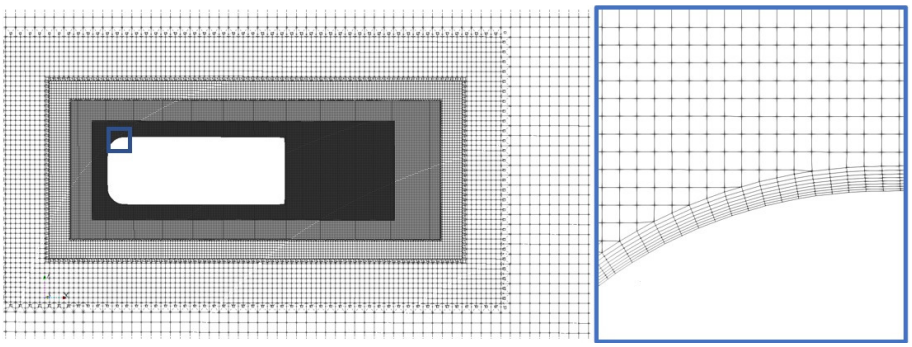

Figure 4.3: Mesh details on the vertical plane (xy). The zoomed view (in the blue box) shows the prism layers on the body surface.

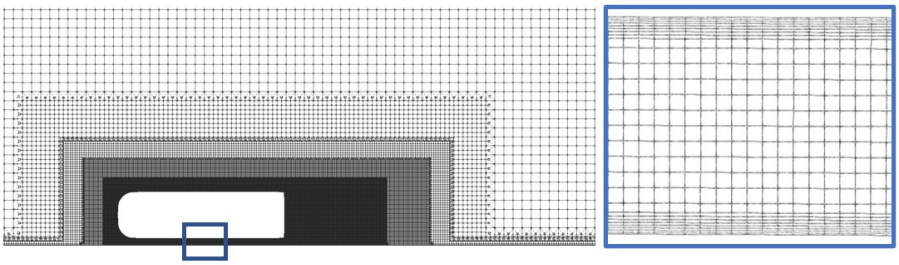

Figure 4.4: Mesh details on the horizontal plane (xz). The zoomed view (in the blue box) shows the prism layers used to resolve the boundary layers on both the body and the ground surfaces.

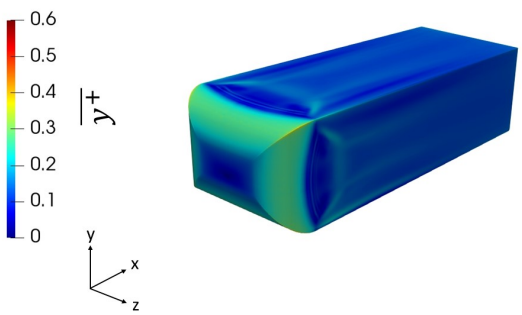

Figure 4.5: $\overline{y^+}$ distribution on the Ahmed body for the mesh size of 11×10^6 cells.

4.2 Time-averaged flow

This subsection discusses the time-averaged flow past the square-back Ahmed body. Figure 4.6 and 4.7 show the top and side views on mid-body planes, shown in figure 4.2, of the mean flow. Four separation bubbles are identified, where the separation bubble is defined as the envelope of zero streamwise mean velocity. The boundary layers on the top and side surfaces separate just aft the body nose, creating small separation bubbles on the three surfaces, then reattach to the surfaces prior to the body rear-end, i.e. the body base. Similar upstream separations were reported in Spohn and Gilliéron (2002), Krajnovic and Davidson (2003), Franck et al. (2007) and the experiments by Grandemange et al. (2013b). The top and side boundary layers separate at $x/L \sim 0.08$, then reattach at $x/L \sim 0.30$ on the top surfaces and at $x/L \sim 0.26$ on the sides. The boundary layers on both the bottom surface and the ground remain attached. A detailed investigation of the characteristics of these boundary layers will be shown in chapter 6.

At the rear end of the body, the four boundary layers separate off the longitudinal body surfaces, forming the wake behind the body. Each of these shear layers forms a sub-recirculation zone in the wake, as indicated by the streamlines shown in figures 4.6 and 4.7. The time-averaged wake looks horizontally symmetric, but the side view (figure 4.7) shows that the sub-recirculation region formed by the top shear layer is slightly larger than the bottom, indicating a slight vertical asymmetry. The average length of the bubble in the wake is $\sim 1.42H$, defined as the maximum streamwise distance between the base and the separation bubble profile. The mean pressure coefficient on mid-body planes is shown in figure 4.8, indicating the presence of a toroidal vortex in the wake. Figure 4.9 shows three-dimensional views of this vortex, identified by an isosurface of $\overline{C_P} = -0.22$. This matches previous studies by Bearman (1997), Krajnovic and Davidson (2003), Minguez et al. (2008), Rouméas et al. (2009), Khalighi et al. (2012), Grandemange et al. (2013b) and Volpe et al. (2015). The low-pressure recirculation bubble imposes low pressure on the base. The mean base pressure is $\overline{C_{Pbase}} = -0.22$, which influences the mean drag. The low base pressure, $\overline{C_{Pbase}}$, contributes $\sim 60\%$ to drag similar to Ahmed et al. (1984), Grandemange et al. (2013b) and Ahmed and Morgans (2022), making it an essential parameter in controlling the wake flow for drag reduction. The mean drag coefficient $\overline{C_D}$ is 0.36, matching the value reported in Eulalie et al. (2014), Lucas et al. (2017) and Hesse and Morgans (2021).

The base pressure is also influenced by the shear stresses in the recirculation region, which can be thought of as a balance between the pressure, shear and normal stresses. Similar to the analysis done by Balachandar et al. (1997) in the wake of a two-dimensional bluff body, the streamwise momentum balance in the wake of the Ahmed body is shown in equation 4.1 (neglecting the viscous force), where n_i is a unit vector normal to the mean separation bubble (SB) in the wake and $i \in [x, y, z]$. The pressure gradient on the separation bubble can be defined using the normal

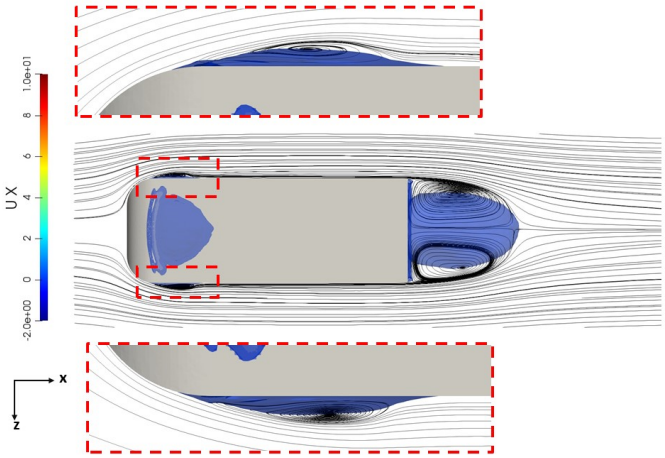

Figure 4.6: Top view of the separation bubble in the wake superimposed with in-plane streamlines at the mid-plane of $y/H = 0$. Zoomed views (in the red dashed box) show the frontal separation bubbles caused by the boundary layer separation on the sides.

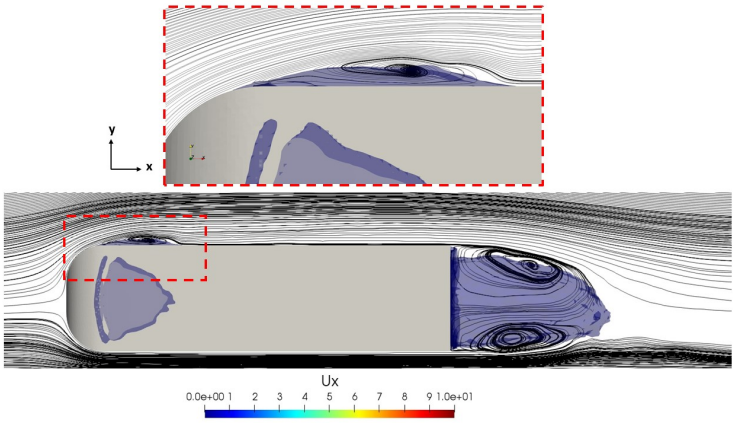

Figure 4.7: Side view of the separation bubble in the wake superimposed with in-plane streamlines at the mid-plane of $z/W = 0$. A zoomed view (top) showing the frontal separation bubble caused by the boundary layer separation on the top body surface.

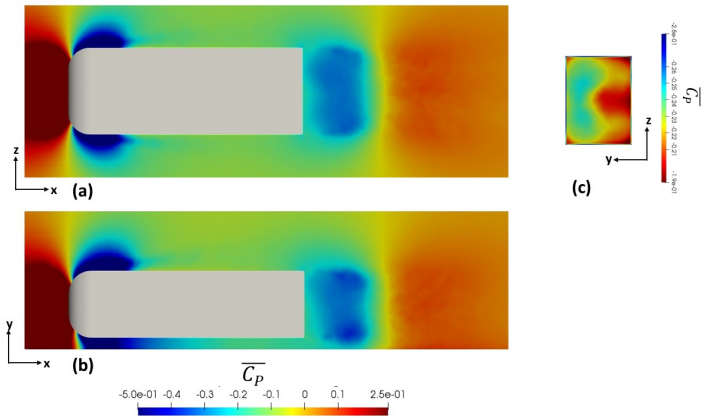

Figure 4.8: Top (a) and side (b) views of the distribution of mean pressure coefficient $\overline{C_P}$ at mid-body planes and mean base pressure coefficient (c).

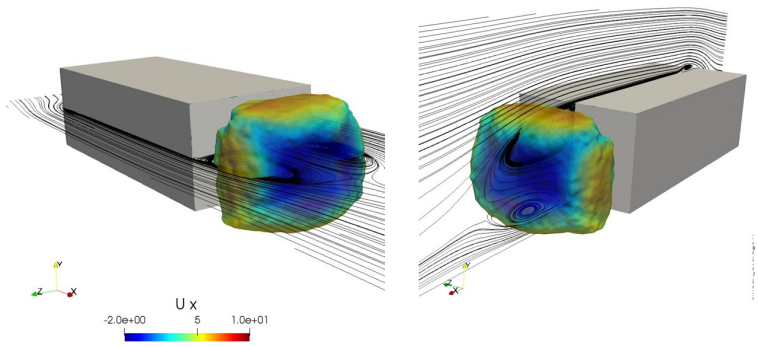

Figure 4.9: Three-dimensional view of the toroidal-vortex in the near-wake region, defined as iso-surface of $C_p = -0.22$ coloured by the time-averaged streamwise velocity and superimposed with streamlines projected on plane $y/H = 0$ (left) and plane $z/W = 0$ (right).

momentum balance as shown in equation 4.2, where k is the local curvature of the separation bubble and u_s and u_n are the tangential and normal velocities on the separation bubble (Bradshaw, 1973). This indicates that Reynolds stresses are essential for the equilibrium of the recirculation region, as they affect both the entrained momentum and the pressure gradient along the separation bubble.

$$\int_{Base} \overline{C_P} ds = 2 \int_{SB} \overline{u_x{}' u_i{}'} n_i ds + \int_{SB} \overline{C_P} n_x ds \tag{4.1}$$

$$\frac{d\overline{C_P}}{dn} = 2k\overline{u_s}^2 - 2\frac{\overline{\partial u_n{}' u_n{}'}}{\partial n} \tag{4.2}$$

Figure 4.10 shows Reynolds stresses on the mid-height plane, superimposed by the separation bubbles. It can be seen that the streamwise Reynolds stress, $\overline{u_x'^{\,2}}$, peaks at the frontal separation bubbles and has relatively higher intensity on the shear layers in the wake with the symmetric spatial distribution. The normal component of Reynolds stress $\overline{u_z'^{\,2}}$ peaks towards the end of the separation bubble and also at the frontal separation bubbles. Similarly, the forebody boundary layer separation on the top surfaces exhibits the higher intensity of Reynolds stresses as shown in figure 4.11. The intensity of the streamwise Reynolds stress $\overline{u_x'^{\,2}}$ is higher in the bottom shear layer compared to the top, correlating with the weak vertical asymmetry of the wake due to the ground effect. The distribution of $\overline{u_y'^{\,2}}$ indicates higher values at the top surfaces separation bubble and along the edge of the separation bubble in the wake. These results are in good agreement with the experimental studies by Khalighi et al. (2001) and Grandemange et al. (2013b).

4.3 Wake dynamics

Following the literature, four modes are expected to be seen in the wake of the square-back Ahmed body, three of which are periodic, and one of which is stochastic. These include:

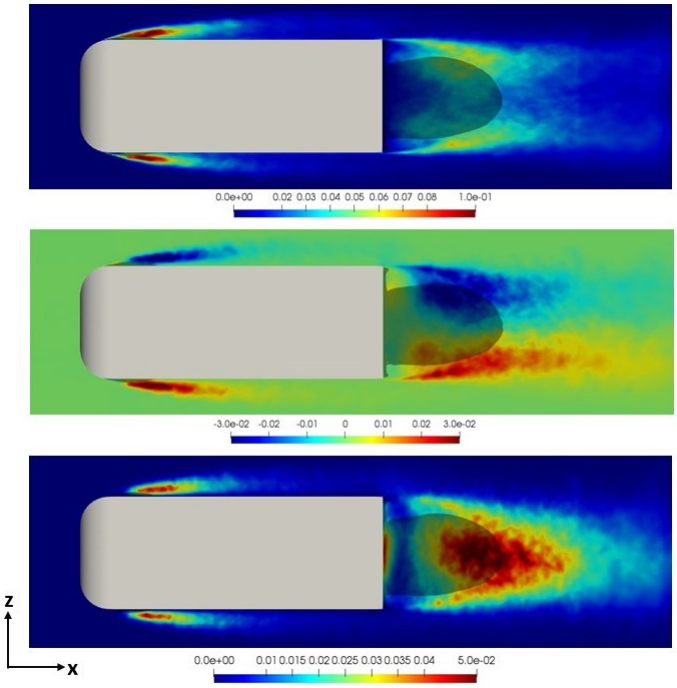

Figure 4.10: $\overline{u'_x{}^2}$ (top), $\overline{u'_x u'_z}$ (middle) and $\overline{u'_z{}^2}$ (bottom) at the mid-plane of $z/W = 0$ superimposed with separation bubbles, coloured with grey.

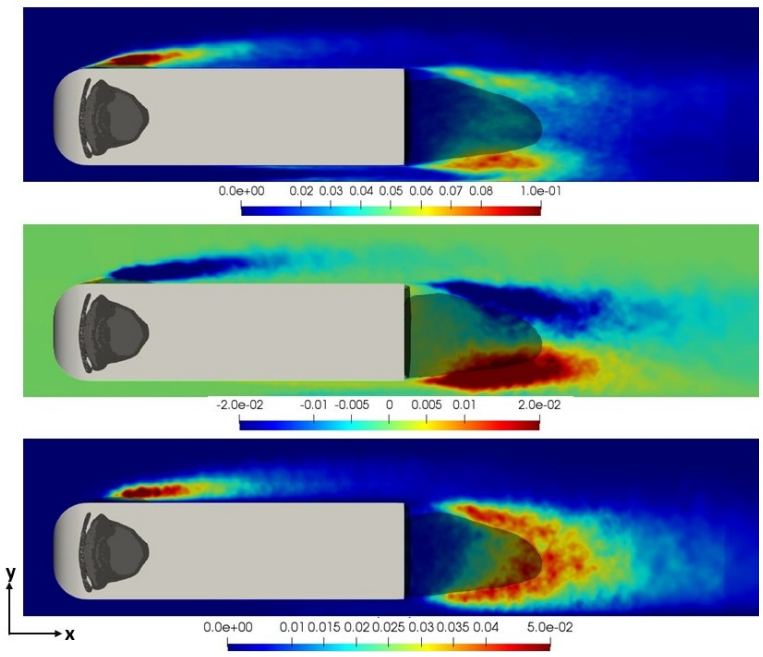

Figure 4.11: $\overline{u'_x{}^2}$ (top), $\overline{u'_x u'_y}$ (middle) and $\overline{u'_y{}^2}$ (bottom) at the mid-plane of $y/H = 0$ superimposed with separation bubbles, coloured with grey.

- The stochastic switching of the wake in one of the cross-flow directions (wake bi-modality) with a relatively long evolution time.
- The global oscillating dynamics due to the interaction of each free shear layer with its parallel counterpart, typically representing the horizontal and vertical vortex shedding.
- The streamwise bubble breathing or pumping mode.
- The dynamics related to the mixing layers in the wake.

This subsection explores the wake dynamics in more detail, considering the wake bi-modality first in section 4.3.1 followed by the periodic modes in section 4.3.2.

4.3.1 Wake bi-modality

The spatial gradients of the pressure coefficient on the base of the Ahmed body are used to investigate the wake configuration. Based on Grandemange et al. (2013a) map, with the body width, W, being larger than its height, H, horizontal bi-modality is expected. Figure 4.12 depicts the instantaneous gradient of the pressure coefficient in the horizontal and vertical directions, denoted as $\partial C_p/\partial z$ and $\partial C_p/\partial y$, respectively, where z and y are normalised by W and H, respectively, as shown in equation 3.19. The dimensionless time t^* is defined as $t^* = (tU_\infty)/H$. The wake randomly exhibits horizontal bi-modal switching, with the simulation over 2000 convective time units capturing four switches of the wake. The wake is approximately symmetric in the vertical direction, and its slight asymmetry is caused by the jet generated by the underbody flow. The most probable asymmetric positions of the wake correspond to a horizontal gradient of pressure coefficient of ± 0.20, similar to the values obtained numerically for the same Re_H but using a different code (StreamLES) (Dalla Longa et al., 2019). The maximum time the wake maintains in one asymmetric position is 750 normalised time units, with an average switch duration being 50 normalised time units, defined as the duration the wake takes to switch from the mean asymmetric position to its counterpart on the other side. The switching time is random in different simulations and the maximum switching time is slightly less than the $o(100)$ time units reported in the numerical study by Podvin et al. (2021). The wake recovers symmetry in the long time-average statistics, as seen in section 4.2.

Figure 4.13 shows a top view of the toroidal vortex in the near wake region at three time points corresponding to $\partial C_P/\partial z = \pm 0.20$ and $\partial C_P/\partial z = 0$. The toroidal vortex is defined as the iso-surface of $\overline{C_p} = -0.22$ similar to figure 4.9 for the time-averaged wake flow. Horizontal bi-modal switching causes the near wake toroidal structure to tilt towards and away from the base stochastically. During the switching period, the toroidal structure becomes instantaneously parallel to the base, representing a symmetric wake ($\partial C_P/\partial z = 0$). This effect is projected onto

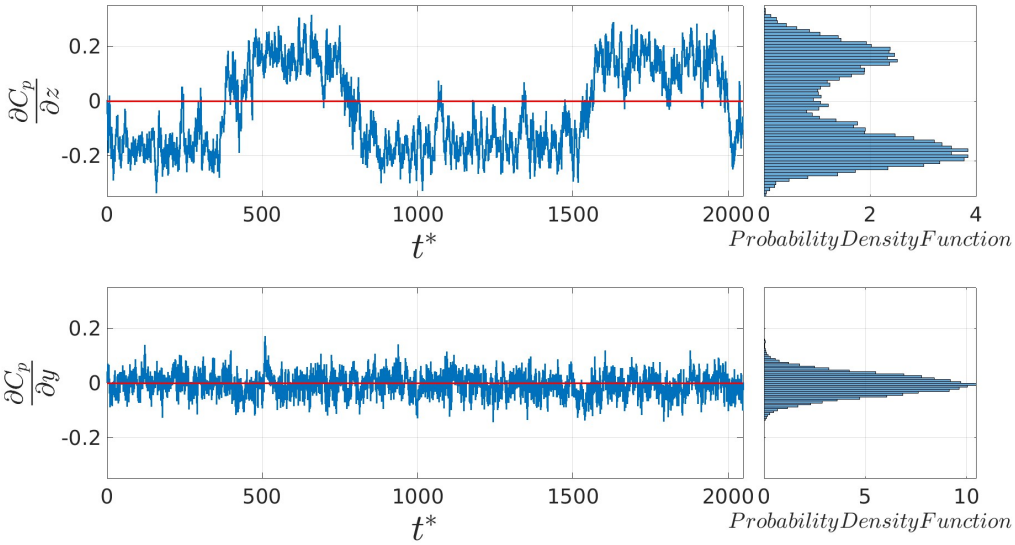

Figure 4.12: Time evolution of the horizontal (top) and vertical (bottom) gradients of pressure coefficient on the base.

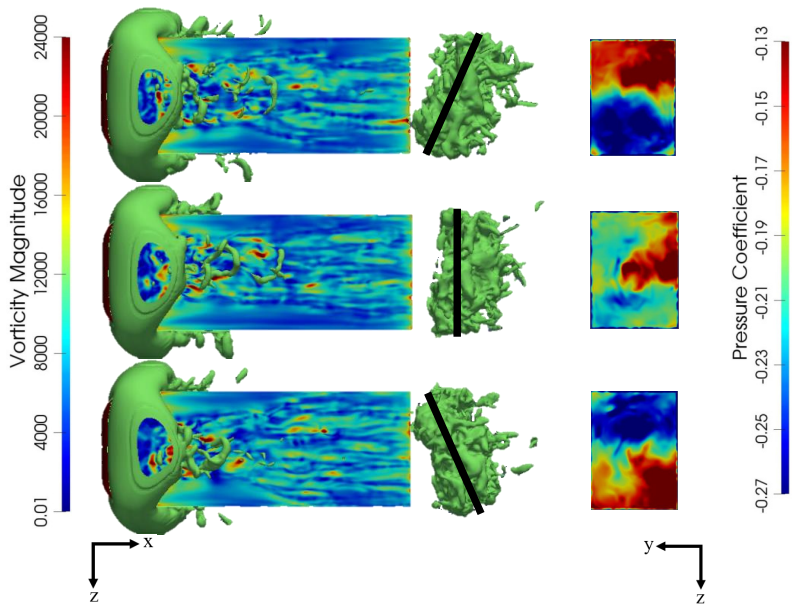

Figure 4.13: Left: Iso-contours of the coefficient of pressure $C_P = -0.22$, as well as the vorticity distribution on the body top surface, indicating the near wake vortical structures for different wake positions. Right: The associated C_p on the base.

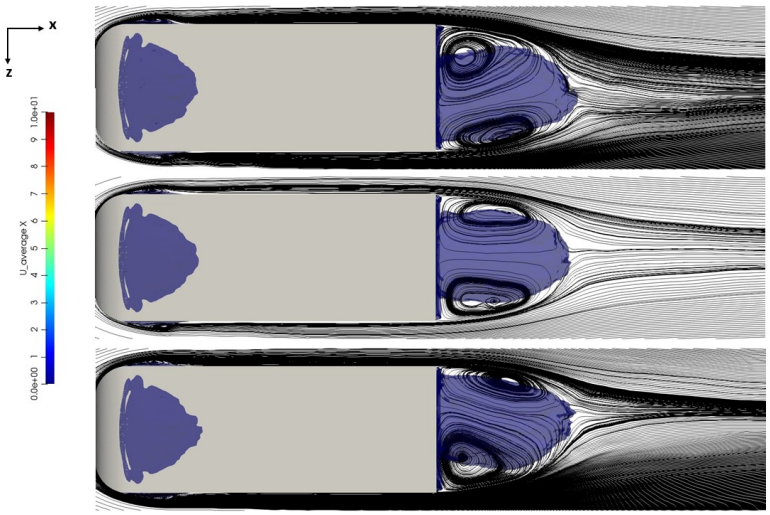

Figure 4.14: Top view of the separation bubble in the wake superimposed with in-plane streamlines at the mid-plane of $y/H = 0$. The asymmetric wake associated with $\partial C_p/\partial z < 0$ is shown on the top, $\partial C_p/\partial z = 0$ is shown on the middle and $\partial C_p/\partial z > 0$ is shown on the bottom of the figure.

the base pressure as a low-pressure region associated with the vortical structure being locally close to the base. Figure 4.13 shows this behaviour and the associated base pressure for the three cases, when the wake is tilted towards the positive z direction, during switching when the wake is instantaneously symmetric and after the switching when it is tilted towards the negative z direction. The conditional-averaged base pressure coefficient during the switching, when the wake is instantaneously symmetric, is -0.21 compared to -0.232 for the asymmetric wake states. The asymmetric wake increases the average base pressure by 10% compared to the symmetric wake, which matches the experimental results by Haffner et al. (2020). These results are consistent with previous experimental (Grandemange et al., 2013b) and numerical results (Dalla Longa et al., 2019, Hesse and Morgans, 2021), which capture side-to-side bi-modality.

Conditional averaging of the velocity field for the asymmetric wake shows that the reflectional symmetry breaking influences the separation bubble. Figure 4.14 shows that for a negative horizontal pressure gradient ($0 \leq t^* \leq 350$ and $800 \leq t^* \leq 1500$), the bubble is oriented towards $+z$ direction. The bubble is superimposed with in-plane streamlines at the mid-height of the body, showing that the recirculation region is dominated by the shear layer separated off the $-z$ side. This shear layer exhibits higher curvature than the parallel layer, coinciding with a relatively higher curvature of the bubble on the same side. The opposite effect can be seen for the conditional average of the flow when the wake switched to the reflected asymmetric position ($450 \leq t^* \leq 650$ and $1600 \leq t^* \leq 1900$). This is aligned with the switching mechanism proposed by Haffner et al. (2020), that for a horizontally-asymmetric wake, the shear layer on one side forms a relatively stronger sub-recirculation compared to the parallel shear layer. Both sub-recirculation regions have the same strength during the switching, which leads to an instantaneously symmetric wake. This will

further be discussed in section 5.4.3. The length of this curved recirculation region exhibits no change in both cases, with a value of $\sim 1.42H$ measured as the maximum streamwise distance from the base of the bubble. This effect disappears in the time-averaged flow field as indicated in figure 4.14 (middle case), with the bubble being symmetric horizontally. Flow separations on both sides are depicted in the same figure with small upstream separation bubbles. Upstream separations hold for both wake asymmetric configurations.

The vertical position of the wake exhibits no change for the different horizontal asymmetric positions of the wake. The conditional average for both wake orientations is similar to figure 4.7. The bubble is tilted slightly towards the ground indicating vertical asymmetry due to the underbody effect. The wake is dominated by a downwash flow from the top shear layer, shown by the larger recirculation region compared to the bottom. Figure 4.7 also shows the upstream separation bubble caused by boundary separation on the top body surface just aft of the body nose. The relevance of these upstream separation bubbles to the wake configuration will be further discussed in Chapters 6 and 7. No separation bubbles were seen in the underbody region, meaning that both the bottom surface and the ground boundary layers remain attached throughout, similar to the time-averaged flow. The time-history of the area-averaged base pressure coefficient, $< C_{P-base} >$, shown in figure 4.15a, does not show a clear mark of wake bi-modality, nor the time-history of the drag coefficient C_D, shown in figure 4.15b.

Wake bi-modality also influences the Reynolds stress intensities and distributions in the wake region. An asymmetric distribution is evidenced for both the normal and the shear stresses on the mid-body plane shown in figure 4.16. Compared to the time-averaged wake, both $\overline{u_x{}'^2}$ and $\overline{u_z{}'^2}$ exhibit increased intensities in the wake region. On the side view, shown in figure 4.17, the streamwise Reynolds stress peaks at the mid-height zone, not the top and bottom shear layers. This could be related to the bi-modal switching of the wake. The distribution of $\overline{u_y{}'^2}$ looks similar to the time-averaged case with less intensity. The upstream separation bubbles experienced higher intensities of Reynolds stresses, similar to the time-averaged case. The effect of horizontal bi-modality on the stresses in the wake correlates very well with the experimental results by Grandemange et al. (2013b). To conclude, these results confirm that bi-modality affects the coherent structure of the wake flow and the base pressure, which both directly affect the aerodynamic drag. Symmetrising the wake has a favourable effect on base pressure recovery and drag. The next chapter will explore detailed investigations into suppressing bi-modality using different control techniques.

4.3.2 Periodic modes in the wake

This subsection investigates the periodic modes in the wake of the square-back Ahmed body. The symmetric and anti-symmetric base pressure signals considered in the following analysis are defined

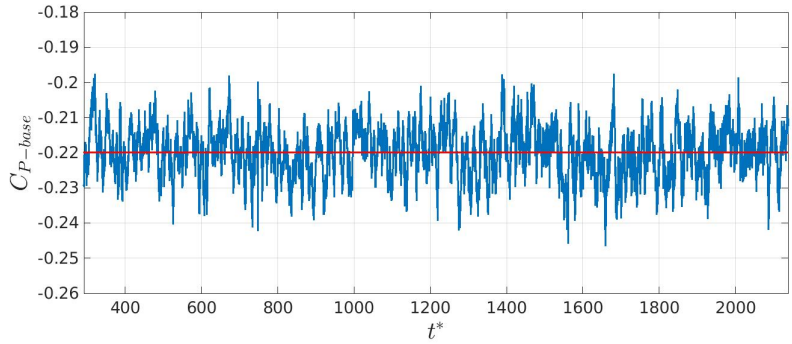

(a)

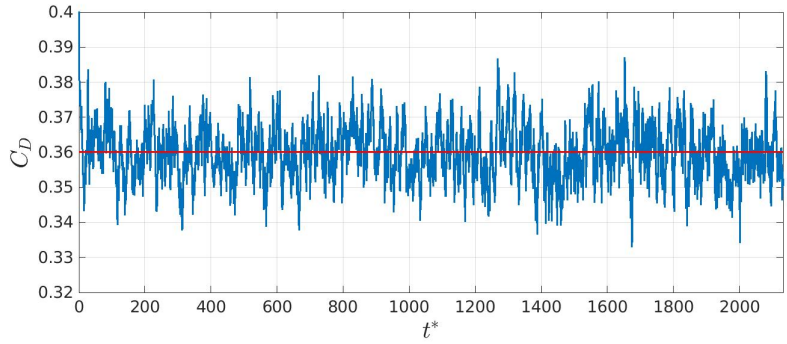

(b)

Figure 4.15: Time history of the area-averaged base pressure coefficient $< C_{P-base} >$ (a) and drag coefficient $< C_D >$ (b). The red line indicates the mean values in the presence of horizontal bi-modality.

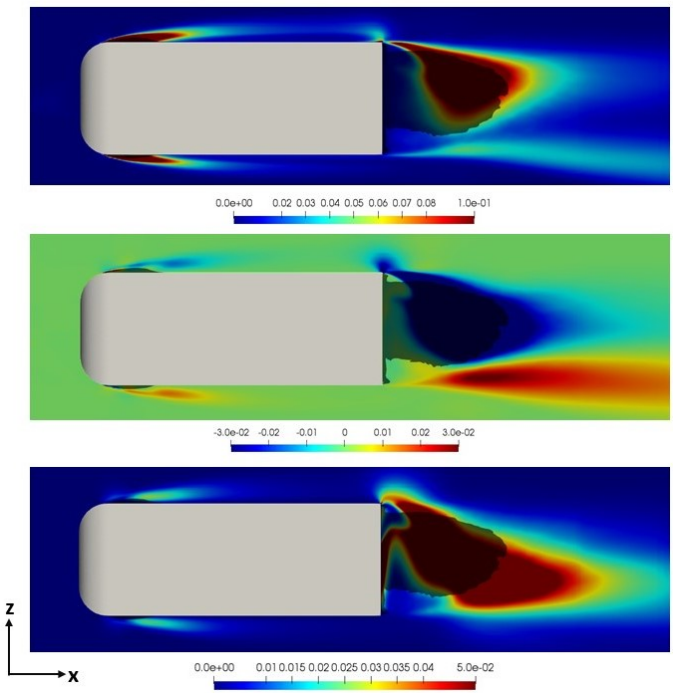

Figure 4.16: $\overline{u'_x{}^2}$ (top), $\overline{u'_x u'_z}$ (middle) and $\overline{u'_z{}^2}$ (bottom) at the mid-plane of $z/W = 0$ superimposed with separation bubbles, coloured with grey for the asymmetric wake.

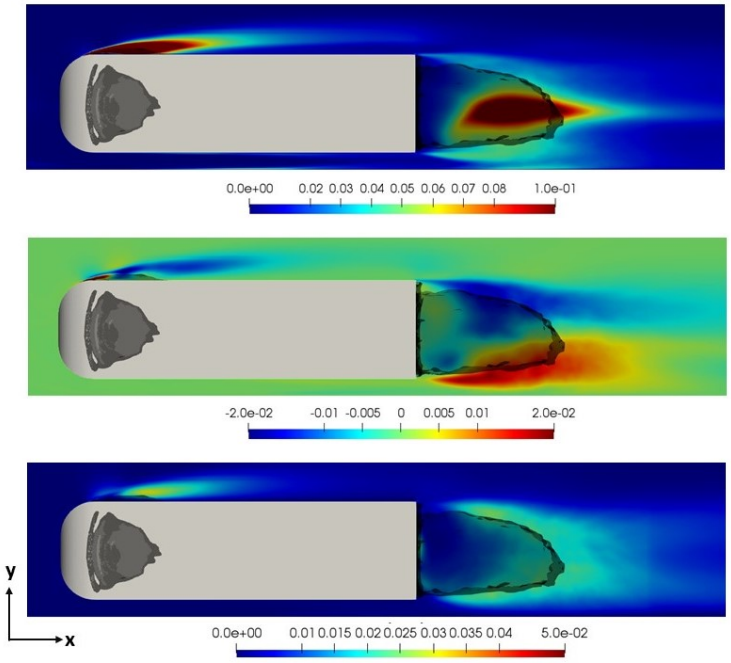

Figure 4.17: $\overline{u'_x{}^2}$ (top), $\overline{u'_x u'_y}$ (middle) and $\overline{u'_y{}^2}$ (bottom) at the mid-plane of $y/H = 0$ superimposed with separation bubbles, coloured with grey for the asymmetric wake.

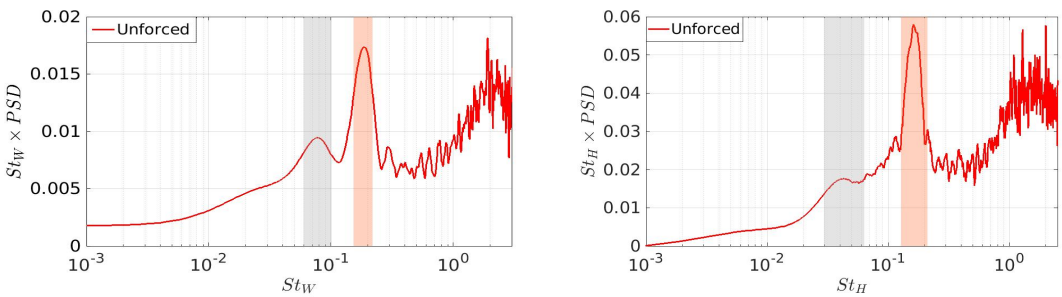

(a) (b)

Figure 4.18: Premultiplied spectra of the (a) horizontal and (b) vertical anti-symmetric base pressure signals for the unforced wake flow. Gray and red shaded areas indicate the broad frequency band related to the bubble pumping mode and vortex shedding frequency, respectively.

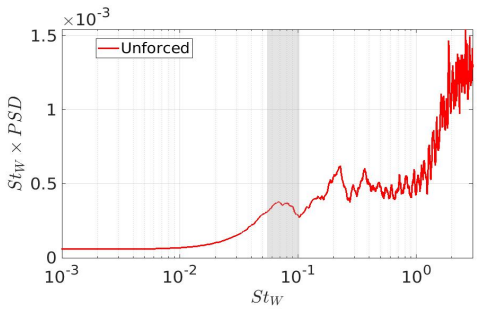

Figure 4.19: Symmetric premultiplied base pressure signals the unforced wake flow. The gray shaded area indicates the broad frequency band related to the bubble pumping mode.

in equation 4.3 and 4.4, respectively, where M is the number of the pressure probes, n_1 and n_2 are the distance of the pressure probes on the base to its centre in either of the crossflow directions (y, z) as shown in figure 4.1.

$$\Delta P\big|_{\text{Symmetric}} = \frac{1}{M}\left[\sum_M P(x,y,z)\big|_{n_1} + \sum_M P(x,y,z)\big|_{n_2}\right] \tag{4.3}$$

$$\Delta P\big|_{\text{Anti-symmetric}} = \frac{1}{M}\left[\sum_M P(x,y,z)\big|_{n_1} - \sum_M P(x,y,z)\big|_{n_2}\right] \tag{4.4}$$

Figure 4.18 shows the anti-symmetric base pressure spectra in both the horizontal and vertical directions. The Strouhal number, St, is calculated based on the body length in the direction of the anti-symmetric base pressure. The unforced signal in both directions indicates three periodic modes. The first appears with a broadband frequency around $St_W \sim 0.07$ in the horizontal signal (figure 4.18a) and around $St_H \sim 0.05$ in the vertical signal (figure 4.18b), is associated with the streamwise bubble pumping mode. This mode was detected in the base pressure spectrum in experiments by Khalighi et al. (2001) and has been hypothesised to occur due to a periodic interaction of the top and bottom halves of the toroidal vortex trapped in the near wake region, causing a periodic change in the recirculation region. A further suggestion relates it to a non-linear interaction between the vertical and horizontal vortex shedding (Volpe et al., 2015). Although a linear stability analysis of the wake behind an axisymmetric body has not captured this mode (Rigas et al., 2017), it has been detected in spectral analysis of the wakes of an axisymmetric body (Rigas et al., 2014), a circular disc and a sphere wake (Berger et al., 1990). The second mode is associated with a peak at $St_W = 0.19$ in the horizontal direction (figure 4.18a) and $St_H = 0.17$ in the vertical direction (figure 4.18b) and relates to vortex shedding in both directions. The same frequencies were reported in experimental studies by Volpe et al. (2015) and Lahaye et al. (2014). The vortex shedding frequencies in both directions are consistent with the range of frequencies reported in the literature of $0.13 - 0.19$ (Grandemange et al., 2013b, Lucas et al., 2017, Kang et al., 2021). The third dynamical mode, for the unforced base pressure, appears in figure 4.18 at $St_W \sim 1.9$ and $St_H \sim 1.6$ and is linked to the higher frequency dynamics of the shear layers in both directions, which will be seen in the spectral proper orthogonal decomposition of the unforced flow in section 7.1. The unforced symmetric base pressure signal (equivalent to $< C_P >$ with limited measurement probes), shown in figure 4.19, captures a broad frequency band around $St_W \sim 0.07$ related to the bubble pumping and high-frequency shear layers dynamics at $St_W \sim 2.4$.

To summarise, this chapter has investigated the flow past blunt bluff Ahmed body. The time-averaged and the time-resolved results were compared to the experimental and numerical studies in the literature body. A further analysis of the unforced wake using SPOD is provided in chapter 7.

Validating this unforced case represents the first step towards applying different control techniques for drag reduction, which will further be discussed in the following chapters.

Chapter 5

Feedback control for a square-back Ahmed body

This chapter covers the design and application of a nonlinear model-based feedback controller to suppress bi-modality in the wake of a square-back Ahmed body. It starts with a description of the bi-modality model followed by the design procedure for the nonlinear feedback control. The results of implementing this controller are then discussed in more detail. A sensitivity study of the controller parameters is then performed followed by some insight into the mechanism of wake bi-modality. Finally, Proper orthogonal Decomposition (POD) is used to investigate the effect of the nonlinear feedback controller on the wake.

The feedback control setup employs base pressure sensing and synthetic jet actuation through a small gap around the perimeter of the base, as shown in figure 5.1. The detailed modelling, sensing and actuation are provided in the next subsections.

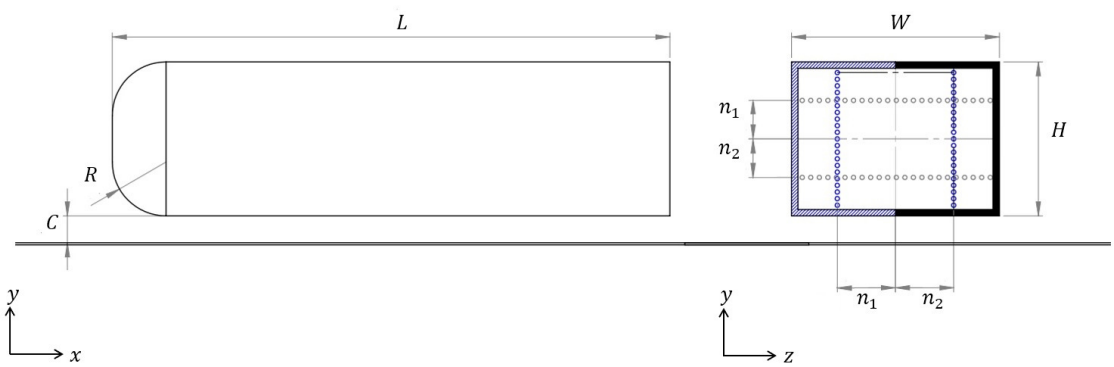

Figure 5.1: Ahmed body scaled by one fourth, with height $H = 72mm$. The circles on the base show the sensor positions used to calculate the vertical (grey) and horizontal (blue) pressure gradients. Actuation is via synthetic jets placed around the base perimeter with a thickness of $0.04H$; actuation is antisymmetric in z as shown by the blue dashed and the black solid areas.

5.1 Model for wake bi-modality

The present work adopts a nonlinear feedback control approach in order to suppress the bi-modal switching, which is itself a non-linear phenomenon Rigas et al. (2015). Synthesising a closed-loop controller for fluid flow can be achieved using one of three approaches. These are models based on high dimensional discretization of the governing equations (NS), low dimensional models derived from the governing equations and black-box model identified through system identification. The first approach captures the physics of the flow but typically leads to inapplicable controllers in real-time, due to their high dimensionality. The third approach has proven success for some flows but suffers from a limited region of validity when the assumption of dynamic linearity is used. The second approach of low dimensional nonlinear model-based control represents a good compromise between the first approach of fully resolving the nonlinear physics of the flow and the limitations of the "black-box" approach (King et al., 2005). The model-based non-linear approach is considered in the present work to facilitate the design of a non-linear feedback controller. The controller will be based upon a model in the form of a nonlinear Langevin equation, which captures both the deterministic and the stochastic evolution of the reflectional symmetry breaking in the turbulent wake of the Ahmed body. This model was initially developed to characterise the random symmetry breaking behaviour in the turbulent wake of an axisymmetric body, this exhibiting multi-modal behaviour (Rigas et al., 2015). It is based on the premise that multi-modality occurs due to the persistence of the laminar global modes at high Reynolds number, with the turbulent fluctuations acting to push stochastically between asymmetric stable positions. The deterministic part (the drift) of the Langevin model captures the nonlinear dynamics of the reflectional symmetry breaking in the laminar flow regime, employing the typical Landau equation. The stochastic part represents the effect of turbulent fluctuations.

$$\frac{dr(t)}{dt} = -\lambda r^3 + \alpha r + \sigma\zeta(t) \tag{5.1}$$

Brackston et al. (2016) adapted the model for rectilinear bodies exhibiting bi-modality, such as the square-back Ahmed body. Barros et al. (2017) employed a coupled Langevin model to represent the transition of the wake from the vertical asymmetric state to a horizontal bi-modal with vertical symmetry. The adapted Langevin model is shown in equation (5.1). The parameter $r(t)$ is some measure of the modal amplitude, α is the growth rate and λ the saturation parameter. The first two terms on the right hand side represent the spatial reflectional symmetry breaking (RSB) mode, which arises due to a supercritical pitchfork bifurcation at laminar Reynolds numbers, as described in section 2.1.1. The last term represents the turbulent broadband forcing acting on the coherent structures of this mode, with $\zeta(t)$ the random dynamics of a standard Wiener process and σ^2 the

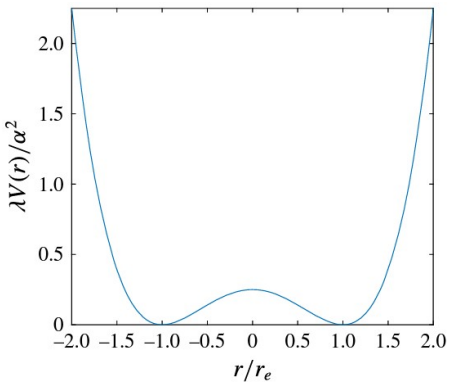

Figure 5.2: Double-well potential function of the deterministic part of the Langevin equation used to model bi-modality Brackston et al. (2016). $V(r)$ is the potential function and $r_e = \pm\sqrt{\frac{\alpha}{\lambda}}$.

noise intensity; it is expected to capture all flow disturbances that cause wake switching between the two asymmetric states.

In the present work, the parameter chosen to characterise the wake mode position, *r(t)*, is the horizontal centre of pressure on the base, calculated as shown in equation (5.2), where *P(x,y,z,t)* is the pressure, W the width of the base and A_{base} the base area. A value of *r(t)* $= 0$ corresponds to a symmetric wake. Based on the previous model, the deterministic part has a double-well potential, shown in figure 5.2. It has three equilibrium points, at $r_e = 0, \pm\sqrt{\frac{\alpha}{\lambda}}$. $r_e = 0$ is an unstable equilibrium point, which will be targeted by the controller to symmetrise the wake. According to the model, *r(t)*, moves within closed bounds around one of the two asymmetric states until sufficiently perturbed by the stochastic term to switch to the other. The corresponding probability density function of *r(t)*, obtained experimentally at different *Re*, shows little dependence on *Re* in the turbulent regime (Brackston et al., 2016).

$$r(t) = \frac{1}{W \iint_{A_{base}} P(x,y,z,t)\, dA} \iint_{A_{base}} zP(x,y,z,t)\, dA \tag{5.2}$$

The model parameters for the current Ahmed body, (α,λ,σ^2), were identified by fitting the model to the unforced flow data. The time-averaged mean square displacement (MSD) of the horizontal centre of pressure, *r(t)*, is shown in figure 5.3a. Its value is calculated as $\langle (r(t+\delta t) - r(t))^2 \rangle$, where δt here has the same value as the simulation timestep. The findings are consistent with those of Rigas et al. (2015): the MSD is found to be proportional to the lag time, δt, before starting to plateau. A linear least square fit was used to estimate the value of the noise intensity (diffusion coefficient) for the short time scale region, where $\langle (\Delta r(\delta t))^2 \rangle = 2\sigma^2 \times \delta t$. The value of the noise intensity is found to be $\sigma^2 = 0.64$. The probability density function (PDF) of the model, obtained using the steady-state Fokker Plank equation (equation (5.3), where C represents a normalising constant), was matched to the probability density function of *r(t)* from the unforced simulation (figure 5.3b). This allowed estimates of both α and λ to be obtained as 3.6 and 91.0

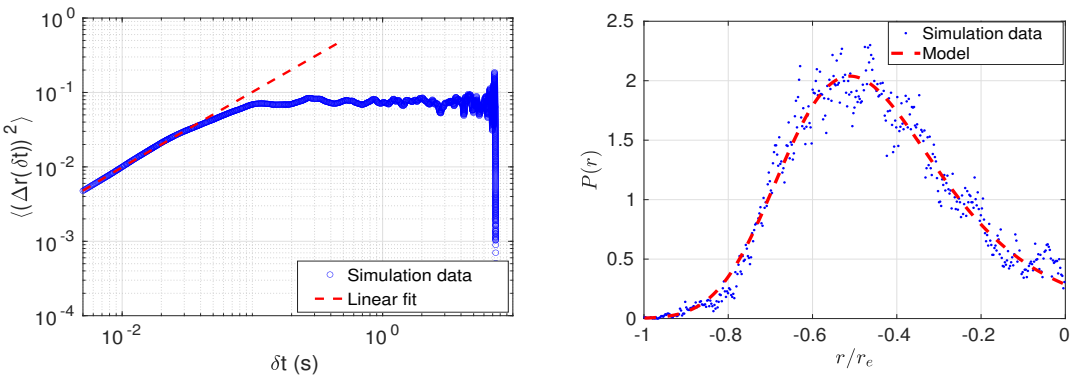

(a) (b)

Figure 5.3: (a) Mean Square Displacement (MSD) of the horizontal centre of pressure $r(t)$ in the unforced case (blue) and a linear fit (red dashed line) to estimate the noise intensity σ^2. (b) Probability Density Function of the model (dashed red line) and the data of one asymmetric stable position of the wake (blue dots).

respectively. With reference to Barros et al. (2017), the values of these parameters are for a weakly vertically asymmetric wake, as identified for the unforced case.

$$P(r) = C \exp\left(\frac{\alpha}{\sigma^2} r^2 - \frac{1}{2}\frac{\lambda}{\sigma^2} r^4\right) \tag{5.3}$$

5.2 Feedback Control Design

Due to the strongly non-linear behaviour underpinning the bi-modal switching (Rigas et al., 2015), a nonlinear feedback controller based upon the above Langevin model is targeted. The sensor signal, *r(t)*, which acts as the input signal to the controller, is a measure of the horizontal centre of pressure on the base. *r(t)* is calculated by placing 48 sensors on the base of the square-back Ahmed body at a horizontal normalised distance of $\Delta z = 0.125$ between each successive sensors and a vertical normalised distance of $\Delta y = 0.17$. The output signal from the controller is then fed to the synthetic jet actuators, which are located in a gap around the outer perimeter of the base with a width of $0.04H$. The jet actuation is purely in the streamwise i.e. x-direction. It is horizontally antisymmetric, such that the actuation on the right is in anti-phase with the actuation on the left as shown in figure 5.1. At any instant in time, the actuation has zero-net-mass-flux, since the left and right mass injection cancels: streamwise momentum is sucked from one side of the base and blown through the other. Thus a single signal dictates the spatial variation around the whole actuation perimeter. The block diagram of the single-input single-output (SISO) feedback control is shown in figure 5.4.

Based on the above model different nonlinear controllers were synthesized, employing three different controller design methods. These were the Lyapunov function-based method, robust

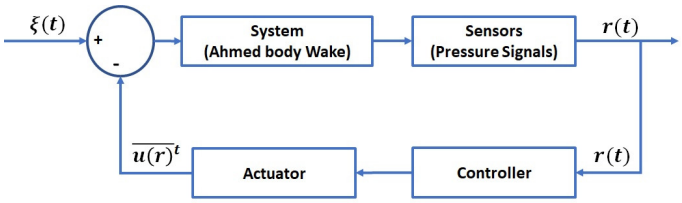

Figure 5.4: Block diagram of the feedback control loop.

control under matching conditions (backstepping) and optimal control using the Hamiltonian-Jacobi-Isaacs. In the first instance, these were applied to a simplified toy model of the *RSB* described above, using the Simulink Control Design tool in MATLAB. The system is assumed to be a single-input single-output system (SISO) with an arbitrary values of the input $-4 \leq r \leq 4$. The stochastic term in the Langevin model is represented by adding a white Gaussian noise to the input signal. The signal-to-noise ratio for this is specified as $0.1dB$. The motivation for this is that it can show the performance of the different model-based controllers using less computational power. The design procedure for the nonlinear controller based on the Lyapunov function method is discussed in more detail in the following paragraphs, with the design procedure for the other control methods discussed in appendix A.

The application of Lyapunov function technique for controlling nonlinear systems was introduced by Artstein (1983), who established a link between the continuous stabilisation of a nonlinear system and the existence of a control Lyapunov function. In this study, a quadratic Lyapunov function is used, as defined through equation (5.4). $V(r)$ is a positive definite function which is continuously differentiable and decreases with time, i.e. $V(r) > 0, \forall \mid r \mid > 0$ and $V(0) = 0$. The negative definite derivative of the Lyapunov function, shown in equation (5.5), guarantees the asymptotic stability of the closed-loop controlled system for the given range of $r(t)$ that corresponds to the position of the asymmetric wake in the unforced case (Wong et al., 1998). The control law is represented by equation (5.6), where *u(r)* is the controller signal sent to the actuator, A and B are time-independent amplification factors and λ and α are the model parameters estimated from the unforced case results in section 5.1. The controller signal *u(r)* represents the non-dimensional actuator jet velocity, i.e. $u(r) = U_{jet}(t)/U_{\infty}$. The robustness of the controlled system to variations in the controller parameters was was examined. The controller was found to be asymptotically stable for $0 < (\alpha, \lambda) \leq \infty$. The amplification parameter B, must be a positive value to maintain the asymptotic stability of the controlled system. A represents a scaling parameter of the controlled signal ($A \geq 1$).

$$V(r) = \frac{1}{2}\, r^2 \tag{5.4}$$

$$\frac{dV}{dt} = \frac{dV}{dr} \times (\dot{r} + u(r)) \;,\; \dot{V} < 0 \;,\; \dot{V}(0) = 0 \;,\; \forall \mid r \mid > 0 \tag{5.5}$$

Controller	Controller design method	Control law
Controller-1	Lyapunov function	$u(r) = -A(-\lambda r^3 + (B+\alpha)r)$
Controller-2	Artstein-Sontag	$u(r) = -(-\lambda r^3 + \alpha r) - \lvert\sqrt{(-\lambda r^3 + \alpha r)^2 + r^2}\rvert$
Controller-3	Backstepping	$u(r) = -(-\lambda {r_1}^3 + \alpha r_1 + r_2) + (\alpha - \mu - 1)r_1$ $+(\alpha r_1 + r_2 - \lambda {r_1}^3)(3\lambda {r_1}^2 - \mu)$ $r_2 = \lambda {r_1}^3 - \mu r_1$
Controller-4	Backstepping-II	$u(r) = -(\alpha r_1 + r_2) - r_1 - \alpha(\alpha r_1 + r_2 - \lambda {r_1}^3)$ $r_2 = -\mu r_1$
Controller-5	HJI	$u(r) = \lambda r^3 - \alpha r - r\sqrt{\lambda^2 r^4 - 2\lambda\alpha r^2 + (\alpha^2+1)}$

Table 5.1: Summary of the nonlinear model-based control laws synthesized to suppress wake bi-modality. Note that r_1 used in the control law based on Backstepping method is equivalent to r, i.e. the base center of pressure.

$$u(r) = -A(-\lambda r^3 + (B+\alpha)r) \tag{5.6}$$

The nonlinear controllers based on other design tools (details in appendix A) are summarised in table 5.1. When the different controllers were applied to the "toy SIMULINK model" of the *RSB* behaviour, figure 5.5 shows their effect on the probability density function of system. In the absence of control, the PDF of the unforced system indicates two peaks, presenting the two stable asymmetric positions of the wake. The figure shows that all controllers resymmetrise the system around the centre i.e. $r = 0$, except controller-2 which employs the Artstein-Sontag universal controller. In this case the curve has a maxima at $r < 0$, which means that the wake will be asymmetric and shifted to the left. Another key observation is that the behaviour depends on the initial condition of the system, i.e. if the initial position of the wake was at $r > 0$ the controller drives the wake towards the centre temporarily (local stability point), however, if the initial condition of the wake was at $r < 0$ the controller shifts the wake directly towards the left. Thus, $r = 0$ is not a global stable point in this case, but an inflection point, which leads to exclude controller-2 from the options.

Figure 5.6 indicates the time-history of $r(t)$ (shown in blue), and the controlled signal for each case. When the controller based on the Lyapunov function method is used, the system is symmetrised around $r = 0$, i.e. the controller suppresses the bi-modal behaviour of the system, as shown in figure 5.6a. Figure 5.6b confirms the results indicated by the PDF profile for the Artestin-Sontag controller, that the wake is stabilized at an off-centered asymmetric position. Figures 5.6c and 5.6d shows the controlled signals when the nonlinear controllers based on the recursive backstepping method are applied. Two different variations were compared, one employing

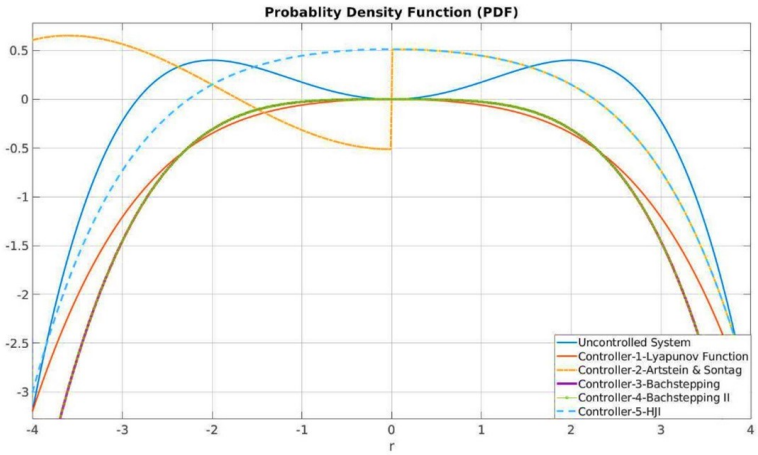

Figure 5.5: Probability Density Function (PFD) for the bi-modality model in the absence and the presence of the nonlinear controllers designed using different methods.

a nonlinear bi-modality subsystem model (controller-3) and one employing a linear bi-modality model (controller-4). Both controllers suppressed the bi-modal behaviour, however, controller-4 (figure 5.6d) resulted in higher noise amplitude (spatial bounds of the remaining oscillations) compared to controller-3 (figure 5.6c). Figure 5.6e shows the time-history of the controlled signal using the nonlinear controller designed based on the Hamilton-Jacobi-Isaacs formulation. The switching is suppressed with the system symmetrised around $r = 0$. Based on wake symmetrisation behaviour and stability, any of controllers-1, 3 and 5 could be applied to the LES simulations of the Ahmed body. Due to the heavy computational resources required for the simulations, only one nonlinear controller method will be implemented in the full LES, and the simplicity of the Lyapunov controller method, means that it will be chosen.

5.3 Feedback Control Implementation

Having validated the LES approach for accurately simulating the wake flow in chapter 4, we now describe the adaptations to the simulations needed in order to implement feedback control. As shown in figure 5.1, synthetic jet actuation is applied through the base perimeter following the base pressure signal. For the actuation, a time-dependent boundary condition is needed (only) at the location of the actuator slots. The actuation signal, given by the controller output value, must be calculated at each timestep in response to the time-varying input sensor signal from the pressure probes. This is implemented using the *SWAK4FOAM* (SWiss Army Knife for OpenFOAM) library (Gschaider, 2020). *SWAK4FOAM* is a plugin $C++$ library, which allows the use of a user-defined time-varying equation to prescribe the values at the boundary, instead of the default constant value in OpenFOAM.

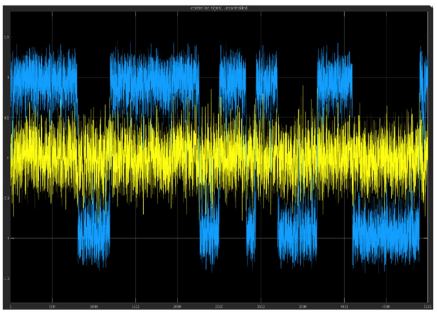

(a)

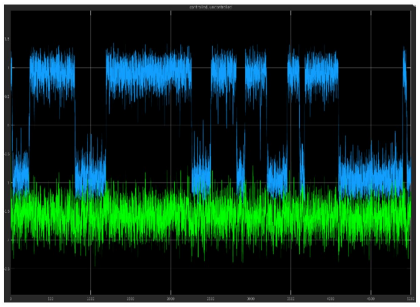

(b)

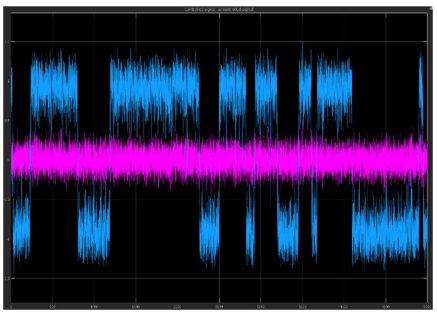

(c)

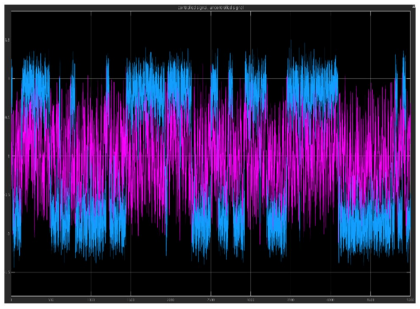

(d)

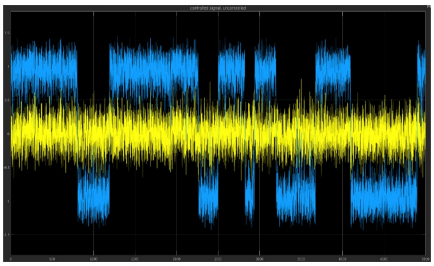

(e)

Figure 5.6: Time-history of $r(t)$ as applied to toy model of *RSB* behaviour. The controller input signals are shown in the presence (yellow, green and pink) and absence (blue) of the nonlinear feedback controllers. The unforced signal shown in blue and the controlled signal based on Lyapunov function (a), Artestin-Sontag universal controller (b), backstepping-1 (c), backstepping-2 (d) and Hamiltonian-Jacobi-Isaacs (e).

The value of the center of pressure (input), $r(t)$, is calculated in real time at the relevant simulation timestep and fed to the controller. The inherent nonlinearities of the flow necessitate a response time of the wake flow. This is accounted for by employing the weighted moving average of $u(r)$, denoted $\overline{u(r)}^t$ and shown in equation (5.7) where β is a weighting coefficient given by the ratio of the simulation timestep (Δt) to a characteristic time equivalent to $St_H \sim 2$, taken to be the maximum frequency resolved in the unforced flow. Applying the weighted moving average limits the unsteadiness introduced to the streamwise momentum in the wake, which contributes to the drag (Dalla Longa et al., 2017).

$$\overline{u(r)}^t = \beta u(r)^t + (1-\beta)\overline{u(r)}^{t-\Delta t} \tag{5.7}$$

The feedback controller is implemented in simulations, initially with controller parameters $A = 10$ and $B = 60$. The simulation shown in figure 5.7 initially has control switched off, during which time the wake switches once in the horizontal direction. The controller is switched on at $t^* = 640$, with the convective time for the controlled duration of the simulation being 1230. This is significantly greater than the maximum residence time of the wake in a given asymmetric state the unforced case ($t^* = 750$) and is thus deemed statistically sufficient for investigating the controller performance. The effect of the feedback controller are explored in the following subsections, assessing first its effect on the main control objective – suppressing the wake bi-modal switching – as well as its effect on the mean flow properties, the mean body drag and the other dynamical wake modes.

5.3.1 Bi-modality suppression

The main control objective is to suppress the stochastic switching of the wake, as characterised by the horizontal base pressure gradient. The effect of the controller on both the horizontal and vertical pressure gradients is shown in figure 5.7. It is evident that the wake switching behaviour in the horizontal direction is completely suppressed. The probability density function of the horizontal base pressure gradient ($\partial C_P/\partial z$) exhibits just a single peak around the center in the presence of control.

Although the controller was designed to target the deterministic part of the bi-modality model – the static RSB modes – as discussed in section 5.1, it also affects the wake oscillations around the main wake position. These oscillations, which we will term "residual oscillations", are caused by the turbulent disturbances modelled via the stochastic term in the absence of control in equation (5.1). A reduction in the level of these residual oscillations – in the horizontal direction – is achieved after switching the controller on. Thus an advantage of the nonlinear controller is that it results in much

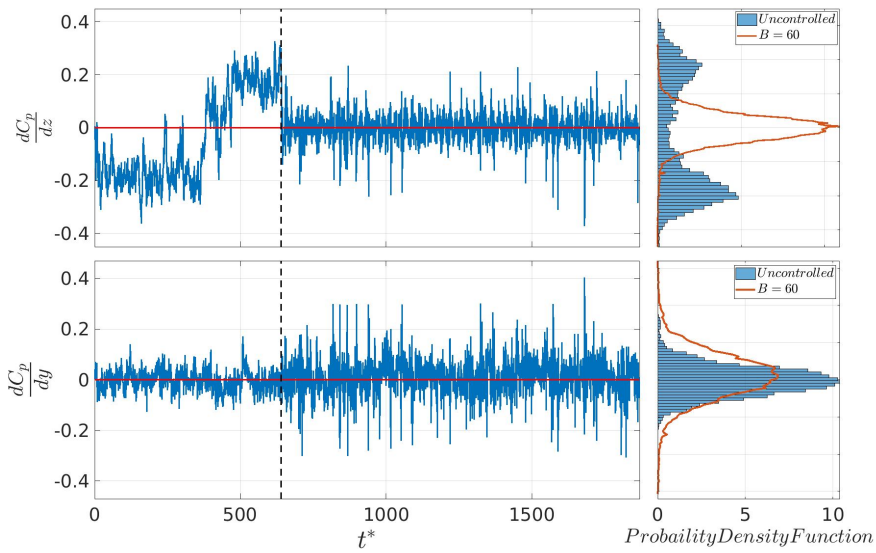

Figure 5.7: Horizontal (top) and vertical (bottom) gradients of the coefficient of pressure C_P (left) before and after switching the controller on (black dashed line). The corresponding Probability Density Functions, PDF (right) for the uncontrolled case (blue bars) and the controlled case (orange line). the controller parameters A and B are 10 and 60, respectively.

reduced maximum horizontal wake offset positions. In the presence of control, the maximum offset wake position corresponds to a horizontal pressure gradient of $\sim \pm 0.08$, which is a 72% reduction in the uncontrolled value of ± 0.29. This is partly due to the wake symmetrisation and partly due to the reduced amplitude of the residual oscillations.

Thus, the effect of the controller extends beyond reorienting the asymmetric wake to also alter the higher frequency wake dynamics. These residual oscillations are linked to interactions between the lateral shear layers and the asymmetric wake, consistent with the switching mechanism recently proposed by Haffner et al. (2020), and may also be partially related to the disturbances convected from the upstream boundary layer dynamics. The degree of reduction in the residual oscillations depends on the ratio between the non-linear and linear terms of the control law, as it will further be discussed in section 5.4. The amplitude of the residual oscillations value can be quantified by the root-mean-square of the trajectory of r_{RMS} at any main position of the wake (equation 5.8, where N is the number of data points of the controlled convective time). The feedback controller reduces the amplitude of the horizontal residual oscillations by up to 20% compared to the unforced case. The wake then exhibits regular time-periodic behaviour with a distinguishable frequency, St_{control}. Similar time periodic behaviour has been observed after implementation of other control strategies, as in case of the opposition control by Li et al. (2016) and the adaptive control by Varon et al. (2019). It is notable that the residual wake oscillations are not only reduced compared to the unforced case, they are also much smaller than has been observed so far after application of linear controllers (Brackston et al., 2016, Li et al., 2016). For the latter,

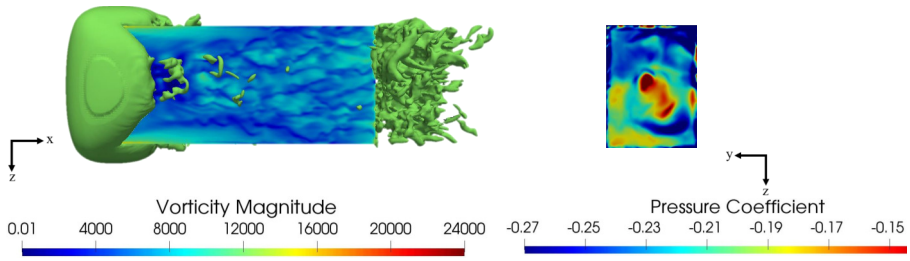

Figure 5.8: Iso-contours of the coefficient of pressure $C_P = -0.2$ (left) and vorticity distribution on the body surface, indicating the effect of the feedback controller on the near wake vortical structures, with the associated C_p projected on the base (right).

the amplitude of residual oscillations of the symmetrised wake matched the original asymmetric extremes of the wake, two orders of magnitude larger than for the unforced flow. This suggests that the underpinning non-linear dynamics of the wake, when neglected, amplify the wake residual oscillations in the bi-modality direction.

In the orthogonal (vertical) direction, the controller is observed to have a negligible effect on the mean wake position, but to slightly amplify the vertical residual oscillations, as shown in figure 5.7 ($\partial C_P/\partial y$).

$$r_{\mathrm{RMS}} = \left[\frac{1}{N}\sum_{i=0}^{N} {r_i}^2\right]^{1/2} \tag{5.8}$$

5.3.2 Mean flow properties and wake topology

This section will explore the effect of the controller on the mean flow properties and the near wake toroidal-vortex structure, for which stochastic bi-modal switching resulted in tilt variations for the unforced case. The effect of control is to orientate this toroidal structure parallel to the base, so that it is approximately horizontally symmetric, as shown in figure 5.8. This matches the instantaneous orientation of the wake during a switching event for the unforced case (figure 4.13), with the symmetric state being unstable in the absence of control. The resulting base pressure coefficient exhibits a higher pressure region near the centre of the base surrounded by a region of lower pressure, as shown in figure 5.8. The base pressure coefficient here differs to the unforced case of figure 4.13, where it has minima and maxima on the sides of the base for the asymmetric wake, and looks similar to the instantaneous unstable symmetric wake. The time-averaged base pressure coefficient of the controlled wake is $\overline{C_{\mathrm{Pbase}}} = -0.227$, which represents $\sim 2\%$ reduction in the base pressure compared to the asymmetric wake. This value depends on the amplification parameter, B, in the control law (equation 5.6), which will further be discussed in section 5.4.

The effect of the controller suggests that changing momentum within the wake region directly effects the streamwise position of the toroidal-vortex. Comparing the topology of the symmetrised wake to that when a base-cavity is used (Evrard et al., 2016), for the latter drag reduction was

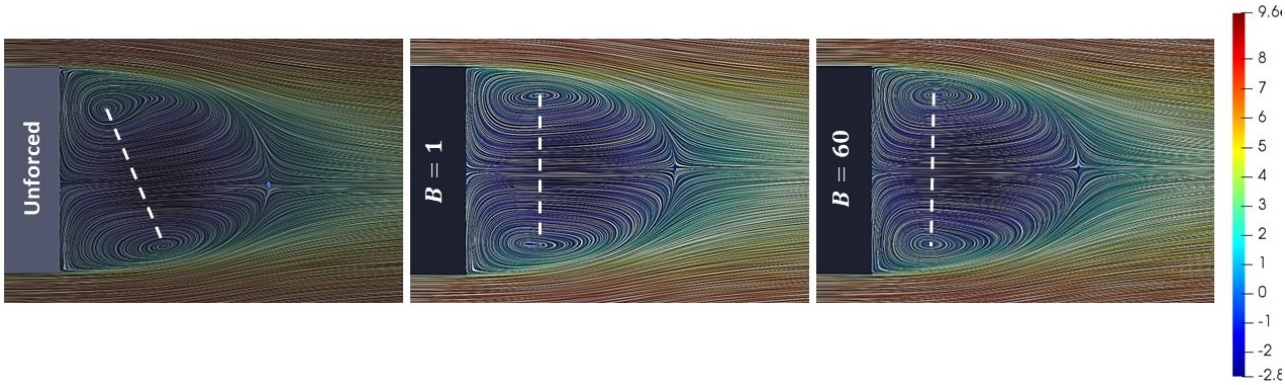

Figure 5.9: Streamlines based on the time-averaged streamwise velocity projected on a plane at mid-height of the body. The unforced case is shown on the left and the controlled case with $B = 1$ and $B = 60$ are shown on the middle and the right, respectively.

associated with minimizing the imprint of the toroidal-vortex on the base, this being correlated with an increase in the average base pressure. For the present feedback control, the proximity of the toroidal-vortex to the base slightly hinders the recovery in average base pressure, which is likely to limit the reduction in pressure drag. The length of the recirculation region for the controlled case is reduced by 8% compared to the unforced case, with a value $\overline{L_{R-cont}} = 1.32H$. Thus the feedback control reduces the length of the recirculation bubble while also reducing the drag. This differs to findings in the absence of unsteady actuation or feedback control, where shorter recirculation bubbles imply increased drag (Lorite-Díez et al., 2020, Hsu et al., 2021), but is consistent with other feedback control studies, where the change in the recirculation length was more related to actuation location than drag reduction (Dahan et al., 2012). Figure 5.9 shows the streamlines on a horizontal plane at the mid-height of the body. The unforced streamlines indicate the tilt of the toriodal vortex via a skewness of the vortex centers, while the controller restores the alignment of these centers, shortens the bubble length and slightly reduces the streamlines curvature closer to the base. Comparing the controlled cases with $B = 1$ and $B = 60$, it can be seen that the for higher B the centers of the recirculation region move closer to the base. This will have an effect on base pressure recovery, which will be discussed in section 5.4. The streamlines also show that the current actuation reduce the streamlines curvature locally, allowing for base pressure recovery.

5.3.3 Ahmed body drag

As mentioned earlier, previous studies have suggested that a symmetric wake corresponds to $\sim 9\%$ base pressure recovery (Grandemange et al., 2013a, Haffner et al., 2020). This was estimated based on comparing the average base pressure during switching events, when the wake is instantaneously symmetric, to its value while the wake is asymmetric. This suggests potential for reducing the pressure drag by suppressing wake bi-modality.

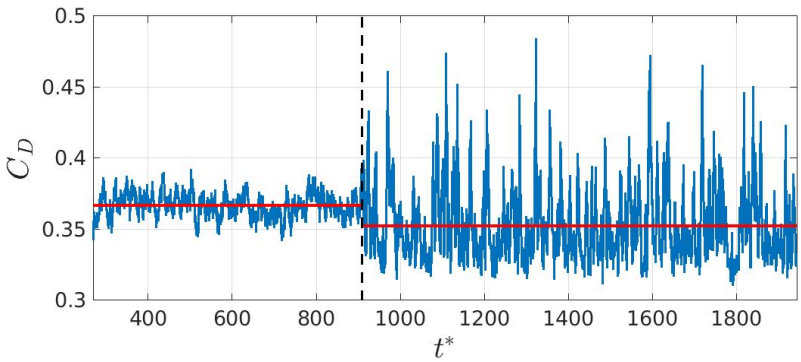

Figure 5.10: Effect of feedback control on the drag coefficient (C_D). The controller is switched on at $t^* = 935$ shown with black dashed line. The values of the controller parameters A and B are 10 and 60, respectively. The red line indicates the mean values of C_D prior and after switching on the controller.

The current results confirm that resymmetrising the wake using nonlinear feedback control increases the average base pressure and reduces the pressure drag. The time-averaged drag is reduced with higher fluctuations of C_D, as shown in figure 5.10. $\overline{C_D}$ is reduced by 2.5% for the case with the controller parameters $A = 10$ and $B = 60$. Similar to mean flow properties, the percentage of drag reduction has a strong dependence on the value of B, that controls the contribution of the linear terms in the control law. This dependence leads to the parametric study in section 5.4.1. In case of $B = 1$, the time-averaged drag is reduced by 7.4%, which represents the maximum drag reduction achieved using the current nonlinear feedback controller. This reduction is lower than the expected 9%, due to the streamwise position of the toroidal vortex in the near wake. These simulations reveal that the drag reduction achieved by symmetrising the wake, depends on the way of suppressing wake bi-modality and its effect on the mean flow in the wake. To conclude, these results confirms that pressure drag is sensitive to wake bi-modality. The application of the nonlinear controller symmetrised the wake by affecting the separated shear layers in the separatix. This effect alters the balance of disturbances in shear layers and the streamwise position of the disturbances, which will be further discussed in section 5.4.3. The level of the disturbances imposed influences the base pressure and accordingly the drag.

5.3.4 Periodic modes in the wake

Similar to the analysis in section 4.3.2, the symmetric and anti-symmetric base pressure signals are considered for analysing the periodic modes in the wake. A quick summary for the periodic modes in the absence of control will be provided first, as it has been discussed with more details in section 4.3.2. Figure 5.11 shows the horizontal and vertical spectra of the anti-symmetric base pressure. The normalised frequency, St number, is defined based on W and H in the horizontal and vertical directions, respectively. The three periodic modes reported in the literature are seen

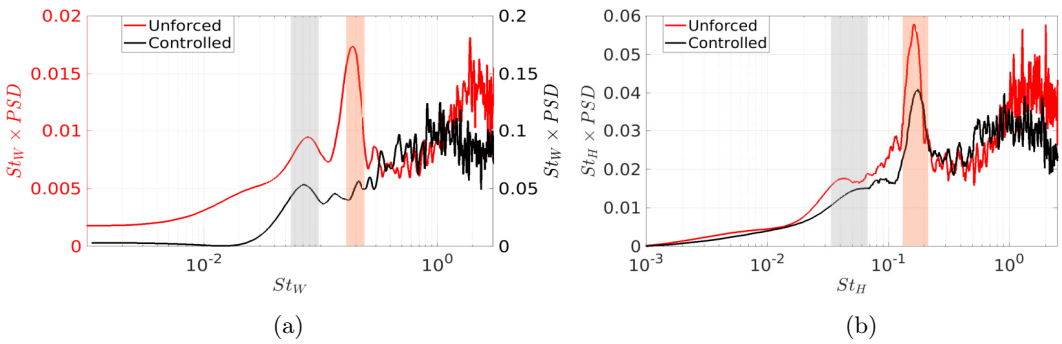

Figure 5.11: Premultiplied spectra of the (a) horizontal and (b) vertical anti-symmetric base pressure signals for both the unforced (red) and the controlled (black) cases. Gray and red shaded areas indicate the broad frequency band related to the bubble pumping mode and vortex shedding frequency, respectively.

in the unforced spectra in both directions. The streamwise bubble pumping mode is captured with low frequency bands around $St_H \sim 0.05$ and $St_W \sim 0.07$ in the vertical and horizontal directions, respectively. The frequency peaks around $St_W \sim 0.19$ in figure 5.11a is related to the horizontal vortex shedding, equivalent to $St_H \sim 0.17$ for the vertical vortex shedding (figure 5.11b). Higher frequency dynamics are seen in both directions around $St_W \sim 1.9$ and $St_H \sim 1.6$, which are linked to the shear layers in both directions.

The base pressure spectra, horizontally and vertically antisymmetric are shown in the presence of feedback control in figures 5.11a and 5.11b, respectively. Both signals capture the same periodic modes evidenced in the absence of the controller. In the horizontal direction, the controller amplifies the energy content of all these modes. The horizontally anti-symmetric base pressure signal (figure 5.11a), captures the symmetric bubble pumping mode at the same frequency of the unforced case. Unlike for the unforced case, the controlled signal does not capture a clear peak for the horizontal vortex shedding. A relatively smaller peak around $St_W = 0.2$ is seen, this suggesting that the anti-phase low frequency forcing of the controller disturbs the dynamics of the horizontal vortex shedding. This will be further discussed using the POD analysis in section 5.5. The energy content of the free shear layers is increased by an order of magnitude in the presence of the feedback controller, with a relatively lower frequency of $St_W \sim 1$ compared to the unforced case ($St_W \sim 1.9$). Similarly, the vertically antisymmetric spectrum (figure 5.11b) shows how the controller slightly reduces the energy content of these three modes. The energy content of the vertical vortex shedding mode is reduced with a slight increase in the associated frequency from $St_H = 0.17$ without control to $St_H = 0.19$ with control. This shift in the vortex shedding frequency is consistent with the recent experimental results by Plumejeau et al. (2020), which concluded that the symmetric wake configuration is associated with a higher shedding frequency in both cross-flow directions. The vertically anti-symmetric signal captures the shear layer dynamics at a frequency equivalent to $St_H \sim 1$, this frequency having shifted downwards compared to the uncontrolled case

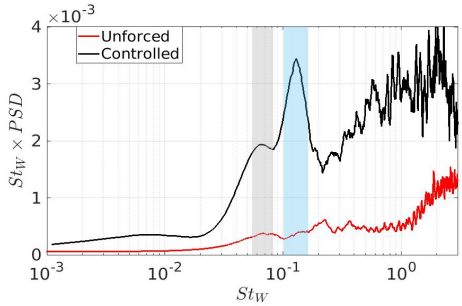

Figure 5.12: Symmetric premultiplied base pressure signals for both unforced (red) and controlled (black) cases. Gray and blue shaded areas indicate the broad frequency band related to the bubble pumping mode and the frequency associated with the streamwise motion of the toroidal vortex, respectively.

($St_H \sim 1.6$).

The unforced symmetric base pressure signal, shown in figure 5.12, captures a broad frequency band around $St_W \sim 0.07$ related the bubble pumping and high frequency shear layers dynamics at $St_W \sim 2.4$. The controller increases the energy content of the whole spectrum without changing the bubble pumping frequency. A clear frequency peak at $St_W \sim 1.3$ is evidenced in the presence of the feedback controller. This is attributed to a new symmetric behaviour linked to the effect of the momentum exchanged in the wake after control has been switched on. The new symmetric behaviour associated with frequencies of $St_W = 0.13$ ($St_H = 0.1$ in the vertical direction), is found to be related to streamwise motion of the near-wake toroidal vortex structure after it has symmetrised. Figure 5.13 shows the time evolution of the steamwise position of the toroidal-vortex represented by the pressure coefficient iso-surface. The time interval between each successive snapshot is equivalent to $St_W = 0.13$. In symmetrising the wake, the controller causes a transitional motion of this toroidal vortex. The dynamics of the shear layers are also captured in the controlled signal with an associated frequency of $St_W \sim 2$.

The effect of the controller on the dynamical modes in the wake can be concluded as follows; the low-frequency bubble pumping mode is largely unaffected by suppressing the horizontal bi-modal switching, and by the reduction in the high-frequency horizontal residual oscillations. The vertical vortex shedding frequency increases due to the action of control. The horizontal vortex shedding, however, has not been clearly evidenced, as the interaction of the horizontal shear layers is now disturbed by the controller. The different effects of the controller on the vortex shedding mode in the horizontal and vertical directions is attributed to the setup of the actuation slots, shown in figure 5.1. The horizontal shear layers are subjected to anti-phase forcing, while the vertical shear layers are forced in-phase. The stochastic horizontal switching of the wake is replaced by an oscillatory motion of the toroidal vortex structure in the streamwise direction, due to exchanging momentum between the lateral sides of the wake. Finally, the spectral analysis of the antisymmetric controlled signals indicates an increased energy level relative to the unforced case in the horizontal

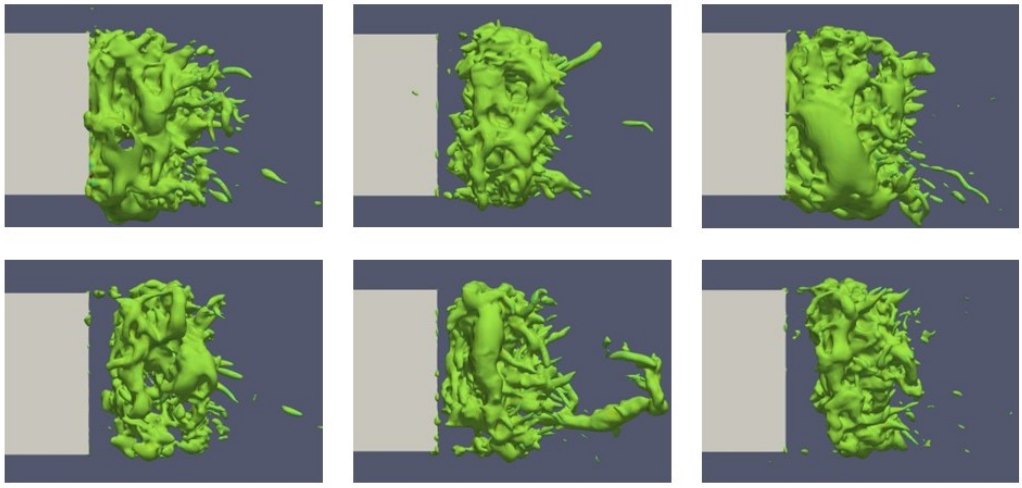

Figure 5.13: Instantaneous snapshots of the near-wake toroidal-vortex indicated by the iso-contours of the pressure coefficient ($C_P = -0.2$). It indicates the time evolution of the streamwise location of the toroidal vortex with a time interval corresponding to $St_W = 0.13$ between each successive snapshots starting on the top-left to the bottom-right.

direction, while in the vertical direction the energy has decreased.

5.4 Non-linearity and Bi-modality Suppression

As mentioned in Section 5.3, the performance of the feedback controller depends on the choice of controller parameters in the control law given by equation (5.6). A parametric study of the feedback control law parameters, A and B, is now carried out to investigate the effect on bi-modality suppression, drag and wake dynamics. Parameter A amplifies the control effort and directly affects the wake response time, resulting in a faster wake response for $A > 1$. The threshold value to symmetrise the wake is A=10, yet as A increases, the drag reduction decreases. This is likely to be because larger values of A increase the momentum coefficient and subsequently enhance the near wake entrainment. This directly affects the shear layers and their associated interactions, amplifying the higher frequency dynamics in the near wake region. Parameter B represents an amplification factor of the linear term of the control law. A range of $0 < B \leq 90$ is investigated for $A = 10$. Exploring the contribution of the linear term offers an insight into the effect of nonlinearity on suppressing bi-modality and its associated interactions in the wake. The effect of varying B is discussed in detail in the following subsections.

5.4.1 Wake symmetry, wake oscillations and body drag

The effect of varying B on the wake symmetry, residual oscillations, base pressure and drag reduction is firstly explored. The effect of varying B on the degree of wake-symmetry, which is

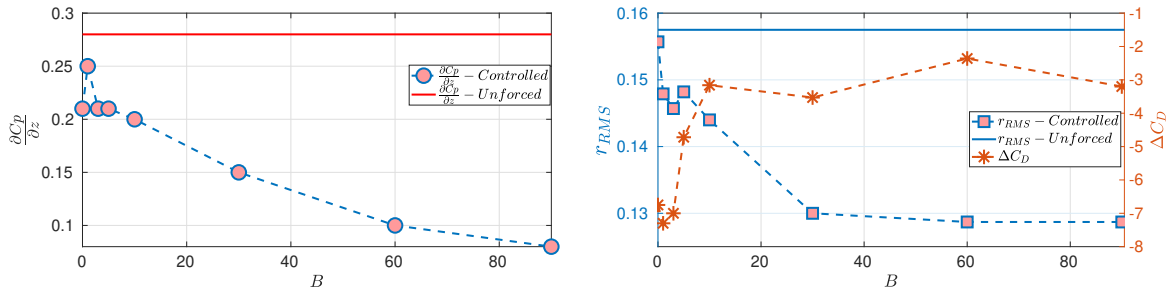

(a) (b)

Figure 5.14: (a) The variation of the horizontal gradient of the base pressure coefficient (used to indicate the level of wake-symmetry) with the controller parameter B. The red line indicates the value of $\partial C_p/\partial z$ for the unforced case. (b) Blue: Root Mean Square (RMS) of the instantaneous horizontal centre of pressure for different values of the controller parameter , B. The blue solid line shows the RMS value for the uncontrolled case. Orange: the variation in drag reduction with B.

B	$\overline{C_{\text{Pbase}}}$	$\frac{\overline{L_R}}{H}$	$-\Delta\overline{C_D}\%$	$\overline{C_\mu} \times 10^3$	St_{control}
Unforced (Asymmetric wake)	-0.232	1.44	0.00	0.0	0
0.01	-0.209	1.36	6.75	1.2	0.021
1	-0.207	1.38	7.40	1.2	0.024
3	-0.208	1.37	7.00	1.2	0.025
5	-0.214	1.34	4.72	2.0	0.033
10	-0.217	1.33	3.16	3.0	0.034
30	-0.216	1.34	3.53	3.3	0.040
60	-0.218	1.32	2.50	3.9	0.054
90	-0.217	1.33	3.20	3.9	0.050

Table 5.2: The effect of changing the amplification parameter B on the mean flow parameters; the time-averaged base pressure coefficient ($\overline{C_{\text{Pbase}}}$), the recirculation bubble length ($\overline{L_R}$), the average drag reduction ($\Delta\overline{C_D}$) and the control effort characterised by the momentum coefficient ($\overline{C_\mu}$) and the resultant frequency of the periodic switching in the wake (St_{control})

characterised by the value of the horizontal gradient of the base pressure coefficient, $\partial C_p/\partial z$, is shown in figure 5.14a, with a more symmetric wake associated with lower values of $\partial C_p/\partial z$. It can be seen that the level of wake symmetry increases with B. For $0 < B < 10$, the same order of magnitude as the growth rate α, fluctuations in $\partial C_p/\partial z$ show a maximum reduction of 25% compared to the unforced case, and the wake exhibits little sensitivity to B. When B is one order of magnitude higher than α, i.e. $B > 10$, the wake symmetry starts to increase with B, the maximum reduction in wake asymmetry being reached at $B = 90$, beyond which no further reduction is achieved. The value of $\partial C_p/\partial z$ is then reduced by 72% compared to the unforced case and the wake can be considered symmetrised in this region. In this case (i.e. $B = 90$), the linear term dominates the control effort, with B almost two orders of magnitude higher than α. Relating the value of the linear term parameter, B, to the growth rate parameter, α, suggests that the growth of the mode r could be suppressed with a linear controller.

The residual wake oscillations around the mean wake position, characterised by the root mean square of r, r_{RMS}, are also affected by the tuning of B. As shown in figure 5.14b, r_{RMS} exhibits a decreasing trend as B increases, reaching a minimum when $B = 60$, without further reduction for higher values of B. This confirms a significant benefit of the present non-linear controller over the linear controllers employed in previous studies. There, control led to amplification of the horizontal residual oscillations, and this was linked to low values of drag reduction of less than $\sim 2\%$ (Brackston et al., 2016, Li et al., 2016, Schmidt et al., 2018). Figure 5.14b also depicts the variation of the drag reduction as B varied. For the present results, low levels of horizontal residual oscillations do not seemed to be directly linked to drag reduction; when the residual oscillations are small, the mean drag reduction is also small. The maximum drag reduction achieved by feedback control is 7.4%, a significant increase on the 2% reported previously using a linear controller. For this maximum reduction, $B = 1$ (hence $0 < B \leq \alpha$), which means that the nonlinear term dominates the control effort, the wake then oscillates at a frequency of $St_{\mathrm{control}} = 0.024$.

The drag reduction decreases as B increases and hence the contribution of the linear controller term increase. A minimum drag reduction of 2.5% occurs for a fully symmetrised wake, the residual fluctuations of the wake are also smallest. Comparing figures 5.14a and 5.14b, a trade-off between drag reduction and wake-symmetry is evident, suggesting that drag reduction is not directly related to symmetrising the wake, but linked to suppression of the nonlinear interactions between the stochastic bi-modality and other periodic modes in the wake. A favourable manipulation of these nonlinear interactions is attained when the nonlinear term of the controller dominates the control effort (i.e. $B \leq \alpha$), suggesting the need for a nonlinear controller in order to reduce the drag.

Table 5.2 shows the change in the mean flow properties as B varies. The time-averaged base pressure coefficient, $\overline{C_{\mathrm{Pbase}}}$, decreases with B, inhibiting the reduction in pressure drag. A linear

relation between $\overline{C_{\text{Pbase}}}$ and $-\Delta\overline{C_D}\%$ can be seen here, confirming the dominant effect of the base pressure on pressure drag (Ahmed et al., 1984). For all values of B, some base pressure recovery is evidenced compared to the unforced case. The maximum average increase in the base pressure was less than the 9% indicated in the literature. This is suggested to be a result of the controller shifting the near-wake toroidal vortex closer to the base, limiting the base pressure recovery. The minimum value of $\overline{C_{\text{Pbase}}}$ occurs for $B = 60$, and is associated with the least drag reduction. This case achieves a relatively high level of wake symmetry, with the linear control term dominating the control effort. The length of the recirculation bubble, $\overline{L_R}$, is reduced in presence of the feedback control for all values of B compared to the unforced case. This length also decreases as B increases. A reduction of 3.5% in $\overline{L_R}$ is reported for the case of maximum drag reduction ($B = 1$) compared to the asymmetric unforced wake, while a 9% reduction in $\overline{L_R}$ is reported for the minimum drag reduction. Comparing the controlled cases, it can be seen that a longer bubble allows for higher base pressure recovery and consequently reduced drag (Brackston et al., 2016, Evrard et al., 2016). However, we suggest that the underlying mechanism of drag reduction achieved here is not limited to the bubble length but is also influenced by the change of the curvature along the separated bubble and the suppression of wake symmetry breaking.

5.4.2 Control performance

The effect of tuning B can also be characterised using the barycenter of pressure, r(t), i.e. the controller input defined in equation (5.2). The maximum deviation of the wake from the center of the base in the absence of control corresponds to $r = \pm 0.32$, which represents the switching bounds of the unforced wake. The contribution of the controller nonlinear term was assessed for different values of B. For $B = 0.01$, the controller is linear when the spatial position of the wake lies in the space $-0.05 \leq r \leq 0.05$. That is, the contribution of the nonlinear part of the controller is negligible when the wake is close to being symmetric. The contribution of the controller nonlinearity then increases as the wake deviates from the linearly dominated region. The range of r for which $u(r)$ is almost linear increases with B, implying a larger linearly dominated region for higher values of B. For $B = 90$, the linearly dominated region extends to $-0.14 \leq r \leq 0.14$, beyond which, the contribution of the nonlinear term in the control effort does not exceed 10%. This suggests the possibility of suppressing wake bi-modality using purely linear controllers, even though the nonlinearity inherent in the interactions of this mode with the other dynamical modes and the effect on drag reduction remain open questions.

Figure 5.15 shows the time history of the controller input, $r(t)$, and the output, $u(r)$. Both signals are periodic with a frequency corresponding to $St_{\text{control}} = 0.024$ for $B = 1$, the case where maximum drag reduction is achieved. The time delay between the signals is related to

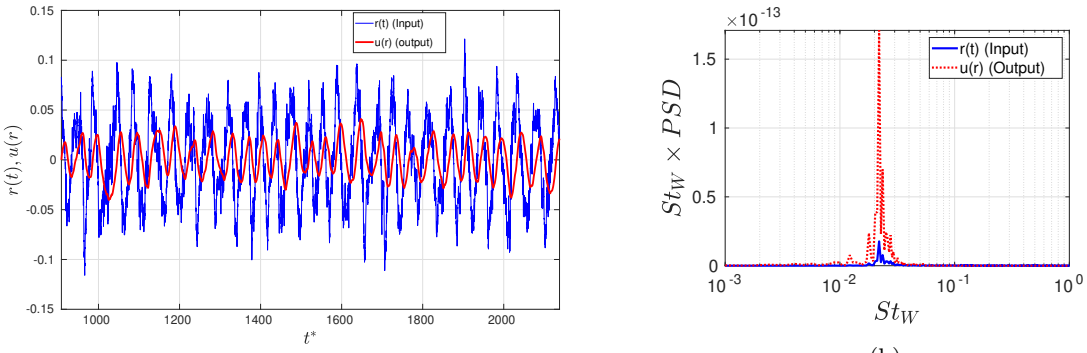

(a) (b)

Figure 5.15: (a) Time evolution of the input and output signals of the nonlinear controller for the case of $B = 1$. The associated frequency of both signals corresponds to $St_{\text{control}} = 0.024$.

the wake response time to actuation. The value of St_{control}, which is associated with the wake oscillations that occur in the presence of feedback control, increases as B increases. For B in the range $0 < B \leq 90$, the frequency lies in the range $0.02 < St_{control} < 0.054$, as indicated in table 5.2. The drag reduction decreases as St_{control} becomes closer to the bubble pumping frequency. The interaction between the periodic switching and the bubble pumping modes is seen to limit the drag reduction. Comparing the sensor signal, $r(t)$, for the controlled and uncontrolled cases, figure 5.16 indicates a cut-off frequency, $St_{cut\text{-}off}$, where the action of control starts to amplify rather than attenuate oscillations. Dynamical modes below $St_{cut\text{-}off}$ are attenuated, by the action of the control, while those above are amplified. Across different controller parameters, $St_{cut\text{-}off}$ has a similar order of magnitude to the peak bi-modality frequency, its value increasing as B increases, reaching a maximum value of $St_{cut\text{-}off} = 0.013$ for the case in which the linear control term exceeds the nonlinear term by two orders of magnitude and the wake is fully symmetrised ($B = 90$). Tighter switching bounds of the wake are associated with higher cut-off frequency. This indicates that the model considered here, based on Langevin dynamics, successfully captures the low frequency dynamics associated with bi-modality. If the synthetic jet actuators can be assumed to have an efficiency of $\eta_{\text{actuator}} = 0.95$ (95%), the maximum power utilised by the controller, $Pw_{\text{actuation}}$ would not exceed 0.5% of the total power saved due to drag reduction, Pw_{saved}.

The momentum coefficient of the actuation associated with control, C_μ, increases with B. The maximum C_μ for the case of maximum drag reduction ($B = 1$) was 8.5×10^{-3} with an average value of 1.2×10^{-3} (table 5.2). As the momentum coefficient increases, the drag reduction decreases, reaching its minimum value when $C_\mu = 7.9 \times 10^{-2}$ with an average of 3.9×10^{-3}. This suggests that higher levels of momentum in the wake increase the level of turbulent entrainment in the near wake region. Increasing C_μ enhances the unsteadiness of the streamwise momentum, which has an unfavourable effect on the drag. The higher levels of momentum in the wake further increase the disturbances on the free shear layers that have been balanced due to wake reorientation, as

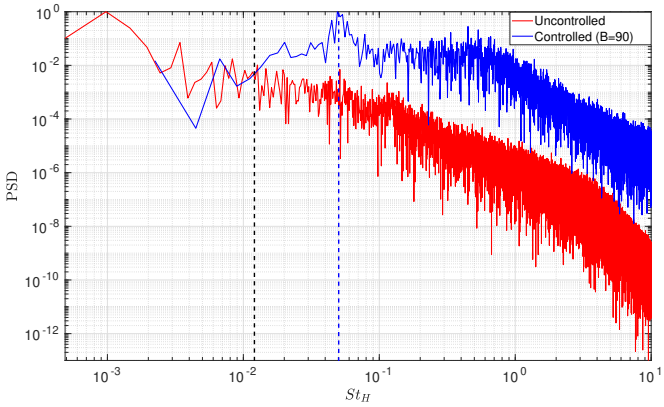

Figure 5.16: Power Spectral Density (PSD) of the uncontrolled (red) and the controlled (blue) horizontal centre of pressure for the case of $B = 90$, indicating the cut-off frequency $St_{\text{cut-off}} = 0.013$ (back dashed line) and the frequency peak for the controlled wake $St_{\text{control}} = 0.05$ (blue dashed line).

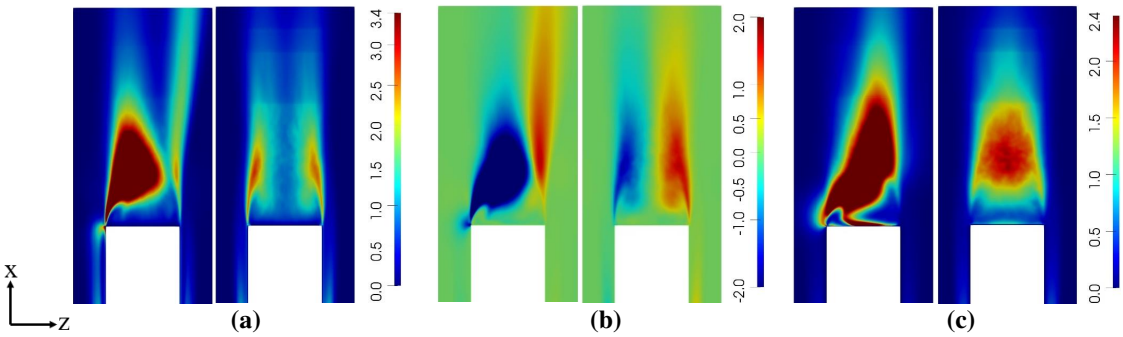

Figure 5.17: Time-averaged Reynolds stress components on a central horizontal plane at $y/H = 0.5$. Comparing the uncontrolled asymmetric wake (on the left for each component) and the controlled case (on the right for each component). (a) The streamwise Reynolds stress $\overline{u'_x u'_x}$. (b) The $\overline{u'_x u'_z}$ Reynolds stress. (c) The horizontal (lateral) Reynolds stress $\overline{u'_z u'_z}$. Air flows from bottom to top.

discussed previously, which hinders the gain in drag reduction. This suggests that a new control strategy which attenuates the disturbances in the free shear layers might be more effective for reducing the drag.

5.4.3 Insights into bi-modal switching mechanism

The results suggest that bi-modality indirectly affects the drag through the interaction of the asymmetric recirculation region and the shear layers that are shed from the vertical base edges between which switching takes place. Haffner et al. (2020) recently proposed a mechanism for the wake switching based on flow entrainment related to the lateral shear layer dynamics. Their experimental results suggest that the formation of an asymmetric recirculation region is caused by the large curvature of one shear layer. This curved shear layer triggers the parallel layer downstream of the base, causing a roll-up in the wake which leads to a shedding of a hairpin vortex

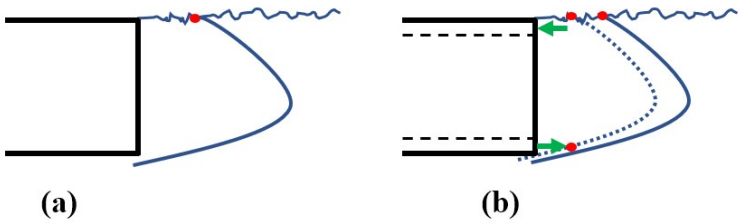

Figure 5.18: Schematic description of the effect of the controller on the shear layers in the switching direction. The asymmetric recirculation region formed by the bottom shear layer and its triggering to the top shear layer in the unforced case is shown in (a). The effect of momentum exchange on both shear layers is indicated in (b), where the continuous and dashed lines represent the unforced and the controlled recirculation regions respectively.

in the wake (Dalla Longa et al., 2019). This roll-up creates an engulfed flow that increases the flow entrained into the recirculation region. As this roll-up gets stronger, the triggered shear layer starts to curve forming a new recirculation region opposite to the existing one, leading to a transient symmetric wake. This mechanism is consistent with the present simulations, as shown through the projected streamlines based on the streamwise velocity during the switching event included in the supplementary movie. The drag reduction associated with this transient symmetric wake is related to inhibiting both the trigger of the shear layers and the coherent recirculating motion in the near wake region (Haffner et al., 2020). The trigger of the shear layers can be indicated by Reynolds stresses in the wake.

Figure 5.17 compares the Reynolds stresses on a horizontal plane at the mid-height of the body for the asymmetric unforced wake and the controlled wake. An asymmetric pattern is indicated in all three components ($\overline{u'_x u'_x}$, $\overline{u'_x u'_z}$, $\overline{u'_z u'_z}$) for the unforced case. The triggering of the shear layer on the right side of the body ($+z$ direction) is indicated by relatively higher stresses in the streamwise direction ($\overline{u'_x u'_x}$) downstream of the base, while the curved shear layers forming the asymmetric recirculation region exhibit higher levels of both the $\overline{u'_x u'_x}$ and $\overline{u'_x u'_z}$ shear stress components. The spanwise component ($\overline{u'_z u'_z}$) has higher levels towards the triggered shear layer side. For the controlled symmetric wake, the wake exhibits balanced shear stresses on both shear layers.

In the presence of the controller, exchanged momentum through the actuation slots imposes direct disturbances on both shear layers at the separation edges. These disturbances disrupt the switching mechanism discussed above. When the wake resides on one side, the actuation starts to blow air, introducing disturbances on the curved shear layer, while the parallel triggered layer is now subjected to suction by the actuator slot, i.e. shifting the triggering location upstream towards the base and increasing its curvature. The application of the controller with anti-phase forcing – blowing on the large curved shear layer and suction on the triggered layer – will have the following effect (figure 5.18):

- The blowing on the curved shear layer increases the curvature of this shear layer and accordingly reduces the length of the recirculation region.

- This effect forces the triggering location of the parallel layer to take place further upstream, closer to the base.

- Applying suction on the other side will have two effects; imposing disturbances on this shear layer closer to the base, promoting earlier growth and promoting the formation of the opposite recirculation region.

- When the level of momentum exchanged between the lateral sides and the wake increases, this significantly amplifies the balanced disturbances on the shear layers and accordingly decreases the base pressure (table 5.2).

Although the application of the controller here inhibits the coherent recirculation in the near-wake, which has a favourable effect for drag reduction similar to the symmetric transient state of the unforced case, the disturbances imposed on both shear layers limits the gain in drag reduction. The shear layers disturbances are now balanced, and shifted upstream closer to the base, yielding a more pronounced effect on the base pressure and limiting the drag reduction. The maximum gain in drag reduction is achieved for the case where minimum shear layer disturbances are imposed due to the exchanged momentum. The imposed disturbances on the shear layers amplifies the higher frequency dynamics in the near wake region, which is confirmed by comparing the power spectral density of r in the absence and presence of control, shown in figure 5.16. Although bi-modality is a random behaviour of the wake, the unforced flow exhibits a broad peak at $St_H \sim 10^{-3}$. The effect of control is to amplify the higher wake frequencies, which are associated with $St_H > St_{\text{cut-off}}$. We speculate that this amplification creates a coupling between bi-modality and the low frequency bubble pumping mode, consequently driving the random dynamics of bi-modality into regular oscillations of the toroidal-vortex within spatial bounds closer to the centre. This can be evidenced by the match between the frequency range of the wake oscillations and the bubble pumping frequency. This coupling further causes streamwise oscillations of the toroidal-vortex, similar in behaviour to the bubble pumping at a frequency of $St_H = 0.1$, as indicated in section 5.3.4. Thus, the controller changes the stochastic switching of the toroidal-vortex into spatially-bounded oscillatory switching with streamwise oscillations of this vortex. To conclude, drag reduction is found to be related to the effect of bi-modality on the shear layers in the switching direction. Bi-modality suppression balances the disturbances in the two parallel shear layers and shifts the streamwise position of the shear layers triggers upstream closer to the base, which found to be unfavorable for base pressure recovery.

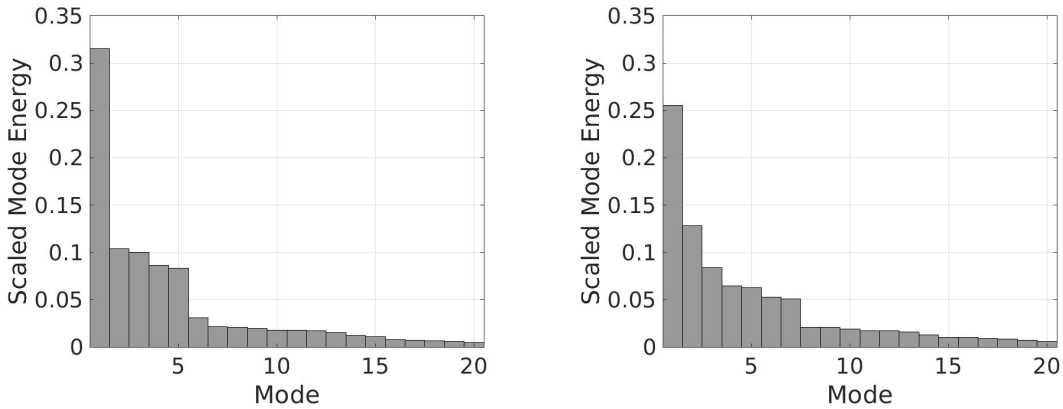

Figure 5.19: Energy content of the first 20 pressure POD modes for the unforced (a) and the controlled case for $B = 60$ (b).

5.5 Proper Orthogonal Decomposition

In order to obtain more insights into the effect of control on bi-modality suppression, Proper Orthogonal Decomposition (POD) of the pressure data on a horizontal plane - parallel to the ground - at mid-height of the body, is now considered. The total acquisition time was 1000 convective time units, which was deemed sufficient for statistical convergence. The wake residence time within each asymmetric position was equal to that for the unforced case. The sampling frequency corresponded to $St_W = 2.84$, with $St_W = fW/U_\infty$, where f is the frequency in Hz. This sampling frequency resolves the highest frequency in the wake.

5.5.1 Unforced POD

The energy content of the first twenty modes is shown in figure 5.19a. The most energetic first six modes contain $\sim 73\%$ of the total energy. The Reflectional Symmetry Breaking *(RSB)* mode, represented by mode-1 in figure 5.20, is the most energetic, with an energy content of 32%, similar to the experimental results by Schmidt et al. (2018). This mode is antisymmetric and captures the dynamics of the toroidal vortex structure in the near-wake region, consistent with the recent DNS results by Podvin et al. (2020). Spectral analysis of the time coefficient of this mode indicates a broad energy peak at very low frequencies of an order of $St_W \sim 0.001$. The next four modes capture the dynamics of the frontal separation bubble and the free shear layers in the wake, containing $\sim 37\%$ of the POD total energy. These modes are associated with the separation and the reattachment of the turbulent boundary layers on the side surfaces of the body. A causal link between the frontal separation bubble dynamics and bi-modality was recently suggested by Hesse and Morgans (2021). The power spectral densities of the POD coefficients exhibit peaks at $St_W \approx 1 \sim 2$. The higher frequency $St_W \sim 2$ is linked to the frontal separation bubble, as

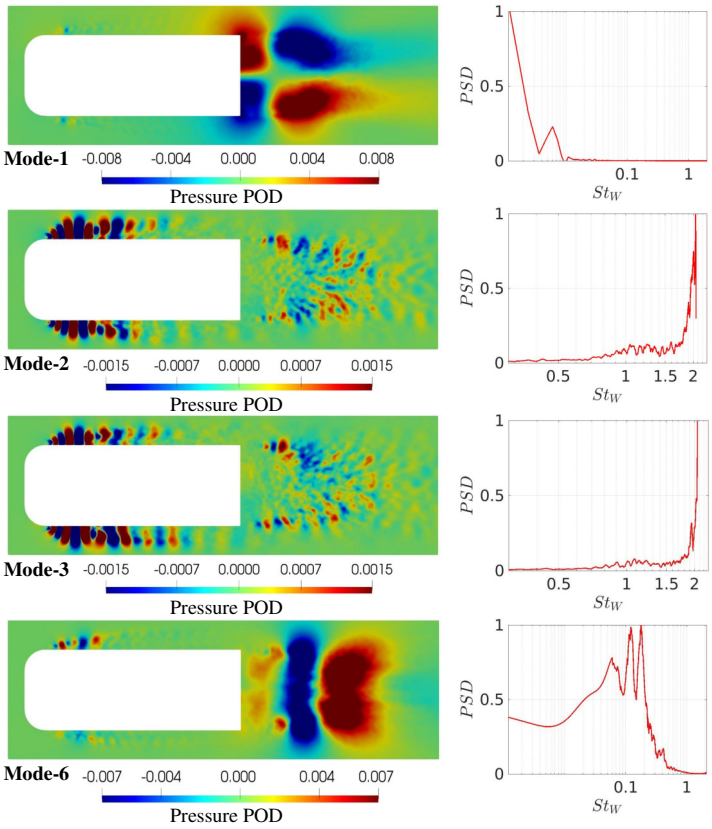

Figure 5.20: Pressure POD on a horizontal mid-plane for the unforced case (left) and their associated power spectral density of their coefficients (right).

it matches the dominant frequency of the pressure signal at the bubble location. The broadband dynamics around $St_W \sim 1$ are related to shear layer roll-up in the wake, which is suggested to be related to the switching mechanism (Haffner et al., 2020). Mode-2 and mode-4 have similar structures with a shift in space denoting the convective nature of these modes; the same is true for mode-3 and mode-5. Both mode-4 and mode-5 are not shown for brevity.

Mode-6 in figure 5.20 further shows a mode of combined vortex shedding and bubble pumping. Spectral analysis of the modes' temporal coefficient indicates three peaks at $St_W = 0.06$, $St_W = 0.15$ and $St_W = 0.17$, the first frequency indicating the bubble pumping and the last two associated with the vortex shedding. The time evolution of this combined mode indicates that the energy level varies between the two sides of the wake, depending on the side of the vortex shedding, associated with the asymmetric position of the wake. These results match the POD analysis of the Ahmed body wake using direct numerical simulation by Podvin et al. (2020).

5.5.2 Controlled POD

The effect of the controller ($B = 60$ case) on the horizontal POD modes is shown in figure 5.21. Similar to the unforced case, the RSB mode, represented by mode-1 in figure 5.21, remains as the

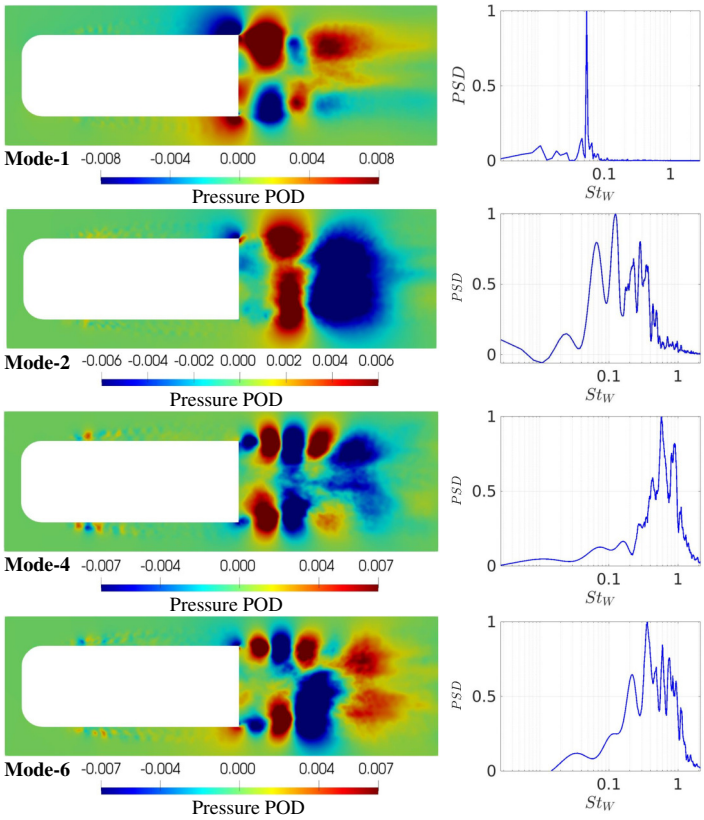

Figure 5.21: Pressure POD on a horizontal mid-plane (left) and the associated power spectral density of their coefficients (right) for the controlled case ($B = 60$).

most energetic mode, although, its energy content is reduced by 10% compared to the unforced case (figure 5.19b). It is associated with a frequency of $St_W = 0.054$, indicating the effect of the controller in replacing the stochastic switching with periodic oscillations. Figure 5.21 shows that the second POD mode is symmetric and dominated by the streamwise oscillation of the torioidal vortex at a frequency of $St_W = 0.13$, which was captured previously by the base pressure signal (figure 5.11a) and the time-resolved wake topology (figure 5.13). This mode contains 13% of the total energy of the flow and further captures the dynamics of the bubble pumping associated with $St_W \sim 0.06$ and the shear layer roll-ups at $St_W \sim 0.5$. Similarly, the third POD mode is symmetric and captures both the streamwise oscillations of the toroidal vortex and the shear layer dynamics represented as a symmetric shedding, and it is not shown for brevity.

Figure 5.21 shows the fourth mode, which indicates a symmetric shedding of the free shear layers in the wake at a frequency of $St_W \sim 0.5$. These dynamics were captured by Haffner et al. (2020), and were suggested to be subharmonics of the shear layer roll-ups occurring downstream of the base (at $x/H \approx 0.3$ from the base) in the unforced case. However, in the presence of the controller, the anti-phase forcing exchanges momentum between the lateral sides of the wake, shifting these dynamics upstream closer to the base. Compared to the unforced case, the shedding of each shear layer in the controlled case is partially attributed to the actuation, while in the

unforced case it was triggered by the interaction with the parallel shear layer. The horizontal vortex shedding is evidenced in anti-symmetric mode-6 at $St_W \sim 0.22$. The energy content of the vortex shedding is doubled compared to the unforced flow. Mode-5 and mode-7 have the same patterns and frequencies as mode-4 and mode-6, respectively, hence are not shown.

The effect of the non-linear feedback controller on the pressure POD can then be summarised as follows; the energy content of the static RSB mode is reduced and the stochastic switching of the wake is changed to periodic oscillations accompanied by streamwise oscillations of the near-wake toroidal vortex. The energy content of both the horizontal (spanwise) vortex shedding and the free shear layer dynamics are intensified by exchanging momentum in the wake. The increase in the energy level of these modes is expected to limit the drag reduction achieved by wake symmetrisation. This increase in the energy content, which is associated with the symmetrisation of the toroidal vortex structure, is consistent with the DNS results of Podvin et al. (2020).

The current controller, despite forcing the locked-in toroidal vortex in the near wake region, is seen to also significantly affect the separated shear layers affecting other periodic modes in the wake. This confirms the complexity of the interaction between the bi-modality and other dynamical modes of the flow. To conclude, the interaction between the wake and the side shear layers can be viewed as an external forcing on the shear layers. This is consistent with the recent experimental study by Haffner et al. (2020) on the mechanism of bi-modality inline with the previous study by Gerrard (1966) on the mechanism of formation of the recirculation region and its relation the entrainment caused by the shear layers in the wake of 2D bodies.

5.6 Conclusion

The turbulent wake behind a squareback Ahmed body has been investigated using high fidelity wall-resolved large eddy simulations. The simulations successfully captured stochastic bi-modal switching from side-to-side as well as three time-periodic modes in the wake: vortex shedding in both cross-flow directions, roll-up of the free shear layers and a streamwise pumping motion of the recirculation bubble. The latter showed a distinguishable mark on the base pressure, which has not been detected in most previous experimental studies. Bi-modality was found to be the most energetic dynamical mode in the wake.

Wake bi-modal switching has previously been suppressed with linear control but resulted in large amplitude oscillations of the wake around the center. This study represents a first attempt to employ a nonlinear model-based controller to suppress the bi-modal switching. Bi-modality is modelled using Langevin dynamics. The controller, derived using a quadratic Lyapunov function, successfully suppresses the bi-modal switching. Furthermore, the resulting levels of wake fluctua-

tions are significantly lower than for previous linear controllers. The extent of the fluctuations in asymmetry is significantly reduced. The nonlinear term of the controller is significant when the asymmetric positions of the wake deviates away from the linearly dominated region. The action of control changes the stochastic horizontal switching of the wake to an oscillatory motion of the large coherent structure in the near wake region, with frequency close to the bubble pumping frequency. The controller does not affect the bubble pumping frequency in the wake, yet leads to stronger and more energetic vortex shedding in both the horizontal and vertical directions.

Changing the relative contributions of the linear and nonlinear terms in the control law significantly changes the wake response. The general trend of driving the stochastic bi-modality to time-periodic oscillations holds in all cases, with a trade-off between drag reduction and level of wake asymmetry. A maximum drag reduction of 7.4% is achieved for a semi-symmetrised wake, for which the wake switches periodically between asymmetric positions. A fully symmetrised wake with a minimum in residual oscillations around the center of the base corresponds to 2.5% reduction in the drag. Suppressing the wake bi-modality using feedback control was shown to re-orient the toroidal vortex structure in the near wake region so that it becomes parallel to the base as well as closer to the base. This consequently disturbs the near-wake shear layers close to the base, limiting the base pressure recovery. It is proposed that this is the main reason that drag reduction is hindered in the case of a full-symmetrised wake. An indirect link between bi-modality suppression and drag reduction is shown. Drag reduction is found to be more sensitive to the interaction between the wake bi-modal behaviour and the shear layers in the switching direction. The effect of this interaction on drag depends on two effects: the unbalanced disturbances imposed on the shear layers and the streamwise position of the disturbances. The latter has a pronounced effect on the base pressure and hence the pressure drag. Controlling this interaction may offer more significant drag reductions, similar to those previously achieved using a base-cavity. The current results suggest that control strategies should focus more on suppressing or delaying the interaction between the separated shear layers and the coherent structures in the near-wake region to reduce drag. It also suggests that the actuation position is crucial for suppressing bi-modality without amplifying the disturbance on these shear layers.

Chapter 6

The effect of the upstream body boundary layers on the wake dynamics

In this chapter, an investigation of parameters that may have causal effect on wake bi-modality is explored. Specifically, the link between wake bi-modality and the frontal separation bubble close to the body fore-end is investigated. The effect of the underbody flow will also be further discussed. The chapter is arranged to provide a brief introduction to the parameters which are known to affect wake bi-modality, followed by a description of the control mechanism used in the present work to suppress the formation of the frontal separation bubble. Finally, both time-averaged and time-resolved results are discussed and compared to the unforced flow case.

6.1 Introduction

Following the discussion in the previous chapters, the modes captured in the turbulent wake of the square-back Ahmed body in close proximity to the ground can be summarised as follows:

- The stochastic bi-modal switching of the wake in one of the crossflow directions (either side-to-side or top-to-bottom).
- The typical Karman vortex shedding in both crossflow directions which arises due to the interaction between each parallel shear layer in the wake.
- The streamwise bubble pumping or bubble breathing.

- The dynamics related to the mixing layers in the wake.

This investigation focuses on the stochastic wake bi-modality, which is characterised by the random switching of the center of the wake between two asymmetric reflected positions. As mentioned previously, the wake loses its spatial symmetry in the laminar flow regime following a series of bifurcations (Evstafyeva et al., 2017, Grandemange et al., 2012). The wake then resides in an asymmetric position. Symmetry-breaking persists in the turbulent flow regime, where the turbulent fluctuations act to force the wake stochastically from one asymmetric position to the reflected asymmetric position. Bi-modality is governed by both geometric and flow conditions. The former controls the switching direction of the wake, which tend to occur in the direction parallel to the longer length of the body base. Wake bi-modality is found to be sensitive to the under-body flow emanating from the clearance between the body and the ground (Grandemange et al., 2013b, Barros et al., 2017), the free-stream turbulence level (Cadot et al., 2020, Burton et al., 2021, Kang et al., 2021) and the dynamics of the boundary layers developed along the longitudinal surfaces of the body (Hesse and Morgans, 2021). Examining the sensitivity of this behaviour is crucial to inform an effective control strategy for drag reduction. With this aim, some of the recent studies about bi-modality investigate this point.

The experimental study by Barros et al. (2017) investigated the effect of disturbing the underbody flow on the wake configuration. Disturbances were introduced using passive devices in the clearance between the body and the ground upstream of the base, which disturbed the boundary layer developing along the bottom surface, affecting the rate of entrainment in the wake. These included quasi-two-dimensional disturbances using a horizontal cylinder extending along the spanwise direction, three-dimensional disturbances employing vertical cylinders, and an underbody grid. The size of the disturbing device and the resulting effective forcing frequency were found to be important for changing the wake configuration to bi-modal states. When the disturbing device introduced high-frequency forcing the state of the wake changes from a vertically asymmetric uni-modal wake to a horizontally (spanwise) bi-modal switching wake. In contrast, a relatively low-frequency forcing switches the vertical balance of the wake without introducing bi-modal switching in the vertical direction. The effect of the underbody flow on the wake configuration was also investigated by Castelain et al. (2018) for a flow past square-back truck geometry. The underbody flow bulk velocity was changed using a porous material in the gap between the body and the ground. The results confirmed the sensitivity of the wake configuration to the dynamics of the underbody flow.

Recent studies have shown that the free-stream turbulence level has a prominent effect on wake bi-modal switching, both by directly affecting the wake dynamics and indirectly affecting it via the underbody flow. Kang et al. (2021) numerically investigated the effect of the approach flow

conditions using IDDES. They concluded that bi-modality is completely suppressed when the wake is fully submerged in a thick, turbulent boundary layer whose height exceeds the body height. This change in the flow topology and near wake dynamics is attributed to the momentum deficit in the underbody flow, with bi-modality suppression suggested as being linked to the induced upwash flow.

An experimental investigation by Cadot et al. (2020) found that increasing the free-stream flow's turbulence intensity ($\sim 5\%$) increases the wake residence time in each asymmetric position, reducing the frequency of wake switching events. They suggested that the higher turbulence intensity thickens the free shear layers in the wake, reducing the turbulent local oscillations of the wake around its asymmetric position. However, a different experimental study by Burton et al. (2021) showed that bi-modality persists across a range of free-stream turbulence intensities ($1\% \sim 15\%$). Higher turbulence intensities increase wake meandering and disturb the stability at a given asymmetric position, which, accordingly, significantly increases the occurrence of wake switching events. They attributed this behaviour to the free-stream turbulence changing the momentum distribution in the switching direction, interrupting the wake directly or indirectly by affecting the boundary and separating shear layers. Thus, the effect of changing the free-stream turbulence levels on the switching mechanism remains inconclusive and warrants further investigation.

The effect of boundary layer disturbances on wake bi-modality was the focus of a numerical study by Hesse and Morgans (2021). Using wall-resolved LES, they observed a link between the dynamics of the upstream boundary layers along the body surfaces and wake bi-modality. At $Re_H \approx 3.3 \times 10^4$, the boundary layers on the top and side surfaces of the Ahmed body separate just after the body nose, reattaching a short distance downstream before evolving as they move towards the base. They showed that these disturbances have a prominent effect in triggering the bi-modal switching of the wake. This motivates the current work to investigate the effect of the upstream boundary layer dynamics on bi-modality. The upstream boundary layer separations resolved using LES, was not captured with IDDES at $Re_H \approx 9.4 \times 10^4$ (Fan et al., 2020b). Compared to the experiment at the same Re, where the boundary layers separates near the nose, wake bi-modality persisted in both. This suggests that the effect of the upstream dynamics remains an open question. The main point here that the upstream dynamics represents an inlet condition for the wake, thus modifying these dynamics is expected to affect the wake flow. Concurrent to the current study, Fan and Cadot (2023) modified passively the turbulent boundary layer on the top and side body-surfaces using turbulators. They found that the turbulators affect both the boundary layer thickness and the length scale of the viscous sub-layer independently. The latter found to have more prominent effect on the wake switching rate compared to the former, as decreasing the length scale of the viscous sub-layer, decreases the switching rate.

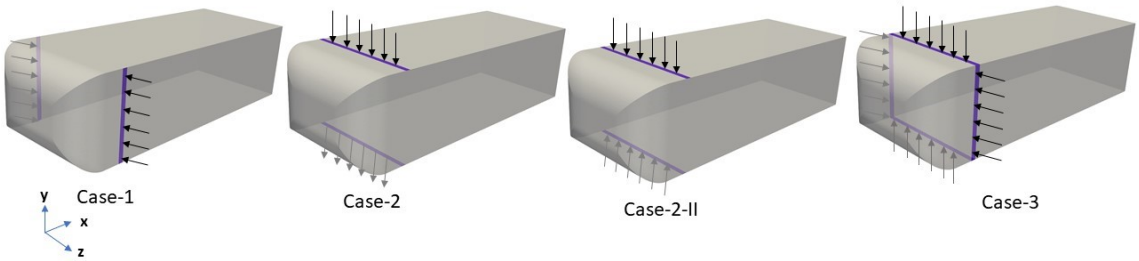

Figure 6.1: Different configurations for suppressing boundary layer separations. Purple slots indicate the actuators location with their width being 3% of the body width (W).

With a general view to investigating the wake dynamics in order to provide insights which inform effective control strategies for drag reduction, the disturbances of the free shear layers and their association with the wake configuration were found to be a key parameter. A control strategy that suppresses wake bi-modality without a direct effect on the free shear layers in the wake is expected to reduce the drag more than the case of forcing the wake region. In the latter case, the disturbances introduced in the shear layers hinder the reduction in drag achieved by wake symmetrisation (Ahmed and Morgans, 2022). Further, the newly established link between wake bi-modality and boundary layer dynamics convected from the upstream opens the door towards investigating new control strategies to suppress bi-modality targeting the upstream dynamics (Hesse and Morgans, 2021), which motivates our current study.

The main objective of this chapter is to investigate the effect of the upstream disturbances caused by boundary layer separations and reattachment on the body surfaces on wake bi-modality to inform a new control strategy for more significant reduction in drag. LES will be used to investigate the effect of applying suction and blowing to suppress the formation of the main body boundary layers separation bubbles and the associated boundary layer dynamics.

6.2 Simulation setup

The geometry considered in the present chapter is the standard square-back Ahmed body of (Ahmed et al., 1984) scaled down to one-fourth, as for the previous investigation (Ahmed and Morgans, 2022). The dimensions of the body and the virtual wind tunnel test section, simulation setup, and mesh independent study are identical to those described in section 4.1. The main difference in this chapter compared to the previous investigation is the position of the actuator, in order to affect the upstream separation bubbles, actuation is located on the longitudinal body surfaces whereas the actuation was base-mounted actuators in the previous chapters.

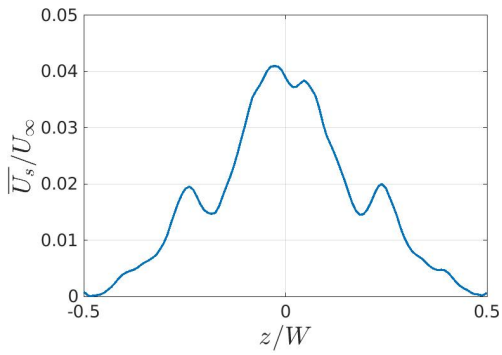

Figure 6.2: Mean suction velocity profile normalised by the free stream velocity, changing along the spanwise direction (z). This is equivalent to the surface-normal velocity at $y^+ = 10$ on the top surface of the body.

6.2.1 Suppressing boundary layer separations

Suppressing the separation of boundary layers on the longitudinal surfaces of the body was achieved by the application of steady suction and/or steady blowing of air normal to the surface. Suction and blowing were applied inside the upstream recirculation region with velocity (U_s). Actuator slots, with a width of $0.03W$, are placed at a streamwise position of $0.41W$ from the fore-end of the body on all the longitudinal surfaces of the body, as shown in figure 6.1. The streamwise location was chosen to be just after the boundary separation line determined in the unforced case based on the streamwise mean velocity.

Two different velocity profiles were considered for the spatial distribution of the suction/blowing velocity through the actuators. A parabolic velocity profile of suction velocity equal to the surface-normal velocity at $y^+ = 10$ was considered. This was considered a rough estimation of the entertainment velocity in the turbulent boundary layer. The mean parabolic suction velocity profile on the top surface as a function of the spanwise position is shown in figure 6.2. Applying this suction velocity was found to have a negligible effect on the separation bubble on the top surface of the Ahmed body, as depicted by figure 6.3b. This indicates that the mass of air sucked through the actuator is not equivalent to the mass entrained from the free stream to the boundary layer causing the flow separation (Jahanbakhshi, 2021).

A spatially-independent steady suction is then considered, with different values of U_s ranging from $-0.1\ U_\infty$ to $-1.0\ U_\infty$. Figure 6.3 compares the effect of different values of suction velocity on the frontal separation bubble caused by the boundary layers separation. It can be seen that for values of $-U_s/U_\infty < 1$ (figure 6.3b,c), flow separation persists with a slight change in the length of the separation bubble. The reattachment point moves upstream as the value of $-U_s/U_\infty$ increases. The most effective case in which boundary layer separation is fully suppressed downstream of the actuator slot was $U_s = -1.0\ U_\infty$, hence this was considered for the following investigations. The value U_s is spatially independent in both the spanwise (z) and vertical (y) directions.

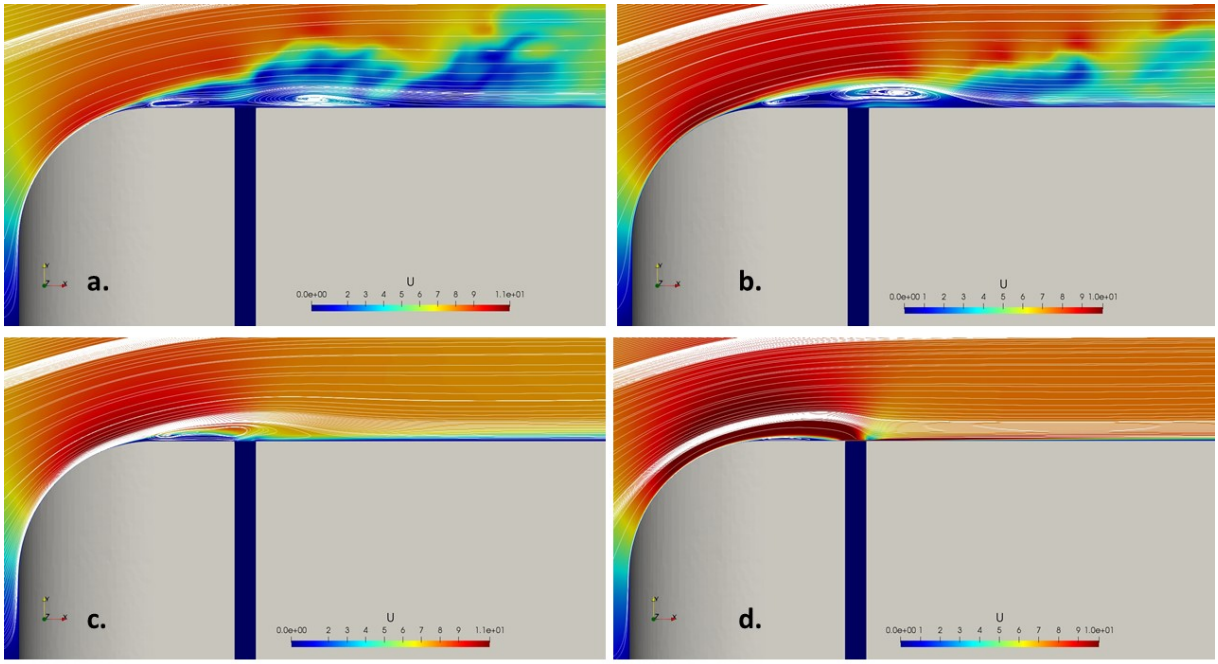

Figure 6.3: Velocity contours at a mid-width plane ($z = 0$), superimposed with in-plane streamlines show the frontal separation bubble on the top-surface of the Ahmed body in the absence of suction and/or blowing (a), parabolic suction velocity profile (b), suction velocity $U_s = -0.5 \times U_\infty$ (c) and suction velocity $U_s = -U_\infty$ (d). The blue slot on the body-surface remarks the actuator position. Air flows from left to right.

Five cases are considered based on the actuator slots' location and the forcing (suction or blowing). The first case is denoted as case-1, where suction is applied on the side surfaces only. This is chosen to ensure that the net side force applied is zero and that the change in the wake configuration is only related to the suppression of boundary layer separations. Suction and blowing are applied on both the top and bottom surfaces of the body, respectively, in case-2, achieving zero-net mass flux. Here the underbody flow is disturbed, and the separation of the boundary layer on the side surfaces persists. Another case denoted case-2-II is considered with suction applied on both the top and bottom surfaces, leading to zero-net force. These two cases allow comparison of the effects of suction and blowing in the underbody region. In case-3, boundary layer separations are suppressed on the top and side surfaces, with air being sucked through the bottom surface of the body to ensure zero-net force. Top-only suction was used for the actuator velocity study but did not affect bi-modality and so will not be considered as a standalone case. These cases are summarised in table 6.1. The following sections will discuss the results of case-1, case-2, case-2-II and case-3 in more detail. A schematic of the four cases showing the actuators' position and the type of force is shown in figure 6.1.

Table 6.1: Summary of the different cases considered to investigate the link between boundary layers separation and wake bi-modality.

Case name	Top	Bottom	Side 1	Side 2	Underbody flow
Case-1	-	-	suction	suction	undisturbed
Case-2	suction	blowing	-	-	disturbed
Case-2-II	suction	suction	-	-	disturbed
Case-3	suction	suction	suction	suction	disturbed

6.3 Unforced flow

The simulation results in the absence of any suction and/or blowing are similar to those discussed previously in chapter 4. This case will be denoted as the unforced flow case in the following discussion and comparisons. Similar to the analysis in chapter 5, the wake configuration downstream of the Ahmed body is determined using the horizontal and vertical base pressure gradients $\partial C_P/\partial z$ and $\partial C_P/\partial y$, respectively. Based on the Grandemange et al. (2013a) map of the switching direction, the base aspect ratio and ground proximity are expected to cause a horizontal (lateral) switching of the wake (switching in the spanwise z direction). The results of the unforced simulation successfully captured this lateral switching between two asymmetric positions. The time history of $\partial C_P/\partial z$ (figure 6.4) indicates six switches of the wake with a random residence time at each asymmetric position over 2000 normalised time units. The period before $t^* = 300$ is considered an initial transient period. The time evolution of the vertical base pressure gradient $\partial C_P/\partial y$, shown in figure 6.4, shows a weak vertical asymmetry of the wake due to the presence of the ground. These results are consistent with previous numerical results (Hesse and Morgans, 2021, Dalla Longa et al., 2019) and experimental results (Grandemange et al., 2013b, Barros et al., 2017).

The unforced results further reveal the formation and convection of hairpin vortices on the longitudinal surfaces of the body. On the top surface of the body, the boundary layer separates at a streamwise position of $0.08L$, then reattaches to the surface at $0.3L$, as shown in figure 6.3a. The boundary layers on the side surfaces follow the same behaviour with a slightly shorter separation bubble. Hairpin vortices then emanate from just downstream of the reattachment points (figure 6.5), with associated flow fluctuations at a relatively high frequency of $St_W = 2.8$, based on the pressure signal at $x/L = 0.45$, as shown in the power spectral density in figure 6.6. Similar frequencies were detected on both sides and top surfaces (not shown for brevity). These hairpin vortices were seen previously in Krajnovic and Davidson (2003), Kang et al. (2021) and Hesse and Morgans (2021). Following the time-evolution of the flow topology, we observe that these vortices grow along the surfaces up to the point where their maximum length scales become of order $H/2$, at a streamwise location of $x/L \sim 0.75$. Thereafter, their interaction with the freestream leads to a breakdown such that their length scales become much smaller. An interaction between the

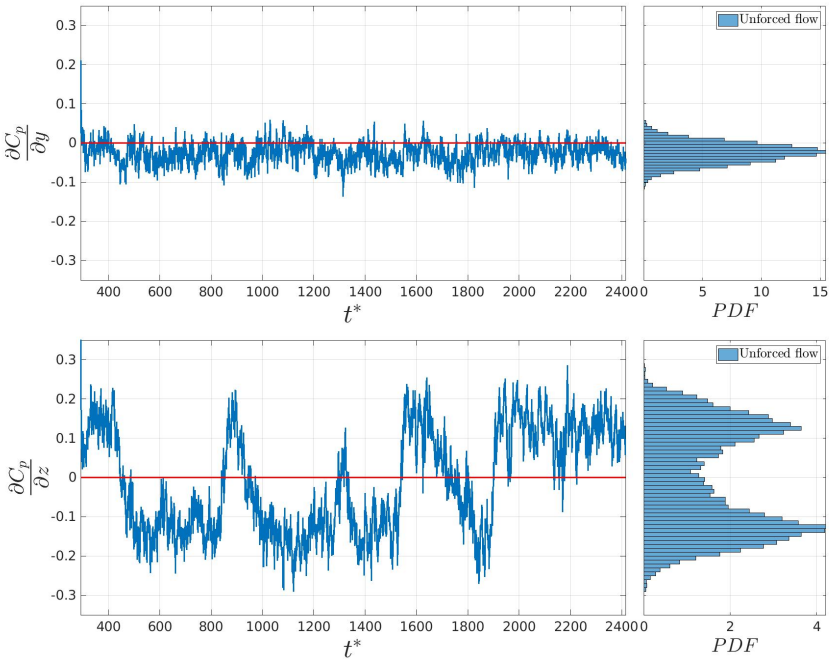

Figure 6.4: Time-history of vertical and horizontal gradients of base pressure coefficient $\partial C_P/\partial y$ (top) and $\partial C_P/\partial z$ (bottom), respectively, for the unforced flow case, indicating weak vertical asymmetry and horizontal bi-modality of the wake. The associated probability density function (PDF) is shown on the right.

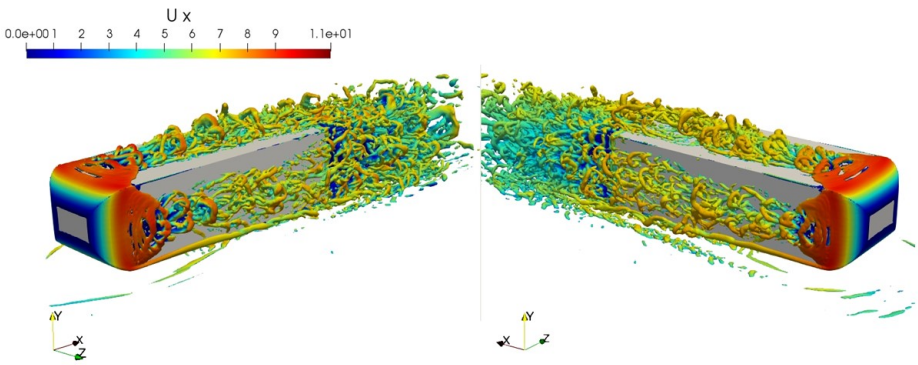

Figure 6.5: Iso-surfaces of Q-criteria of 2×10^5 coloured by the streamwise velocity for the unforced flow, using two different 3D views, showing the hairpin vortices on the body top and side surfaces.

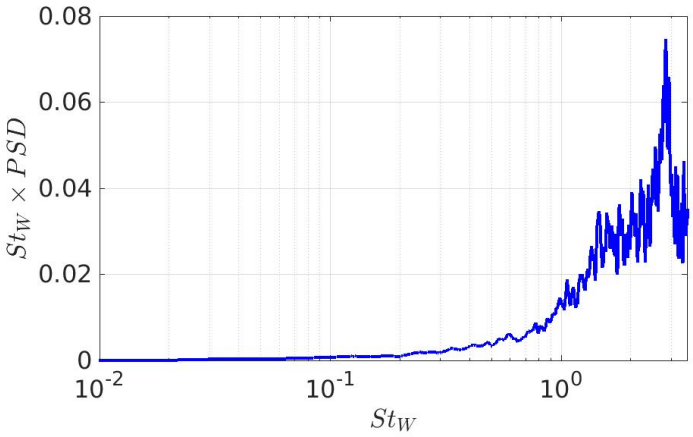

Figure 6.6: Premultiplied power spectral density of pressure signal from a probe placed at $x/L = 0.45$, $y/H = 0.65$ and $z/W = 0$, showing the high-frequency associate with the hairpin vortex.

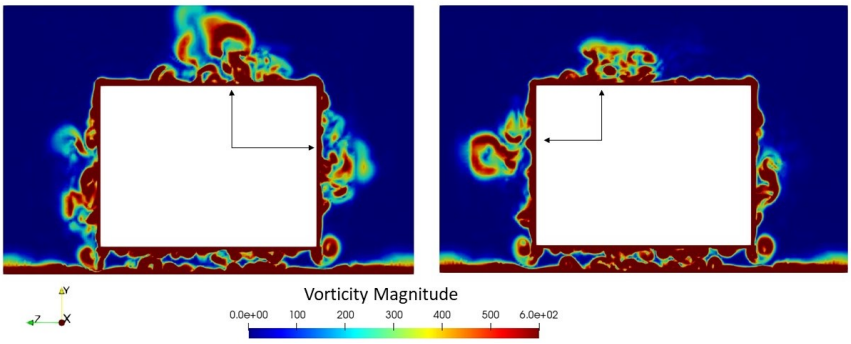

Figure 6.7: Instantaneous snapshots of vorticity magnitude at a streamwise position of $x/L \sim 0.9$, showing the vortices tendency to interact closer to the top right corner (left) and the top left corner (right).

smaller vortices from the top and side surfaces is then observed (supplementary video). Although this may be partially associated with turbulent diffusion, a periodic interaction pattern is evident. Figure 6.7 shows the vorticity magnitude on a cross section plane closer to the base ($x/L \sim 0.9$) at two instants. It indicates that the smaller vortices on the top surface tend to interact with the vortices on either of the sides at any given instant.

On the bottom surface of the body, the confinement caused by the ground changes the flow dynamics and topology compared to the other longitudinal body surfaces. The boundary layer remains attached along the bottom surface up to the body base. However, the interaction of the smaller vortices from the side surfaces with the underbody flow forms two corner vortices on the bottom part of the body (figure 6.5). This disturbs the underbody flow but does not lead to boundary layer separation. The ground boundary layer also does not exhibit any separation dynamics upstream of the wake. Previous studies have shown that wake switching is sensitive to underbody flow. Experimental studies have triggered wake switching by disturbing the underbody flow, for example, using a passive device in the clearance between the body and the ground (Barros

et al., 2017, Bao et al., 2022). Here, we consider that the disturbances in the underbody flow may partly be caused by the interaction of smaller vortices from other surfaces due to boundary layer dynamics. Therefore, we investigate the effect of suppressing the upstream boundary layer disturbances on the underbody flow and wake bi-modality.

Following the time history of the Q-criteria, shown in the supplementary movie, disturbances in these corner vortices are introduced by the smaller vortices from the sides. Considering the vortices on one side surface, it can be seen that they tend to interact with vortices from either the top or the bottom surface in an instant, while the vortices on the other side interact with the opposite surface. This occurs interchangeably, with no evidence of a clear associated frequency. This interaction occurs due to boundary layer separations and is believed to be linked to wake switching.

In conclusion, it is proposed that the dynamics related to boundary layers separation have a direct and indirect effect on wake bi-modality. The direct effect is related to the disturbance convected to the separated shear layers in the wake. The indirect effect is related to the underbody flow. The interaction of the smaller vortices from the three surfaces, where the boundary layer separates, proposed introducing disturbances in the underbody region, which proved to be a controlling parameter of wake bi-modality. The different cases used in this investigation cover these two links in more detail in the following sections.

6.4 Suppression of upstream boundary layer separations

The results of applying suction and/or blowing on the longitudinal surfaces of the Ahmed body are discussed in the following subsections. The time-averaged and instantaneous properties of the flow field are considered, and the results are divided into four sections. In the first section (6.4.1), the effect of suction and/or blowing on the boundary layers will be explored, followed by the corresponding effect on the wake configuration and the mean wake flow in sections 6.4.2 and 6.4.3, respectively. Finally, the effect of modulating the upstream dynamics on the underbody flow will be investigated considering both the full flow field and modal reduction in sections 6.4.4 and 6.4.4, respectively.

6.4.1 Boundary layer separation

The effect of applying the upstream suction and/or blowing on the boundary layers of the longitudinal body surfaces is now investigated. As described in section 6.2.1, spatially-independent steady suction and blowing with a velocity equal to the free stream velocity is applied normal to

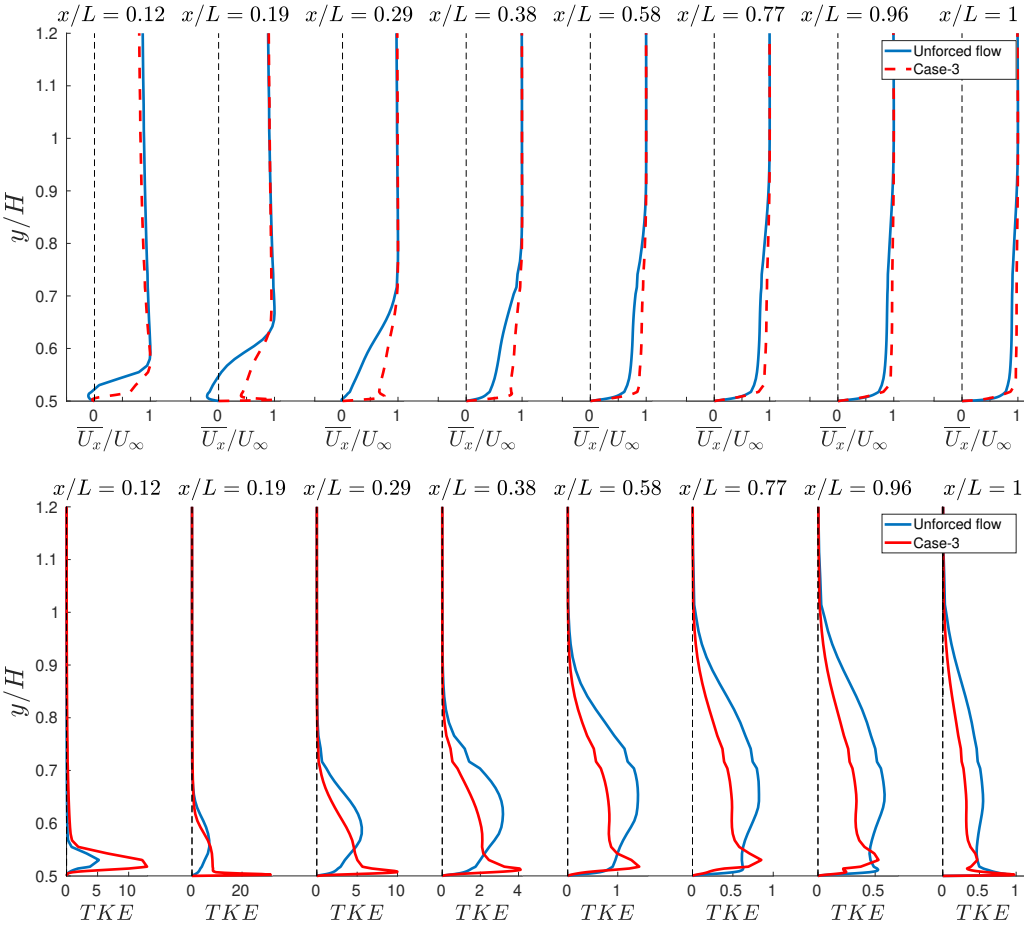

Figure 6.8: Streamwise mean velocity (top) and turbulent kinetic energy at different streamwise locations on the top surface of the Ahmed body at $z/W = 0$ (mid-width), for the unforced flow and case-3 shown by blue and red lines, respectively. Note that the horizontal axes for the TKE plot have different scales.

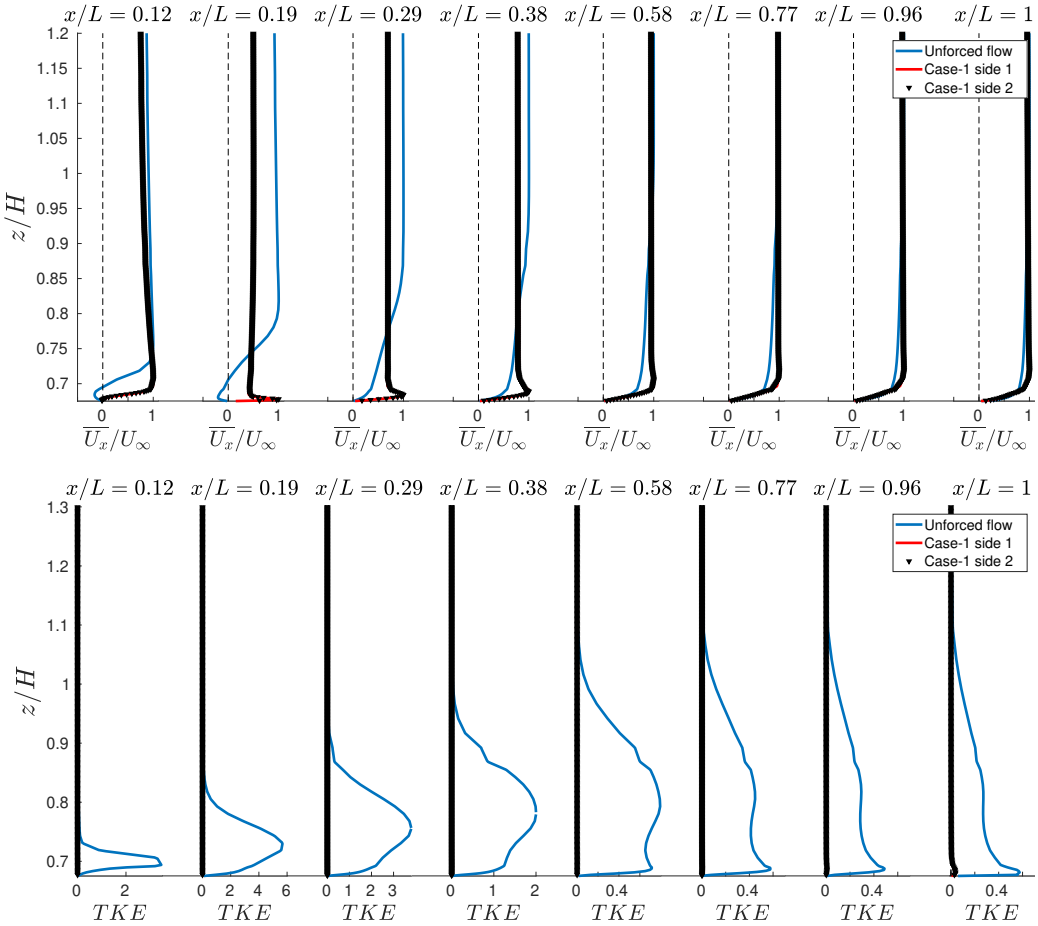

Figure 6.9: Streamwise mean velocity (top) and turbulent kinetic energy at different streamwise locations on the side surfaces of the Ahmed body at $y/H = 0$ (mid-height), for the unforced flow and side 1 and side 2 for case-1, shown by blue, red lines and the black triangles, respectively. Note that the horizontal axes for TKE plot have different scales.

the surfaces. Suction and blowing slits are placed inside the separation bubble formed just aft the body nose at a streamwise position of $x/L \sim 0.15$, just downstream of the smaller recirculation region is shown in figure 6.3a. The same streamwise slit position is used on all body surfaces. The effect of this suction on the Ahmed body boundary layers upstream of their large-scale separation at the base is now investigated.

Figures 6.8 and 6.9 compare the streamwise time-averaged velocity along the top and side surfaces of the body, respectively, for the unforced flow, case-1 and case-3. In the absence of suction, the boundary layers separate at $x/L \sim 0.08$ on the top and side surfaces, reattaching at $x/L \sim 0.30$ on the top surface and at $x/L \sim 0.26$ on the sides. The lengths of the separation bubbles on either side of the body are identical and slightly shorter than on the top. The boundary layers on the bottom surface of the body and the ground remain attached throughout. The shape factor, defined as the ratio of boundary layer displacement and momentum thicknesses, at the separation location is ~ 1.3, indicating that all boundary layers are fully turbulent prior to their separation at the base.

When suction is applied on the top surface, as in case-2, case-2-II and case-3, a tiny extent of boundary layer separation and reattachment are seen upstream of the slit. There is a hint of a tiny boundary layer separation at $x/L \sim 0.12$ in figure 6.8. The boundary layer then grows attached to the wall downstream of the slit, as shown by the streamwise velocity for $x/L > 0.15$. The effect of the suction slit is that the boundary layer effectively grows from zero thickness downstream of the slit with no evidence of significant separation upstream of the base (Schlichting and Gersten, 2003). Figure 6.9 shows that suction has a similar impact on the boundary layers on both sides, also causing them to remain attached along the length of the body.

For the unforced flow, the boundary layer thicknesses at the Ahmed body base (just ahead of where the large-scale flow separation occurs) are identical on the top and side surfaces. Suction is seen to have very little effect on the time-averaged properties of the boundary layers near the base, i.e., at $x/L \sim 1.0$. Top upstream suction slightly reduces the thickness of the top boundary layer, with $\delta_{0.99}/H \sim 0.48$ compared to $\delta_{0.99}/H \sim 0.50$ without suction. Side upstream suction causes a negligible change in the thickness of the side-surface boundary layers. All boundary layers remain turbulent at the base in the presence of upstream suction.

Suppressing the upstream boundary layer separations acts to reduce the turbulent fluctuations arising from the formation and development of the hairpin vortices, as discussed in section 6.3. This can be seen in figure 6.10, which shows the Q-criteria for different forcing arrangements. Both the hairpin and the smaller vortices evidenced in the unforced flow (figure 6.5) are suppressed on the surfaces where suction is applied. Comparing case-1, where suction is applied on the side surfaces, these vortices are suppressed on the sides. This isolates the vortical structures on the top

surface and the underbody flow, suppressing the interactions that occur with side surface vortical structures in the absence of side suction. The proposed mechanism of wake switching depends upon interrupting this interaction, which is expected to affect wake bi-modality, as discussed in section 6.3. Figure 6.11 shows the effect on the turbulent kinetic energy upstream of the base (at $x/L = 0.88$). For case-1, the turbulent kinetic energy on the sides is diminished. This is similarly seen in through figure 6.9, which shows the turbulent kinetic energy profile on both sides at mid-body height and different streamwise positions. Compared to the unforced flow, suction reduced the turbulent kinetic energy on both sides by an order of magnitude. These results are consistent with the experimental results of Fan and Cadot (2023), where tabulators were used on the side surfaces closer to the body fore-end to modify the flow upstream of the base. Similarly, they noticed that the fluctuation velocity is decreased prior to the wake at 9.5×10^4.

Similarly, for case-2 and case-2-II, the application of suction on the top surface suppresses vortices on the top surface as well as their interaction with vortices from the side surfaces. For case-2, where blowing is applied in the underbody, the smaller side vortices were found to have a tendency to interact with the underbody flow, causing the shedding of a pair of corner vortices, shown by the relatively higher values of turbulent kinetic energy in the bottom corners in figure 6.11c. In case-2-II, where the air is sucked from the underbody region, the smaller vortices on the side surfaces interact with both the top boundary layer and underbody flow, increasing the disturbances there, as shown by the relatively higher values of turbulent kinetic energy in figure 6.11d for case-2-II. The effect of bottom-surface suction and blowing on the underbody flow is considered in section 6.4.4.

For case-3, the vortical structures on the top and side surfaces are reduced. In this case, any remaining switching of the wake is attributed to the turbulent fluctuations in the wake region and the underbody flow rather than the turbulent fluctuations caused by boundary layer separations. The turbulent kinetic energy is reduced on the top and side surfaces compared to the unforced case, as shown in figure 6.11e. Figure 6.8 shows a slight increase in the turbulent kinetic energy closer to the wall (in the viscous sub-layer), which was not very obvious in figure 6.11e. The level of increase reduces towards the base.

To conclude, suppressing boundary layer separations was found to have a negligible effect on the boundary layer thickness closer to the base. A more pronounced effect on the fluctuations attributed to the vortical structures is attained, which is believed to contribute partly to the turbulent forcing causing the wake switching. The corresponding effects on the mean and fluctuated flow in the wake are further discussed in the next section.

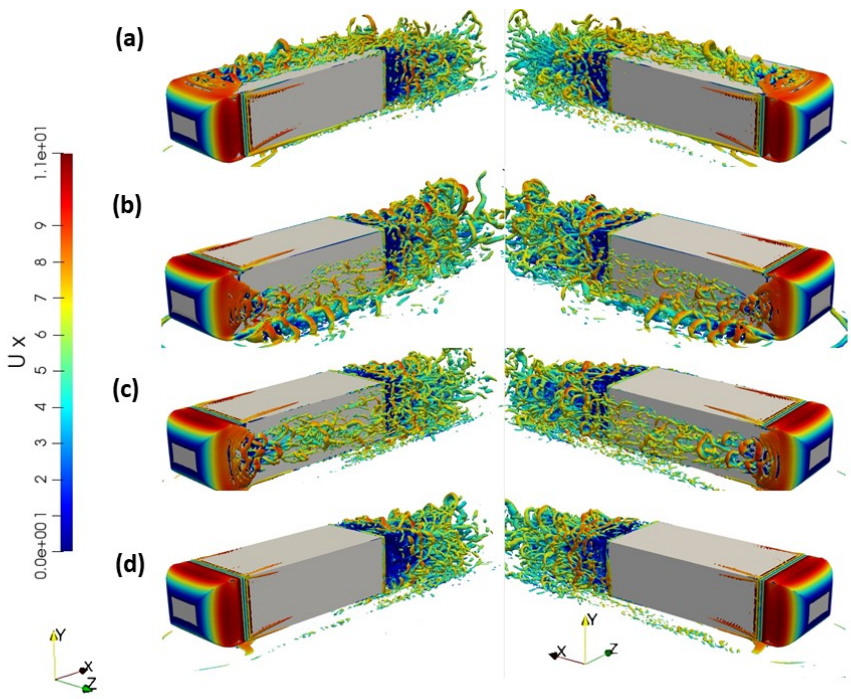

Figure 6.10: Iso-surfaces of Q-criteria of 2×10^5 coloured by the streamwise velocity, using two different 3D views, for case-1 (a), case-2 (b), case-2-II (c) and case-3 (d), showing the effect of suction/blowing on the fluctuations along the body top and side surfaces.

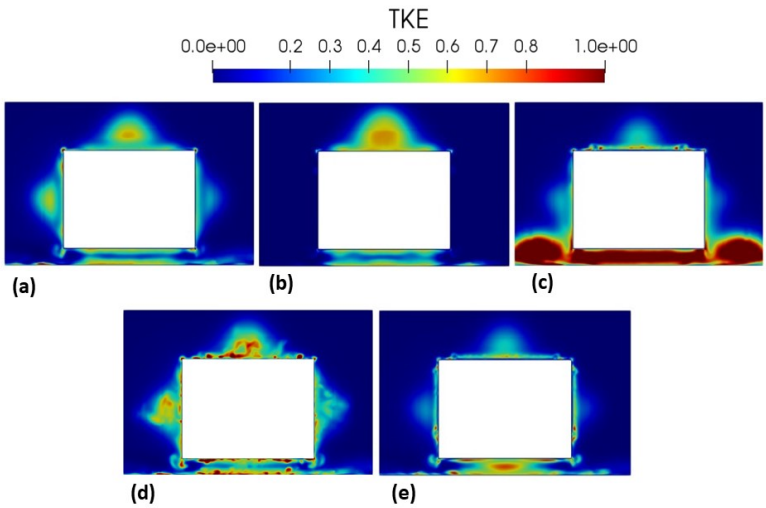

Figure 6.11: Turbulent kinetic energy on a vertical plane at a streamwise position of $x/L = 0.88$, for the unforced flow (a), case-1 (b), case-2 (c), case-2-II (c) and case-3 (e).

Case	Horizontal bi-modality	Vertical asymmetry	$\Delta\overline{L_{rec}}$	$\Delta < \overline{C_{P-base}} >$	$\Delta\overline{U_b}/U_\infty$
Unforced flow	persists	weak	0%	0%	0%
Case-1	suppressed	weak	+3%	+14%	0%
Case-2	suppressed	non-weak	−5%	−6%	−18%
Case-2-II	persists	reflected-weak	0%	+2%	−1%
Case-3	suppressed	reflected-weak	0%	+7%	−3%

Table 6.2: Comparison of the effect of boundary layer separations suppression on the wake horizontal bi-modality, vertical asymmetry, length of the recirculation region ($\overline{L_{rec}}$), area-averaged mean base pressure ($< \overline{C_{P-base}} >$) and underbody bulk velocity ($\overline{U_b}$) (indicating the change in the momentum of the underbody flow).

6.4.2 Effect on wake configuration

The resultant effect of suppressing boundary layer separations on the wake configuration is explored in this section. The time-resolved wake configuration, i.e. wake bi-modality, is explored firstly, followed by the vertical wake balance for the different cases.

Effect on wake bi-modality

The wake horizontal bi-modality in the presence of suction is explored in this section. A summary of the results for the different cases, including the mean properties of the wake flow, is shown in table 6.2. The spatial gradient of the pressure coefficient on the base, $\partial C_P/\partial z$, is used to characterise horizontal bi-modality. Figure 6.12 depicts the time history of $\partial C_P/\partial z$ for the four cases. All simulations initially have no suction/blowing on any of the Ahmed body surfaces; the unforced wake was left to switch naturally for the first 700 convective time units, during which it switches three times. Suction/blowing is then activated to suppress boundary layer separations, as marked by the black dashed line in figure 6.12, with simulations running for 1400 convective time units in the presence of suction/blowing. The time-evolution of $\partial C_P/\partial z$ shows that suppressing the separation of boundary layers near the body fore-end successfully suppresses wake bi-modality for all the cases except case-2-II. Bi-modality suppression is evident from the single peak of the probability density function of $\partial C_P/\partial z$ as shown in figure 6.12. This supports a causal link between the boundary layer separations upstream of the wake and bi-modality, as recently proposed by Hesse and Morgans (2021).

For case-1, where the boundary layer separations on the side surfaces are suppressed, the remaining turbulent forcing in the wake causes a stochastic switching of the wake within spatial bounds closer to the center. The corresponding $\partial C_\mathrm{P}/\partial z$ for these switching bounds is half of their equivalents in the unforced case. The time-evolution of dC_P/dz for case-2 indicates a fully-suppressed bi-modality in the wake. This case confirms the prominent effect of the underbody flow on the wake configuration. In this case, the top-surface boundary layer separation is fully

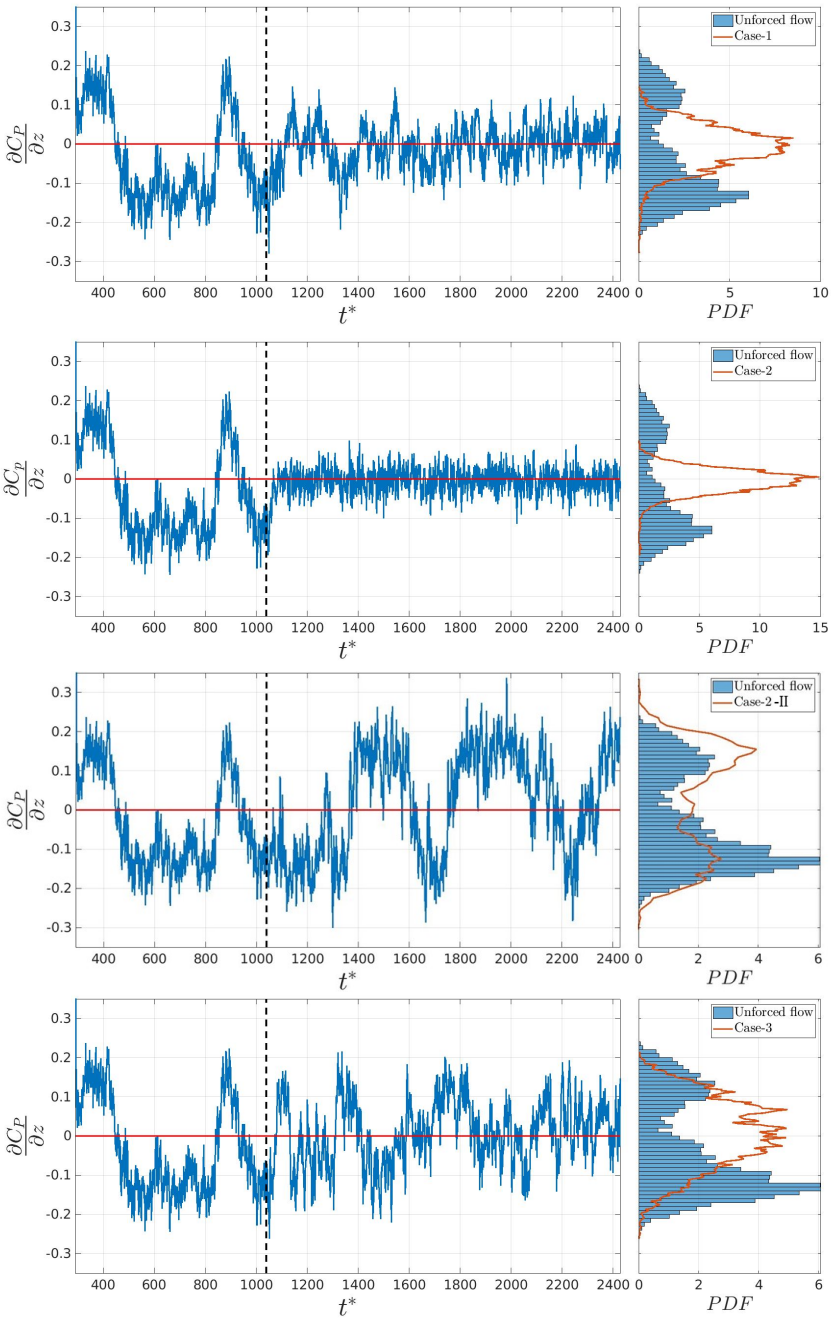

Figure 6.12: Time history of horizontal pressure gradient of the pressure coefficient C_P (left) and the associated probability density function (PDF) for the base flow, case-1 (top), case-2, case-2-II and case-3 (bottom). The black dashed line marks the starting time of the application of suction/blowing.

suppressed, and the air is blown through the bottom surface of the body. The latter caused some disturbances in the underbody flow, leading to boundary layer separation on the bottom surface of the body. In this case, the spatial bounds of the remaining switching are the closest to the centre of the base. The time-evolution of $\partial C_{\mathrm{P}}/\partial z$ for case-2-II indicates the presence of wake bi-modality; the wake switches five times in the presence of suction on both top and bottom body surfaces. For case-3, boundary layer separations are suppressed on the top and sides surfaces and momentum is removed from the underbody flow. This suppresses wake bi-modality, as shown in the associated probability density function in figure 6.12. The time evolution of $\partial C_P/\partial z$ shows that the wake switches between spatial bounds, which are slightly closer to the base center than the unforced case. The wake oscillations about the symmetric position are now more rapid than in the absence of suction.

When suction is applied on the top surface only (case-4), wake bi-modality persists, as shown in figure 6.13. This confirms two points; the first point is the controlling effect of the underbody flow –considering case-2– in changing the wake configuration. The second point is related to the proposed link of the interaction of the smaller vortices, which introduced disturbances in the underbody flow and is believed to be linked to wake switching; this will be discussed in detail in the following sections. Due to its negligible effect on wake bi-modality, this case will not be considered for further analysis.

To conclude, these results confirm that bi-modality is affected by the convected dynamics caused by the upstream separations of the boundary layer. Interrupting the interaction of the vortices upstream of the wake, caused by suppressing the separation of the boundary layer, stabilize bi-modality. Suppressing this separation on the surfaces perpendicular to the plane of bi-modal switching (side surfaces) completely suppressed bi-modality. The result of this case is different to the experimental result of Fan and Cadot (2023) using tabulators. Although, both the show reduction in the fluctuated velocity (thinner viscous sub-layer closer to the base), we believe that the extent of this reduction is a key here. A great reduction was seen in the current study, as shown in figure 6.9. When boundary layer separations are suppressed on the surfaces parallel to the switching direction, the effect on bi-modality depends on (case-4) the underbody disturbance. Bi-modality persists when no or moderated disturbances (case-2-II) are introduced in the underbody region. Bi-modality is completely suppressed when the underbody flow is strongly disturbed (when blowing is applied, as in case-2). In this case, the mechanism of bi-modality suppression will be discussed further. When both parallel and perpendicular surfaces are considered, the symmetrised wake is now switching within larger spatial bounds. In the last two scenarios, the underbody flow is being affected, which is a sensitive parameter for bi-modality. In these cases, bi-modality suppression is related to both interrupting vortices interaction and changing the momentum of the underbody

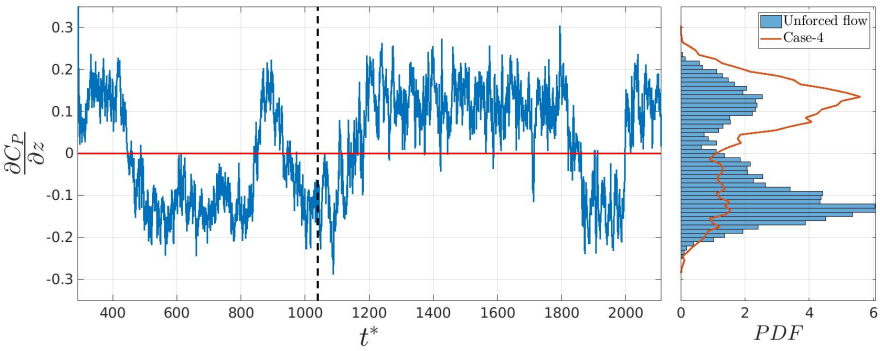

Figure 6.13: Time history of horizontal pressure gradient of the pressure coefficient C_P (left) and the associated probability density function (PDF) for the base flow and case-4 (upstream6) where suction is applied on the top surface only. The black dashed line marks the starting time of the application of suction.

flow. Applying suction on the underbody region in case-3 causes the wake to switch between larger spatial bounds compared to the first scenario where the underbody was undisturbed.

Effect on wake vertical-asymmetry

The vertical position of the wake is characterised by the spatial gradient of the base pressure coefficient in the vertical direction, i.e., $\partial C_P/\partial y$. It is influenced by the disturbances introduced into the underbody flow, as in case-2, case-2-II and case-3. Figure 6.14 shows joint probability density functions of the spatial gradients of the base pressure coefficient, $\partial C_P/\partial z$ and $\partial C_P/\partial y$, in the presence and absence of the upstream suction/blowing. The unforced bi-modal wake exhibits weak asymmetry in the vertical direction, evidenced by the non-zero value of $\partial C_P/\partial y$. This is due to the effect of flow emanating from the underbody, correlating with the experimental results by Grandemange et al. (2013a) for a similar height of the gap to ground. The weak vertical asymmetry is evident from the fact that horizontal bi-modality occurs for $\partial C_\mathrm{P}/\partial y$ values centred within a limited spatial region around zero. This follows the competition between the horizontal and the vertical base pressure gradients proposed by Barros et al. (2017). The wake is tilted towards the ground, as shown in figure 6.17, which depicts different views of the unforced flow wake, defined as an iso-surface of zero mean streamwise velocity. The recirculation region is dominated by downwash flow from the top shear layer similar to Kang et al. (2021). This is also confirmed by the streamlines on the mid-width plane in the wake, shown in figure 6.16a,b, where the top-recirculation zone is larger than the bottom, and the saddle point is closer to the ground.

The vertical position of the horizontally-symmetric wake in case-1, where the separations of the boundary layer on the side surfaces are suppressed, was found to be similar to the unforced case. Figure 6.18 shows the three-dimensional view of the wake of case-1. The bottom view indicates

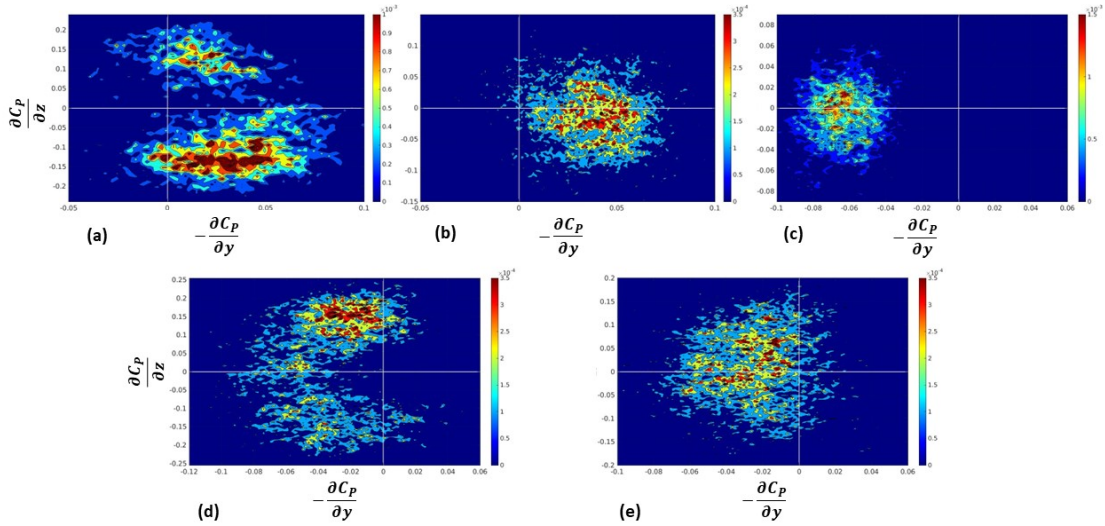

Figure 6.14: Two-dimensional probability density function (PDF) of the spatial gradients of the base pressure coefficient in the horizontal and vertical directions, for the unforced flow (a), case-1 (b), case-2 (c), case-2-II (d) and case-3 (e). Note that different scales are used in the figure.

that the bottom surface and the ground boundary layers remain attached. The streamlines at the mid-width plane, figure 6.16c, shows that the wake is dominated by downwash flow similar to the unforced flow case. The saddle point's location here is approximately similar to the unforced flow case, with the top recirculation zone dominating.

Disturbing the underbody flow by the application of air blowing and suction, as in case-2, case-2-II and case-3, forces the wake to move slightly away from the ground. This is caused by the dominance of the upwash flow for these cases, which is relevant to the change in the momentum of the underbody flow concomitant with the suppression of the separation of the top-surface boundary layer. The wakes of case-2-II and case-3 exhibit weak vertical asymmetry compared to case-2, whose wake exhibits a static vertical asymmetry (figure 6.14) with no horizontal bi-modality allowed. In case-2, horizontal bi-modality faded due to the competition between the vertical and horizontal pressure gradients. These results are consistent with the experimental results by Barros et al. (2017) and Haffner et al. (2020), in which disturbing the underbody flow inverted the vertical (wall-normal) position of the wake with a positive pressure gradient. Both the three-dimensional views of the wake and the streamlines of case-2-II and case-3 indicate weak vertical asymmetry as shown in figures 6.21, 6.20, 6.16e and 6.16f, respectively. In case-2 the shape of the wake becomes irregular as shown in the three-dimensional view of the wake in figure 6.19. Figure 6.16c shows that the bottom recirculation mainly forms the wake, and the top recirculation, which is smaller in shape than the bottom one, is convected downstream, causing this small bulge in the far end of the wake profile. This case is similar to the experimental study of Grandemange et al. (2013a) for

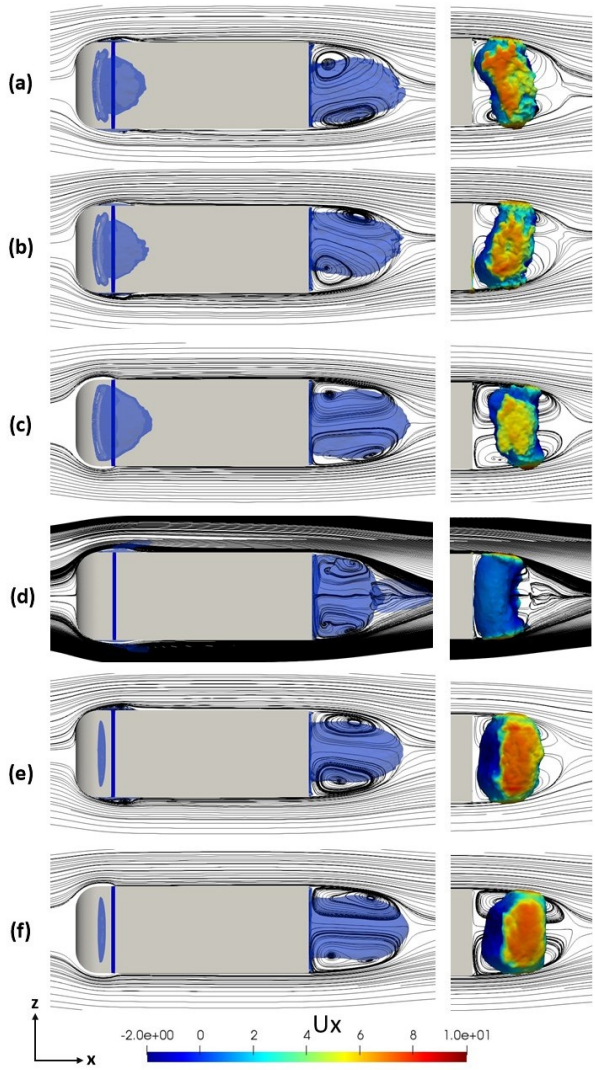

Figure 6.15: Top view of the separation bubble demarcated by the iso-surface of zero streamwise mean velocity for the asymmetric wake when $\partial C_P/\partial z < 0$ (a), asymmetric wake when $\partial C_P/\partial z > 0$ (b), case-1 (c), case-2 (d), case-2-II (e) and case-3 (f). In-plane streamlines at $y/H = 0$ are superimposed for each case. Air flows from left to right. The blue slot on the surface indicates the suction slit. The associated toroidal vortices defined as C_P iso-surface of -0.22 and colored by the mean streamwise velocity are shown on the right side of the graph.

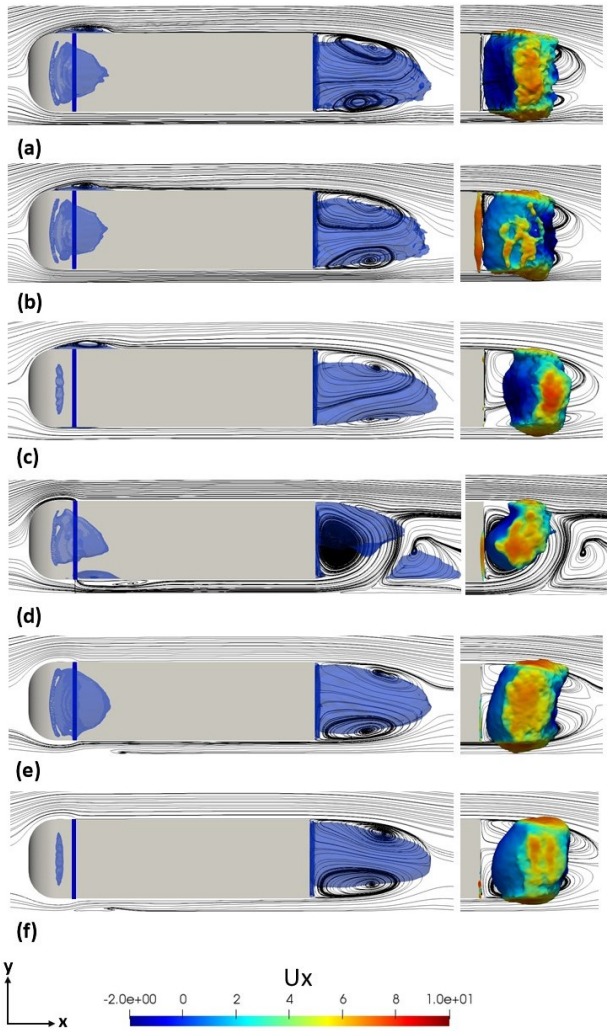

Figure 6.16: Side view of the separation bubble demarcated by the iso-surface of zero streamwise mean velocity for the asymmetric wake when $\partial C_P/\partial z < 0$ (a), asymmetric wake when $\partial C_P/\partial z > 0$ (b), case-1 (c), case-2 (d), case-2-II (e) and case-3 (f). In-plane streamlines at $y/H = 0$ are superimposed for each case. Air flows from left to right. The blue slot on the surface indicates the suction slit. The associated toroidal vortices defined as C_P iso-surface of -0.22 and colored by the mean streamwise velocity are shown on the right side of the graph.

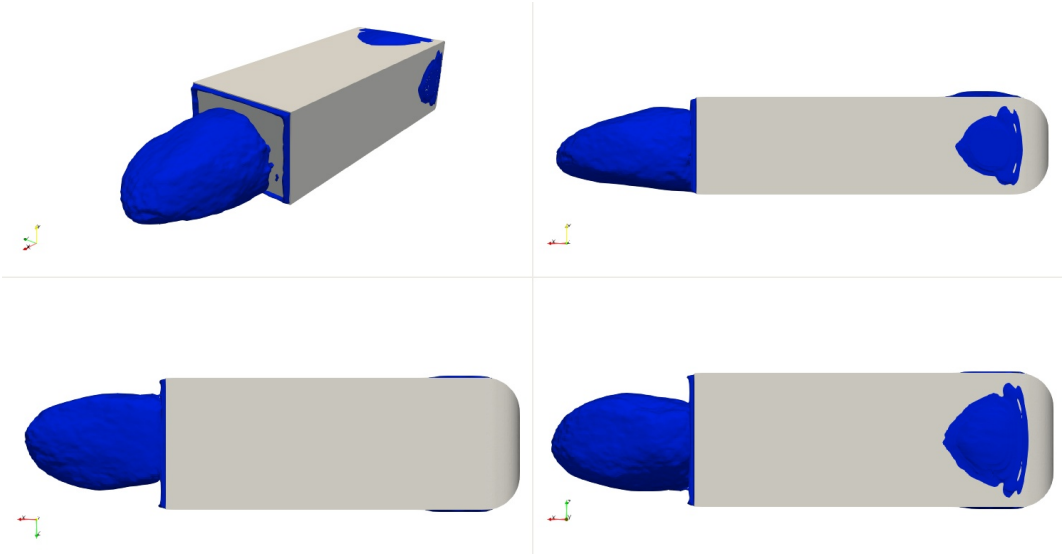

Figure 6.17: The wake of the unforced flow marked by an iso-surface of zero mean streamwise velocity. The top-row shows a 3D view (left) and a 2D side view (right). The bottom-row depicts the bottom view (left) and the top view (right). Air flows from right to left.

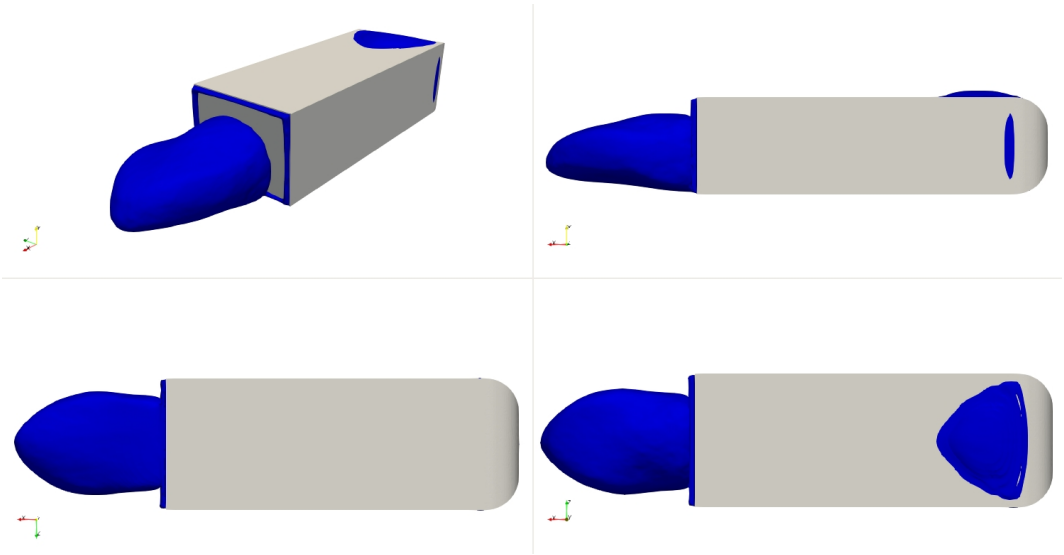

Figure 6.18: The wake of case-1 marked by an iso-surface of zero mean streamwise velocity. The top-row shows a 3D view (left) and a 2D side view (right). The bottom-row depicts the bottom view (left) and the top view (right). Air flows from right to left.

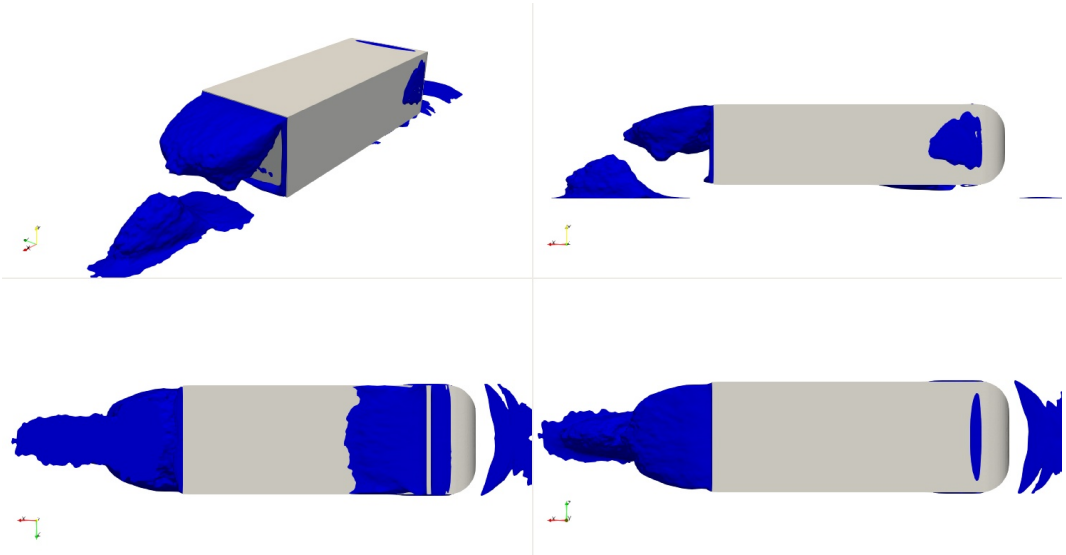

Figure 6.19: The wake of case-2 marked by an iso-surface of zero mean streamwise velocity. The top-row shows a 3D view (left) and a 2D side view (right). The bottom-row depicts the bottom view (left) and the top view (right). Air flows from right to left.

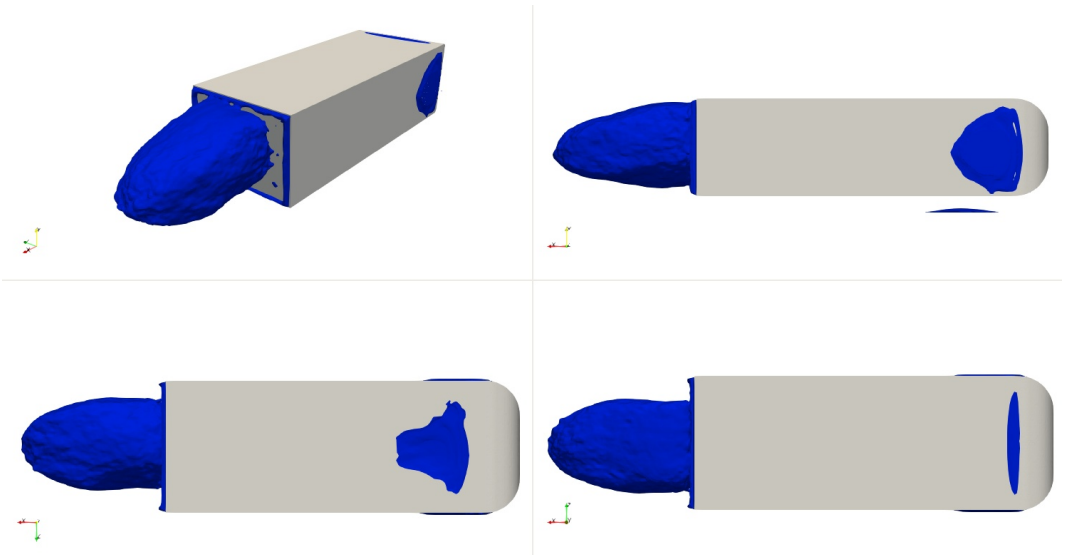

Figure 6.20: The wake of case-2-II marked by an iso-surface of zero mean streamwise velocity. The top-row shows a 3D view (left) and a 2D side view (right). The bottom-row depicts the bottom view (left) and the top view (right). Air flows from right to left.

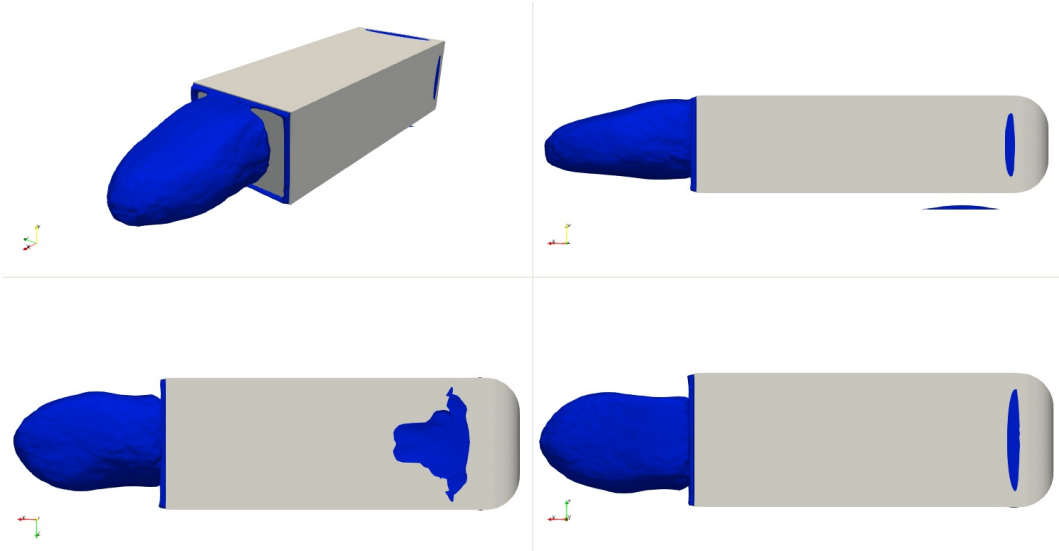

Figure 6.21: The wake of case-3 marked by an iso-surface of zero mean streamwise velocity. The top-row shows a 3D view (left) and a 2D side view (right). The bottom-row depicts the bottom view (left) and the top view (right). Air flows from right to left.

a relatively smaller gap to ground.

To conclude, the unforced flow wake exhibits weak vertical asymmetry, which is dominated by the downwash flow from the top shear layer. The wake's vertical balance is sensitive to the disturbances introduced into the underbody region. The weak-vertical asymmetry of the unforced wake holds for case-1, where no direct disturbances are introduced in the underbody region. The results of case-2, case-2-II and case-3 show that blowing and suction have different effects in the confined underbody region. Both push the wake away from the ground, with the wake exhibiting a reflected vertical asymmetry. A reflected weak-vertical asymmetry is indicated in the wake of case-2-II and case-3, while the wake of case-2 is vertically asymmetric. Since bi-modality only exists when the wake exhibits weak-vertical asymmetry, i.e. case-1, case-2-II and case-3, the suppression of bi-modality in both case-1 and case-3 can now be related to the suppression of upstream dynamics on the side surfaces. However, the suppression of bi-modality in case-2 is due to the bifurcation in the ground clearance, i.e. the underbody disturbances (Cadot et al., 2015).

6.4.3 Effect on mean wake flow

This section explores the effect of suppressing upstream boundary layer separations on the mean wake flow. Different flow properties are considered, including the base pressure, the size and mean position of the recirculation bubble and finally the growth of the separated shear layers in the wake

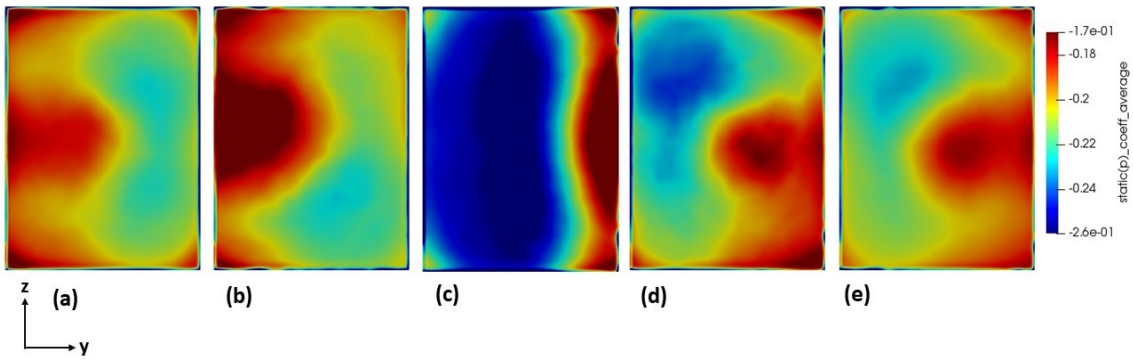

Figure 6.22: Comparison of the time-averaged pressure coefficient, C_P, on the body base. From left to right, unforced (a), case-1 (b), case-2 (c), case-2-II (d) and case-3 (e), respectively.

Effect on base pressure

The effect of suppressing boundary layer separations on the mean base pressure is explored in this subsection. Mean base pressure is an essential parameter for pressure drag. For a square-back Ahmed body, pressure drag increases linearly with the mean base pressure (Ahmed et al., 1984, Ahmed and Morgans, 2022). The wake configuration strongly influences the mean base pressure, i.e., the horizontal bi-modality and vertical asymmetry. Horizontal bi-modality is suppressed in case-1, case-2 and case-3 with different switching bounds of the remaining wake fluctuations, as discussed previously in section 6.4.2. Hereafter, we will discuss the change in the mean base pressure recovery and its link to the vertical asymmetry of the wake, which was previously investigated experimentally by Haffner et al. (2020). As the wake loses its vertical symmetry, base pressure increases and bi-modality disappears, i.e. $\frac{\partial C_P}{\partial y} > \frac{\partial C_P}{\partial z}$. Weak vertical asymmetry is known as the vertical region –around the base centre– where horizontal bi-modality exists in the absence of suction/blowing, following the competition between the horizontal and the vertical base pressure gradients proposed by Barros et al. (2017). The wake vertical balance is mainly affected by the underbody flow momentum and disturbances. Increasing the underbody flow disturbances and reducing its momentum force the wake to move away from the weak vertical asymmetry region, as in case-2, leading to a static vertical asymmetric wake. The impact of suction and/or blowing on base pressure recovery is investigated using the area-averaged mean base pressures denoted as $< \overline{C_{P-base}} >$. The values of $\Delta < \overline{C_{P-base}} >$ for the different cases compared to the base flow are shown in table 6.2.

Figure 6.22 compares the time-averaged base pressure for the unforced flow and cases 1 to 3. Compared to the unforced flow case, horizontal symmetry is evidenced with the horizontally-symmetric distribution of $\overline{C_{P-base}}$ for all cases except case-2-II. The weak-vertical asymmetry, indicated by the relatively higher pressure region in the bottom half $(-y)$ of the unforced case, holds in this case-1. The area-averaged mean base pressure $< \overline{C_{P-base}} >$, in this case, is -0.19

with an increase of 14% compared to the corresponding value for the unforced flow. Base pressure recovery here is attributed to bi-modality suppression, as the vertical asymmetry exhibits negligible change. The value of $< \overline{C_{P-base}} >$ for case-1 is higher than $< \overline{C_{P-base}} >$ during the instantaneous horizontal-symmetry states of the bi-modal wake, i.e. in the absence of suction, which was -0.21 (Ahmed and Morgans, 2022). This might indicate that the suppression of the upstream dynamics related to boundary layers affects other modes in the wake, which will be further discussed in the next chapter.

In case-2, where suction and blowing are applied on the top and bottom body surfaces, respectively, $< \overline{C_{P-base}} >$ is reduced by 6%. The distribution of $\overline{C_{P-base}}$ reflects the wake time-averaged location, with higher pressure closer to the top indicating the reflectional vertical asymmetry and the horizontally-symmetric distribution indicating the disappearance of bi-modality. In this case, the loss in pressure recovery is unfavourable for pressure drag. In case-2-II, the distribution of the base pressure coefficient in figure 6.22d shows the reflected vertical asymmetry compared to the unforced case and horizontal asymmetry (bi-modality persists) due to the wake residing longer time on one side compared to the other. A gain of 2% in $< \overline{C_{P-base}} >$ can be seen here, which might be attributed to the reflected weak-vertical asymmetry. When suction is applied on all longitudinal body surfaces, i.e. case-3, the base pressure distribution indicates horizontal symmetry with a reflected weak vertical asymmetry indicated with the higher pressure region closer to the top part of the body. The mean base pressure increases by 7%, which is attributed to the wake being horizontally symmetrised with reflected weak vertical asymmetry; the large wake oscillations are likely to be limiting the base pressure recovery as compared to case-1.

To conclude, the highest base recovery is achieved for a horizontally-symmetric wake without changing its vertical balance, as in case-1. The remaining oscillations in case-3 reduce the gain in the base pressure recovery to 7%. The non-weak vertical asymmetry exhibited by the wake of case-2 reduces the mean base pressure by 6% compared to the base flow. The weak vertical asymmetry slightly increases the mean base pressure in the presence of wake bi-modality as in case-2-II. These results are consistent with the experimental results by Haffner et al. (2020), where the reflected weak vertical asymmetry promotes the gain in base pressure recovery.

Effect on the recirculation bubble and wake topology

The length of the recirculation bubble, demarcated by the maximum streamwise distance between the base and the profile of zero streamwise mean velocity, also exhibits a slight change due to suppressing boundary layer separations. These changes are summarised in table 6.2 for different forcing configurations. An increase of 3% in the bubble length is indicated for case-1, where the underbody flow remains undisturbed. The bubble length decreases by 5% for case-2, where

suction and blowing are applied on the top and bottom body surfaces, respectively, disturbing the underbody flow. When suction is applied on the top and the bottom surfaces, the bubble length remains similar to the unforced flow. In case-3, where boundary layer separations are fully suppressed on all longitudinal surfaces with a disturbed underbody flow, the bubble length remains similar to the unforced flow case. Bubble length is related to the curvature of the shear layer, as a longer bubble is associated with small curvature, which affects the shear layer's stability.

The associated effect of upstream suction/blowing on the mean wake topology is further discussed. Figures 6.15 and 6.16 depict the top and side views of the separation bubbles, respectively, superimposed with mid-plane streamlines. The associated toroidal vortex, occupying the near-wake region, is also shown for each case. Figures 6.15a and 6.15b show conditional averages of the asymmetric wake corresponding to $\partial C_P/\partial z < 0$ and $\partial C_P/\partial z > 0$, respectively, in the absence of suction. For each asymmetric state, the centre of the wake is tilted towards one side, and the toroidal vortex is skewed towards the base on the opposite side. In the presence of suction, the time-averaged wake is horizontally-symmetric for all the cases, as shown in figure 6.15. The streamwise location of the toroidal vortex influences the base pressure recovery (Ahmed and Morgans, 2022). Comparing the toroidal vortices in the three cases, it can be seen that case-1 has the farthest toroidal vortex-to-base distance with the highest base pressure recovery (14%) of the four cases, as discussed in section 6.4.3. In case-2, the toroidal vortex is the closest to the base with a negative gain in the base pressure recovery, i.e. the base pressure increased compared to the unforced case. The toroidal vortex in case-2-II is closer to the base than in case-1, which reduces the base pressure recovery to 2%. For case-3, the toroidal vortex resides at a mid-streamwise position compared to case-1 and case-2, with a moderate base pressure recovery of 7%.

The side view, shown in figure 6.16, depicts the time-averaged vertical location of the wake. In the absence of suction/blowing, it can be seen that the wake resides towards the ground for both asymmetric positions, as shown in figures 6.16a and 6.16b, where a downwash flow dominates the wake. Similarly, the wake of case-1 is tilted slightly towards the ground, as shown in figure 6.16c. In both case-2, case-2-II and case-3, the wake moves away from the ground following the reflected vertical asymmetry caused by the upwash flow, as shown in figures 6.16d, 6.16e and 6.16f. The toroidal vortices of case-2-II and case-3 have slightly tilted away from the base on the top side, following the reflected weak vertical asymmetry. For case-2, the recirculation region is mainly formed by the bottom shear layer. The weak sub-recirculation region formed by the top shear layer is convected further downstream forming another bubble in the far wake region.

To conclude, suppressing the separation of the boundary layer on the different surfaces of the body was found to have a little effect on the bubble length. These results correlate with the experimental results by Hsu et al. (2021), which proposed a linear relationship between the

bubble length and the base pressure recovery. The relatively longer bubble was found to have a favourable effect on base pressure recovery. Similarly, in case-1, the longer bubble is associated with higher pressure recovery. Reducing the bubble length is associated with a loss in base pressure recovery, as in case-2. It is worth noting that the pressure recovery here is also affected by the wake configurations and the underbody flow, as in case-3, base pressure recovery is achieved with a negligible change in the bubble length.

Different forcing configurations also affect the wake topology differently. When the weak vertical asymmetry holds, the bubble shape remains similar to the unforced, and the toroidal vortex's position and orientation in the near wake region changes. This affects the base pressure and the accordingly drag. For a static vertical asymmetric wake, considerable changes were seen in the topology, as in case-2. Two separate separation bubbles were seen in the wake with irregular shapes compared to the unforced case. The toroidal vortex's position is changed in streamwise and cross-flow directions. This is found to have an unfavourable effect on the base pressure, confirming the importance of preserving the weak-vertical asymmetry for drag reduction.

Effect on shear layers growth in the wake

The effect of suppressing boundary layer separations on the downstream shear layer mean thickness and growth rate in the wake is investigated. These can be characterised using the vorticity thickness, $\delta_{\omega,n}$, defined as the ratio of the maximum velocity difference to the maximum mean shear stress, i.e. $\delta_{\omega,n} = \Delta U_{\max}/|\partial U/\partial n_{\max}|$, where $n \in [y, z]$ (Djilali and Gartshore, 1991). The numerator represents the difference between the maximum local velocity at the centre of the shear layer bounding the separation bubble and the minimum velocity on the low-speed side of the shear layer, i.e., in the separation bubble. The centre of the shear layer is determined based on the maximum fluctuating velocity profile (Djilali and Gartshore, 1991). The visual thickness of the shear layer is double the vorticity thickness $\delta_{\omega,n}$. The slope of the vorticity thickness $d\delta_{\omega,n}/dx$ is used to measure the spread or growth rate of the shear layer in the streamwise direction.

As shown in figure 6.23a, for the unforced flow, the separated wake shear layers initially grow linearly (with different growth rates) in the wake, matching the growth reported by Kang et al. (2021) for the wake of an Ahmed body. The linear growth is similar to that of a free shear layer, with Bres and Colonius (2008) showing that the presence of a recirculation bubble changes the flow entrainment and, accordingly, the shear layer thickness and growth rate. From the gradient of the data in figure 6.23a, it can be seen that the growth rate of the top shear layer varies in the streamwise direction, with a value of 0.38 in the near wake region ($x/H < 1.1$) and 0.20 for $1.1 \leq x/H \leq 1.43$. The near-wake values are similar to those of the shear layer separated from a wall-mounted block (Agelinchaab and Tachie, 2008). Downstream of the recirculation region

(marked by the black dashed line in figure 6.23a), the top shear layer exhibits rapid linear growth with a relatively higher rate due to the suppression of the maximum shear stresses.

Figure 6.23b compares the vorticity thickness of the top shear layer for the unforced flow and for case-3, where the separation of the top-surface boundary layer is suppressed. For case-3, the top-surface shear layer is thinner in the near wake region ($x/L < 1$), but its growth rate higher by 14%. The top-surface shear layers have similar thicknesses for $0.9 < x/L < 1.2$, with the growth rate for case-3 then rapidly increasing towards the end of the recirculation bubble, leading to a thicker shear layer than the unforced flow.

Figure 6.24a compares the shear layer thickness on the two sides for case-3. The upstream side suction has an identical effect on both side shear layers in the wake. Similarly, an identical suction effect on the side surfaces is seen in case-1 (not shown for brevity). Figure 6.24b compares the shear layer on side 1 for case-3 to its counterpart in the unforced flow, showing a negligible difference. This is consistent with the large wake oscillations for both cases, with similar associated shear layer curvatures.

As suction has a similar effect on both sides, we proceed with comparing side 1 only for brevity. Figure 6.24c shows the shear layer thicknesses on side 1 for all the cases. Case-1 exhibits a much thicker shear layer than case-3 (similar to the unforced case), with the thickness almost double for $0.6 < x/L < 1.48$. The shear layer exhibits linear growth with larger growth rates than case-3. Shear layer thickness correlates with the width of the recirculation bubble, as a thinner shear layer on the sides could be associated with a relatively larger width of the wake. The latter is known to have a favourable effect on base pressure recovery Barros et al. (2016). The relatively thicker side shear layers promote base pressure recovery in case-1. For case-2, where upstream dynamics are not suppressed on the sides, and the wake exhibits static vertical asymmetry, the shear layer thickness is almost similar to case-1. A difference in the thickness is seen for $x/L > 0.6$. For case-2-II, there is no upstream suction on the sides. In the near wake region, up to $x/L = 0.9$, the side shear layers exhibit a negligible change in thickness profile compared to case-3 or the unforced flow. Further downstream, a slight reduction in the shear layer thickness can be seen compared to case-3.

We conclude that a given wake shear layer thickness is affected by the dynamics of the corresponding upstream boundary layer and the interaction with the adjacent shear layers. Generally, suppressing the dynamics of the upstream boundary layer only leads to a thicker wake shear layer when the adjacent perpendicular shear layers remain unaffected, as in case-1. The underbody flow is important; disturbing, this has an indirect effect on wake shear layer thickness. When it has sufficient perturbations to push the wake away from the weak vertical asymmetry region, the side shear layer thickens (case-2). Where underbody flow changes are insufficient to push the wake

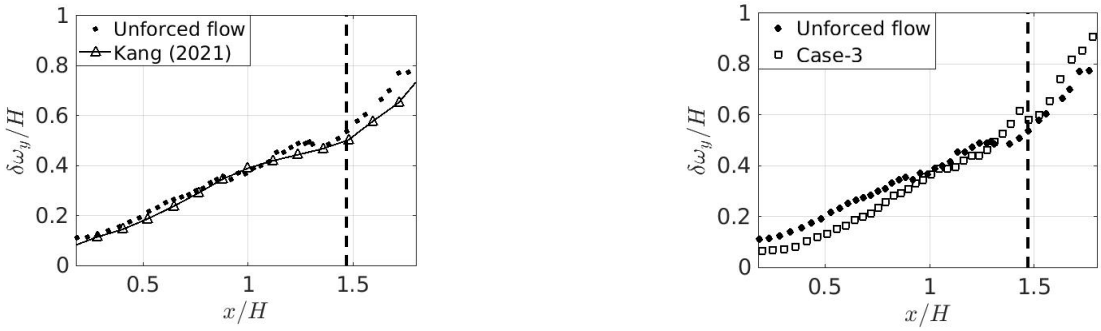

(a) (b)

Figure 6.23: Vorticity thickness on the top-shear layer for the base flow, where the boundary layer separates, compared to data from Kang et al. (2021) (a). The effect of suppressing the upstream boundary layer separation on the top-surface shear layer in the wake of case-3 (b). The black dashed line marks the length of the recirculation region. Note that x is measured from the body base here.

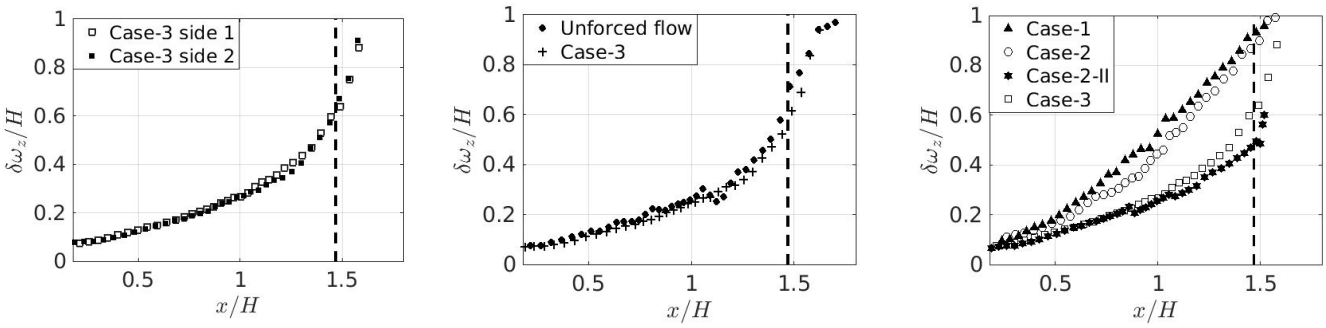

(a) (b) (c)

Figure 6.24: Comparison of vorticity thickness on the side shear layers for case-3 (a). Comparison of the side shear layer thickness between the unforced flow and the side for case-3 (b), between side-1 for case-1, case-2, case-2-II and case-3 (c). The black dashed vertical line marks the length of the base flow recirculation region. Note that x is measured from the body base here.

away from the weak vertical asymmetry region (as will be shown in section 6.4.4), the side shear layer thickness exhibits a slight change in both the presence and the absence of boundary layer separations on the sides, as seen in both case-2-II and case-3. This confirms the complex interaction of all the parameters considered in this analysis.

6.4.4 Effect on the underbody flow

It is known that the momentum flux and disturbances of the underbody flow are important parameters in determining the wake configuration. Grandemange et al. (2013a) and Barros et al. (2017) showed that the underbody momentum influences the vertical balance of the wake. A moderate reduction in the underbody momentum inverts the vertical position of the wake, but its vertical asymmetry remains weak. For a relatively more considerable reduction in the underbody momentum, the wake asymmetry becomes more pronounced such that it can no longer be considered weak, and the wake becomes static, without horizontal switching (Barros et al., 2017). However,

the required change in underbody momentum for the wake to reverse its weak vertical asymmetry or to exhibit strong vertical asymmetry (with bi-modality inhibited) remains unclear. We now consider the effect of the different upstream suction patterns on the underbody flow in the present study.

The effect of suppressing boundary layer separations on the mean underbody flow can be investigated by considering the bulk velocity (U_b) of the underbody flow, which controls the momentum flux in this region. The underbody bulk velocity is calculated by integrating the mean velocity over the cross-sectional area of the underbody region, i.e., $C \times W$. In the absence of suction on the bottom surface, the ratio of the mean bulk velocity to the free stream velocity ($\overline{U_b}/U_\infty$) is about ~ 0.88 close to the back-end of the body, similar to the value obtained by Castelain et al. (2018) for a truck geometry. The changes in the mean bulk velocity with reference to the unforced flow are summarised in table 6.2. Changes are evident for case-2, case-2-II and case-3, for which suction/blowing occurs on the bottom surface of the body.

In case-2, where suction and blowing are applied on the top and bottom body surfaces, the underbody flow's bulk velocity is reduced by 18% and, accordingly, the momentum flux. The bottom-surface boundary layer separates at $x/L = 0.34$, then reattaches at $x/L = 0.42$. The ground boundary layer remains attached along the underbody and separates later in the wake region. In this case, the reduction in the momentum flux of the underbody flow changes the wake configuration from horizontally bi-modal with weak vertical asymmetry to static vertical asymmetric wake. This is similar to the case of Kang et al. (2021), where the reduced momentum of the underbody flow due to immersing the Ahmed body in a thick boundary layer of the ground suppressed wake bi-modality. For case-2-II, in which suction is applied on both the top and bottom body surfaces, the bulk velocity of the underbody flow (and accordingly the momentum flux) is reduced by 1%. The bottom surface boundary layer remains attached while the ground boundary layer separates at $x/L \sim 0.12$ and reattaches at $x/L \sim 0.37$. Similarly, for case-3, with suction on all four surfaces, the ground boundary layer separates at around $x/L \sim 0.12$ and reattaches at $x/L \sim 0.4$, the bottom-surface boundary layer remains attached, and the deficit in the underbody bulk velocity is 3%. The difference between the bulk velocity deficits for case-2 and case-3 suggests that the side boundary layer separations (present for case-2-II but suppressed for case-3) augment underbody disturbances and limit the momentum reduction. For both cases, the wake exhibits a reflected vertical asymmetry, which remains weak, consistent with the link to underbody momentum reduction identified in the literature. We note that for case-3, horizontal bi-modality is suppressed with quite large oscillation bounds, while for case-2, the wake bi-modality persists.

The rest of this section is focused on investigating the underbody disturbances across the

different cases, building on our earlier observation in Section 6.3 that vortices interacting between the different surfaces affect the underbody flow. The disturbances induced in the underbody region can be seen by comparing the turbulent kinetic energy ($0.5 \times (\overline{u'^2} + \overline{v'^2} + \overline{w'^2})$, where u', v', w' are the fluctuating velocity components in the x, y, z directions, respectively) for the different cases. Figure 6.25 compares the area-averaged turbulent kinetic energy, $< TKE >$, at different sections ($C \times W$) along the underbody region for the unforced flow and the different forcing cases. For the unforced flow, the turbulent kinetic energy increases gradually along the underbody, following the development of the boundary layers on the bottom surface and the ground. For case-1, the turbulent kinetic energy exhibits a slight increase around $x/L \sim 0.35$ compared to the unforced flow and decreases for $x/L > 0.8$. This difference is likely linked to the suppression of the side vortices. At the base, the area-averaged turbulent kinetic energy for case-1 is 34% less than for the unforced flow. Its contours are horizontally symmetric, as shown in figure 6.26b, this being attributable to the suppression of the side boundary layer disturbances. For case-2, case-2-II and case-3, where the underbody flow is affected by bottom surface suction/blowing, the turbulent kinetic energy increases by order of magnitude downstream of the slits. It peaks at $x/L = 0.35$, $x/L = 0.23$ and $x/L = 0.2$ for case-2, case-2-II and case-3, respectively, then decays towards the base for all cases due to dissipation. This could be attributable to the separation of the ground boundary layer that occurs in case-2-II and case-3 and the separation of the bottom surface boundary layer in case-2.

Comparing the $< TKE >$ for case-2 and case-2-II, it can be seen that blowing induces higher TKE in the underbody region compared to suction. The area-averaged turbulent kinetic energy at the base is increased by 100% for case-2 where blowing is applied and 18% for case-2-II when suction is applied on the bottom surface. For the former, the bottom-surface boundary layer separates and exhibits higher turbulent kinetic energy than the ground boundary layer. The opposite occurs in the latter case, where suction mainly disturbs the ground boundary layer with no evidence of separation based on mean streamwise velocity. These different effects can be seen in figure 6.27, which compares the turbulent kinetic energy for all cases at a mid-plane in the spanwise direction (z =0). Differences between case-2-II and case-3 must be linked to the effect of suppressing boundary layer separations on the side surfaces. Compared to the unforced flow, the area-averaged turbulent kinetic energy at the base is 4% lower for case-3.

The base $< TKE >$ is reduced compared to the unforced flow for both case-1 and case-3 and appears to be linked to the suppression of the side boundary layer separations. The reduction in base $< TKE >$ for case-1 is an order of magnitude larger than for case-3, suggesting that for case-3 (which has suction on all four surfaces), the reduction in base $< TKE >$ due to suppressing the side disturbances is to some degree compensated by the disturbances induced by the bottom suction. Figure 6.26 shows an approximately horizontally-symmetric base profile for case-3, with

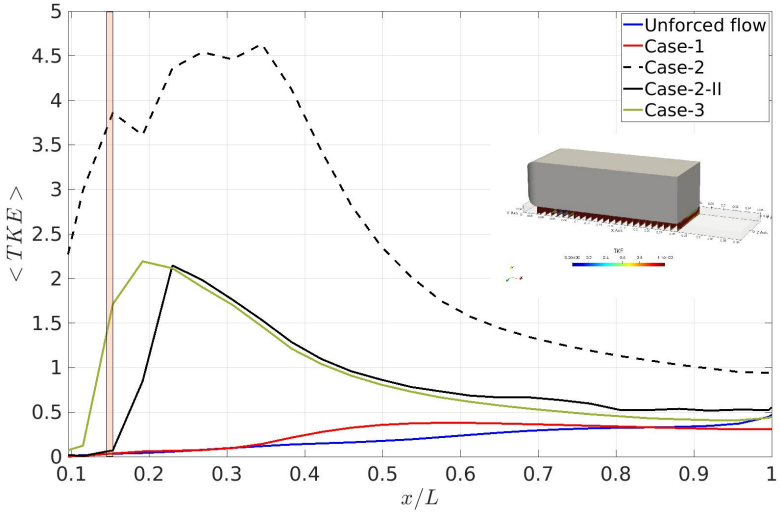

Figure 6.25: Area-averaged turbulent kinetic energy at different sections ($C \times W$) of the underbody in the streawise direction for the unforced flow (blue), case-1 (red), case-2 (dashed black), case-2-II (black) and case-3 (green). The inset shows the cross-sections used to generate the graph. The light red rectangular shows the location of the suction/blowing slit.

higher turbulent kinetic energy in the boundary layers and at mid-height of the gap, showing where the vortical structures are residing. In case-2, slight asymmetry of the turbulent kinetic energy on the base can be seen due to the effect of the side disturbances.

To conclude, these results show that in the absence of bottom suction, the underbody flow is disturbed indirectly by the boundary layer separations on the sides, confirming the proposed interaction of the vortices from the top and the side surfaces, discussed in section 6.3. Suppressing the side separations, as in case-1, is seen to reduce the turbulent kinetic energy of the underbody region at the base. Applying suction through the bottom surface imposes direct disturbances in the underbody flow, indicated by the flow's relatively higher turbulent kinetic energy beneath the base, as seen in case-2; applying blowing increases the turbulent kinetic energy more. Suppressing boundary layer separations on the sides reduces the disturbances introduced due to bottom suction, leading to a slight reduction of the underbody turbulent kinetic energy at the base, as in case-3. These results correlate with the experimental study by Barros et al. (2017), where the underbody flow is disturbed passively with different devices. The change in the turbulent kinetic energy of the underbody flow is expected to affect the entrainment of the shear layer separated from the bottom surface of the body, which accordingly affects the wake dynamics.

To the author's knowledge, no previous studies were done on controlling the wake bi-modality using active control of the underbody flow. These results present an initial step of suppressing wake bi-modality with a new control strategy.

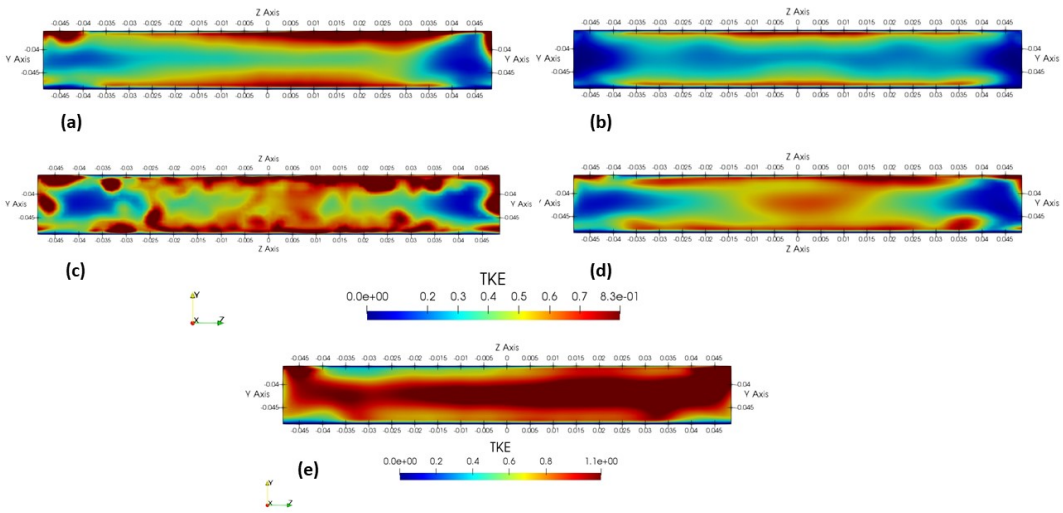

Figure 6.26: Contours of turbulent kinetic energy of the underbody at the base ($x/L = 1$) for the unforced flow case (a), case-1 (b), case-2-II (c) and case-3 (d) and case-2 (e).

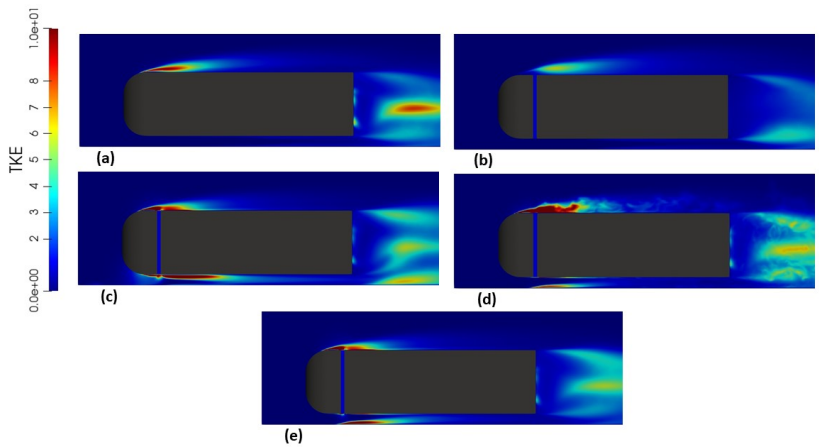

Figure 6.27: Turbulent kinetic energy on an xy plane at $z = 0$ for the unforced flow case (a), case-1 (b), case-2 (c), case-2-II (d) and case-3 (e). The picture shows the sections used to generate the plot. The red box marks the position of the actuator.

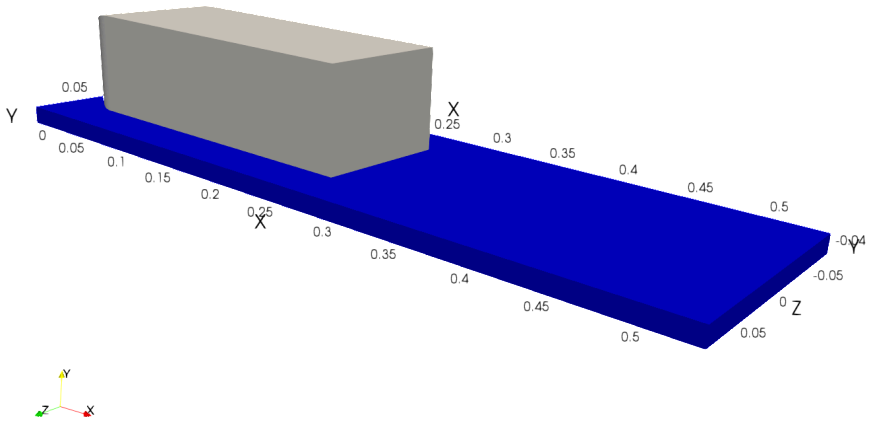

Figure 6.28: The blue box shows the underbody region used to investigate the underflow, with a height similar the gap height C^*, streamwise length of $-0.1 \leq x/L \leq 2.0$, spanwise length of $-1.0 \leq z/W \leq 1.0$, measured from the center fore-end of the body.

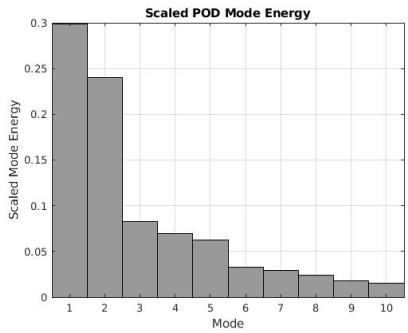

Figure 6.29: Energy content of the ten first most energetic modes for the underflow in absence of suction/blowing.

6.4.5 POD of the underbody flow

Based on the pressure data, three-dimensional Proper Orthogonal Decomposition (POD) has been used to analyse the effect of boundary layer separations on the underbody flow. The region considered for the POD analysis is extended from $x/L = -0.1$ upstream of the body to $x/L = 2.0$ in the wake region as indicated in figure 6.28. The height of the box bounding this region is similar to the gap between the body and the ground. In the spanwise direction, the box is extended from $z/W = -1.0$ to $z/W = 1.0$ measured from the centre of the body's fore-end. The spatial resolution in this region is equivalent to the simulation mesh reduced by $1:20$. The sampling time used for the POD is equivalent to $St_W \sim 13.9$, meaning that the highest frequency that could be captured is equivalent to $St_W \sim 7$. This value is high enough based on the reported frequencies in the literature for the wake of the square-back Ahmed body. The total acquisition time was ~ 1000 convective time units, deemed sufficient for statistical convergence.

The energy content of the first ten modes for the unforced flow is shown in figure 6.29. The results show that the underbody flow is dominated by two modes, which appear in pairs, indicating

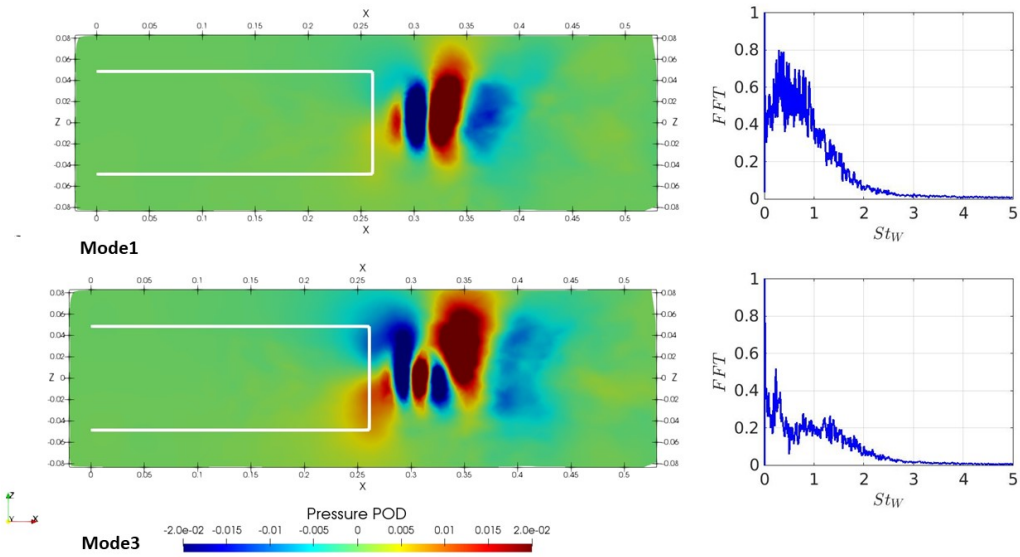

Figure 6.30: First (top) and third (bottom) POD modes for the base flow case. The associated Fast Fourier Transform (FFT) of their time coefficients are shown on the right hand side.

their convective nature. Mode1 and mode2, with an energy content of 54% together, indicate a symmetric mode in the wake, as shown in figure 6.30 (only mode1 is shown for brevity). The FFT of the time coefficient of both modes contains two peak frequencies. The first frequency is equivalent to $St_W \sim 0.005$, which is linked to the bi-modal behaviour of the wake. The second frequency is two orders of magnitude higher with a value of $St_W \sim 0.35$. This frequency is expected to be related to the bottom shear layer dynamics, as it corresponds to higher mode values along the recirculation bubble in the wake. The wake is dominated by the downwash flow from the top-shear layer, as shown with the streamlines in figure 6.16. Thus the bottom shear layer is triggered by the top shear layer, supporting the suggested link of mode1 and mode2 to the bottom shear layer. Further, the frequency associated with this mode, $St_W \sim 0.35$, is equivalent to $St_H \sim 0.25$ based on the distance between the top and bottom shear layers, which is a typical frequency reported for the Karman vortex shedding in the literature.

The next two modes, i.e. mode3 and mode4, are also similar, with mode3 shown in figure 6.30. They showed a combination of a symmetric mode with a similar frequency to mode1 and mode2 and an asymmetric mode on the top part of the graph. The latter is related to the horizontal asymmetry of the wake, leading to asymmetric vortex shedding at a frequency of $St_W \sim 0.23$. The broad frequency band around $St_W \sim 1.2$, shown by the FFT of these modes, is related to the high-frequency dynamics relevant to the bottom shear layer, which be further discussed in the next chapter.

Reconstructing the flow field with the first five most energetic modes showed the link between the wake bi-modality and the disturbances in the underbody flow. Figure 6.31 shows the time his-

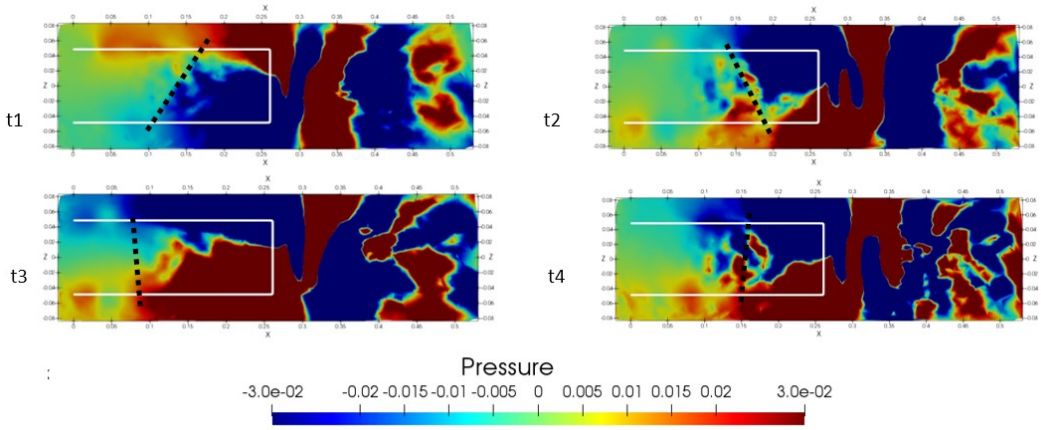

Figure 6.31: Reconstructed fluctuating pressure in the underbody region using the five most energetic modes.

tory of the reconstructed fluctuated pressure. It can be seen that the disturbances of the underflow spanned in the horizontal direction in an asymmetric distribution following the wake instantaneous orientation. To this end, it is unclear whether this link between underbody asymmetry disturbances and wake bi-modality is a cause or effect.

For case-1, where suction is applied on the side body surfaces, and the underbody remains undisturbed, POD modes' energy is shown in figure 6.32a. Similar to the base flow case, the first most energetic modes contain around $\sim 50\%$ of the total flow energy in the underbody region. The modes appear in pairs, indicating their convective nature. Mode1 and mode3, which are similar to mode2 and mode4, respectively, are shown in figure 6.33. Mode1 shows a symmetric mode in the wake region, associated with a frequency of $St_W = 0.24$. Mode3 also indicates a symmetric mode, with two associated frequencies of $St_W = 0.24$ and a broad frequency band around $St_W = 1.3$. Both modes match with the corresponding modes in the unforced flow case, with the asymmetry seen in figure 6.30 being symmetrised in this case (figure 6.33), which is linked to bi-modality suppression. The very low frequency linked to wake switching is not captured in this case.

The modes' energy of the underbody region for case-2 is shown in figure 6.32b. It indicates that the first two modes are less energetic in this case compared to the unforced flow and case-1, with an energy content of $\sim 30\%$ for both. Figure 6.34 shows mode1 and mode3 for case-2 and their associated frequencies. Mode2 and mode4 are similar to mode1 and mode3, respectively, indicating their convective nature. Mode1 is dominated by the effect of blowing in the underbody region. Blowing forces the boundary layer to amplify the high-frequency dynamics downstream of the slit. These high-frequency dynamics, associated with a $St_W \sim 3$, extend to the body sides, triggering the shedding of the corner vortices as discussed. This is also shown in mode3, which carries around $\sim 16\%$ of the energy together with mode4. Additionally, mode3 shows a spatially-asymmetric mode in the wake at a frequency of $St_W \sim 0.27$. This is suggested to be linked to the

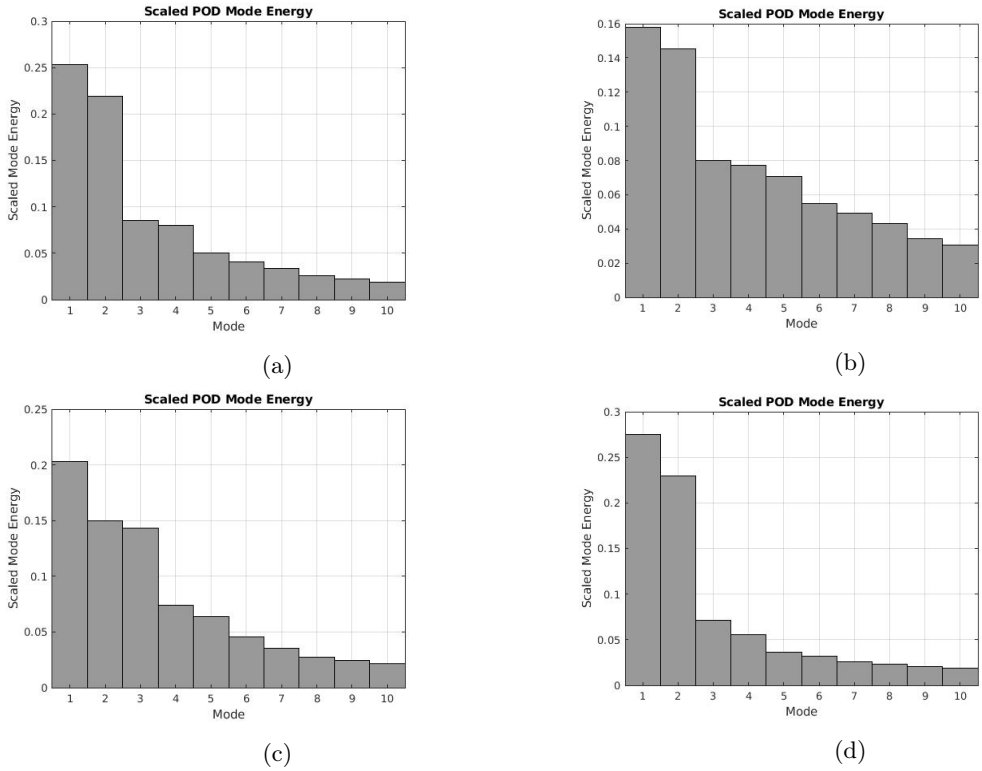

Figure 6.32: Scaled modal energies of the first ten most energetic modes of the underbody flow for case-1 (a), case-2 (b), case-2-II (c) and case-3 (d).

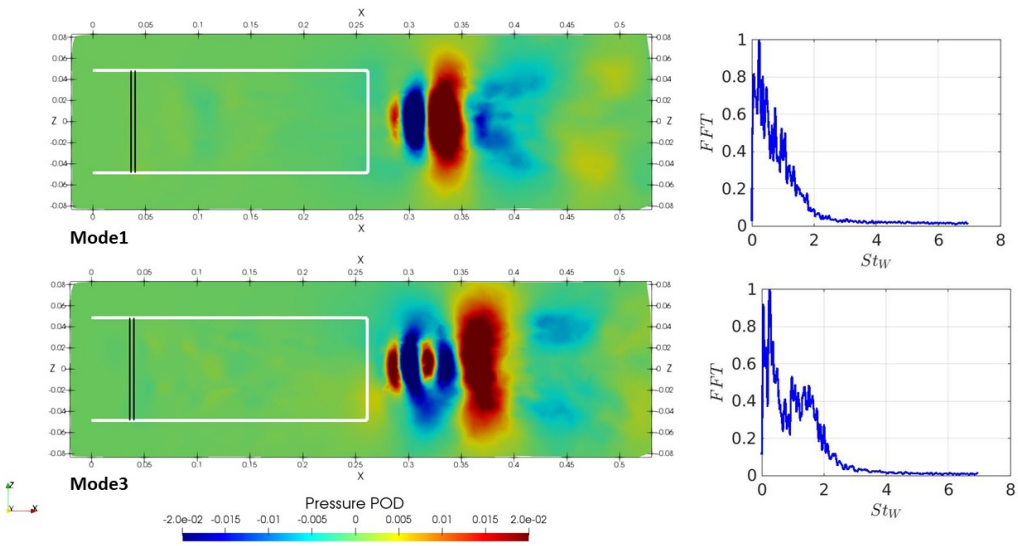

Figure 6.33: First (top) and third (bottom) POD modes for the case-1. The associated Fast Fourier Transform (FFT) of their time coefficients are shown on the right hand side.

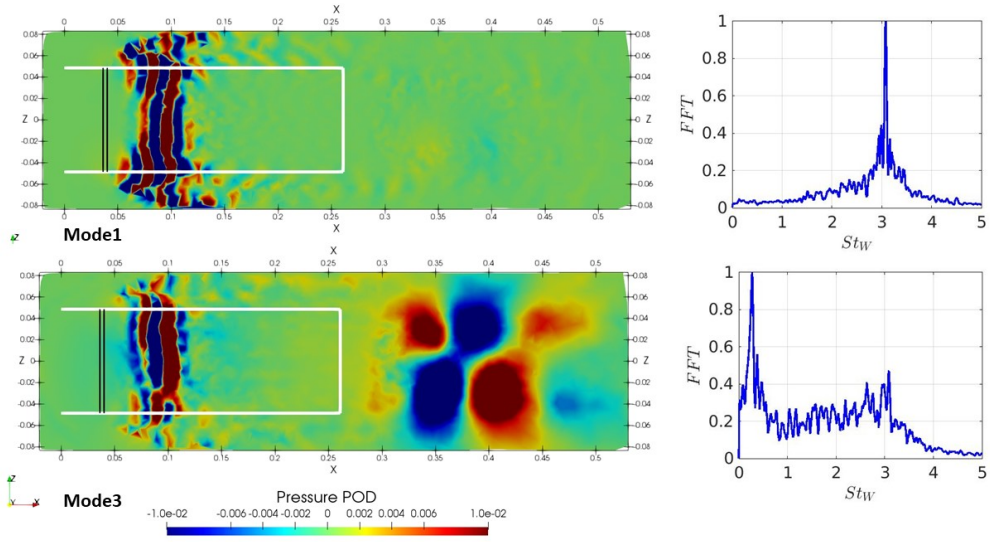

Figure 6.34: First (top) and third (bottom) POD modes for the case-2. The associated Fast Fourier Transform (FFT) of their time coefficients are shown on the right hand side.

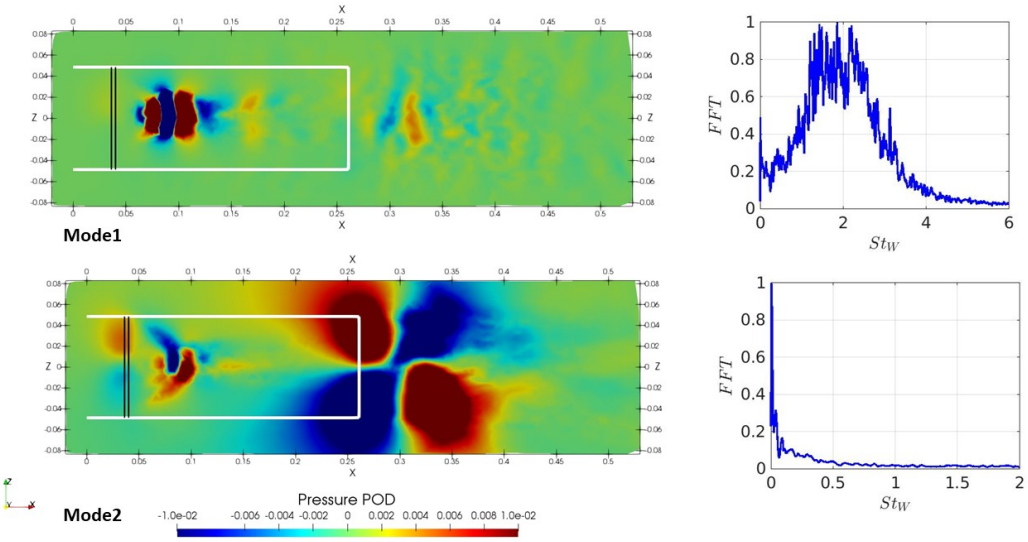

Figure 6.35: First (top) and second (bottom) POD modes for the case-2-II. The associated Fast Fourier Transform (FFT) of their time coefficients are shown on the right hand side.

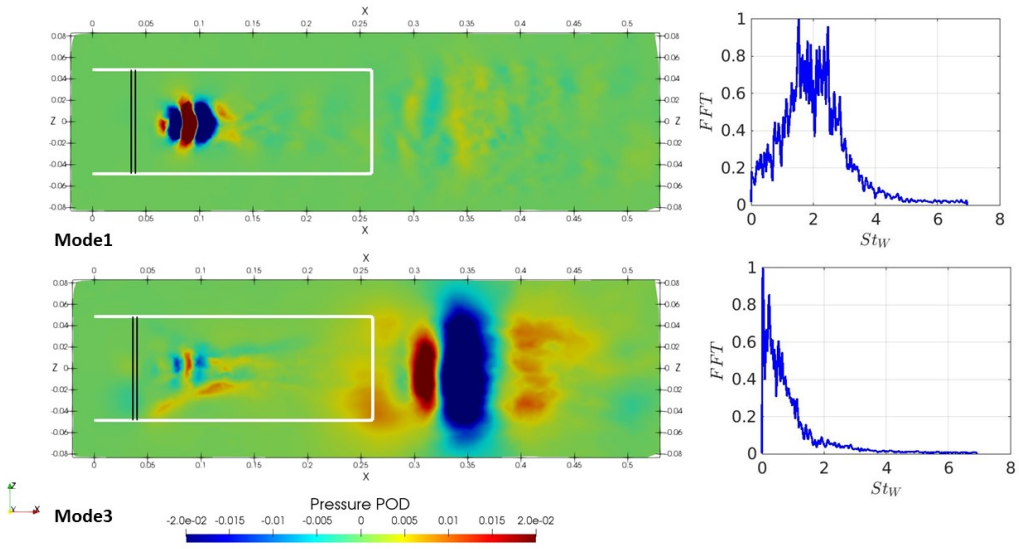

Figure 6.36: First (top) and third (bottom) POD modes for the case-3 (upstream8). The associated Fast Fourier Transform (FFT) of their time coefficients are shown on the right hand side.

interaction of the rolled top-shear layer (causing the bulge shown in figure 6.19) and the separated ground boundary layer in the wake, shown in figure 6.17.

For case-2-II, the modes' energy of the underbody region is shown in figure 6.32c. It indicates that the first most energetic two modes carry 35% of the flow energy. The first mode, mode-1 in figure 6.35, indicates a high-frequency spatially-symmetric mode linked to boundary layer separation on the ground downstream of the suction slit. Mode-2, which is less energetic, shows low-frequency dynamics in the wake, related to wake bi-modality. It also shows low-frequency dynamics related to ground boundary layer separation upstream of the wake.

In case-3, the most energetic first two modes carry 50% of the flow energy, as shown in figure 6.32d. Mode1 is shown in figure 6.36, indicating the effect of suction in the underbody region and similarly, mode2, which is not shown for brevity. Compared to case-2, where blowing is applied through the bottom surface, suction has a limited effect that concentrates near the centre of the bottom surface. Similar to blowing (case-2), suction forces the boundary layer to amplify higher frequency dynamics, which is associated with a $St_W \sim 2$. Mode3 (and mode4) indicate a symmetric mode in the wake associated with $St_W \sim 0.24$, which is similar to case-1.

In conclusion, the pressure POD of the underbody flow shows that disturbing this region with either blowing (case-2) or suction (case-2-II and case-3) promotes high-frequency dynamics downstream of the slits. These disturbances have a stronger effect that extends to the body's sides in case of blowing (case-2) compared to suction (case-3). When air is blown through the bottom surface, a more pronounced effect is noticed in the wake region in case-2 compared to case-3. When the underbody flow is not directly disturbed, as in case-1, reduced disturbances in the underbody

flow are seen towards the body base. This could be linked to the suppression of wake bi-modality and supports the reduction in the turbulent kinetic energy at the base for case-1.

6.5 Conclusion

This section investigated the link between the upstream dynamics – related to boundary layer separations – and bi-modality in the turbulent wake of the square-back Ahmed body in close proximity to the ground. We propose that wake bi-modal switching is triggered by the interaction of the vortices formed on the top and side surfaces of the body, which also affects the underbody flow. Interrupting this interaction suppresses bi-modality and symmetries the wake.

Steady and spatially-independent suction/blowing was used to suppress boundary layer separations on the longitudinal body surfaces. Different cases with suction/blowing on different combinations of body surfaces were investigated. When boundary layer separation is suppressed on only the wall-normal surfaces (side surfaces), the wake becomes horizontally symmetric while retaining its vertical position. In this case, suppressing the side boundary layer disturbances was found to have a direct effect on the disturbances of the free shear layers separated off the side surfaces in the wake region. It also has an indirect favourable effect on the turbulent fluctuations in the underbody flow. These results support the proposed mechanism of the link between wake bi-modality and vortices interaction. This represents a new promising strategy for controlling wake bi-modality indirectly, i.e., without directly forcing the wake.

The wake exhibits bi-modal switching for a weak vertical asymmetry. Bi-modality fades when the latter is disturbed due to the competition between the horizontal and vertical base pressure gradients. In this case, the wake is considered a static vertical asymmetric wake. When suction is applied on the wall-parallel surfaces (top-bottom), suppressing the boundary layer separation on the top surface and disturbing the underbody flow, bi-modality remains, accompanied by an inversion of vertical wake asymmetry.

When suction is applied on all four longitudinal surfaces of the body, suppressing the separation of the boundary layer on the top and side surfaces and disturbing the underbody flow, horizontal bi-modality is suppressed, with the wake exhibiting larger oscillation bounds compared to the side-only suction. The study has shown that the disturbances induced in the underbody flow become partly cancelled close to the base by the compensating effect of suppressing the side boundary layer disturbances. The wake is weakly asymmetric in the vertical direction, with the asymmetry inverted compared to the unforced flow. This suggests that bi-modality suppression is due to suppression of the side boundary layer disturbances, similar to side-only suction. Although upstream boundary layer separations is a Re dependent phenomenon, the current study shows that suppressing the

flow fluctuations prior to the base has prominent effect of wake bi-modality. These results represent a first step towards investigating upstream control strategies for bi-modality suppression. Such an approach offers promise for achieving drag reduction as well as bi-modality suppression, something that actuating the wake directly has been unable to fully achieve, especially when wake actuation affects the free shear layers.

Chapter 7

3D modal reduction of the Ahmed body flow field

In this chapter, the three-dimensional modal reduction will be used to investigate the upstream dynamics and the wake downstream of the square-back Ahmed body. Spectral Proper Orthogonal Decomposition (SPOD) will be considered here, as it allows exploring dynamic modes that occur at multiple frequencies and energy levels. It combines both the energy-ranked approach, i.e. the classical Proper Orthogonal Decomposition (POD) and the frequency-ranked Fourier decomposition, i.e. Dynamic Mode Decomposition (DMD). Initially, the 3D SPOD of the unforced flow will be explored to give an insight into the dynamical modes in the wake. Then the effect of the different arrangements of suction/blowing –used to suppress the boundary layer dynamics– will further be explored and compared to the unforced flow results. The chapter is subdivided into five subsections covering the five cases introduced in the previous chapter, the unforced flow, cases 1, 2, 2-II and case-3.

7.1 Unforced flow

Spectral Proper Orthogonal Decomposition (SPOD) is used to analyse the turbulent wake behind the Ahmed body. Pressure data in the domain shown in figure 7.1 is used for this analysis. The domain extends from $x/L = -0.1$ upstream of the body to $x/L = 2.0$ in the wake region. In the vertical direction, the domain is bounded by the ground and a horizontal surface at $y/H = 0.83$. It extends from $z/W = -1.0$ to $z/W = 1.0$ measured from the centre of the body's fore-end in the spanwise direction. The domain size in the cross-flow directions is chosen based on boundary layer thicknesses. In the streamwise direction, the domain length extends into the far-wake region. Similar to the spatial resolution used in the 3D-POD of the underbody region, the spatial resolution

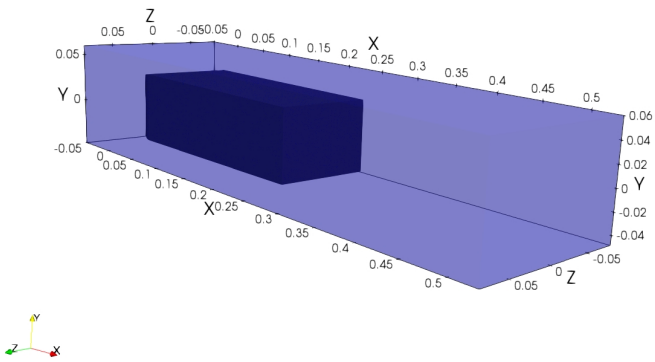

Figure 7.1: The blue box shows the three dimensional region used for the SPOD analysis, with a max height of $y/H = 0.83$, streamwise length of $-0.1 \leq x/L \leq 2.0$, spanwise length of $-1.0 \leq z/W \leq 1.0$, measured from the center fore-end of the body.

used here is equivalent to the simulation mesh reduced by a factor of 20 in all three directions. Data points are clustered near the boundary layers and wake region matching the refined regions of the mesh described earlier.

The estimation parameters for SPOD depends on the maximum and minimum frequencies to be resolved in this domain. The sampling frequency is chosen to be $f_s = 1000\ Hz$ equivalent to $St_W \sim 13.9$. This limits the maximum (Nyquist) resolvable frequency to be $St_W \sim 7$, which is relatively more than double the maximum frequency reported in the regions upstream and downstream of the Ahmed body (Hesse and Morgans, 2021). In SPOD, the time history of the data is subdivided into blocks before calculating the discrete Fourier transform. The minimum non-zero resolvable frequency is governed by the time period of each block of data, i.e. minimum resolvable frequncy equals f_s/N_{FFT}, where N_{FFT} is the number of time-steps per each block of data (Schmidt and Colonius, 2020). N_{FFT} is chosen to be 2048, such that the minimum resolvable frequency is equivalent to $St_W \sim 0.005$. The minimum frequency reported in the turbulent wake of the Ahmed body is related to the bubble pumping mode. This mode is marked by a broadband frequencies around $St_W \sim 0.07$. Although wake bi-modality is characterised as a stochastic behaviour, a relatively low frequency one order of magnitude less than the bubble pumping frequency is reported in association with this behaviour (Ahmed and Morgans, 2022). This makes the number of time steps per block sufficient for the SPOD analysis. In order to avoid any bias caused by the choice of the N_{FFT}, the number of blocks is increased by subdividing the data into overlapping blocks. A typical value of this overlap is 50% of the block size (Schmidt and Colonius, 2020), which is applied in this case. A Hamming window was used to reduce spectral leakage.

The total acquisition time was $\sim$ 1400 convective time units, which were deemed sufficient for statistical convergence based on the energy content of mode-1 at a frequency equivalent to $St_W \sim 2.8$. During this acquisition time, the wake spent approximately equal periods in both

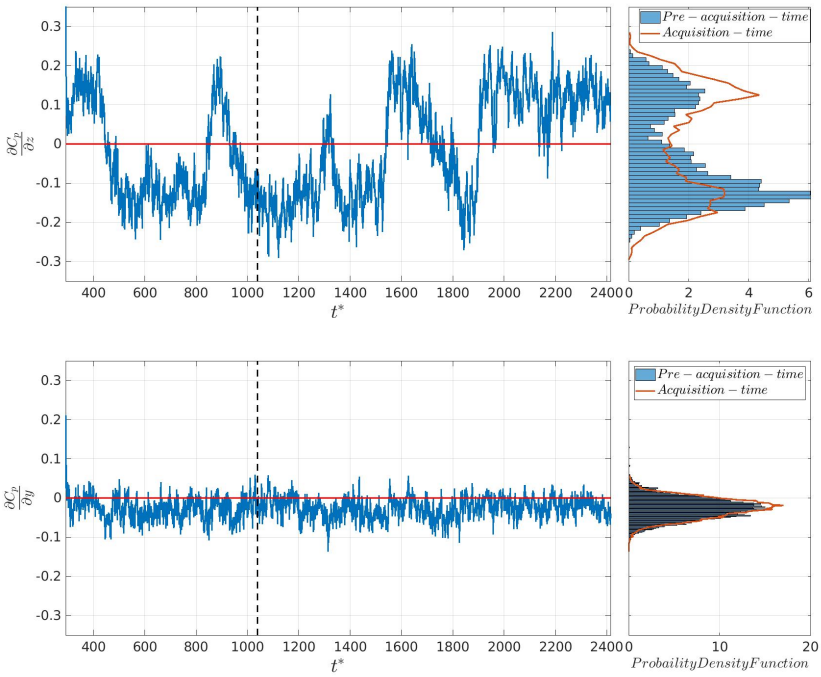

Figure 7.2: Wake horizontal and vertical positions characterised by $\partial C_P/\partial z$ (top) and $\partial C_P/\partial y$ (bottom), respectively. Data acquisition for SPOD started at $t^* = 1040$ and ended at $t^* = 2400$. The associated probability density function of the acquisition period is shown with the orange line.

asymmetric positions in the spanwise (horizontal) direction. The wake switched three times in the horizontal direction. Figure 7.2 shows the time history of the horizontal position of the wake determined by the horizontal gradient of the pressure coefficient $\partial C_P/\partial z$. The start of the data acquisition is marked by the black dashed line and lasts to the end. The probability density function of the data used for the SPOD analysis is shown with the orange line in figure 7.2, indicating the approximately equal residence time of the wake on each side.

The results of the SPOD for the unforced case are shown in figure 7.3 and indicate frequency peaks at $St_W = 0.19$ and 2.8. These frequencies are associated with the vortex shedding and the dynamics of boundary layer separations upstream of the wake, respectively. A broad frequency band around $St_W \sim 0.074$ is likely to represent the dynamics of the bubble pumping. The highest energy content in mode-1 and mode-2 is found to be associated with the lowest frequency $St_W \sim 0.006$. All frequencies were captured in both the first and second modes, as shown in figure 7.3.

The following paragraphs will further investigate the modes associated with these peak frequencies. The scaled mode's energy at the lowest frequency equivalent to $St_W \sim 0.006$ is shown in figure 7.4a. Mode-1 carries more than 90% of the flow energy at this frequency, which is related to the wake switching. A three-dimensional view of the pressure fluctuations iso-volumes for mode-1 at $St_W = 0.006$ is shown in figure 7.5. It is clear that this mode is horizontally-asymmetric, which

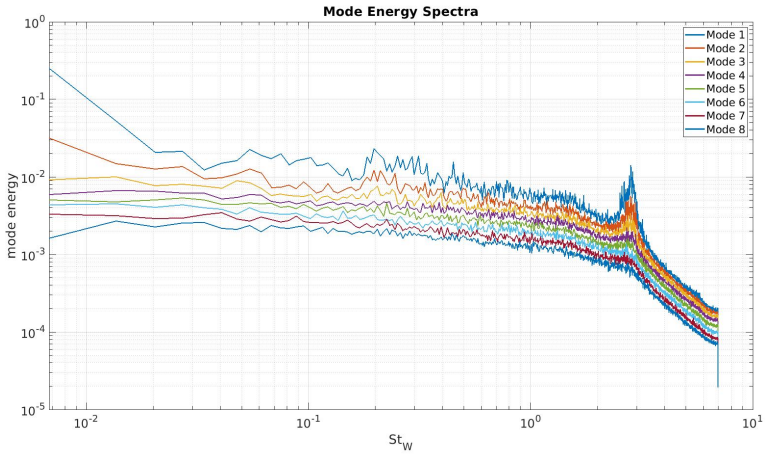

Figure 7.3: SPOD spectra for pressure fluctuations in the region around the Ahmed body and the wake for the unforced flow.

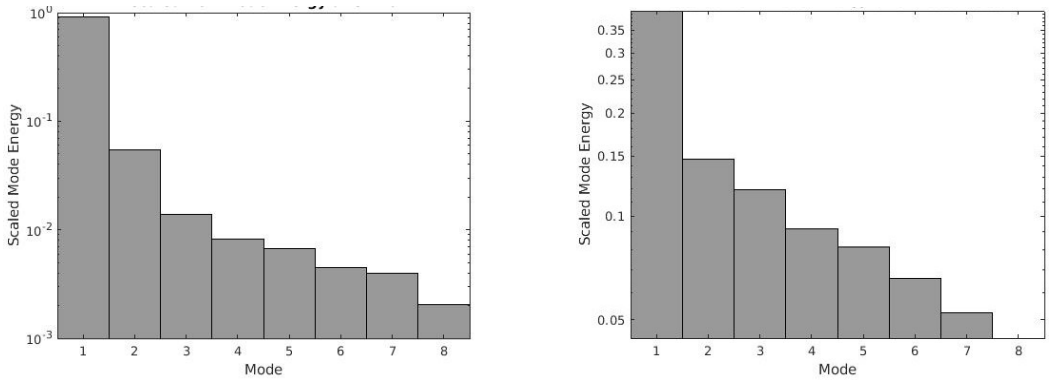

(a) (b)

Figure 7.4: Scaled mode energies at $St_W = 0.006$ (a) and at $St_W = 0.074$ (b) for the first eight modes for the unforced flow case.

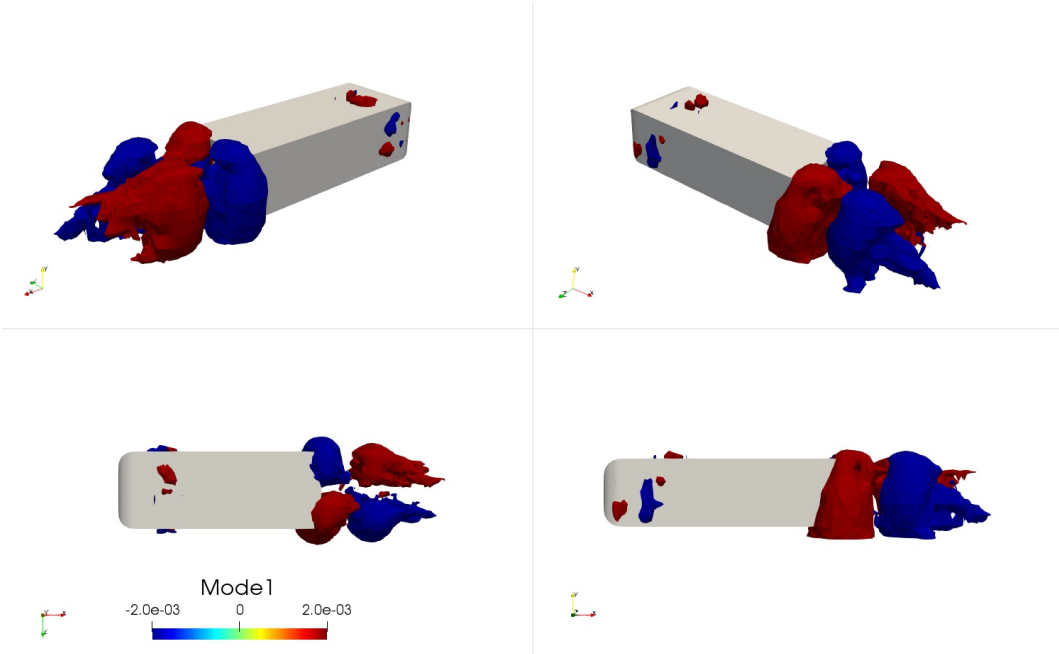

Figure 7.5: Iso-volumes of mode-1 at $St_W = 0.006$, associated with wake horizontal bi-modality. The top row shows a three-dimensional view of the wake on both sides of the body. The bottom row shows a top-view of the domain (left) and a side view of the body (right).

is attributed to the horizontal bi-modality of the wake. Mode-2 (figure 7.6) at the same frequency is suggested to be linked to the weak vertical asymmetry of the wake. Where a vertical asymmetry exists, the wake switches between the two asymmetric horizontal positions through a vertically-asymmetric state (Haffner et al., 2020). This can be seen in the joint probability density function of $\partial C_P/\partial z$ and $\partial C_P/\partial y$ shown in figure 6.14. Mode-2 is suggested to be related to the wake reversal dynamics for the weakly vertical asymmetry. This mode was also seen in the velocity-based POD analysis of Podvin et al. (2021). Its time-coefficient peaked during the switching events supporting its relevance to the switching event.

At $St_W \sim 0.074$, the first mode carries 40% of the total flow energy at this frequency, as shown in figure 7.4b. This mode, shown in figure 7.7, is symmetric in both the horizontal and vertical directions. It is suggested to be linked to the streamwise motion of the bubble, known as bubble pumping or bubble breathing. (Duell and George, 1999) suggested a link between this mode and the boundary layer separation, i.e. the disturbances introduced in the free shear layers due to the separation upstream of the wake. These disturbances increase the turbulence entertainment of the free shear layers that form the recirculation bubble, causing the streamwise pumping motion. The most common interpretation of this mode in the literature is that it results from the interaction between horizontal and vertical vortex shedding.

Asymmetric vortex shedding is reported at $St_W = 0.19$. The most energetic mode at this frequency accounts for 40% of the total energy of the pressure fluctuations, as shown in figure 7.8a. The 3D iso-volumes of the pressure fluctuations associated with this mode are shown in

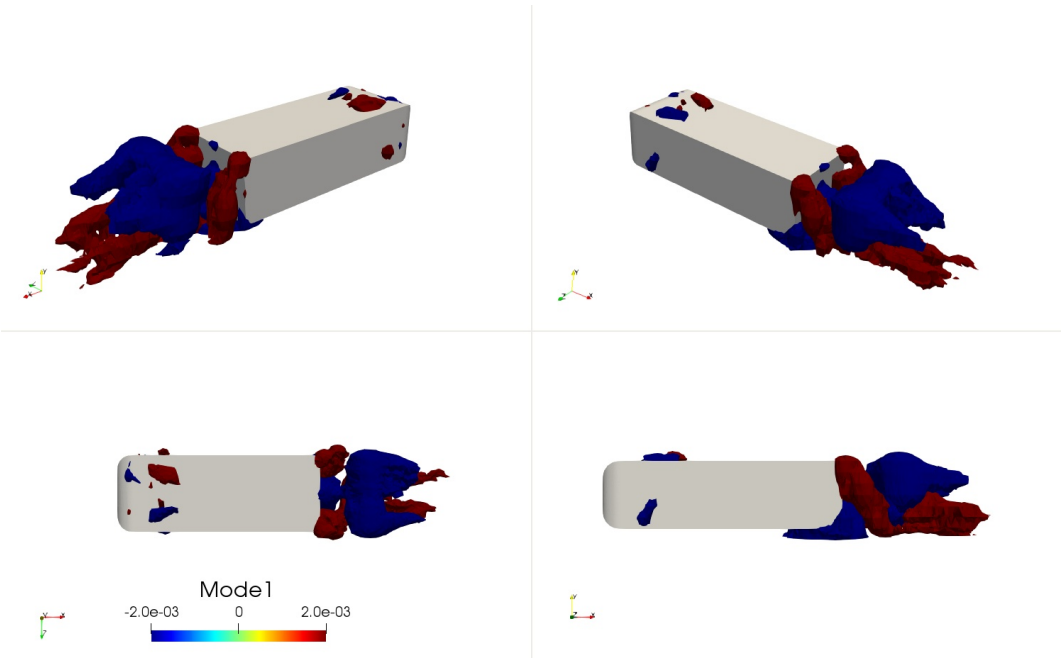

Figure 7.6: Iso-volumes of mode-2 at $St_W = 0.006$, associated with the mechanism of wake switching. The top row shows a three-dimensional view of the wake on both sides of the body. The bottom row shows a top-view of the domain (left) and a side view of the body (right).

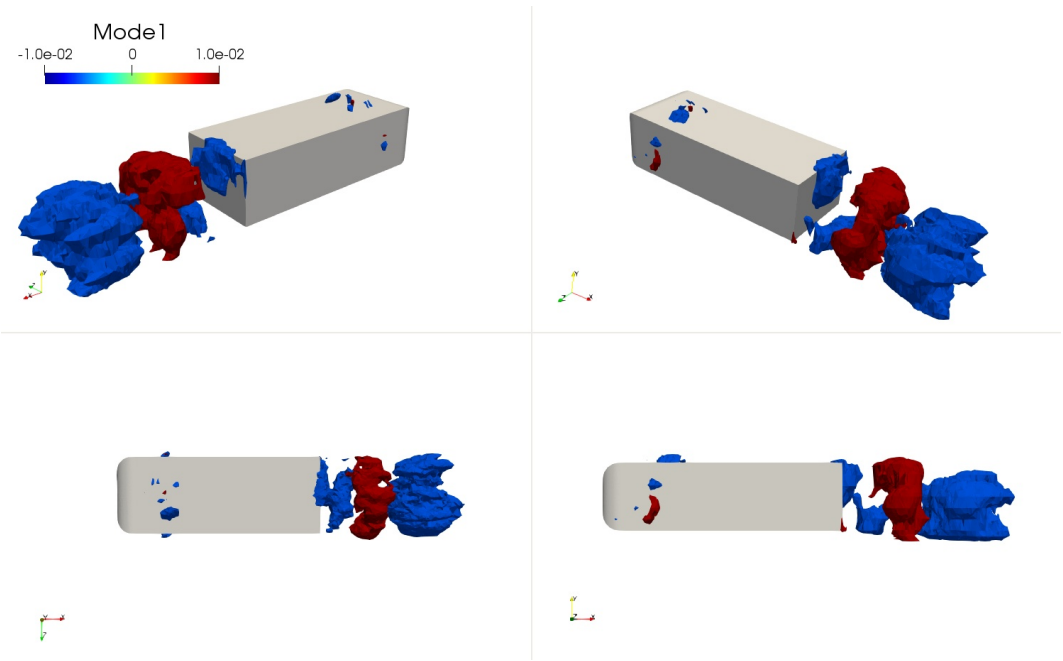

Figure 7.7: Iso-volumes of mode-1 at $St_W = 0.074$, associated with bubble pumping. The top row shows a three-dimensional view of the wake on both sides of the body. The bottom row shows a top-view of the domain (left) and a side view of the body (right).

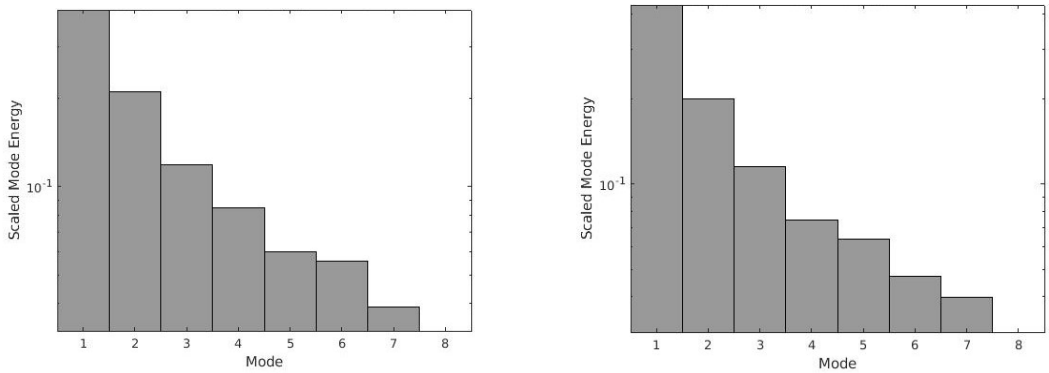

(a) (b)

Figure 7.8: Scaled modal energies at $St_W = 0.19$ (a) and at $St_W = 2.8$ (b).

figure 7.9, which shows an asymmetric shedding from the side shear layers. The figure also shows that the fluctuations occur closer to the base on one side than the other, following the asymmetric position of the wake. Mode-2 at the same frequency, shown in figure 7.10, also indicates horizontal asymmetric vortex shedding. In this mode, the shedding starts earlier on the shear layer from the other side. The vertical vortex shedding, which is attributed to the interaction of the top and bottom shear layers in the wake, is captured in the third mode at this frequency, shown in figure 7.11.

The highest frequency reported is equivalent to $St_W \sim 2.8$. The most energetic two modes at this frequency carry around 65% of the total energy (figure 7.8b). These modes are found to be related to the separation of the boundary layers on the top and side surfaces of the body, as shown in figures 7.12 and 7.13. This frequency is also detected in all four shear layers in the wake. The separation of the boundary layers closer to the body's fore-end generates vortical structures with different length scales and frequencies, the highest of which is discussed above. However, this is clearly shown in the modes associated with all frequency peaks indicated. The effect of suppressing boundary layer separations on the wake is investigated in the following subsections using SPOD for the different cases.

The previous results align with the SPOD results of the experimental data by Haffner et al. (2020). The SPOD results of this previous study were performed using data realization of a horizontally-asymmetric wake. Thus the modes related to wake switching were not captured. However, the vortex shedding and the bubble pumping frequencies matched very well. The high-frequency dynamics linked to boundary layer separations were not captured in the experimental results, as the data only focused on the wake area. Nevertheless, some high-frequency dynamics were marked in the shear layers, similar to the current results. Using pressure rather than velocity was deemed convenient, as the current results match with Schmidt et al. (2018), who performed velocity-based SPOD.

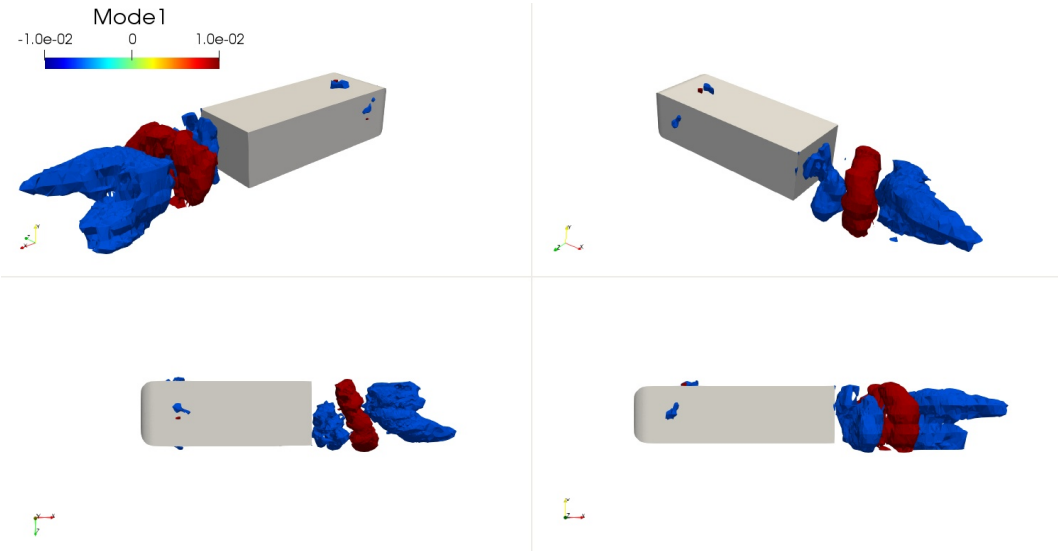

Figure 7.9: Iso-volumes of mode-1 at $St_W = 0.19$, associated with vortex shedding in the wake. The top row shows a three-dimensional view of the wake on both sides of the body. The bottom row shows a top-view of the domain (left) and a side view of the body (right).

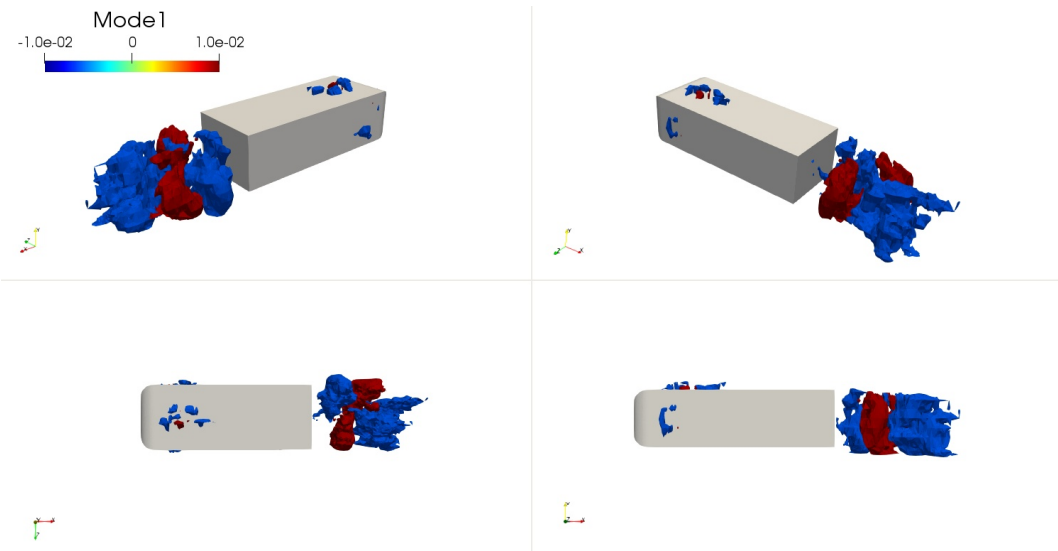

Figure 7.10: Iso-volumes of mode-2 at $St_W = 0.19$, associated with vortex shedding in the wake. The top row shows a three-dimensional view of the wake on both sides of the body. The bottom row shows a top-view of the domain (left) and a side view of the body (right).

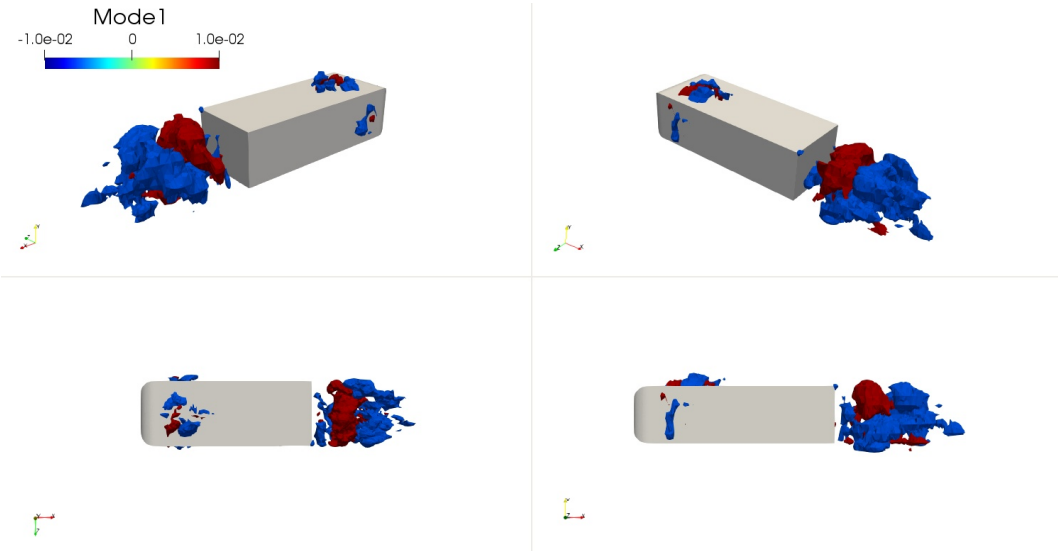

Figure 7.11: Iso-volumes of mode3 at $St_W = 0.19$, associated with vertical vortex shedding in the wake. The top row shows a three-dimensional view of the wake on both sides of the body. The bottom row shows a top-view of the domain (left) and a side view of the body (right).

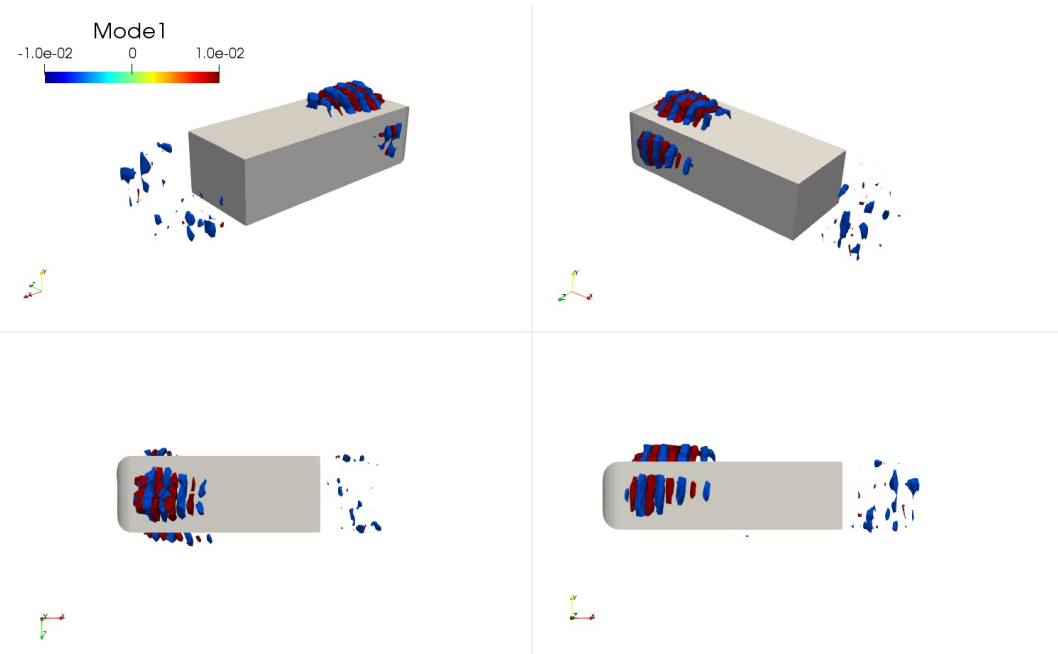

Figure 7.12: Iso-volumes of mode-1 at $St_W = 2.8$, associated with boundary layer dynamics upstream of the wake. The top row shows a three-dimensional view of the wake on both sides of the body. The bottom row shows a top-view of the domain (left) and a side view of the body (right).

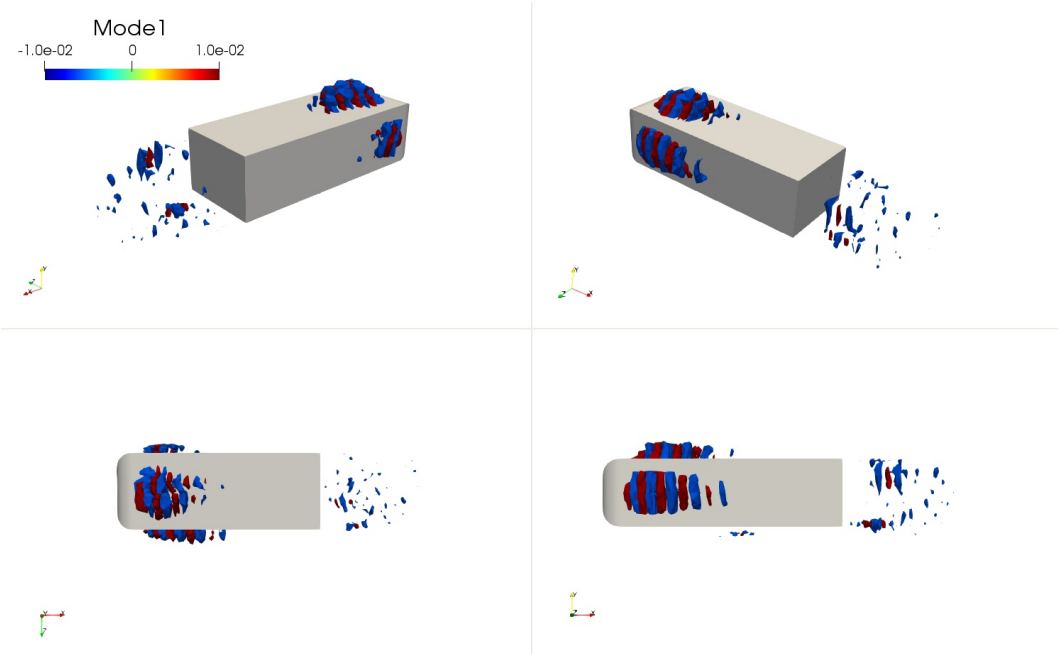

Figure 7.13: Iso-volumes of mode-2 at $St_W = 2.8$, associated with boundary layer dynamics upstream of the wake. The top row shows a three-dimensional view of the wake on both sides of the body. The bottom row shows a top-view of the domain (left) and a side view of the body (right).

7.2 Case-1

In this case, boundary layer separations on the side surfaces of the body are suppressed by applying suction. Accordingly, bi-modality is suppressed, and the wake is fully symmetrised based on the time history of the horizontal gradient of the base pressure coefficient $\partial C_p/\partial z$. This effect on the wake and the upstream region around the body is now investigated using SPOD. SPOD is performed using pressure data, requiring fewer data storage than velocity. The domain considered for data collection is similar to the unforced flow case, shown in figure 7.1. SPOD characteristics for this case are also similar to the unforced flow case. The energy spectra for mode-1 (the most energetic mode) is shown in figure 7.14 and exhibits two frequency peaks: a relatively low frequency at $St_W \sim 0.24$ and a high frequency at $St_W \sim 2.8$. A broad frequency band around $St_W \sim 0.13$ is also captured.

$St_W \sim 0.24$ is expected to be related to vortex shedding. The most energetic two modes carry around 70% of the flow energy at this frequency, as shown in figure 7.15a. Mode-1 ($\sim$ 55% energy) is related to the vortex shedding from the top and bottom shear layers in the wake. Asymmetric shedding from these two shear layers is shown in figure 7.16. The second mode (mode-2), which carries $\sim$ 15% energy, is related to asymmetric vortex shedding from the side shear layers. This can be seen in figure 7.17, where different views of the 3D iso-volume of this mode are shown. In both modes, a mark of the flow separation on the top surface just aft the body nose is evidenced.

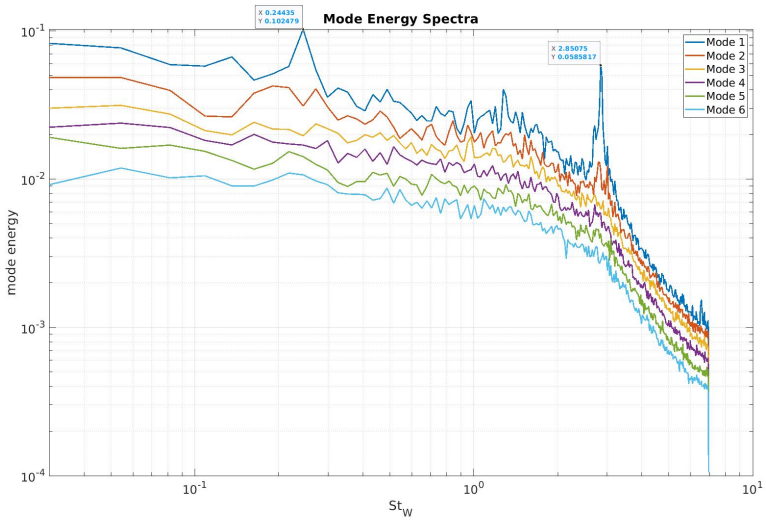

Figure 7.14: SPOD spectra for pressure data in the region around the Ahmed body for case-1, where suction is applied on the side surfaces.

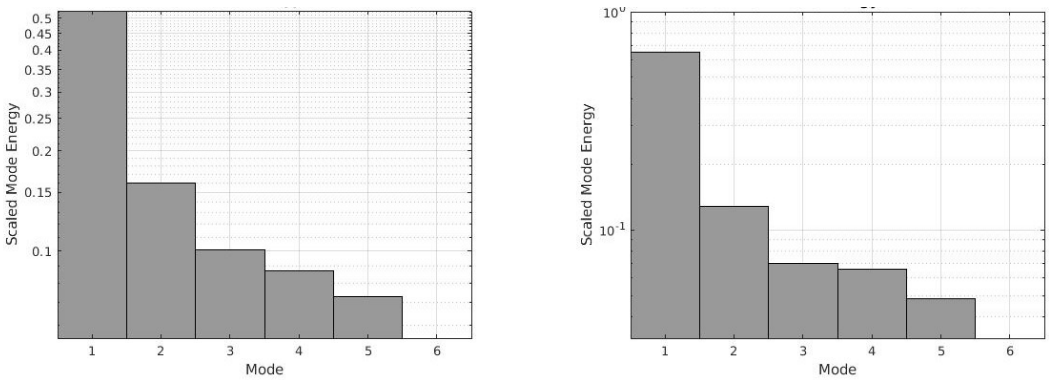

(a) (b)

Figure 7.15: Scaled modal energies at $St_W = 0.24$ (a) and at $St_W = 2.8$ (b) for case-1.

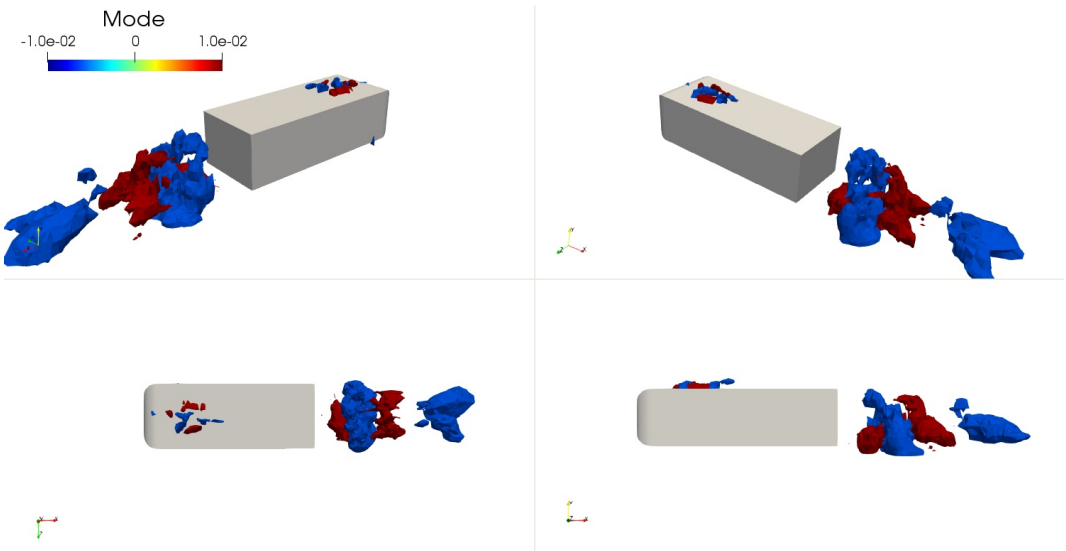

Figure 7.16: Iso-volumes of mode-1 at $St_W = 0.24$, associated with vertical vortex-shedding from the top and bottom shear layers in the wake. The top row shows a three-dimensional view of the wake on both sides of the body. The bottom row shows a top-view of the domain (left) and a side view of the body (right).

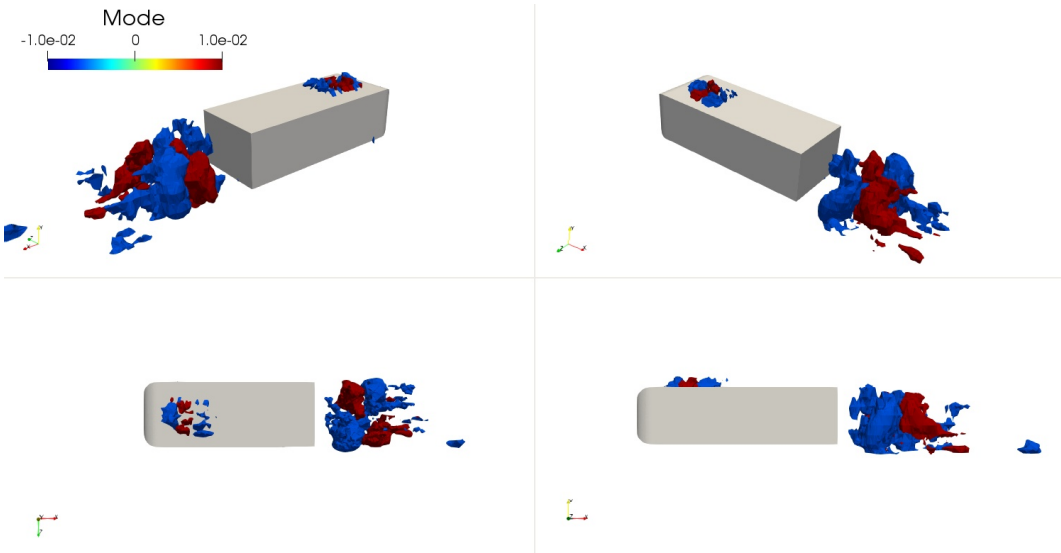

Figure 7.17: Iso-volumes of mode-2 at $St_W = 0.24$, associated with horizontal vortex-shedding from the side shear layers in the wake. The top row shows a three-dimensional view of the wake on both sides of the body. The bottom row shows a top-view of the domain (left) and a side view of the body (right).

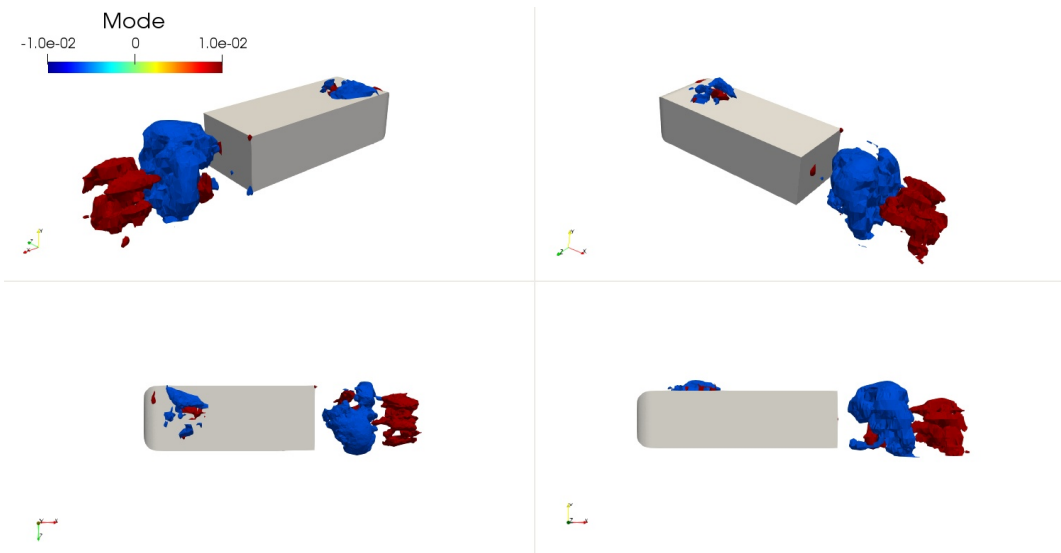

Figure 7.18: Iso-volumes of mode-1 at $St_W = 0.13$ for case-1. The top row shows a three-dimensional view of the wake on both sides of the body. The bottom row shows a top-view of the domain (left) and a side view of the body (right).

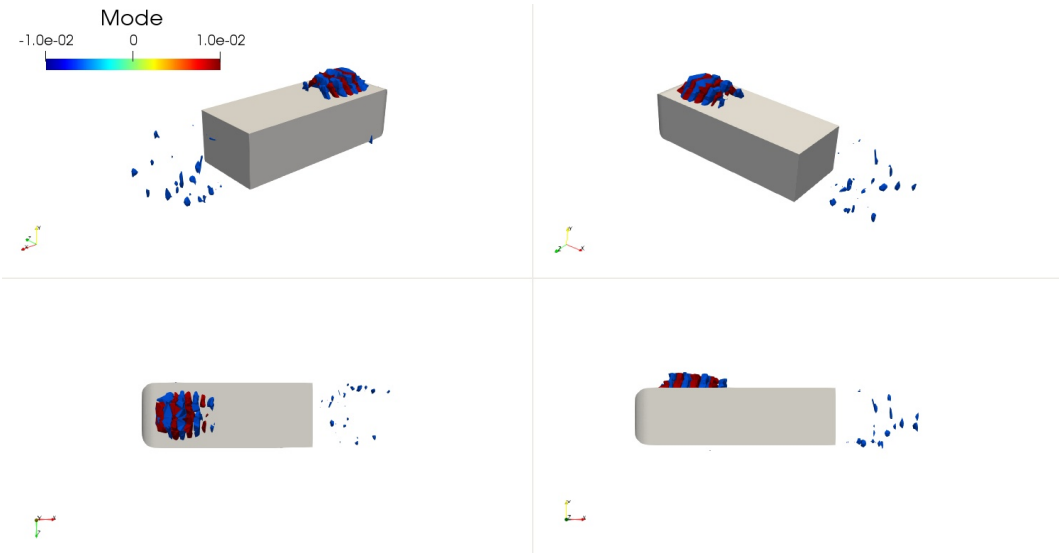

Figure 7.19: Iso-volumes of mode-1 at $St_W = 2.8$, associated with boundary layer dynamics on the top surface of the Ahmed body. The top row shows a three-dimensional view of the wake on both sides of the body. The bottom row shows a top-view of the domain (left) and a side view of the body (right).

At the low-frequency band, around $St_W \sim 0.13$, the most energetic mode carries 50% of the flow energy at this frequency. The 3D iso-volumes of the pressure fluctuations of this mode look similar to the bubble pumping mode evidenced in the unforced flow case. Figure 7.18 shows mode-1 at $St_W \sim 0.13$, indicating a symmetric mode in both the horizontal and the vertical directions.

At $St_W \sim 2.8$, the first two modes carry around $\sim 75\%$ of the flow energy, as indicated in the scaled energy content of the first eight modes of the POD in figure 7.15b. Both modes indicate the shedding caused by the separation of the top-surface boundary layer as shown in figures 7.19 and 7.20 for mode-1 and mode-2, respectively. Mode-2, which is less energetic than mode-1, shows that this high frequency also exists in the wake region, where it is suggested to be linked to the separated shear layers. Higher fluctuations are noticed near the bottom shear layer compared to the top, as the flow here is dominated by downwash velocity, meaning that the top-shear layer might be more stable compared to its counterpart on the bottom. Compared to the unforced flow case, the SPOD modes at high frequency shows clearly the effect of suction on the side boundary layers. The high-frequency dynamics related to boundary layer separations are completely suppressed on the side surfaces. Some disturbances are introduced in the underbody region indicated by mode-3 at $St_W \sim 2.8$ (figure 7.20).

Based on comparison of the SPOD modes for the unforced case and case-1, the effect of suppressing the separation of the side boundary layers can be summarised as follows:

- It suppresses the low-frequency dynamics related to bi-modality.

- The energy content of the horizontal vortex shedding (side shear layers) decreasesd compared

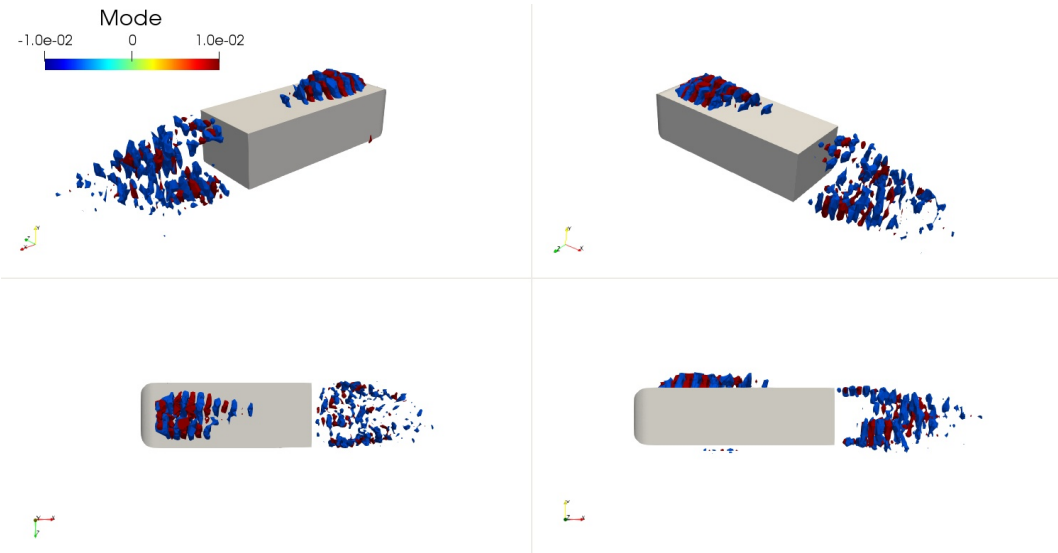

Figure 7.20: Iso-volumes of mode-2 at $St_W = 2.8$, associated with boundary layer dynamics on the top surface of the Ahmed body and the high-frequency dynamics of top and bottom shear layers in the wake. The top row shows a three-dimensional view of the wake on both sides of the body. The bottom row shows a top-view of the domain (left) and a side view of the body (right).

to the vertical vortex shedding (top and bottom).

- The dynamics related to boundary layer separations on the side surfaces are suppressed over all frequencies investigated.
- The broad frequency band related to bubble pumping is augmented compared to the unforced flow case. This supports the previously suggested link in which bubble pumping is related to the upstream disturbance caused by boundary layer separations (Duell and George, 1999).

7.3 Case-2

In this case, suction and blowing are applied on the top and the bottom surfaces, respectively. Based on the time-averaged and time-resolved analysis explored in the previous chapter, horizontal bi-modality is entirely suppressed, and the wake is symmetrised with an inverse vertical asymmetry. The recirculation bubble is dominated by an upwash flow emanating from the underbody region. An SPOD of the pressure data with spatial and temporal resolutions similar to the unforced flow is conducted; the setup and data acquisition are as for the SPOD of the unforced flow case.

The modes energy spectra (figure 7.21) indicate a broad frequency band around $St_W \sim 0.43$ and two frequency peaks; the first is around $St_W \sim 3.04$ and its harmonic around $St_W \sim 6.08$. The most energetic mode at $St_W \sim 0.43$ carries around 45% of the flow energy at this frequency, as shown in figure 7.22a. Figure 7.23 depicts the 3D iso-volumes of pressure fluctuations of this mode, which is suggested to be related to vortex shedding from the top shear layer. Due to the disturbances induced by blowing in the underbody region, the vertical position of the wake, in

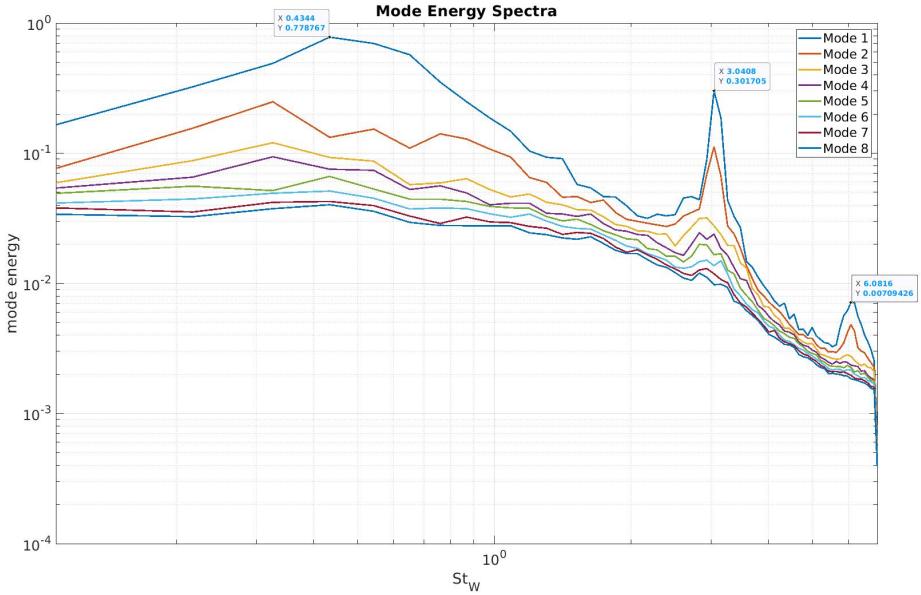

Figure 7.21: SPOD spectra for pressure data in the region around the Ahmed body for case-2, where suction and blowing are applied on the top and bottom surfaces, respectively.

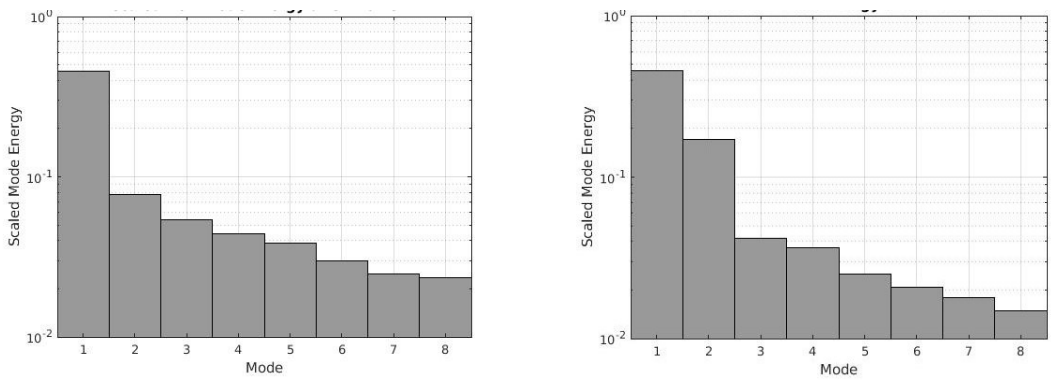

(a) (b)

Figure 7.22: Scaled modal energies at $St_W = 0.43$ (a) and at $St_W = 3.04$ (b) for case-2.

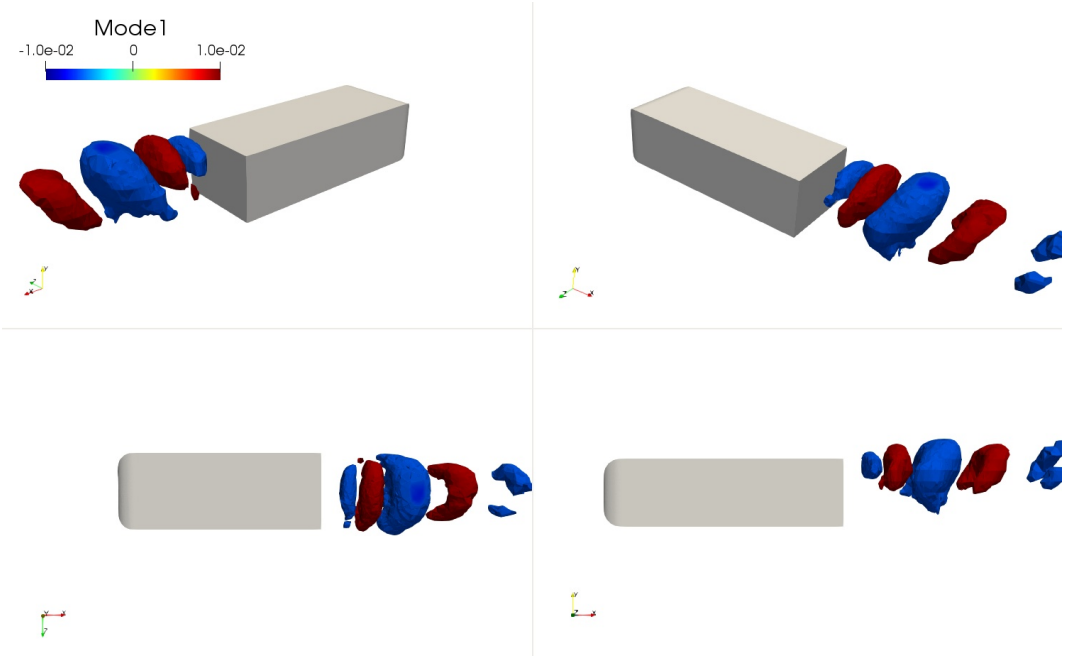

Figure 7.23: Iso-volumes of mode-1 at $St_W = 0.43$, associated with vortex shedding from the top shear layer in the wake. The top row shows a three-dimensional view of the wake on both sides of the body. The bottom row shows a top-view of the domain (left) and a side view of the body (right).

this case, is switched to be closer to the top half of the base. Based on the mechanism of the recirculating region formation (suggested by Haffner et al. (2020)), the bottom shear layer, in this case, exhibits larger curvature forming the recirculation region and triggering the top shear layer closer to the base, leading to the shedding seen in mode-1.

Mode-2 at the same frequency carries around 8% of the flow energy. Following the 3D iso-volumes of pressure for this mode shown in figure 7.24, this mode is suggested to be linked to an asymmetric shedding from the shear layers separated off the side surfaces of the body. This occurs closer to the top half of the body in the near-wake region, as the wake is tilted upwards due to the upwash flow, similar to the case of Kang et al. (2021). Further downstream in the wake, the interaction of this shedding with the shedding due to the separation of the ground boundary layer is also evidenced in this mode.

At $St_W \sim 3.04$, the first two modes carry around 70% of the total flow energy at this frequency, as shown in figure 7.22b. Similar to the unforced flow case, this high frequency is related to the dynamics of the boundary layers. The iso-volume of the pressure fluctuations for mode-1 and mode-2 is shown in figures 7.25 and 7.26, respectively. Applying suction and blowing on the top and bottom surfaces of the body, respectively, were found to have the following effects on the upstream dynamics:

- Suppressing the high-frequency fluctuations on the top surface of the body.

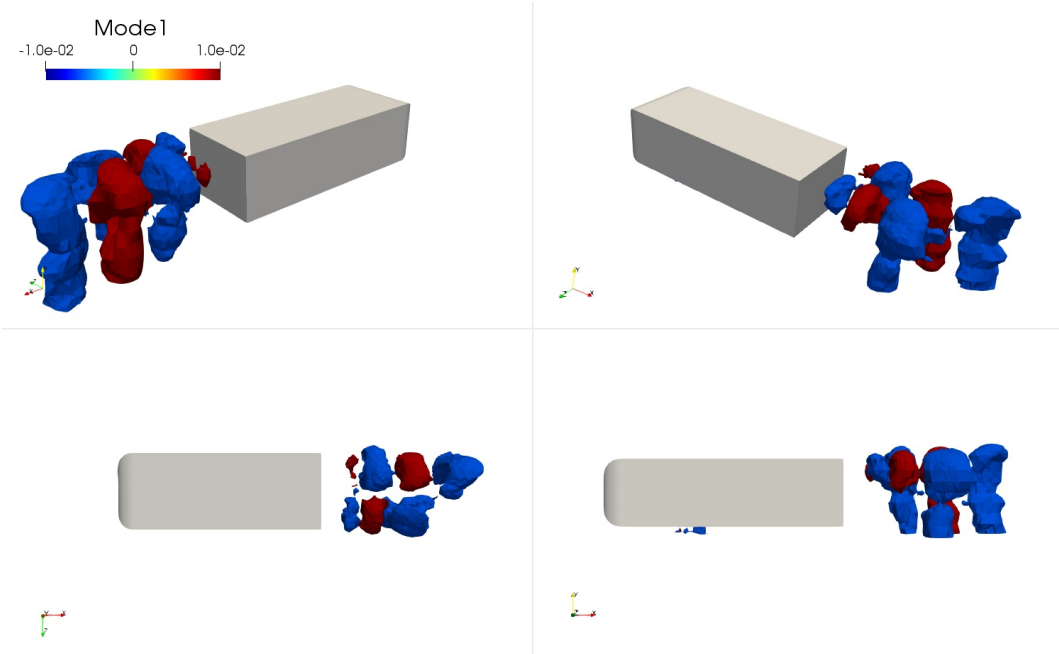

Figure 7.24: Iso-volumes of mode-2 at $St_W = 0.43$, associated with the vortex shedding from the side shear layers. The top row shows a three-dimensional view of the wake on both sides of the body. The bottom row shows a top-view of the domain (left) and a side view of the body (right).

- Shifting the spatial location of the fluctuations on the side surfaces to the bottom half of the body, i.e. promoting the interaction of the side boundary layers with the underbody flow.
- Synthesizing boundary layer separation on the bottom surface of the body, which amplified the disturbances in the underbody flow compared to the unforced flow case.

Figure 7.26 also shows that the high-frequency fluctuations on the top-shear layer in the wake occur closer to the body compared to the bottom-shear layer. This correlates with the wake being oriented towards the body's top half, i.e. reversed vertical position compared to the unforced flow case. Based on the time-averaged streamlines, the bottom shear layers is expected be more stable and have increased curvature compared to the top shear layers in this case, similar to the switching mechanism suggested by Haffner et al. (2020). The peak associated with $St_W \sim 6.08$ is a harmonic of the fluctuations on the sides and the underbody.

7.4 Case-2-II

In this case, suction is applied on the top and bottom body surfaces, suppressing boundary layer separation on the top and introducing disturbances in the underbody region. Bi-modality persists in this case, and the wake exhibits a reflected weak vertical asymmetry. The effect of this on the upstream dynamics and the wake will further be investigated in this section using the same SPOD setup and domain as for the unforced flow. The energy spectra, shown in figure 7.27, indicate higher

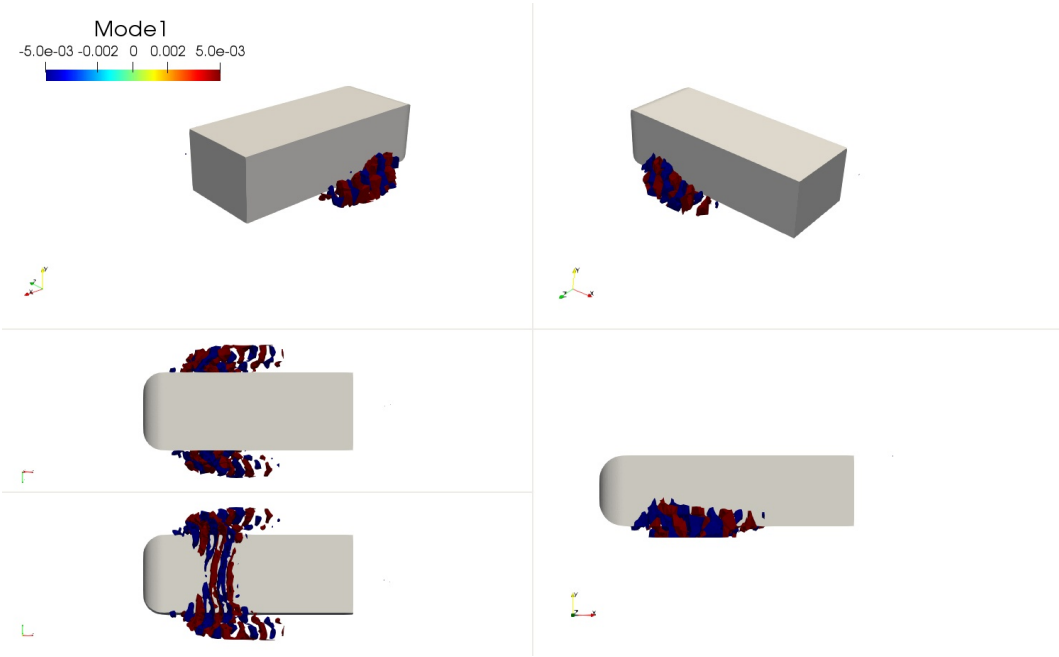

Figure 7.25: Iso-volumes of mode-1 at $St_W = 3.04$, associated with boundary layer dynamics on the bottom and the side surfaces of the Ahmed body. The top row shows a three-dimensional view of the wake on both sides of the body. The bottom row shows a top-view of the domain (left) and a side view of the body (right).

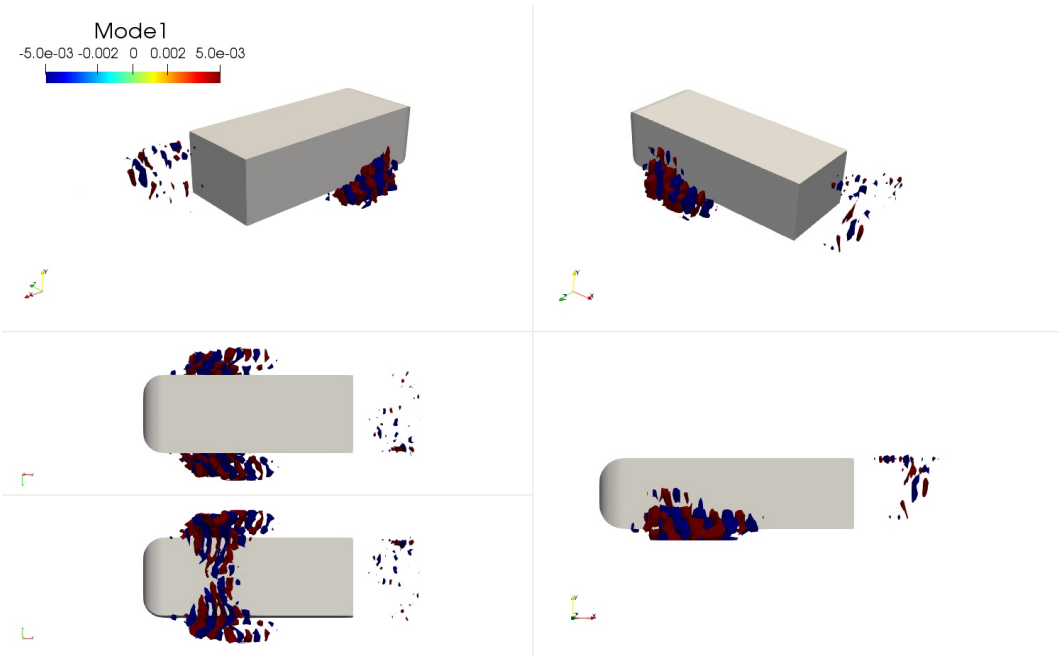

Figure 7.26: Iso-volumes of mode-2 at $St_W = 3.04$, associated with boundary layer dynamics on the bottom and the side surfaces of the Ahmed body. The top row shows a three-dimensional view of the wake on both sides of the body. The bottom row shows a top-view of the domain (left) and a side view of the body (right).

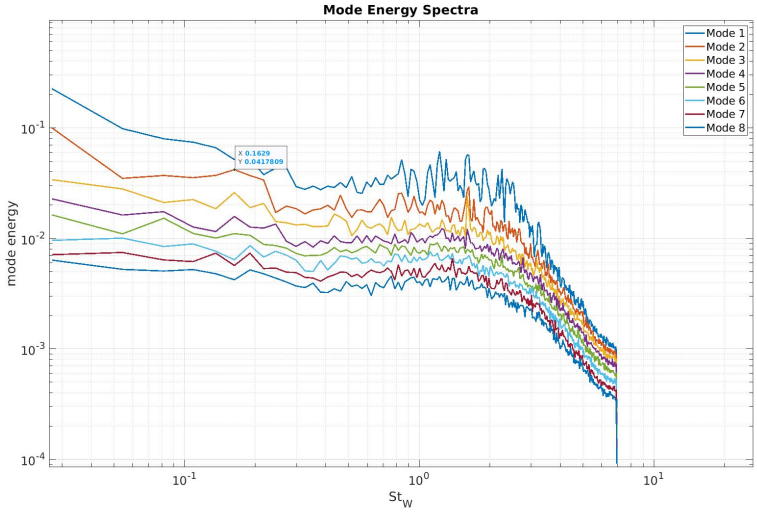

Figure 7.27: SPOD spectra for pressure data in the region around the Ahmed body for case-2-II, where suction is applied on the top and bottom body surfaces.

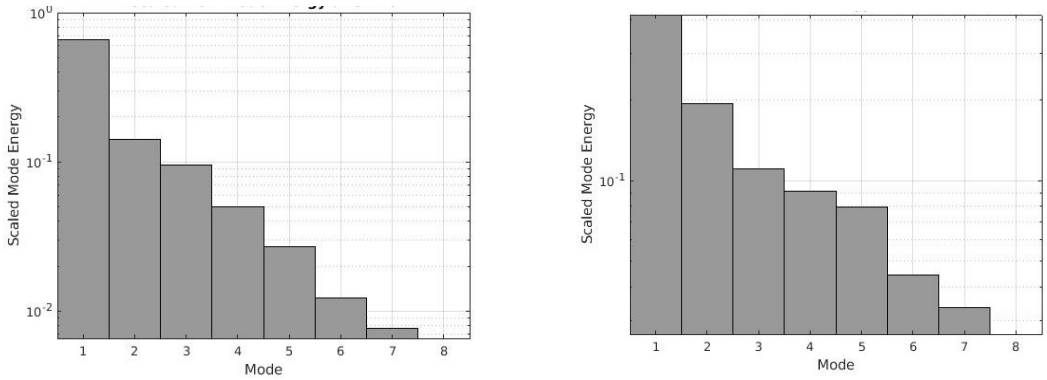

(a) (b)

Figure 7.28: Scaled modal energies at $St_W = 0.006$ (a) and at $St_W = 0.17$ (d) for case-2-II.

energy content at very low frequency for both mode-1 and mode-2. This is linked to the horizontal bi-modality of the wake, similar to the unforced flow. Frequency peaks around $St_W \sim 0.16, 0.24$ and 2.7 are linked to the horizontal vortex shedding, vertical vortex shedding and boundary and free shear layers dynamics, respectively. A broad frequency band can be seen around $St_W \sim 0.08$, linked to the bubble pumping mode.

Similar to the unforced flow, the 3D view of mode-1 at $St_W \sim 0$ shows an asymmetric distribution in the horizontal direction linked to the wake bi-modality, which can be seen in figure 7.29. Mode-2, at the same frequency, denotes the reflected weak vertical asymmetry of the wake due to suction being applied on the top and bottom surfaces, shown in figure 7.30. Compared to mode-2 at the same frequency for the unforced flow (figure 7.6), a switch between the negative and positive mode values can be seen, which is suggested to be caused by the reflected vertical asymmetry. Both mode-1 and mode-2 capture the low-frequency dynamics of the side boundary layers (upstream of the wake) but not the top surface, as seen in the unforced flow. At $St_W \sim 0.08$, mode-1 indicates

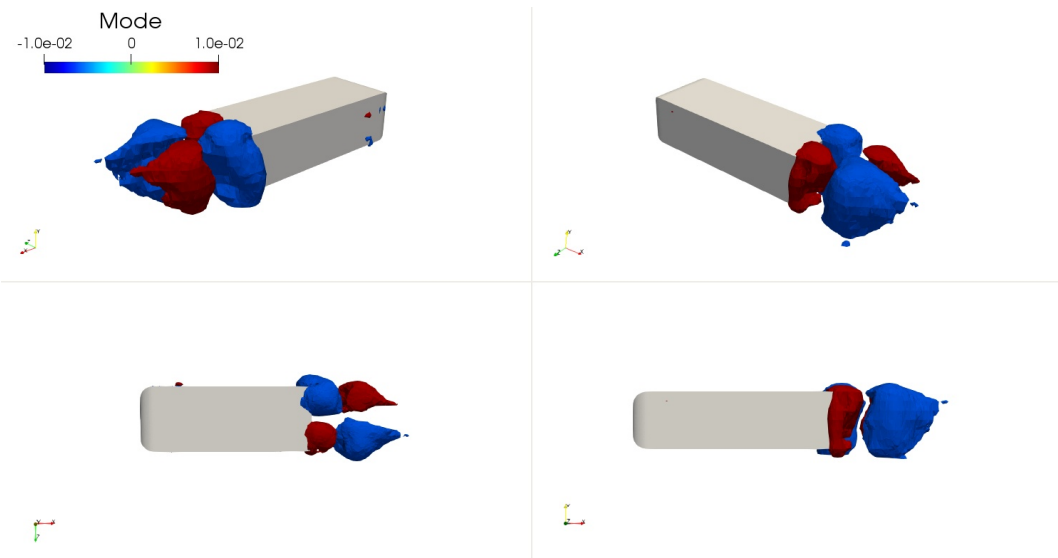

Figure 7.29: Iso-volumes of mode-1 at $St_W \sim 0$, associated with wake bi-modality. The top row shows a three-dimensional view of the wake on both sides of the body. The bottom row shows a top-view of the domain (left) and a side view of the body (right).

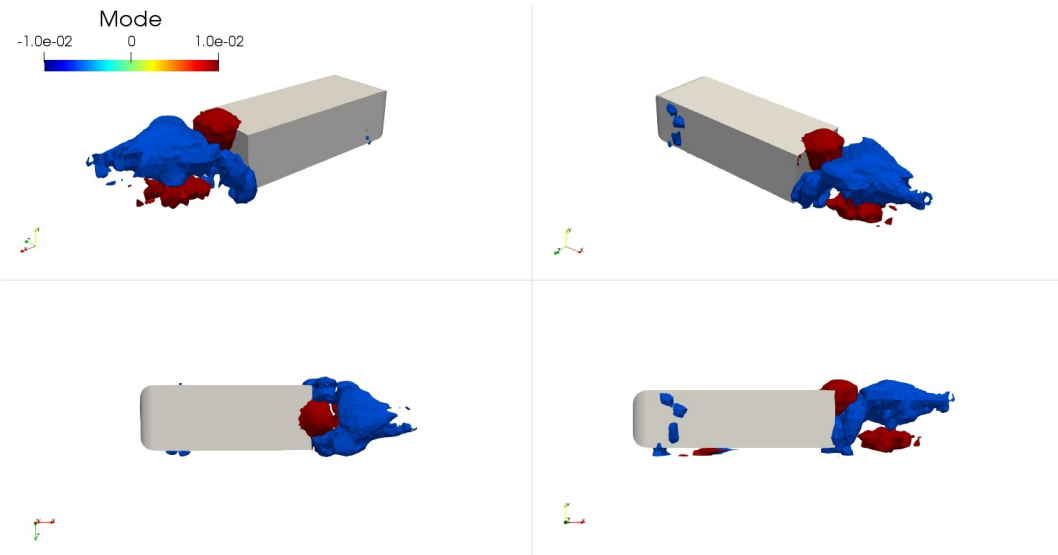

Figure 7.30: Iso-volumes of mode-2 at $St_W \sim 0$, associated with wake vertical asymmetry. The top row shows a three-dimensional view of the wake on both sides of the body. The bottom row shows a top-view of the domain (left) and a side view of the body (right).

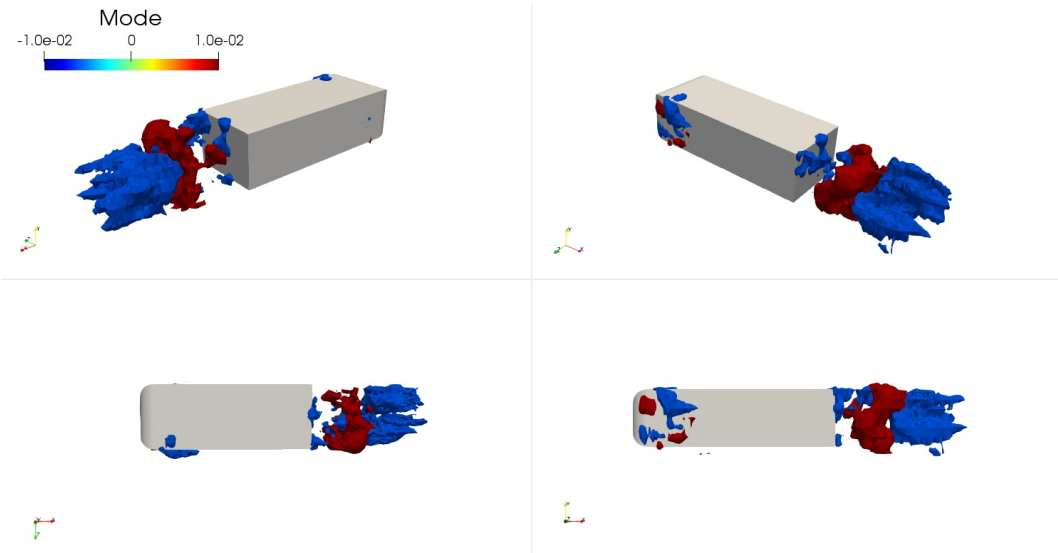

Figure 7.31: Iso-volumes of mode-1 at $St_W \sim 0.08$, associated with the bubble pumping mode. The top row shows a three-dimensional view of the wake on both sides of the body. The bottom row shows a top-view of the domain (left) and a side view of the body (right).

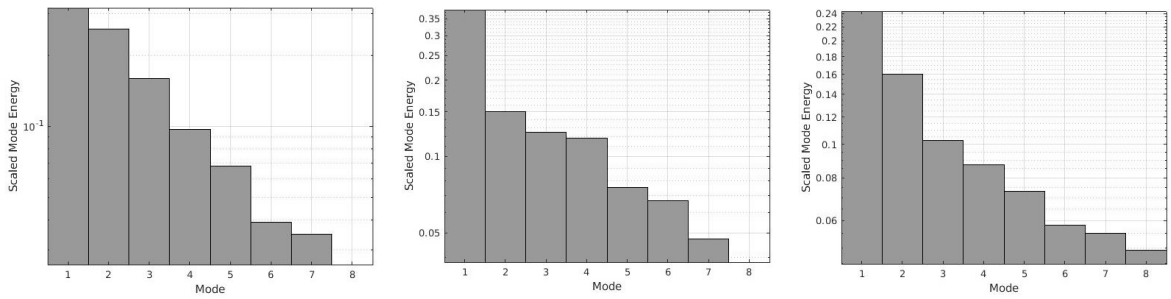

Figure 7.32: Scaled modal energies at $St_W = 0.16$ (a), at $St_W = 0.24$ and at $St_W = 2.7$ (c) for case-2-II.

a symmetric distribution in both cross-flow directions, as shown in figure 7.31 matches with the bubble pumping mode in the unforced case (figure 7.7). This confirms that applying suction on both the top and bottom surfaces does not affect the bubble pumping mode.

The scaled modal energies at $St_W \sim 0.16$, 0.24 and 2.7 are shown in figure 7.32. Figure 7.33 shows mode-1 at $St_W \sim 0.16$, which indicates an asymmetric horizontal vortex shedding, with the vortical structures being closer to the body top. The vertical vortex shedding is shown in figure 7.34 at $St_W \sim 0.25$. This occurs at a higher frequency compared to the unforced flow. The most energetic mode at the highest frequency, i.e. $St_W \sim 2.7$, is shown in figure 7.35. This indicates the dynamics of the upstream boundary layers on both sides and the underbody region. In addition, it indicates high-frequency dynamics on the top and bottom shear layers in the wake region. Compared to case-1 (figure 7.20), it can be seen that higher fluctuations are associated with the top shear layer, in contrast to to case-1, where the bottom shear layer exhibits higher fluctuations. This could be attributed to the reflected vertical asymmetry and the wake being

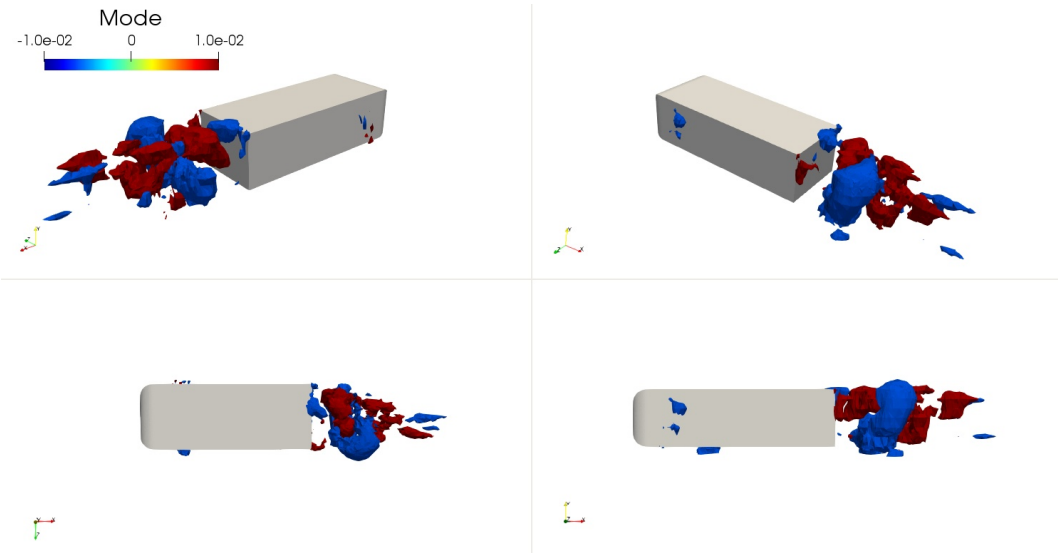

Figure 7.33: Iso-volumes of mode-1 at $St_W \sim 0.16$, associated with wake horizontal asymmetry. The top row shows a three-dimensional view of the wake on both sides of the body. The bottom row shows a top-view of the domain (left) and a side view of the body (right).

dominated by an upwash flow, augmenting the disturbances in the top shear layer.

To conclude, applying suction on both the top and bottom body surfaces was found to have a negligible effect on bi-modality and vortex shedding in both the horizontal and vertical directions. The main change seen is the suppression of the boundary layer dynamics on the top surfaces and high-frequency dynamics in the underbody region due to ground boundary layer separation. Higher disturbances are evidenced in the top shear layer compared to the bottom one, indicating the reflected vertical asymmetry of the wake.

7.5 Case-3

In this case, boundary layer separations on the top and side surfaces were suppressed using suction. The underbody flow is disturbed by sucking air through the bottom body surface. SPOD analysis with a similar setup to the previous cases is used.

The spectra of the modal energies, shown in figure 7.36, shows two frequency peaks around $St_W \sim 0.24$ and $St_W \sim 0.32$. Compared to the previous cases, the high-frequency peak associated with $St_W > 2$ has disappeared. $St_W > 2$ is shown to be related to the fluctuations caused by boundary layer separations. This correlates with the results discussed in the previous chapter that boundary layer separations are suppressed on all the surfaces in this case.

A broad frequency band exists at very low-frequency equivalent to $St_W \sim 0.027$. The most energetic two modes carry around 65% of the flow energy at this frequency, as shown in figure 7.37a. These modes are associated with the rapid switching of the wake in the horizontal direction, as indicated by $\partial C_P/\partial z$. Mode-1, shown in figure 7.39, is related to the reflected vertical asymmetry,

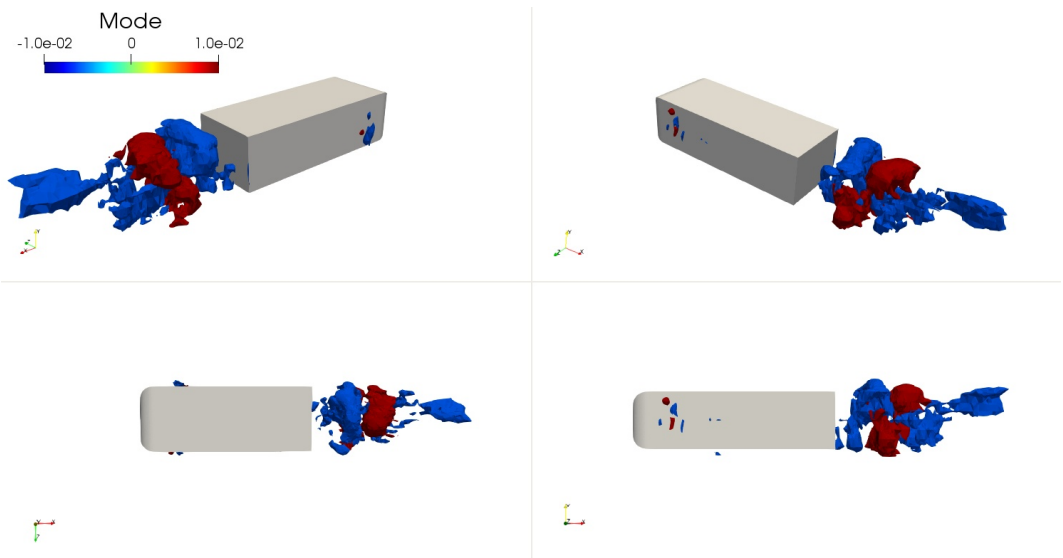

Figure 7.34: Iso-volumes of mode-1 at $St_W \sim 0.16$, associated with wake vertical asymmetry. The top row shows a three-dimensional view of the wake on both sides of the body. The bottom row shows a top-view of the domain (left) and a side view of the body (right).

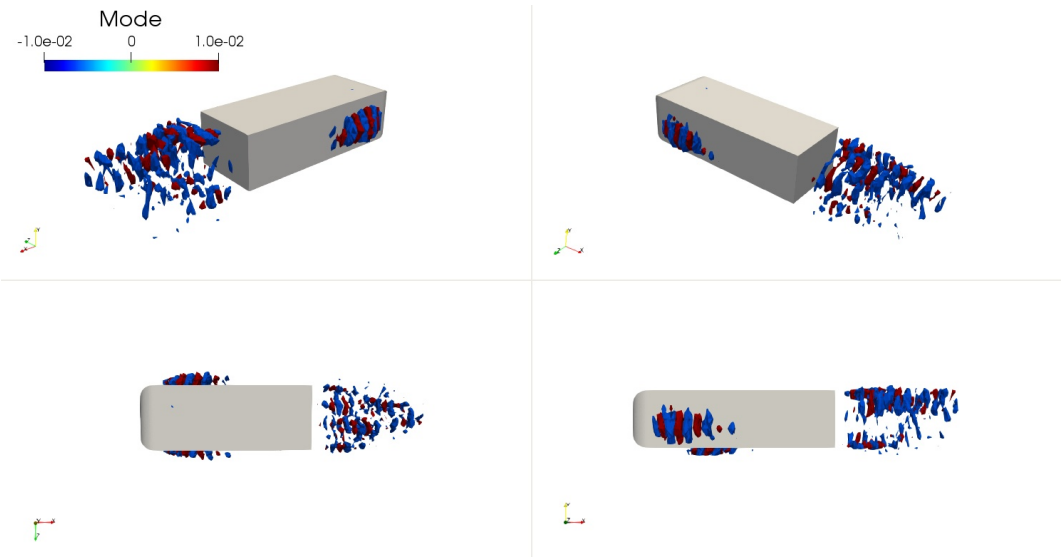

Figure 7.35: Iso-volumes of mode-1 at $St_W \sim 2.7$, associated with boundary and shear layers dynamics. The top row shows a three-dimensional view of the wake on both sides of the body. The bottom row shows a top-view of the domain (left) and a side view of the body (right).

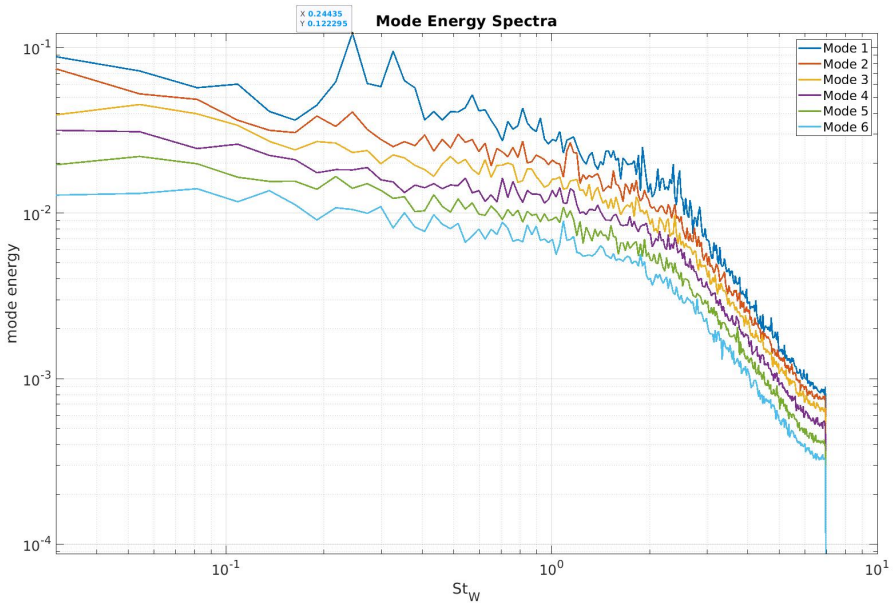

Figure 7.36: SPOD spectra for pressure fluctuations in the region around the Ahmed body for case-3, where blowing is applied on the bottom and side surfaces and suction is applied on the top and the other side surfaces.

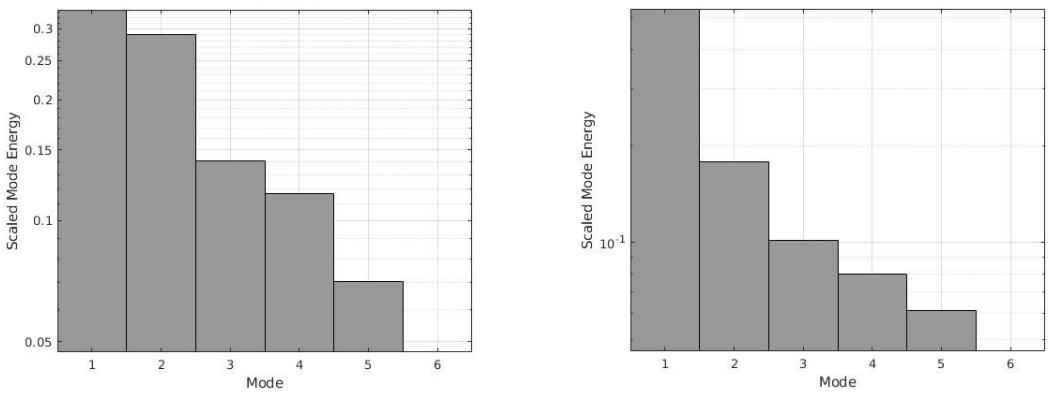

(a) (b)

Figure 7.37: Scaled modal energies at $St_W = 0.027$ (a) and at $St_W = 0.244$ (b) for case-3.

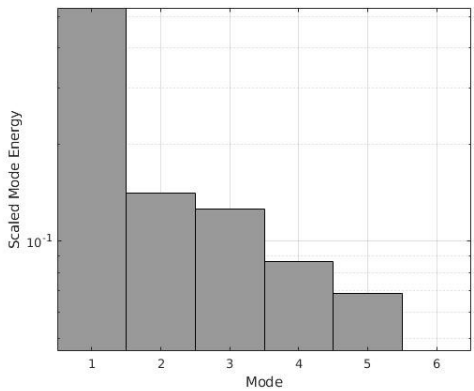

Figure 7.38: Scaled modal energies at $St_W = 0.32$ for case-3.

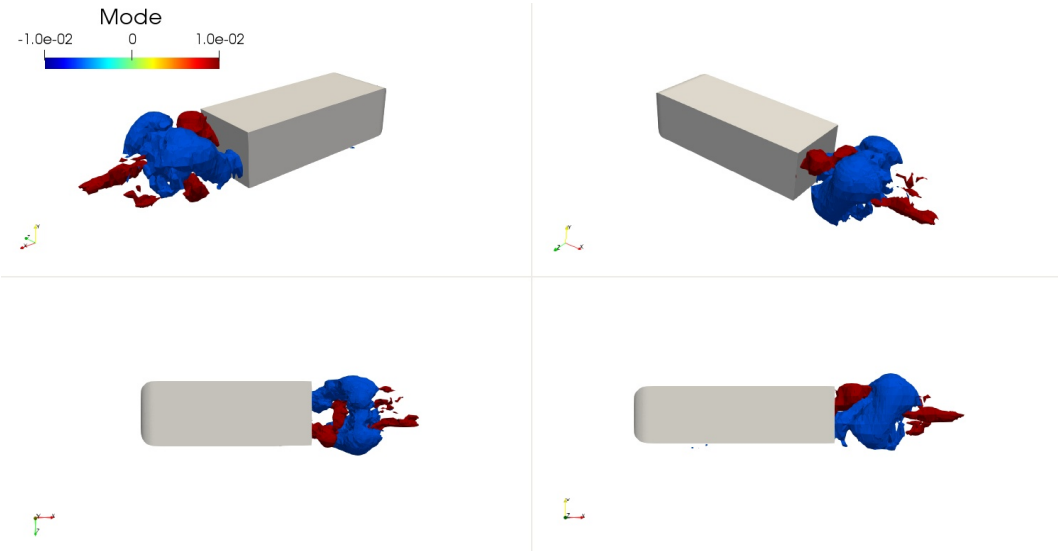

Figure 7.39: Iso-volumes of mode-1 at $St_W = 0.027$, associated with the switching mechanism of wake bi-modality. The top row shows a three-dimensional view of the wake on both sides of the body. The bottom row shows a top-view of the domain (left) and a side view of the body (right).

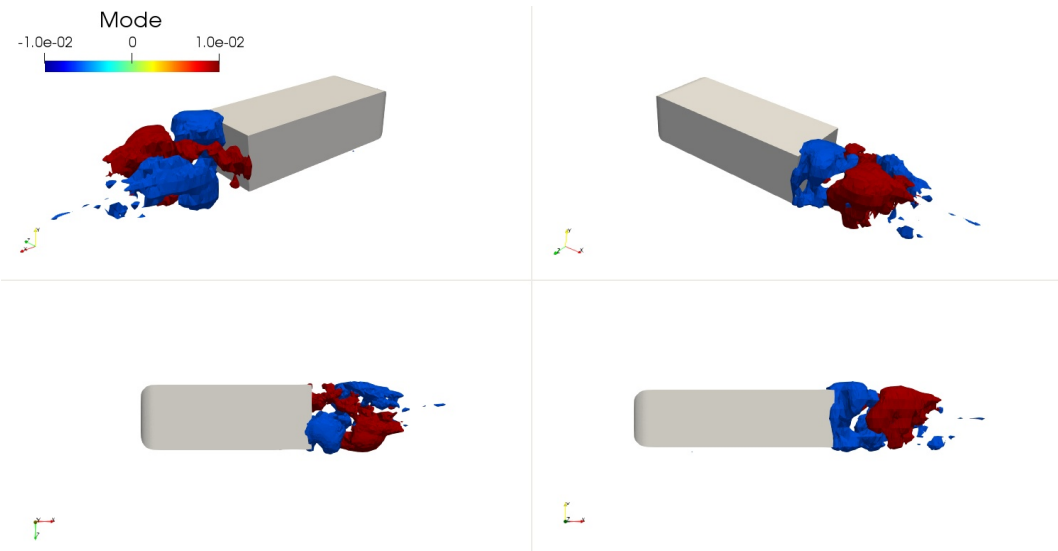

Figure 7.40: Iso-volumes of mode-2 at $St_W = 0.027$, associated with wake bi-modality. The top row shows a three-dimensional view of the wake on both sides of the body. The bottom row shows a top-view of the domain (left) and a side view of the body (right).

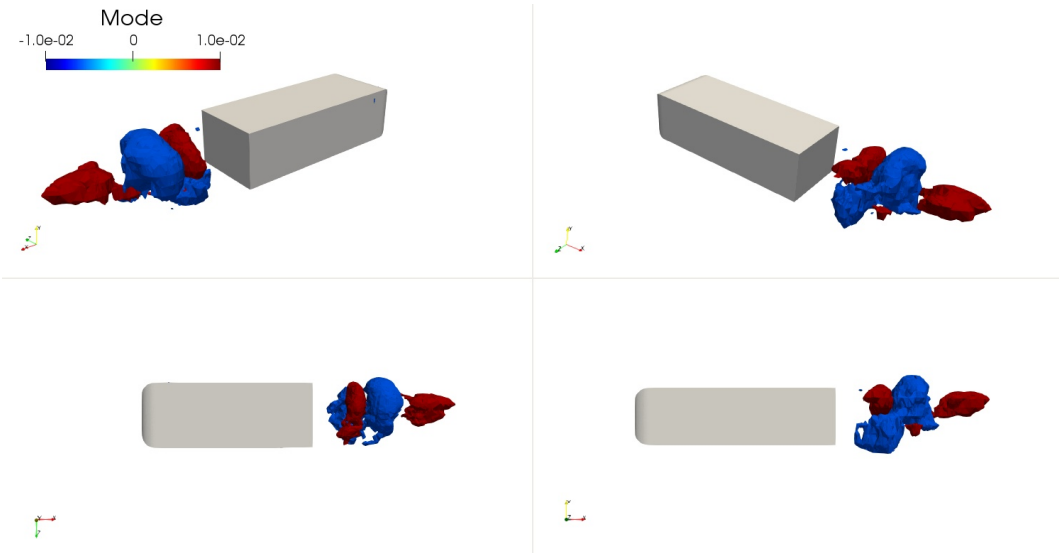

Figure 7.41: Iso-volumes of mode-1 at $St_W = 0.24$, associated with vertical vortex shedding in the wake. The top row shows a three-dimensional view of the wake on both sides of the body. The bottom row shows a top-view of the domain (left) and a side view of the body (right).

which is suggested to be an intermediate state of the wake during the horizontal switching event. For a vanished vertical asymmetry, this intermediate state passes through the centre of the base. As the wake loses its vertical symmetry, this intermediate switching state moves in the vertical direction accordingly Haffner et al. (2020). Mode-2, shown in figure 7.40, indicates the horizontal switching of the wake. The energy content of this mode is slightly lower than mode-1 (vertical asymmetry), as shown in figure 7.37a. This opposes the unforced flow case, where horizontal switching is more energetic than vertical asymmetry. This is attributed to the rapid switching of the wake in this case compared to the unforced flow. The frequency at which these dynamics are captured is an order of magnitude higher than the associated frequency in the unforced flow case ($St_W \sim 0.006$), i.e. the wake passes through the intermediate state more frequently, indicating the rapid switching.

At $St_W \sim 0.24$, the most energetic mode carries half of the total fluctuations energy at this frequency, as indicated in figure 7.37b. The 3D iso-volumes of the pressure fluctuations associated with this mode are shown in figure 7.41. This mode is horizontally-symmetric and suggested to represent the asymmetric vortex shedding in the vertical direction, i.e. from the top and bottom shear layers. Mode-2 at the same frequency carries around 18% of the pressure fluctuations energy. As shown in figure 7.42, the iso-volumes of the pressure fluctuations indicate that this mode is horizontally-asymmetric, suggested to be linked to vortex shedding from the side shear layers. This mode also captured the effect of the fluctuations induced in the underbody flow due to suction through the bottom body surface.

Similarly, at $St_W \sim 0.32$, the most energetic mode (figure 7.38) is suggested to be linked to vertical vortex shedding. At this frequency, mode-1 is dominated by shedding from the top shear

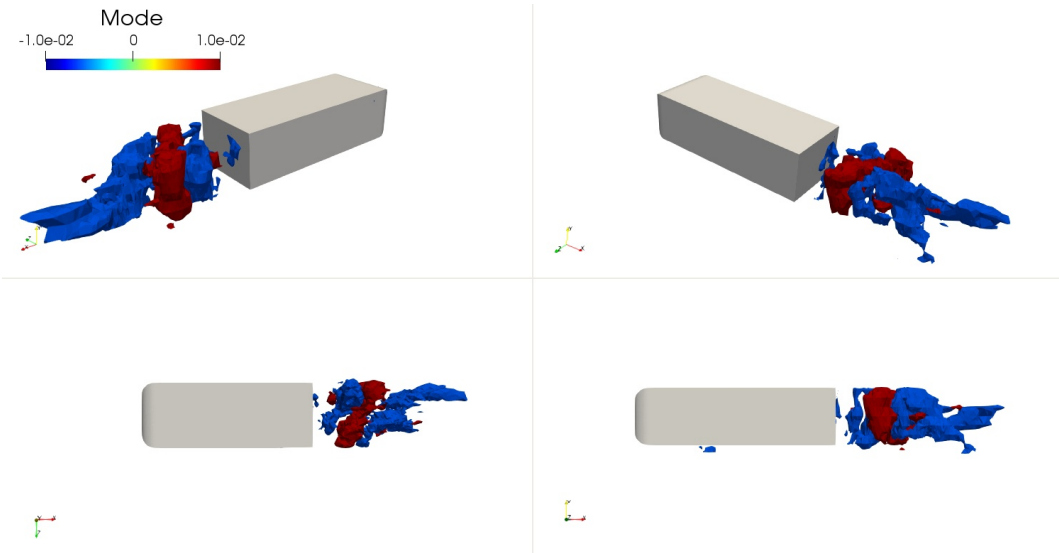

Figure 7.42: Iso-volumes of mode-2 at $St_W = 0.24$, associated with horizontal vortex shedding in the wake. The top row shows a three-dimensional view of the wake on both sides of the body. The bottom row shows a top-view of the domain (left) and a side view of the body (right).

layer. The wake resides closer to the top half of the base due to the upwash flow, as indicated by the time-averaged results. This means that the bottom shear layer will have higher curvature and is expected to be more stable, while the top shear layer is triggered closer to the base leading to this shedding, shown in figure 7.43. Similar behaviour is captured in case-2. Mode-2 at this frequency is asymmetric in both the horizontal and vertical directions, as indicated in figure 7.44. This suggests that this mode might be linked to an interaction between the vertical and the horizontal vortex shedding from the four shear layers separated off the base edges.

7.6 Summary

In this chapter, SPOD has been used to investigate different dynamical modes in the wake and to explore the effect of suppressing the boundary layer separations on the wake. Three-dimensional views of the structures associated with the different modes –ranked by their energy content at each frequency– represent a good investigation tool for exploring the wake dynamics. The SPOD of the unforced flow case gives an insight into the wake dynamics, confirming that pressure data can capture the dynamics reported in the literature using velocity data. Three dynamical modes exist in the turbulent wake of the square-back Ahmed body; the stochastic bi-modal switching of the wake, the low-frequency bubble pumping and the vortex shedding in both cross-flow directions. Vortex shedding in both the horizontal and vertical directions is captured at the same frequency. The horizontal vortex shedding resulting from the interaction between the side shear layers is more energetic than the vertical vortex shedding caused by the top and the bottom shear layers. Further, the dynamics related to boundary layer separations near the body's fore-end occur at

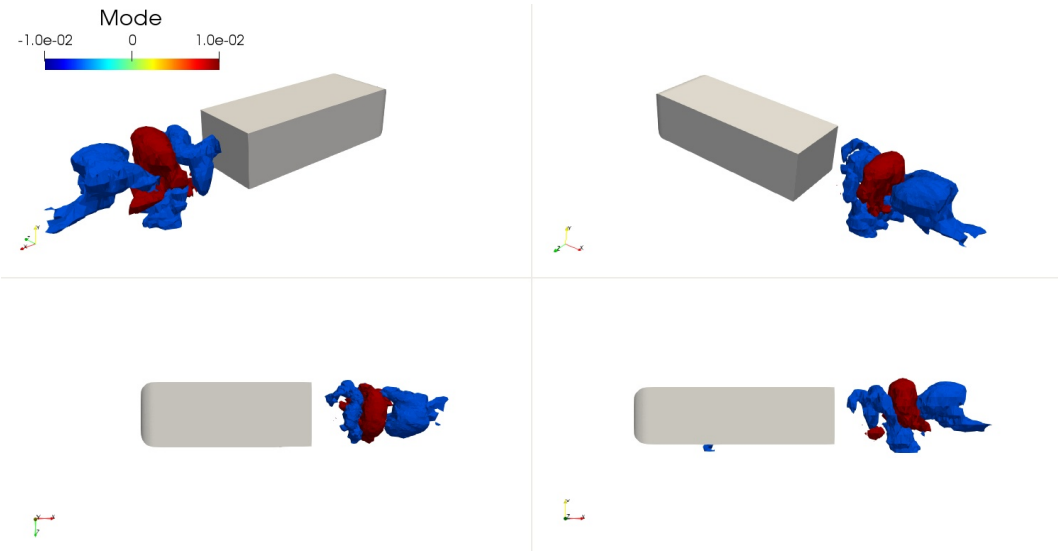

Figure 7.43: Iso-volumes of mode-1 at $St_W = 0.32$, associated with vertical vortex shedding in the wake. The top row shows a three-dimensional view of the wake on both sides of the body. The bottom row shows a top-view of the domain (left) and a side view of the body (right).

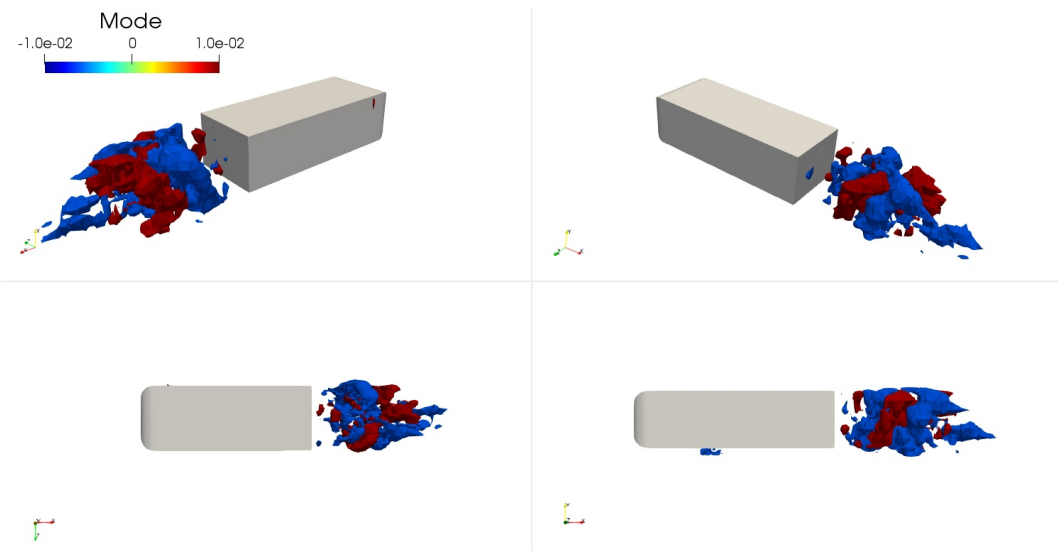

Figure 7.44: Iso-volumes of mode-2 at $St_W = 0.32$, associated with an interaction of the horizontal and vertical vortex shedding in the wake. The top row shows a three-dimensional view of the wake on both sides of the body. The bottom row shows a top-view of the domain (left) and a side view of the body (right).

different frequencies. The most energetic vortices were found to have a relatively high frequency ($St_W > 2$). This high frequency is found to be relevant to the dynamics of the shear layers separated off the base edges.

When the separations of the boundary layers on the sides are suppressed (case-1), SPOD does not capture bi-modal switching. The frequency associated with the bubble pumping is doubled. The vortex shedding frequency slightly increases, with the vertical vortex shedding being more energetic than the horizontal vortex shedding. This is attributed to the suppression of the fluctuations caused by the side boundary layers. The high-frequency dynamics related boundary layer separation are suppressed on the sides and remain on the top surface.

Similar to case-1, bi-modality is suppressed when suction and blowing are applied on the top and bottom body surfaces, respectively. The energy content of the vertical vortex shedding outweighs the horizontal vortex shedding, and both modes are captured at a frequency higher than the corresponding frequency in the unforced flow. The frequency associated with boundary layers dynamics is slightly increased due to the separation induced on the bottom surface, which also amplifies the disturbance in the underbody region. The latter is believed to be the main factor affecting the wake configuration in this case.

When suction is applied on both the top and the bottom surfaces, boundary layer dynamics are suppressed on the top surfaces and amplified in the underbody region. The reflected vertical asymmetry of the wake introduced higher disturbances on the top shear layer in the wake compared to the bottom shear layer, opposite to the shear layers dynamics seen in case-1. Other dynamics in the wake and the upstream regions remain similar to the unforced case.

When boundary layer separation is suppressed on the top and side surfaces (case-3), the high-frequency dynamics are totally suppressed in both the upstream region and the wake. The stochastic horizontal bi-modality is replaced by rapid switching of the wake at a frequency of $St_W \sim 0.027$. The frequency related to vortex shedding in the wake is similar to case-1, with the energy content of the horizontal vortex shedding being lower than the vertical vortex shedding.

To the author's best knowledge, SPOD of the wake flow, where upstream dynamics are suppressed, is not reported previously. However, as the SPOD of the unforced flow matches the SPOD using experimental data (Schmidt et al., 2018, Haffner et al., 2020), the results of the effect of the boundary layer suppression on the wake can be trusted to a good level of confidence at this stage.

Chapter 8

Conclusions and future perspectives

The turbulent wake behind a square-back Ahmed body has been investigated using high-fidelity wall-resolved large eddy simulations. The Reynolds number based on the body height was 3.3×10^4. The simulations successfully captured stochastic bi-modal switching from side-to-side (horizontal bi-modality) as well as three time-periodic modes in the wake: vortex shedding in both cross-flow directions, roll-up of the free shear layers and a streamwise pumping motion of the recirculation bubble. The latter showed a distinguishable mark on the base pressure, which has not been detected in most previous experimental studies. Bi-modality was found to be the most energetic dynamical mode in the wake and found to contribute 9% to pressure drag.

Wake bi-modal switching has previously been suppressed with linear control but resulted in large amplitude oscillations of the wake around the center. This study represents a first attempt to employ a nonlinear model-based controller to suppress bi-modal switching. The unidirectional nature of bi-modality allows using a one-dimensional Langevin equation to model bi-modality. Different approaches were used to design the nonlinear controller, and all of them suppressed wake bi-modality and symmetrised the wake when examined on a toy model.

A controller derived using a quadratic Lyapunov function, was chosen to be applied to the simulation due to its simplicity. The feedback control setup employed base-mounted pressure sensors and actuators (on the based perimeter). Upon implementation in the LES, the controller suppressed bi-modal switching and the resulting levels of wake fluctuations were significantly lower than for previous linear controllers. The extent of the fluctuations in asymmetry was significantly reduced. The nonlinear term of the controller is significant when the wake's asymmetric positions deviate from the linearly dominated region. The action of control changes the stochastic horizontal switching of the wake to an oscillatory motion of the large coherent structure in the near wake region, with a frequency close to the bubble pumping frequency. The controller does not affect the bubble pumping frequency in the wake, yet leads to more energetic vortex shedding in both the

horizontal and vertical directions.

Changing the relative contributions of the linear and nonlinear terms in the control law significantly changes the wake response. The general trend of driving the stochastic bi-modality to time-periodic oscillations holds in all cases, with a trade-off between drag reduction and level of wake asymmetry. A maximum drag reduction of 7.4% is achieved for a semi-symmetrised wake, for which the wake switches periodically between asymmetric positions. A fully-symmetrised wake, with a minimum in residual oscillations around the center of the base, corresponds to a 2.5% reduction in the drag. Suppressing the wake bi-modality using feedback control was shown to re-orient the toroidal vortex structure in the near wake region so that it becomes parallel to the base as well as closer to the base. This consequently disturbs the near-wake shear layers close to the base, limiting the base pressure recovery. It is proposed that this is the main reason that drag reduction is hindered in the case of a full-symmetrised wake. An indirect link between bi-modality suppression and drag reduction is shown. Drag reduction is found to be more sensitive to the interaction between the wake bi-modal behaviour and the shear layers in the switching direction. The effect of this interaction on drag depends on two effects: the unbalanced disturbances imposed on the shear layers and the streamwise position of the disturbances. The latter has a pronounced effect on the base pressure and hence the pressure drag. Controlling this interaction may offer more significant drag reductions, similar to those previously achieved using a base cavity. The current results suggest that control strategies should focus more on suppressing or delaying the interaction between the separated shear layers and the coherent structures in the near-wake region to reduce drag. It also suggests that the actuation position is crucial for suppressing bi-modality without amplifying the disturbance on these shear layers.

The second part of this study investigated the link between the dynamics in the boundary layers on the Ahmed body longitudinal surfaces – related to boundary layer separations – and bi-modality. We proposed that wake bi-modal switching is triggered by the interaction of the vortices formed on the top and side surfaces of the body, which also affects the underbody flow. Interrupting this interaction might then suppress bi-modality and symmetrise the wake.

Steady and spatially-independent suction was used to suppress boundary layer separations on the longitudinal body surfaces. Different cases with suction/blowing on different combinations of body surfaces were investigated. When boundary layer separation is suppressed on only the wall-normal surfaces (side surfaces), the wake becomes horizontally symmetric while retaining its vertical position. In this case, suppressing the side boundary layer disturbances was found to have a direct effect on the disturbances of the free shear layers separated off the side surfaces in the wake region. It also has an indirect favourable effect on the turbulent fluctuations in the underbody flow. These results support the proposed mechanism of the link between wake bi-modality and interaction of

upstream BL vortices. The base pressure is increased by 14% compared to the unforced case. Base pressure recovery achieved by symmetrising the wake indirectly (suppressing upstream dynamics) is almost double the value for when the wake is directly actuated. This represents a new promising strategy for controlling wake bi-modality indirectly, i.e. without actuating the wake region. In light of the Langevin dynamics model, suppressing the upstream dynamics on the sides, which will be thought of as turbulent forcing, was expected to stabilise the wake on an asymmetric position. However, suppressing the upstream dynamics affected both the mean and fluctuated wake flows, leading to a symmetric wake. The results of this case open doors for further investigations of the proposed link.

When boundary layer separation is suppressed on only the wall-parallel surface (top), and the air is sucked through the bottom surface, the wake bi-modality remains, accompanied by an inversion of vertical wake asymmetry. The latter is related to the suppression of top boundary layer separation with little effect on the momentum reduction in the underbody flow due to bottom suction, preserving the weak vertical asymmetry of the wake.

When suction is applied on all four longitudinal surfaces of the body, suppressing the separation of the boundary layer on the top and side surfaces and disturbing the underbody flow, horizontal bi-modality is suppressed, with the wake exhibiting larger oscillation bounds compared to the side-only suction. The study has shown that the disturbances induced in the underbody flow become partly cancelled close to the base by the compensating effect of suppressing the side boundary layer disturbances. The wake is weakly asymmetric in the vertical direction, with the asymmetry inverted compared to the unforced flow. This suggests that bi-modality suppression is due to suppression of the side boundary layer disturbances, similar to side-only suction.

The effect of different forcing configurations on the periodic modes in the wake was investigated using spectral proper orthogonal decomposition. When bi-modality is suppressed without changing the wake vertical balance, the energy content of the horizontal vortex shedding is found to decrease, while an opposite effect is observed for the vertical vortex shedding. The low-frequency bubble pumping mode remains unaffected. The results showed that the base pressure recovery is influenced by the streamwise position and the orientation of the toroidal structure occupying the near wake region. Its orientation represents the wake configuration, i.e. the horizontal bi-modality and the vertical balance. For a base-parallel toroidal vortex, higher base pressure recovery is associated with this structure being moved farther downstream of the base.

These results represent a first step towards investigating upstream control strategies for bi-modality suppression. Such an approach offers promise for achieving drag reduction and bi-modality suppression, something that actuating the wake directly has been unable to fully achieve, particularly when wake actuation affects the free shear layers.

Appendix A

The details of the different methods used to design a nonlinear control to suppress bi-modality are discussed in this appendix.

A.1 Artstein-Sontag Universal controller

A controller based on the Artstein-Sontag Universal controller (Sontag and Sussmann, 1995) (equation A.1) using a quadratic Lyapunov function $V(r) = 1/2\ r^2$, is synthesised.

$$\begin{cases} \frac{-\frac{\partial V}{\partial r} f(r) + \sqrt{(\frac{\partial V}{\partial r} f(r))^2 + (\frac{\partial V}{\partial r} g(r))^4}}{\frac{\partial V}{\partial r} g(r)} & , \quad \frac{\partial V}{\partial r} g(r) \neq 0 \\ 0 & , \quad \frac{\partial V}{\partial r} g(r) = 0 \end{cases} \tag{A.1}$$

Assuming the system is represented by equation A.2.

$$\dot{r} = f(r) + g(r)u(r) \tag{A.2}$$

The control law is given by equation A.3.

$$u(r) = -(-\lambda r^3 + \alpha r) - |\sqrt{(-\lambda r^3 + \alpha r)^2 + r^2}| \tag{A.3}$$

A.2 Backstepping method

Backstepping is a recursive procedure that interlaces with choosing a suitable Lyapunov function. It includes breaking the design of the non-linear control of the system into sequences of design problems of sub-systems. It requires defining the sub-system and using the stability of the sub-system to stabilize the whole system. The sub-system represents the error state or the uncertainty (Hua et al., 2005). Subsequently, the backstepping method involves finding the Lyapunov function for the sub-system and the augmented Lyapunov function for the whole system. The RSB model can be assumed to be described by equations A.4 and A.5.

$$\dot{r_1} = -\lambda {r_1}^3 + \alpha r_1 + r_2 \tag{A.4}$$

$$\dot{r_2} = u(r_1, r_2) \tag{A.5}$$

The backstepping method seeks r_2 to stabilise the first equation of the system (equation A.4), then to find $u(r_1, r_2)$ (equation A.5) to stabilise the whole system. Assume the state r_2 can be represented by equation A.6 where μ is an arbitrary constant.

$$r_2 \approx \alpha_1(r_1) = \lambda {r_1}^3 - \mu r_1 \qquad \alpha_1(0) = 0 \tag{A.6}$$

The error (subsystem) is defined as the difference between $\alpha_1(r_1)$ and r_2; this error system is defined in equations A.7 and A.8.

$$z_1 = r_1 \tag{A.7}$$

$$z_2 = r_2 - \alpha_1(r_1) \tag{A.8}$$

Assuming a same quadratic Lyapunov function $V(z_1) = 1/2{z_1}^2$, the condition to force a negative definite time-derivative of $V(z_1)$ is $\mu > \alpha$. The augmented Lyapunov function for the whole system is given by equation A.9.

$$V(z_1, z_2) = \frac{1}{2}\ {z_1}^2 + \frac{1}{2}\ {z_2}^2 \tag{A.9}$$

The resultant control law, in this case, is shown in equation A.10.

$$u(r) = -(-\lambda {r_1}^3 + \alpha r_1 + r_2) + (\alpha - \mu - 1) r_1 + (\alpha r_1 + r_2 - \lambda {r_1}^3)(3\lambda {r_1}^2 - \mu) \quad , \quad r_2 = \lambda {r_1}^3 - \mu r_1 \tag{A.10}$$

Figure A.1 shows the time derivative of the augmented Lyapunov function, which indicates that it is a negative definite function, i.e. the system will be asymptotically stable.

Another control law is designed using the same backstepping method. In this case, the controller utilises the benefit of the non-linear term of the model equation in resymmetrising the system. The design is based on the same subsystems shown in equation A.4 and A.5 and assuming that the second state r_2 is only suppressing the linear terms, as shown in equation A.11.

$$r_2 \approx \alpha_1(r_1) = -\mu r_1 \qquad \alpha_1(0) = 0 \tag{A.11}$$

Thus, the origin of $\dot{r_1} = -(-\lambda {r_1}^3 + \alpha r_1 + r_2)$ is asymptotically stable, and the resulting controller is given by equation A.12.

$$u(r) = -(\alpha r_1 + r_2) - r_1 - \alpha(\alpha r_1 + r_2 - \lambda {r_1}^3) \qquad , \qquad r_2 = -\mu r_1 \tag{A.12}$$

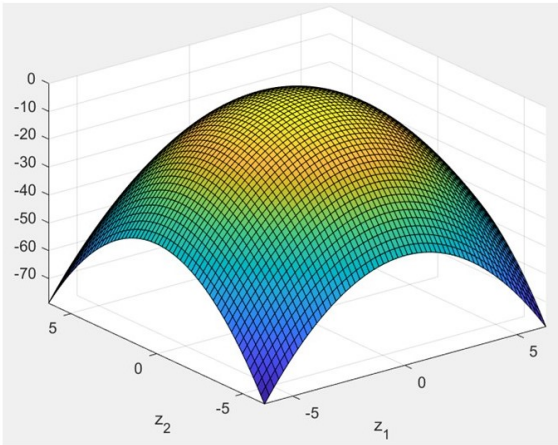

Figure A.1: Time-derivative augmented Lyapunov function for the system considered using the Backstepping method

The above four control laws synthesised based on Lyapunov functions ensure the system's asymptotic stability at r=0 within a region of attraction that includes the entire state space.

A.3 Optimal control - Hamiltonian-Jacobi-Isaacs

The Hamiltonian-Jacobi-Isaacs method is employed to design a non-linear controller, assuming a cost function of equal weights of the state and the control law, as shown in equation A.13.

$$J = \min_{u(t)\in R} \int_0^\infty [r^2(t) + u^2(t)]dt \tag{A.13}$$

The system's initial condition is considered to be unknown. Previous work by Grandemange et al. (2013b) confirmed that in the turbulent case, the wake shifts to one of the asymmetric positions at the beginning; thus, an assumption made in this case that the system, described by equation A.14, has a non-zero initial condition.

$$\begin{cases} \dot{r} = -\lambda r^3 + \alpha r + u(r) \\ r(0) = C \end{cases} \tag{A.14}$$

Equation A.15 defines the Hamiltonian equation of the system Berkovitz (1999).

$$H(r(t), u(t), \lambda^*(t), t) = r^2(t) + u^2(t) + \lambda^*(t)(-\lambda r^3 + \alpha r + u) \tag{A.15}$$

This leads to the dynamical system shown by equation A.16, and the solution for this system using the time-elimination method leads to equation A.17. Solving equation A.17, the control law $u(r)$

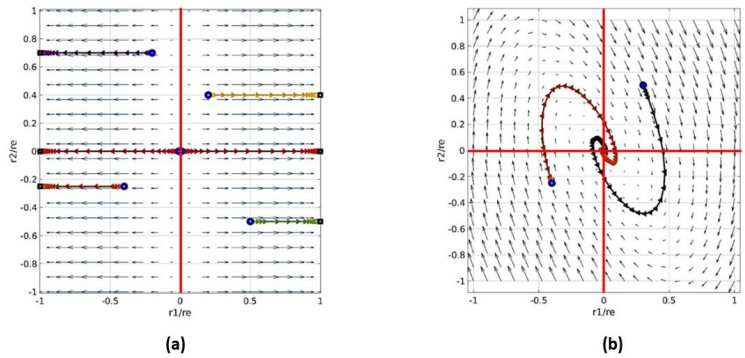

Figure A.2: Phase-plane portrait for the unforced system (a) and the controlled system using backstepping controller (b). The blue dots represent the initial condition of the system, which is always driven to $r_1/r_e = \pm 1$ in the unforced case. The controlled case indicates that $r = 0$ is an asymptotically stable point of the system.

is found, as shown in equation A.18.

$$\begin{cases} \dot{r} = -\lambda r^3 + \alpha r + u(r) \\ \dot{u} = -r + u(\alpha - 3\lambda r^2) \end{cases} \tag{A.16}$$

$$\frac{\dot{u}}{\dot{r}} = \frac{du}{dr} = \frac{-r + u(\alpha - 3\lambda r^2)}{-\lambda r^3 + \alpha r + u(r)} \tag{A.17}$$

$$u(r) = \lambda r^3 - \alpha r - r\sqrt{\lambda^2 r^4 - 2\lambda\alpha r^2 + (\alpha^2 + 1)} \tag{A.18}$$

Figure A.2 depicts the phase-plane portrait for both the uncontrolled and the controlled system. The unforced case indicates that the system model drives the state r_1 to $r_1/r_e = \pm 1$, with a probability that depends on the initial state, except for $r = 0$, the endpoint of the trajectory is equiprobable. The trajectory of the evolution of r is linear. When backstepping control is used, another state r_2 is defined in addition to r_1. The phase portrait shown in figure A.2b indicates that for a given initial state of (r_1, r_2), the controller forces this state towards the centre $(0, 0)$ through an elliptical trajectory. This confirms that $(0, 0)$ is an asymptotically stable point of the system.

Appendix B

Table B.1 shows the status of of the permissions for reproducing figures from copyright holders.

Fig. No.	Fig. Source	Permission
1.1	Buysse and Miller (2021)	Approved
1.2	Office of Scientific and Technical Information (2000)	Pending
2.1	Li (2017)	Approved
2.2	Choi et al. (2014)	CCC-pending
2.3	Choi et al. (2014)	CCC-pending
2.4	Krajnovic and Davidson (2003)	ASME-Approved
2.5	Grandemange et al. (2012)	Approved
2.6	Grandemange et al. (2013a)	Approved
2.7	Dalla Longa et al. (2019)	Approved
2.8	Choi et al. (2008)	CCC-pending
2.10	Choi et al. (2014)	CCC-pending
2.11	Choi et al. (2014)	CCC-pending
2.12	Hsu et al. (2021)	Approved
2.13	Li et al. (2016)	Approved
2.14	Strzelczyk and Gil (2016)	Approved
2.14	Aram et al. (2010)	Approved
3.2	Schmidt and Towne (2019)	Approved
5.2	Brackston et al. (2016)	Approved
6.23	Kang et al. (2021)	Approved

Table B.1: Permissions for figures reproduction from Copyright holders.

Bibliography

M. Agelinchaab and M. F. Tachie. PIV study of separated and reattached open channel flow over surface mounted blocks. *Journal of Fluids Engineering*, 130(6), 2008.

D. Ahmed and A. S. Morgans. Nonlinear feedback control of bimodality in the wake of a three-dimensional bluff body. *Physical Review Fluids*, 7:084401, Aug 2022. doi: 10.1103/PhysRevFluids.7.084401. URL https://link.aps.org/doi/10.1103/PhysRevFluids.7.084401.

S. R. Ahmed, G. Ramm, and G. Faltin. Some salient features of the time-averaged ground vehicle wake. *SAE Transactions*, pages 473–503, 1984.

E. Aram, R. Mittal, and L. Cattafesta. Simple representations of zero-net mass-flux jets in grazing flow for flow-control simulations. *International Journal of Flow Control*, 2(2), 2010.

Z. Artstein. Stabilization with relaxed controls. *Nonlinear Analysis: Theory, Methods and Applications*, 7(11):1163–1173, 1983.

S. Balachandar, R. Mittal, and F. Najjar. Properties of the mean recirculation region in the wakes of two-dimensional bluff bodies. *Journal of Fluid Mechanics*, 351:167–199, 1997.

S. R. Balkanyi, L. P. Bernal, and B. Khalighi. Analysis of the near wake of bluff bodies in ground proximity. In *ASME International Mechanical Engineering Congress and Exposition*, volume 36576, pages 705–713, 2002.

D. Bao, J. Borée, Y. Haffner, and C. Sicot. Near wake interactions and drag increase regimes for a square-back bluff body. *Journal of Fluid Mechanics*, 936, 2022.

J. Barlow, R. Guterres, R. Ranzenbach, and J. Williams. Wake structures of rectangular bodies with radiused edges near a plane surface. Technical report, SAE Technical Paper, 1999.

D. Barros, J. Borée, B. R. Noack, A. Spohn, and T. Ruiz. Bluff body drag manipulation using pulsed jets and coanda effect. *Journal of Fluid Mechanics*, 805:422–459, 2016.

D. Barros, J. Borée, O. Cadot, A. Spohn, and B. R. Noack. Forcing symmetry exchanges and flow reversals in turbulent wakes. *Journal of Fluid Mechanics*, 829, 2017.

I. E. Barton. Comparison of simple-and piso-type algorithms for transient flows. *International Journal for Numerical Methods in Fluids*, 26(4):459–483, 1998.

P. W. Bearman. Near wake flows behind two-and three-dimensional bluff bodies. *Journal of Wind Engineering and Industrial Aerodynamics*, 69:33–54, 1997.

J. S. Bendat and A. G. Piersol. *Random data: analysis and measurement procedures.* John Wiley & Sons, 2011.

E. Berger, D. Scholz, and M. Schumm. Coherent vortex structures in the wake of a sphere and a circular disk at rest and under forced vibrations. *Journal of Fluids and Structures*, 4(3):231–257, 1990.

N. Berkeley, D. Jarvis, and A. Jones. Analysing the take up of battery electric vehicles: An investigation of barriers amongst drivers in the uk. *Transportation Research Part D: Transport and Environment*, 63:466–481, 2018.

L. D. Berkovitz. A generalized hamilton—jacobi—bellman equation for deterministic optimal control problems. In *Stochastic Analysis, Control, Optimization and Applications*, pages 223–235. Springer, 1999.

G. Bouchet, M. Mebarek, and J. Dušek. Hydrodynamic forces acting on a rigid fixed sphere in early transitional regimes. *European Journal of Mechanics-B/Fluids*, 25(3):321–336, 2006.

R. D. Brackston, J. M. García De La Cruz, A. Wynn, G. Rigas, and J. F. Morrison. Stochastic modelling and feedback control of bistability in a turbulent bluff body wake. *Journal of Fluid Mechanics*, 802:726–749, 2016.

P. Bradshaw. Effects of streamline curvature on turbulent flow. Technical report, ADVISORY GROUP FOR AEROSPACE RESEARCH AND DEVELOPMENT PARIS (FRANCE), 1973.

G. A. Bres and T. Colonius. Three-dimensional instabilities in compressible flow over open cavities. *Journal of Fluid Mechanics*, 599:309–339, 2008.

A. Burkert, H. Fechtner, and B. Schmuelling. Interdisciplinary analysis of social acceptance regarding electric vehicles with a focus on charging infrastructure and driving range in germany. *World Electric Vehicle Journal*, 12(1):25, 2021.

D. Burton, S. Wang, D. T. Smith, H. Scott, T. Crouch, and M. Thompson. The Influence of Background Turbulence on Ahmed-Body Wake Bistability. *Journal of Fluid Mechanics*, 2021.

C. Buysse and J. Miller. TRANSPORT COULD BURN UP THE EU'S ENTIRE CARBON BUDGET, 2021. URL https://theicct.org/transport-could-burn-up-the-eus-entire-carbon-budget/.

S. Cabitza. *Active control of the wake from a rectangular-sectioned body.* PhD thesis, Imperial College London, 2014.

O. Cadot, A. Evrard, and L. Pastur. Imperfect supercritical bifurcation in a three-dimensional turbulent wake. *Physical Review E*, 91(6):063005, 2015.

O. Cadot, M. Almarzooqi, A. Legeai, V. Parezanović, and L. Pastur. On three-dimensional bluff body wake symmetry breaking with free-stream turbulence and residual asymmetry. *Comptes Rendus. Mécanique*, 348(6-7):509–517, 2020.

T. Castelain, M. Michard, M. Szmigiel, D. Chacaton, and D. Juvé. Identification of flow classes in the wake of a simplified truck model depending on the underbody velocity. *Journal of Wind Engineering and Industrial Aerodynamics*, 175:352–363, 2018.

H. Choi, W.-P. Jeon, and J. Kim. Control of flow over a bluff body. *Annual Review of Fluid Mechanics*, 40:113–139, 2008.

H. Choi, J. Lee, and H. Park. Aerodynamics of heavy vehicles. *Annual Review of Fluid Mechanics*, 46:441–468, 2014.

J. A. Dahan, A. Morgans, and S. Lardeau. Feedback control for form-drag reduction on a bluff body with a blunt trailing edge. *Journal of Fluid Mechanics*, 704:360–387, 2012.

L. Dalla Longa, A. S. Morgans, and J. A. Dahan. Reducing the pressure drag of a D-shaped bluff body using linear feedback control. *Theoretical and Computational Fluid Dynamics*, 31(5): 567–577, 2017.

L. Dalla Longa, O. Evstafyeva, and A. S. Morgans. Simulations of the bi-modal wake past three-dimensional blunt bluff bodies. *Journal of Fluid Mechanics*, 866:791–809, 2019.

N. Djilali and I. Gartshore. Turbulent flow around a bluff rectangular plate. part i: Experimental investigation. *Journal of Fluids Engineering*, 1991.

E. G. Duell and A. R. George. Experimental study of a ground vehicle body unsteady near wake. *SAE Transactions*, pages 1589–1602, 1999.

R. J. Englar. Advanced aerodynamic devices to improve the performance, economics, handling and safety of heavy vehicles. Technical report, SAE Technical Paper, 2001.

Y. Eulalie, P. Gilotte, I. Mortazavi, and P. Bobillier. Wake analysis and drag reduction for a square back Ahmed body using LES computations. In *ASME 2014 4th Joint US-European Fluids Engineering Division Summer Meeting collocated with the ASME 2014 12th International Conference on Nanochannels, Microchannels, and Minichannels*. American Society of Mechanical Engineers Digital Collection, 2014.

European Environmental Agency. Is europe reducing its greenhouse gas emissions?, 2022. URL https://www.eea.europa.eu/themes/climate/eu-greenhouse-gas-inventory.

A. Evrard, O. Cadot, V. Herbert, D. Ricot, R. Vigneron, and J. Délery. Fluid force and symmetry breaking modes of a 3D bluff body with a base cavity. *Journal of Fluids and Structures*, 61: 99–114, 2016.

O. Evstafyeva. *Simulation and feedback control of simplified vehicle flows*. PhD thesis, Imperial College London, 2018.

O. Evstafyeva, A. Morgans, and L. Dalla Longa. Simulation and feedback control of the ahmed body flow exhibiting symmetry breaking behaviour. *Journal of Fluid Mechanics*, 817, 2017.

D. Fan, B. Zhang, Y. Zhou, and B. R. Noack. Optimization and sensitivity analysis of active drag reduction of a square-back ahmed body using machine learning control. *Physics of Fluids*, 32 (12), 2020a.

Y. Fan and O. Cadot. Reynolds number effect on the bistable dynamic of a blunt-base bluff body. *Physical Review E*, 107:025103, 2023.

Y. Fan, C. Xia, S. Chu, Z. Yang, and O. Cadot. Experimental and numerical analysis of the bistable turbulent wake of a rectangular flat-backed bluff body. *Physics of Fluids*, 32(10):105111, 2020b.

J. H. Ferziger. Large eddy numerical simulations of turbulent flows. *AIAA Journal*, 15(9):1261–1267, 1977.

T. Flinois. *Modelling and linear feedback control of bluff body flows*. PhD thesis, Imperial College London, 2015.

G. Franck, N. M. Nigro, M. A. Storti, and J. D'Elia. Numerical simulation of the Ahmed vehicle model near-wake. *Cuadernos de Matemática y Mecánica*, 2007.

J. H. Gerrard. The mechanics of the formation region of vortices behind bluff bodies. *Journal of Fluid Mechanics*, 25(2):401–413, 1966.

P. Gilliéron and A. Kourta. Aerodynamic drag reduction by vertical splitter plates. *Experiments in Fluids*, 48(1):1–16, 2010.

A. Glezer and M. Amitay. Synthetic jets. *Annual Review of Fluid Mechanics*, 34(1):503–529, 2002.

M. Grandemange, O. Cadot, and M. Gohlke. Reflectional symmetry breaking of the separated flow over three-dimensional bluff bodies. *Physical Review E*, 86(3):035302, 2012.

M. Grandemange, M. Gohlke, and O. Cadot. Bi-stability in the turbulent wake past parallelepiped bodies with various aspect ratios and wall effects. *Physics of Fluids*, 25(9):095103, 2013a.

M. Grandemange, M. Gohlke, and O. Cadot. Turbulent wake past a three-dimensional blunt body. part 1. global modes and bi-stability. *Journal of Fluid Mechanics*, 722:51–84, 2013b.

M. Grandemange, M. Gohlke, and O. Cadot. Statistical axisymmetry of the turbulent sphere wake. *Experiments in Fluids*, 55(11):1–11, 2014a.

M. Grandemange, M. Gohlke, and O. Cadot. Turbulent wake past a three-dimensional blunt body. Part 2. Experimental sensitivity analysis. *Journal of Fluid Mechanics*, 752:439–461, 2014b.

C. Greenshields and H. Weller. *Notes on Computational Fluid Dynamics: General Principles*. CFD Direct Ltd, Reading, UK, 2022.

B. F. W. Gschaider. README for swak4Foam - Version for OpenFOAM 2.x. https://github.com/Unofficial-Extend-Project-Mirror/openfoam-extend-swak4Foam-dev/blob/master/README, 2020.

Y. Haffner, J. Borée, A. Spohn, and T. Castelain. Mechanics of bluff body drag reduction during transient near-wake reversals. *Journal of Fluid Mechanics*, 894, 2020.

T. Han. Computational analysis of three-dimensional turbulent flow around a bluff body in ground proximity. *AIAA Journal*, 27(9):1213–1219, 1989.

L. Henning and R. King. Drag reduction by closed-loop control of a separated flow over a bluff body with a blunt trailing edge. In *Proceedings of the 44th IEEE Conference on Decision and Control*, pages 494–499. IEEE, 2005.

F. Hesse. *Flow control for road vehicle drag reduction*. PhD thesis, Imperial College London, 2021.

F. Hesse and A. Morgans. Simulation of wake bimodality behind squareback bluff-bodies using LES. *Computers & Fluids*, 223:104901, 2021.

R. J. A. Howard and M. J. B. M. Pourquie. Large eddy simulation of an Ahmed reference model. *Journal of Turbulence*, 3(1):012, 2002.

R. M. Howard. *Principles of random signal analysis and low noise design: The power spectral density and its applications*. John Wiley & Sons, 2004.

J. Howell, A. Sheppard, and A. Blakemore. Aerodynamic drag reduction for a simple bluff body using base bleed. *SAE Transactions*, pages 1085–1091, 2003.

E.-C. Hsu, L. Pastur, O. Cadot, and V. Parezanović. A fundamental link between steady asymmetry and separation length in the wake of a 3D square-back body. *Experiments in Fluids*, 62 (5):1–5, 2021.

C. Hua, X. Guan, and P. Shi. Robust backstepping control for a class of time delayed systems. *IEEE Transactions on Automatic Control*, 50(6):894–899, 2005.

B. Hubbard. Mercedes vision eqxx: 625-mile ev with ground-breaking drag coefficient, 2022. URL https://www.whichev.net/2022/01/07/mercedes-vision-eqxx-625-mile-ev-with-ground-breaking-drag-coefficient.

W. Hucho and G. Sovran. Aerodynamics of road vehicles. *Annual Review of Fluid Mechanics*, 25 (1):485–537, 1993.

W.-H. Hucho, editor. *Aerodynamics of Road Vehicles*. Butterworth-Heinemann, 1987. ISBN 978-0-7506-1267-8. doi: https://doi.org/10.1016/B978-0-7506-1267-8.50001-4. URL https://www.sciencedirect.com/science/article/pii/B9780750612678500014.

IEA. World energy outlook 2018, 2018. URL https://www.iea.org/reports/world-energy-outlook-2018.

IEA. Transport, iea, 2022. URL https://www.iea.org/reports/transport.

R. I. Issa. Solution of the implicitly discretised fluid flow equations by operator-splitting. *Journal of Computational Physics*, 62(1):40–65, 1986.

R. Jahanbakhshi. Mechanisms of entrainment in a turbulent boundary layer. *Physics of Fluids*, 33(3):035105, 2021.

S. Jakirlic, R. Jester-Zürker, and C. Tropea. 9th ERCOFTAC/IAHR. In *COST workshop on refined turbulence modelling*, pages 36–43, 2001.

N. Kang, E. E. Essel, V. Roussinova, and R. Balachandar. Effects of approach flow conditions on the unsteady three-dimensional wake structure of a square-back Ahmed body. *Physical Review Fluids*, 6(3):034613, 2021.

B. Khalighi, S. Zhang, C. Koromilas, S. Balkanyi, L. P. Bernal, G. Iaccarino, and P. Moin. Experimental and computational study of unsteady wake flow behind a bluff body with a drag reduction device. *SAE Transactions*, pages 1209–1222, 2001.

B. Khalighi, K. Chen, and G. Iaccarino. Unsteady aerodynamic flow investigation around a simplified square-back road vehicle with drag reduction devices. *Journal of Fluids Engineering*, 134 (6), 2012.

T. I. Khan, V. Parezanović, L. Pastur, and O. Cadot. Suppression of the wake steady asymmetry of an ahmed body by central base bleed. *Physical Review Fluids*, 7(8):083902, 2022.

R. King, M. Seibold, O. Lehmann, B. Noack, M. Morzyński, G. Tadmor, et al. Nonlinear flow control based on a low dimensional model of fluid flow. In *Control and Observer Design for Nonlinear Finite and Infinite Dimensional Systems*, pages 369–386. Springer, 2005.

A. Kourta and C. Leclerc. Characterization of synthetic jet actuation with application to Ahmed body wake. *Sensors and Actuators A: Physical*, 192:13–26, 2013.

S. Krajnovic and L. Davidson. Numerical study of the flow around a bus-shaped body. *Journal of Fluids Engineering*, 125(3):500–509, 2003.

A. Lahaye, A. Leroy, and A. Kourta. Aerodynamic characterisation of a square back bluff body flow. *International Journal of Aerodynamics*, 4(1-2):43–60, 2014.

A. Leonard. Energy cascade in large-eddy simulations of turbulent fluid flows. In *Advances in Geophysics*, volume 18, pages 237–248. Elsevier, 1975.

M. A. Leschziner and S. Lardeau. Simulation of slot and round synthetic jets in the context of boundary-layer separation control. *Philosophical Transactions of the Royal Society A: Mathematical, Physical and Engineering Sciences*, 369(1940):1495–1512, 2011.

R. Li. *Aerodynamic Drag Reduction of a Square-Back Car Model Using Linear Genetic Programming and Physic-Based Control*. PhD thesis, ISAE-ENSMA Ecole Nationale Supérieure de Mécanique et d'Aérotechique-Poitiers, 2017.

R. Li, D. Barros, J. Borée, O. Cadot, B. R. Noack, and L. Cordier. Feedback control of bimodal wake dynamics. *Experiments in Fluids*, 57(10):158, 2016.

R. Littlewood and M. A. Passmore. Aerodynamic drag reduction of a simplified squareback vehicle using steady blowing. *Experiments in Fluids*, 53(2):519–529, 2012.

M. Lorite-Díez, J. Jiménez-González, L. Pastur, C. Martínez-Bazán, and O. Cadot. Experimental analysis of the effect of local base blowing on three-dimensional wake modes. *Journal of Fluid Mechanics*, 883, 2020.

J.-M. Lucas, O. Cadot, V. Herbert, S. Parpais, and J. Délery. A numerical investigation of the asymmetric wake mode of a squareback Ahmed body–effect of a base cavity. *Journal of Fluid Mechanics*, 831:675–697, 2017.

J. L. Lumley. The structure of inhomogeneous turbulent flows. *Atmospheric Turbulence and Radio Wave Propagation*, pages 166–178, 1967.

R. Manceau. Report on the 10th joint ERCOFTAC (SIG-15)/IAHR/QNET-CFD Workshop on Refined Turbulence Modelling, Poitiers, october 10-11, 2002. *ERCOFTAC Bulletin*, 57:11–14, 2003.

W. T. Mason and P. S. Beebe. The drag related flow field characteristics of trucks and buses. In *Aerodynamic Drag Mechanisms of Bluff Bodies and Road Vehicles*, pages 45–93. Springer, 1978.

C. Meneveau and J. Katz. Scale-invariance and turbulence models for large-eddy simulation. *Annual Review of Fluid Mechanics*, 32(1):1–32, 2000.

M. Minguez, R. Pasquetti, and E. Serre. High-order large-eddy simulation of flow over the "Ahmed body" car model. *Physics of Fluids*, 20(9):095101, 2008.

T. Moghaddam and N. B. Neishabouri. On the active and passive flow separation control techniques over airfoils. In *IOP Conference Series: Materials Science and Engineering*, volume 248, page 012009. IOP Publishing, 2017.

P. Moin and K. Mahesh. Direct numerical simulation: a tool in turbulence research. *Annual Review of Fluid Mechanics*, 30(1):539–578, 1998.

M. Mruzek, I. Gajdáč, L. Kučera, and D. Barta. Analysis of parameters influencing electric vehicle range. *Procedia Engineering*, 134:165–174, 2016.

F. Nicoud and F. Ducros. Subgrid-scale stress modelling based on the square of the velocity gradient tensor. *Flow, Turbulence and Combustion*, 62(3):183–200, 1999.

H. J. Nussbaumer. The fast fourier transform. In *Fast Fourier Transform and Convolution Algorithms*, pages 80–111. Springer, 1981.

Office of Scientific and Technical Information (U.S. Department of Energy). Technology Roadmap for the 21st Century Truck Program, a government-industry research partnership. 2000. doi: 10.2172/777307. URL https://www.osti.gov/biblio/777307.

A. R. Oxlade, J. F. Morrison, A. Qubain, and G. Rigas. High-frequency forcing of a turbulent axisymmetric wake. *Journal of Fluid Mechanics*, 770:305–318, 2015.

R. Pasquetti and N. Peres. A penalty model of synthetic micro-jet actuator with application to the control of wake flows. *Computers & Fluids*, 114:203–217, 2015.

S. V. Patankar and D. B. Spalding. A calculation procedure for heat, mass and momentum transfer in three dimensional parabolic flows. *International Journal of Heat and Mass Transfer*, 15:1787–1805, 1972.

U. Piomelli. Large-eddy simulation: achievements and challenges. *Progress in Aerospace Sciences*, 35(4):335–362, 1999.

U. Piomelli and J. R. Chasnov. Large-eddy simulations: theory and applications. In *Turbulence and Transition Modelling*, pages 269–336. Springer, 1996.

B. Plumejeau, L. Keirsbulck, S. Delprat, M. Lippert, and W. Abassi. Behavior of the square-back Ahmed body global modes at low ground clearance. *Physical Review Fluids*, 5(8):084701, 2020.

B. Podvin, S. Pellerin, Y. Fraigneau, A. Evrard, and O. Cadot. Proper orthogonal decomposition analysis and modelling of the wake deviation behind a squareback ahmed body. *Physical Review Fluids*, 5(6):064612, 2020.

B. Podvin, S. Pellerin, Y. Fraigneau, G. Bonnavion, and O. Cadot. Low-order modelling of the wake dynamics of an ahmed body. *Journal of Fluid Mechanics*, 927:R6, 2021.

A. N. Rao, G. Minelli, J. Zhang, B. Basara, and S. Krajnović. Investigation of the near-wake flow topology of a simplified heavy vehicle using PANS simulations. *Journal of Wind Engineering and Industrial Aerodynamics*, 183:243–272, 2018.

S. Rashidi, M. Hayatdavoodi, and J. A. Esfahani. Vortex shedding suppression and wake control: A review. *Ocean Engineering*, 126:57–80, 2016.

G. Rigas, A. Oxlade, A. Morgans, and J. Morrison. Low-dimensional dynamics of a turbulent axisymmetric wake. *Journal of Fluid Mechanics*, 755, 2014.

G. Rigas, A. S. Morgans, R. D. Brackston, and J. F. Morrison. Diffusive dynamics and stochastic models of turbulent axisymmetric wakes. *Journal of Fluid Mechanics*, 778, 2015.

G. Rigas, L. Esclapez, and L. Magri. Symmetry breaking in a 3D bluff-body wake. *arXiv preprint arXiv:1703.07405*, 2017.

M. Rouméas, P. Gilliéron, and A. Kourta. Analysis and control of the near-wake flow over a square-back geometry. *Computers & Fluids*, 38(1):60–70, 2009.

P. Sagaut. *Large eddy simulation for incompressible flows: an introduction*. Springer Science & Business Media, 2006.

H. Schlichting and K. Gersten. *Boundary-layer theory.* Springer Science & Business Media, 2003.

P. J. Schmid. Dynamic mode decomposition of numerical and experimental data. *Journal of Fluid Mechanics*, 656:5–28, 2010.

H.-J. Schmidt, R. Woszidlo, C. N. Nayeri, and C. O. Paschereit. The effect of flow control on the wake dynamics of a rectangular bluff body in ground proximity. *Experiments in Fluids*, 59(6): 107, 2018.

O. T. Schmidt and T. Colonius. Guide to spectral proper orthogonal decomposition. *AIAA Journal*, 58(3):1023–1033, 2020.

O. T. Schmidt and A. Towne. An efficient streaming algorithm for spectral proper orthogonal decomposition. *Computer Physics Communications*, 237:98–109, 2019.

A. Seifert, O. Stalnov, D. Sperber, G. Arwatz, V. Palei, S. David, I. Dayan, and I. Fono. Large trucks drag reduction using active flow control. In *The Aerodynamics of Heavy Vehicles II: Trucks, Buses, and Trains*, pages 115–133. Springer, 2009.

E. Serre, M. Minguez, R. Pasquetti, E. Guilmineau, G. B. Deng, M. Kornhaas, M. Schäfer, J. Fröhlich, C. Hinterberger, and W. Rodi. On simulating the turbulent flow around the Ahmed body: A French–German collaborative evaluation of LES and DES. *Computers & Fluids*, 78:10–23, 2013.

L. Sirovich. Turbulence and the dynamics of coherent structures. I. Coherent structures. *Quarterly of Applied Mathematics*, 45(3):561–571, 1987.

E. Sontag and H. J. Sussmann. Nonsmooth control-lyapunov functions. In *Proceedings of 1995 34th IEEE Conference on Decision and Control*, volume 3, pages 2799–2805. IEEE, 1995.

A. Spohn and P. Gilliéron. Flow separations generated by a simplified geometry of an automotive vehicle. In *IUTAM Symposium: Unsteady Separated Flows*, volume 1. Kluwer Academic,, 2002.

P. Strzelczyk and P. Gil. Properties of velocity field in the vicinity of synthetic jet generator. In *Journal of Physics: Conference Series*, volume 760, page 012029. IOP Publishing, 2016.

M. N. Sudin, M. A. Abdullah, S. A. Shamsuddin, F. R. Ramli, and M. M. Tahir. Review of research on vehicles aerodynamic drag reduction methods. *International Journal of Mechanical and Mechatronics Engineering*, 14(02):37–47, 2014.

TheOpenFOAMFoundation. OpenFOAM v6 User Guide. https://cfd.direct/openfoam/user-guide-v6, 2018.

P. Tokumaru and P. Dimotakis. Rotary oscillation control of a cylinder wake. *Journal of Fluid Mechanics*, 224:77–90, 1991.

A. Towne, O. T. Schmidt, and T. Colonius. Spectral proper orthogonal decomposition and its relationship to dynamic mode decomposition and resolvent analysis. *Journal of Fluid Mechanics*, 847:821–867, 2018.

E. Varon, J. Aider, Y. Eulalie, S. Edwige, and P. Gilotte. Adaptive control of the dynamics of a fully turbulent bimodal wake using real-time PIV. *Experiments in Fluids*, 60(8):1–21, 2019.

D. Veerasamy, A. Tajik, L. Pastur, and V. Parezanović. Effect of base blowing by a large-scale fluidic oscillator on the bistable wake behind a flat-back ahmed body. *Physics of Fluids*, 34(3): 035115, 2022.

H. K. Versteeg and W. Malalasekera. *An introduction to computational fluid dynamics: the finite volume method*. Pearson education, 2007.

R. Verzicco, M. Fatica, G. Iaccarino, P. Moin, and B. Khalighi. Large eddy simulation of a road vehicle with drag-reduction devices. *AIAA Journal*, 40(12):2447–2455, 2002.

R. Volpe, P. Devinant, and A. Kourta. Experimental characterization of the unsteady natural wake of the full-scale square back Ahmed body: flow bi-stability and spectral analysis. *Experiments in Fluids*, 56(5):1–22, 2015.

E. Wassen, S. Eichinger, and F. Thiele. Simulation of active drag reduction for a square-back vehicle. In *Active Flow Control II: Papers Contributed to the Conference" Active Flow Control II 2010", Berlin, Germany, May 26 to 28, 2010*, pages 241–255. Springer, 2010.

J. Weiss. A tutorial on the proper orthogonal decomposition. In *AIAA aviation 2019 forum*, page 3333, 2019.

D. Wilcox. Turbulence modeling-an overview. In *39th Aerospace Sciences Meeting and Exhibit*, page 724, 2001.

L. Wong, F. H. Leung, and P. K. Tam. Lyapunov-function-based design of fuzzy logic controllers and its application on combining controllers. *IEEE Transactions on Industrial Electronics*, 45 (3):502–509, 1998.

W. Yi, W. SaGong, and H.-C. Choi. Drag reduction of a three-dimensional car model using passive control device. In *Proceedings of the KSME Conference*, pages 2868–2872. The Korean Society of Mechanical Engineers, 2007.